MA-HIP processing of yttria dispersion strengthened copper alloys for fusion application

MA Bing

DOCTOR OF PHILOSOPHY

Department of Fusion Science

School of Physical Sciences

The Graduate University for Advanced Studies, SOKENDAI

2021.09

Supervisors:

Dr. Yoshimitsu Hishinuma, Associate Prof.

Dr. Hiroyuki Noto, Assistant Prof.

Dr. Takeo Muroga, Prof.

Abstract

As the core component of fusion device, the divertor is expected to service in the extreme environment with high heat flux and irradiation damage, which require the heat sink materials of divertor should have excellent thermal conductivity and remarkable strength at elevated temperature. Cu-based materials were chosen as the primary heat sink materials because of its excellent thermal conductivity, but mechanical strength improvements through the strain hardening or the grain refinement or the solid solution strengthening or the precipitation strengthening or the dispersion strengthening of the Cu-based material are necessary. Among several precipitation strengthening due to the fine secondary phase formation through the conventional solution annealing and aging treatment is popular relatively because of its mature fabrication procedures. But the softening due to the coarsening of precipitates at high temperature and recrystallization during brazing limit the divertor operation range. The dispersion strengthening, introducing dispersive oxide particles by the powder metallurgy or the internal oxidation, is more attractive method because of better irradiation resistance, high thermal stability and the suppression of recrystallization at higher temperature. Compared to the oxide dispersion strengthened copper (ODS-Cu) with Al_2O_3 particles (Glidcop®), the ODS-Cu alloy with Y_2O_3 has potential advantages because of the higher enthalpy of Y_2O_3 formation, which is beneficial to maintain the thermal stability. In addition, the lower solubility of Y in the Cu matrix is also beneficial to the thermal conductivity. While, low solubility of Y to Cu leads to the unacceptable to apply the internal oxidation method, which is conventionally used to fabricate Glidcop®. The main route to fabricate the ODS-Cu alloy with Y_2O_3 must use the different process from the internal oxidation method, such as the mechanical alloying and hot isostatic pressing (MA-HIP). During the conventional MA-HIP process, the Y_2O_3 originated from the external addition still remains a larger size with Fe impurities after HIP. These Y_2O_3 are thermodynamically unstable and easily aggregate. Innovative MA-HIP process by in-situ fabrication method, in which the Y_2O_3 were in-situ formed by chemical reaction between the Y precursor and the O element, will be more attractive than the conventional process, because the in-situ formed dispersive particles has finer size and thermodynamically stable. Considering the fine dispersive particles with a high number density is the key factor in developing high strengthened ODS-Cu alloy, the objective of this doctoral thesis is that developing the innovative MA-HIP fabrication process by in-situ fabrication method to enhance the Y distribution, to refine the dispersive Y_2O_3 and to reduce the contamination.

Abstract

In this thesis, the ODS-Cu alloys with in-situ formed Y_2O_3 through innovative MA-HIP process by an in-situ fabrication method were investigated through adding not only pure metal Y but also Cu-Y compounds. For comparison, the ODS-Cu alloy with Y_2O_3 from the external addition was also fabricated by conventional MA-HIP process. Mechanical properties were evaluated by Vicker hardness test, tensile test. Physical properties were evaluated in the relative bulk density test by Archimedes principle, electrical resistance test by the four-probe method, thermal conductivity test by laser flash analysis method and phase transition by thermogravimeter-differential thermal analysis method. The crystal structure was explored by X-ray diffraction (XRD). The morphology and microstructure on the MA powers and the consolidated samples and the fracture surface after the tensile test were observed by optical microscopy (OM), field emission scanning electron microscopy (FE-SEM) equipped with energy dispersive spectrometry (EDS) and electron backscatter diffractometry (EBSD). Moreover, the particles distribution was analysis by transmission electron microscopy (TEM) equipped with EDS.

Based on the pure metal Y sourced ODS-Cu alloys, the influence of fabrication parameters (HIP temperature from 850 °C to 950°C, MA time from 32 h to 96 h) on the ODS-Cu alloys, and the mechanism of size distribution for MA powders were investigated. For the influence of HIP temperature explored in chapter 2, the enhanced diffusivity of Y and O in the Cu matrix at elevated temperature improved the correspondence between Y and O, promoting the in-situ formation of Y_2O_3. Besides, the increase in HIP temperature decreased the number density of micro holes, corresponding to the increase in relative density from 95.8 % to 98.9 %. Elevated HIP temperature is effective at enhancing the in-situ formation of Y_2O_3 and decreasing the porosity of the ODS-Cu alloys. For the influence of MA time from 32 h to 96 h explored in chapter 3, it was found that extending MA time enlarged the lattice parameter of MA powders from 3.596 Å to 3.6158 Å, because of the increase in Y solid solubility, resulting in the increase in Vickers hardness of MA powders from 100 Hv to 380 Hv. Extending MA time can enhance the uniform distribution of elements, while introducing more Fe impurities because of the abrasion between MA powders and steel balls. For the size evolution of MA powders explored in chapter 4, the coarse MA powders ($d > 200$ μm) with a shell structure occupied 80 wt. % of all MA powders. The shell of coarse MA powders had a larger Vickers hardness of 325 Hv and a higher oxygen content of 20 at. %, similar to the fine MA powders. On the other hand, the central region of coarse MA powders had an atomic ratio of Y and O being 2:3, same to the atomic ratio of Y_2O_3. Combing the morphology by SEM and diffraction patterns by TEM, the

peeled O rich fragments from the surface of coarse MA powders were the main source of finer MA powders with oxide-like microstructures, which have great influence on the thermal conductivity. Therefore, screening the alloyed MA powders before HIP is an effective way to improve the thermal conductivity of the ODS-Cu alloys.

In chapter 5, considering the more brittle Cu-Y compounds with lower Y enrichment could distribute homogeneously during the MA, the ODS-Cu alloys were fabricated through MA-HIP process by in-situ fabrication method using Cu-Y compound as the source of Y_2O_3. For the Cu-Y compound sourced ODS-Cu without oxidant, the Y distribution in the Cu_6Y sourced sample was more uniform compared with the Cu_2Y sourced sample at a lower Y content (0.39 wt. %). The XRD results and thermodynamic analysis showed that Y_2O_3 particles were successfully formed by the oxidation reaction between Y and the desorbed O impurity from the Cu matrix. The Cu-Y compounds can improve the purity of the Cu matrix. This method can expand the source material selection of dispersion particles for the ODS-Cu fabrication using Cu contained intermetallic compounds. On the other hand, the most of the unoxidized Y were aggregated and precipitated during HIP for Cu-Y sourced samples with higher Y content (2.36 wt. %), because of the HIP temperature being 1000 ℃ which is higher than the melting point of 927 ℃ for Cu_6Y, resulting in the aggregated phases during cooling process. For the sample with Cu_2O addition, the Cu_6Y compounds were oxidized at 847 ℃ before melting, forming fine dispersive Y_2O_3 particles with typical size of 15 nm and higher number density of $1.7 \times 10^{21}/\mathrm{m}^3$. Therefore, the oxidant addition is feasible and necessary to oxidize effectively the Cu_6Y compound before the melting under the in-situ fabrication process.

Furthermore, the comparisons among the direct Y_2O_3 sourced sample, the pure metal Y sourced and the Cu_6Y sourced sample with oxidant were conducted using the ODS-Cu with nominal content of 1.5 wt. % Y_2O_3. The fine particle sized Y_2O_3 formation using the brittle Cu_6Y compound can enhance Y dissolution and suppress the growth of MA powders. Finer Y_2O_3 particles (19 ±7 nm) with higher number density (18.0 x $10^{20}/m^3$) were formed in Cu_6Y sourced samples, compared to the direct Y_2O_3 sourced sample with larger (73±33 nm) Y_2O_3 particles having lower number density (2.5 x $10^{20}/m^3$) and the other ODS-Cu alloys in the world. The finer Y_2O_3 particles formed by Cu_6Y compound contributed to increase about 100 MPa on the estimated yield strength based on the Orowan mechanism. The estimated values agreed with the measured values very well but there was small mismatch. This would be possibly caused by the unoxidized Y and the contamination in the Cu matrix. It should be noted that the improvement of the estimated yield strength will be expected to enhance mechanical stability

under high temperature and neutron irradiation. The stable and finer Y_2O_3 particles and the interfaces between matrix and particles will act effectively as the pinning of the dislocation and the sink ability for irradiation defects. On the other hand, the Y and Cu_6Y sourced samples through the in-situ fabrication method had more Fe impurities, because of the oxidation of milling balls by O-rich layers, which are formed when the oxidant was added at the middle of MA process. More Fe impurities increased and hardened the surface layer of MA powders, introducing holes, thereby deteriorating the elongation of the ODS-Cu alloys.

In order to suppress the introduction of contamination, reducing the Y_2O_3 content from 1.5 wt. % to 0.5 wt. % for Cu_6Y sourced samples with an oxidant was carried out in chapter 6. It was found that the sample with 0.5 wt. % Y_2O_3 still remained at a higher number density of Y_2O_3 ($10^{21}/m^3$), accompanied by a decrease of Y_2O_3 particle size from 19±7 nm to 14±6 nm. This is because the low concentrated solid solute Y is beneficial in forming finer Y_2O_3 during the HIP process. Furthermore, lower Y_2O_3 content decreased the introduction of Fe impurities, and reduced the thickness of the Fe accumulated boundaries and porosity, thereby improving ductility. The reducing Y_2O_3 content also improved the thermal conductivity from 68.6 % ICAS to 81.2 % ICAS, because of the forming the thinner oxide-like O rich layers and lower Fe content impurities, which had great influence on the thermal conductivity.

Finally, it should be noted that the Cu_6Y sourced sample with a fine sized Y_2O_3 in high number density has a larger potential for future application once the Fe impurities and holes are reduced by modifying the grind mediums and oxidant addition. For grind mediums, the Cu coating to the steel mediums or the use of the tungsten (W) mediums are also expected to be an effective method for reducing the impurity. The W with extremely higher Mohs hardness is insoluble in the Cu matrix, which is beneficial to maintain the high purity of the Cu matrix. On the oxidant addition process, the modifying of the oxidant material selection and the oxidation method such as pre-oxidation by air and the optimizing of the oxidant content are also feasible and effective method to suppress the introduction of impurities.

In my doctoral thesis, the innovative MA-HIP process of the ODS-Cu with Y_2O_3 by the in-situ fabrication method was developed. The brittle Cu-Y compound, especially Cu_6Y compound was firstly proposed as the source of Y_2O_3. Several fabrication parameters, Y_2O_3 sources and content were investigated to enhance the uniform distribution of Y, to form finer dispersive particles and to suppress the introduction of impurities. The further improvements of the ODS-Cu with Y_2O_3 particles were also presented.

The main conclusions of my doctoral thesis are:

1. For the in-situ fabrication process, an elevated HIP temperature, a longer MA time (but introducing more impurities) and classification of MA powders can effectively enhance uniform distribution of Y and O elements, and optimize the microstructure and properties of the ODS-Cu alloys.

2. Cu-Y compounds, especially the Cu_6Y compound can act as the source of Y_2O_3 and enhance the Y distribution and Y_2O_3 refinement. Besides, adding oxidant is feasible and necessary for in-situ fabrication process.

3. Compared to the direct Y_2O_3 sourced sample with Y_2O_3 in a size of 73±33 nm and a number density of 2.5 x $10^{20}/m^3$, the Cu_6Y sourced sample in-situ formed fine Y_2O_3 particles 19±7 nm with a higher number density of 18.0 x $10^{20}/m^3$, but more impurities were introduced during the in-situ fabrication process.

4. Decreasing the Y_2O_3 content can refine the dispersive particles, maintain a high number density, and decrease the introduction of Fe impurities.

List of symbols

A: Constant vary between 0.3 and 0.6 based on the crystal structure

α: Coefficient of barrier strength

a_{hkl}: Lattice parameter, and h, k, l are the miller indices of the Bragg plane

$a(T)$: Thermal diffusivity at temperature of T

B: Burgers vector magnitude

β: Unit contribution of specific solute impurity to the electrical resistivity

C: Concentration of the solute atoms

$C_P(T)$: Specific heat at T

C_∞: Solubility

d: Inter-planner distance

d_K: Average diameter of grains

D: Diffusion coefficient

ΔG_f: Gibbs free energy of formation

$\Delta\rho^i(T)$: Resistivity contributed by the solid solute elements i

$\Delta\rho^{GB}(T)$: Resistivity contributed by grain boundary

$\Delta\rho^{poro}(T)$: Resistivity contributed by porosity

$\Delta\rho^{sec}(T)$: Resistivity contributed by second phases

$\Delta\sigma$: Increase of strength

$\Delta\tau$: Increase of shear stress

ε: Lattice strain

f: Volume fraction

g: Gravity constant

G: Shear modulus of matrix

G^{Cu_xY}: Gibbs free energy of Cu_xY

γ: Particle surface tension

k: Thermal conductivity

k_y: Hall-Petch coefficient

L: Lorenz number

λ: Wavelength of X-ray

λ(T): Thermal conductivity at temperature of *T*

M: Taylor factor

Ω: Partial molar volume

ρ: Density of dislocation

$\rho^{dis}(T)$: Electrical resistivity contributed by dislocation

$\rho^{gb}(T)$: Specific electrical resistivity by grain boundary

$\rho^{multi}(T)$: Electrical resistivity of the multi-phase materials

$\rho^{met}(T)$: Electrical resistivity of metal at temperature of *T*

$\rho^{pure}(T)$: Electrical resistivity of pure metal

ρ_s: Density of solid

ρ_w: Density of water

r: Radius of particles

$r^{dis}(T)$: Specific resistivity of dislocation

r_o: Initial radius of dispersive particles

R: Gas content

t: Time

T: Temperature

T_m: Melting point of Cu

τ: Shear stress

τ_o: Initial shear stress

S/*V*: Grain boundary area per unit volume

θ: Scattering angle

σ: Electrical conductivity

σ_o: Initial stress

σ_y: Yield strength

V_w: Volume of water

V_s: Volume of the sample

Contents

Chapter 1. Introduction

1.1 Advantages of fusion energy

The fossil fuels, which built the civilization of last two century with the sacrificing of pollution and greenhouse gases emission, gradually can't satisfy the requirement of the world development. The energy consumption will be higher and higher with the civilization development and reach three times of current level at the end of this century [1-3]. Besides, increasingly severe pollution and excessive greenhouse gas emission lead to the increase in global temperature, threatening the human environment. Carbon neutrality, which is a very hot topic recently, means that greenhouse gas emission equal to zero, and the greenhouse gas emissions by human beings equal to removing greenhouse gas from the atmosphere [4]. Carbon neutralities have to be achieved before 2050 if limit the rise of the global temperature within 1.5°C [5]. Besides, reaching the goal of energy safety by self-sufficiency is a primary concern for every country to ensure security and stability. Japan, as a resource limited country, is urgently needed to develop the replacement of fossil fuels, such as nuclear energy and renewable energy to ensure the self-sufficient and stable energy supplement, making contribution to the carbon neutrality at the same time.

Among the alternative energy, fusion energy has great promise. Fusion means that two or more light atomic nucleus combine to form one heavier nucleus, and release large quantities energy, which come from the conversation of mass loss from the fusing nuclei. Deuterium-tritium reaction (DT reaction) is the easiest reaction, whose Lawson's criterion is $n\tau > 1.5 \times 10^{14} s/cm^3 and\ T > 26\ keV$ [6], compared to various kinds of other fusion reaction, such as deuterium-deuterium reaction (DD reaction) with Lawson's criterion of $n\tau > 10^{16} s/cm^3\ and\ T > 100\ keV$ [6, 7]. DT reaction can produce alpha particles with energy of 3.5 Mev, and high energy neutron (14 Mev).

$$ {}_1^2D + {}_1^3T \rightarrow {}_2^4He(3.52\ MeV) + n^0(14.06\ MeV) \quad (1.1) $$

$$ {}_1^2D + {}_1^2D \rightarrow {}_1^3T(1.01\ MeV) + p^+(3.02\ MeV) \quad 50\% \quad (1.2) $$

$$ {}_1^2D + {}_1^2D \rightarrow {}_2^3He(0.82\ MeV) + n^0(2.45\ MeV) \quad 50\% \quad (1.3) $$

As an innovative, carbon neutral, and sustainable energy, fusion has many clear advantages:

(1) No greenhouse gas emission: the main production of fusion reaction is helium, which is inert gas, and no greenhouse gases are produced during fusion reaction. So, fusion is a good energy form to pursue the goal of the carbon neutrality.

(2) Abundant energy supplement and sustainability: For the same mass of fuels, the energy produced by fusion reaction is nearly four times larger than fission reaction and even four million times more than fossil fuels [8]. As the fuels of fusion reaction, the deuterium and tritium are widely available on the earth and almost inexhaustible. Deuterium, as one of most important fuels for fusion reaction, is a very stable isotope of hydrogen. The nucleus of deuterium is composed by one neutron and one proton. It is widely distributed in nature with content of around 0.014%, especially in the sea [9, 10]. Tritium can be produced during fusion reaction through interaction between neutron and lithium, whose land storage can supply the operation of fusion reactor for thousands of years, and sea storage can supply millions of years. So, fusion can provide abundant and sustainable energy for human beings' growing energy demand.

(3) No long-lived radioactive waste: Different from fission reaction, which can produced plenty of long-lived radioactive waste, fusion reaction only produce high energy neutrons and helium, without long-lived radioactive waste. The only potential radioactive hazard from components activated by neutrons is limited and the active material can be recycled within handed years through decaying.

(4) No risk of nuclear accident: Different from fission reaction mode, for which severe accidents happened in the last 40 years such as the Fukushima Daiichi in 2011 (Japan), the Chernobyl in 1986 (Russia) and the Three Mile Island in 1979 (USA) [11], such nuclear accidents can't occur in fusion reaction because of its intrinsic safety. The fusion reaction will suddenly stop if any disturbance occurs, and it is very difficult to maintain the fusion reaction. The fuels in the vessel used for fusion reaction at any time only enough for several seconds and there is no risk of chain reaction under the out of control.

Therefore, as a sustainable and innovative energy, fusion energy has bright prospects, without emission of greenhouse gases and potential radioactive hazard. The realization of fusion energy will make great contribution for the carbon neutrality and abundant energy supplement.

1.2 Types of fusion reaction

Before fusion reaction occur, a very high energy barrier supplied by electrostatic force must be overcame. Each nucleus repels due to the repulsive electrostatic force at longer distance. With the distance closer, the gradually larger attractive nuclear force, which is much stronger at close distance, can overcome the repulsive electrostatic force, combining the nuclei and releasing energy at same time. It is very difficult to realize the fusion reaction under control, because not only need the extremely high temperature (T) to enhance the particles to overcome the coulomb barrier, but also need sufficient confinement time (τ) with extremely high density (n), reaching the $\mathrm{nT}\tau > 10^{21}\ keV \cdot s/m^3$ [6]. The main modes to realize fusion reaction are inertial confinement fusion and magnetic confinement fusion.

1.2.1 Inertial confinement

Inertial confinement fusion is accomplished by hitting the fusion target, including deuterium and tritium, with the high energy laser from a series of ultra-high devices. The target is compressed and heated by the high intensity beams to realize the thermonuclear fusion ignition. The Fast Ignition Realization EXperiment (FIREX) Project, which is a big science research concerned with the laser fusion in Japan, has been progressed in Osaka University with the fusion development community in the world [12]. The advantage of FIREX is that the energy used for ignition is one tenth compared to central ignition.

1.2.2 Magnetic confinement

Magnetic confinement fusion is that containing a self-ignition plasma using high magnetic fields. The magnetic field is built by the plasma current induction and the coils surround the chamber to confine the plasma away from the vessel wall. The both the tokamak and helical type are the most two popular modes as shown in Figure 1.1.

(1) TOKAMAK, invented by Russia, is a confinement device in which high-temperature symmetrical toroid-shaped plasma is confined by ultra-high magnetic fields, which consist of toroidal magnetic field and poloidal magnetic field. Toroidal magnetic field is created by the electric current in toroidal coils, and poloidal magnetic field is produced by the current in the plasma and poloidal coils [13].

As the world's largest TOKAMAK currently, the International Thermonuclear Experimental Reactor (ITER) is the first commercial sized fusion experimental device, which device investigated to the development of the integrated and material technologies and the construct

fusion plasma physic regimes necessary to realize for commercial fusion power reactor. As the development route for tokamak, decision to transition to the DEMO will be taken in the 2030s based on the results of the JT-60SA and the joint international fusion experiment between Japan and Europe. And these results will be contributed to the beginning scenario of the ITER operation and the first DT reaction in ITER [14]. The DEMO's objective is that realizing steady electrical power output more than hundred thousand kilowatts, sufficient availability for commercialization, and self-sufficiency for tritium [15].

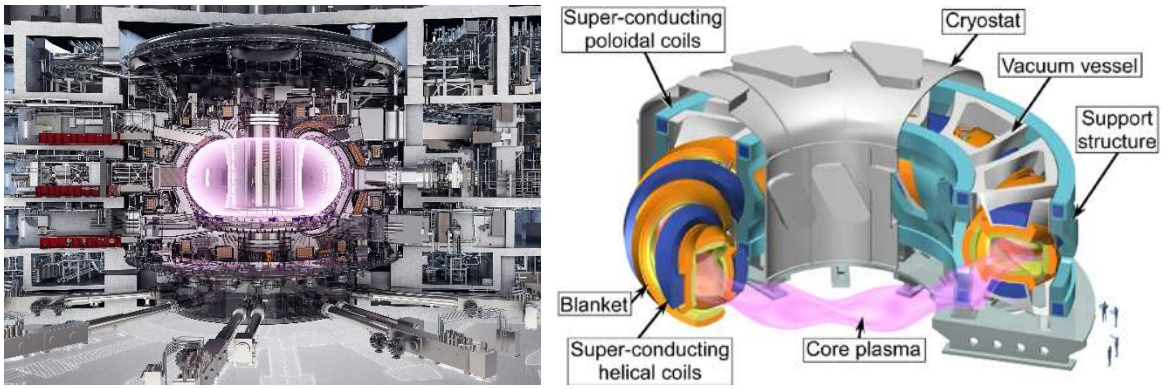

Figure 1.1 The schematic diagrams of Tokamak type (left) and Helical type (right) fusion reactors.

(2) Helical type, different from tokamak-type system, is a confinement system in which a non-symmetrical toroidal-shaped magnetic field is formed without requirement the plasma current [16]. Both toroidal and poloidal magnetic fields provided by external coils is also necessary. It has advantages of steady state operation and controllability compared with the plasma confinement system which rely on the current in the plasma.

1.3 Divertor

The divertor, as the one of the core components in both tokamak type and helical type fusion devices at the bottom of the vacuum vessel, is used to remove the helium ash produced by the fusion reaction and impurities released from the first wall, minimize plasma contamination, maintain high purity plasma and sustain the fusion reaction [17]. The divertor converts the charged particles in the plasma to molecules or atoms, and guide them to divertor plates along the magnetic lines on the outside of the confined plasma. Besides, it can protect the first wall of vessel from high energy neutron and ultra-thermal loads.

Flat plate type and mono-block type divertors are the most popular devices used in fusion capabilities as shown in Figure 1.2 [18-20]. Flat type divertor is armored by tungsten flat tiles, which are joined with the heat sink block fabricated by Cu alloys. This design type has

relatively simple fabrication procedures and stability. Besides, this simple design has more flexibility for cooling scheme. But the global stability strong depends on the initial local joint quality, and the cascade failure caused by neighboring fail tiles might occur [20]. Mono-block type divertor has common geometric shape with array of rectangular mono-blocks fabricated by tungsten, and cooling pipe at the middle as the heat sink. Mono-block type divertor has larger capability for the heat load, and cascade fail can't occur. It has been proved the robust stability under irradiation environment. However, compared to the mature technology for flat plate type in industrial level, the more difficult manufacture for mono-block type only reaches the prototypical level, and need further improvement [21].

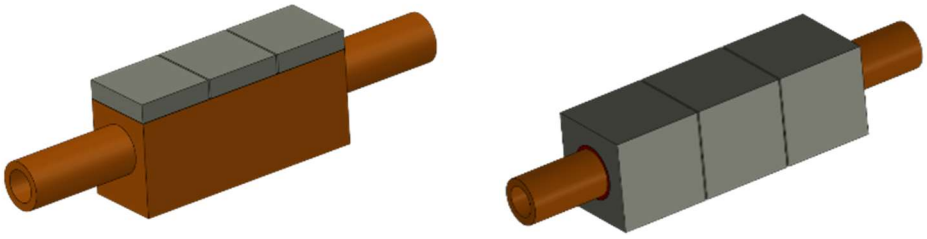

Figure 1.2 The schematic diagrams of Flat type (left) and Mono-block type (right) divertors.

As the most critical component in fusion capability, the divertor is expected to operate in the environment with high heat flux, high neutron irradiation damage [19]. The He particles and neutrons with high energy produced by the fusion reaction are guided to hit the divertor. The high energy particles and the heat sink materials are interacted in the form of collisions and scattering, inducing neutron irradiation damage. The cascade collisions can introduce various kinds of defects, including vacancies and interstitial particles, causing irradiation hardening, swelling and degradation of the thermal conductivity. Besides, the high energy neutron can react with the nuclei of target by neutron activation. The atoms in excited condition will decay through radiation, causing long lifetime radioactive isotopes. And some transmutation products will make great influence on materials, such as embrittlement caused by the He interaction. Moreover, during burning of the fusion plasma, the divertor will suffer various steady and unsteady combined force caused by the relative movement of vessels, thermal bowing, and neutron induced swelling in high temperature and irradiation condition.

1.4 Requirements of the heat sink materials for divertor

The severe environment put high requirements for the heat sink materials. The design specification for ITER divertor requires smooth operation such as at least 300 loading cycles at 20 MW/m^2. The irradiation damage dose for the heat sink materials was calculated to be 1.7

dpa (Displacement Per Atom) per full power year in the case of ITER [23, 24]. These environments will be even worse, and the requirement will be much stricter for DEMO and commercial fusion reactor in future. This severe operation environment requires the heat sink materials should have better thermal and mechanical properties under elevated temperature and neutron irradiation [25].

(1) Thermal properties: Excellent thermal conductivity (>250 W/m·K) is the primary parameter for the heat sink materials of divertor. Lower coefficient of thermal expansion is also better.

(2) Mechanical properties: High mechanical properties at elevated operation temperature (<400 °C), including fatigue resistance, creep resistance and tensile strength. Besides, ductile with higher fracture toughness is also needed.

(3) Irradiation resistance: Irradiation by fast neutrons with higher energy and flux is one of the most critical key issues for the heat sink materials. The heat sink materials should have better irradiation resistance, including irradiation creep resistance, irradiation hardening and embrittlement resistance, and lower irradiation swelling rate. Besides, lower active elements should be used.

There are some other requirements, such as coolant compatibility, lower H and isotope solubility, lower cost, and availability.

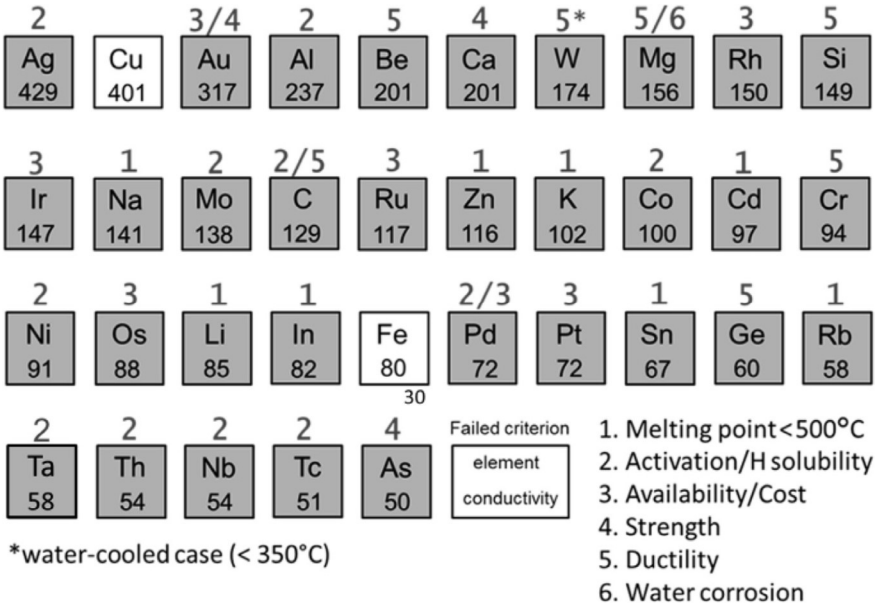

Figure1.3 The potential element with the conductivity higher than 50 W/m·K marked with important parameters for the heat sink application [26].

Figure 1.3 shows the potential metallic elements with important parameters should be overcame if used for the heat sink materials, including higher melting point, low activation and hydrogen (H) solubility, available and economical, excellent strength and ductility, water corrosion resistance and so on. The potential elements were listed in the descending list based on the thermal conductivity. The elements with dark grey box demonstrate that there is at least one parameter can't satisfy the requirement. The numbers marked on the top of element are the failed parameters. It found that only Cu can satisfy all the requirements as the heat sink material except Fe, which has much poor thermal conductivity compared to Cu. Therefore, copper-based materials are the only choice for the heat sink materials.

1.5 Strengthening mechanisms

Pure Cu has poor performances in the form of strength, thermal stability, and irradiation resistance. The strength will deteriorate at high temperature. Besides, irradiation swelling, hardening, embrittlement will occur during neutron irradiation. Cu should be strengthened to improve the mechanical properties, irradiation resistance, and maintain their thermal conductivity at the same time to meet the requirements. The strength of materials is closely related to the movement of dislocations, and it can be improved by impeding, hindering, or even preventing the movement of dislocation. There are several methods to achieve this purpose shown as follows.

1.5.1 Strain hardening

Strain hardening is that introducing more dislocations to strengthen the metals through plastic deformation by cold working. The increased dislocations can combine to network, forming nodule to lock each other and inhabit the movement, rendering the metal harder, while more brittle. The influence of dislocation on shear stress τ can be described as follows [27]:

$$\tau = \tau_o + A\sqrt{\rho} \tag{1.4}$$

Where τ_o is the initial shear stress, A is a constant that vary between 0.3 and 0.6 based on the crystal structure, and ρ is the density of dislocation introduced by cold working.

The strength of pure Cu can be obviously improved by cold working. However, the dislocations introduced by cold deformation can be recovered at relative higher temperature (0.3 T_m, where T_m is the melting point of Cu).

1.5.2 Grain boundary strengthening

The essence of grain boundary strengthening lies in the hindering effect of grain boundaries on the movement of dislocations. The finer grains introduce more grain boundaries and make greater hindering effect on the movement of dislocations, thereby improving the strength of materials. When a migrated dislocation glide to contact with the grain boundary, formed between two misoriented grains, the glide plane is not continued fluently, and can form dislocation pile-up group. The hindrance level meanly depends on the misorientation angle and the average grain size. The grain can be controlled by metallurgical treatment, thermomechanical treatment, and multi-physical treatment. For metallurgical treatment, adding grain refinement agent, increasing subcooled temperature, and heat treatment at the recrystallization temperature can form smaller grains through increasing the nucleation density. For thermomechanical treatment, large deformation at specific temperature can break the grains, such as rolling, forging, Equal channel angular pressing (ECAP), High pressure torsion (HPT), Dynamic plastic deformation (DPD), mechanical alloying (MA) and so on. For multi-physical treatments, the melt-solidification processes using the magnetic field, electrical field, or ultrasonic field can also enhance the formation of smaller grains [28].

The influence of grain boundary on yield strength σ_y is governed by Hall-Petch rule shown as follows [29]:

$$\sigma_y = \sigma_o + \frac{k_y}{\sqrt{d_K}} \tag{1.5}$$

Where σ_o is the initial stress of metals; k_y is the Hall-Petch coefficient, represents the resistance of grain boundary; d_K is the average diameter of grains.

Pure Cu strengthened by strain hardening or grain boundary, exhibit the excellent thermal conductivity, but poor mechanical performance at elevated temperature, which limit the application range.

1.5.3 Solid solution strengthening

Solid solution strengthening introduces solute atoms into the matrix, resulting in high lattice distortion because of the different size between solute atoms and solvent atoms. The solute atoms and the surrounded distorted lattice can act as the pinning the dislocations and suppress their movement. There are two kinds of solid solution mechanisms, substitutional solid solution

and interstitial solid solution, depending on the size difference of solute elements and solvent element.

The strengthening mechanism depends on the concentration of solute atoms, and the size difference between solute and solvent atoms [30].

$$\Delta\tau = Gb\varepsilon^{\frac{3}{2}}\sqrt{C} \tag{1.6}$$

Where $\Delta\tau$ is the increase of shear stress by solid solution strengthening, G is the shear modulus of matrix, b is the burgers vector magnitude, ε is the lattice strain caused by solute atoms, C is the concentration of the solute atoms.

The tensile strength of Cu alloys strengthened by solute atoms is obviously improved but sacrificing the thermal conductivity. The solute atoms into the Cu matrix cause lattice distortion and have great influence the thermal conductivity [30]. Besides, solid solution strengthened metals have the similar downward trend with pure Cu in irradiation environment [25, 31, 32].

1.5.4 Precipitation & dispersion hardening

The movement of dislocations can not only be obstructed by the mechanisms shown above, but also be obstructed by the second phases, which can be introduced in the form of precipitated particles (precipitation hardening) or dispersive particles (dispersion hardening). The precipitated particles are soluble and can be dissolved into the matrix at elevated temperature, and then precipitated by quenching and aging at specific temperature. The dispersive particles are stable and can be introduced by mechanical alloying or internal oxidation method. Different from precipitated particles, the dispersive particles have negligible solubility in the matrix even at elevated temperature. The representatives are oxides, carbides, nitrides, borides and so on.

The interface between the second phases and matrix can be partly coherent or incoherent. For the coherent or semi-coherent boundaries, the dislocations can move through the second phase by shearing them, creating additional phase boundaries. The energy of shearing and new boundary formation is supplied by the stress. The improved strength $\Delta\sigma$ can be described [33, 34]:

$$\Delta\sigma \approx 6G\left(\frac{r}{b}\right)^{0.5} f^{0.5}\varepsilon^{1.5} \tag{1.7}$$

Where G is shear modulus, r is the radius of particles, b is the burgers vector, f is the volume fraction of particles, and ε is the strain field factor.

For the incoherent boundaries, the dislocations bend around and bypass them by Orowan bowing mechanism. The improved yield strength $\Delta\sigma$ can be described [30]:

$$\Delta\sigma = M\alpha Gb/\lambda \tag{1.8}$$

$$\lambda = \frac{4(1-f)r}{3f} \tag{1.9}$$

Where M is Taylor factor, α is the coefficient of barrier strength, f is the volume fraction of particles, and r is the radius of particles. The precipitation and dispersion strengthening are great influenced by the number density and particles size of the precipitate particles and dispersive particles. Figure 1.4 shows the two models of the passage of dislocations described above. The Rösler-Arzt theory shows that the optimum size of dispersive particles is 8~18 nm in Cu alloys [35].

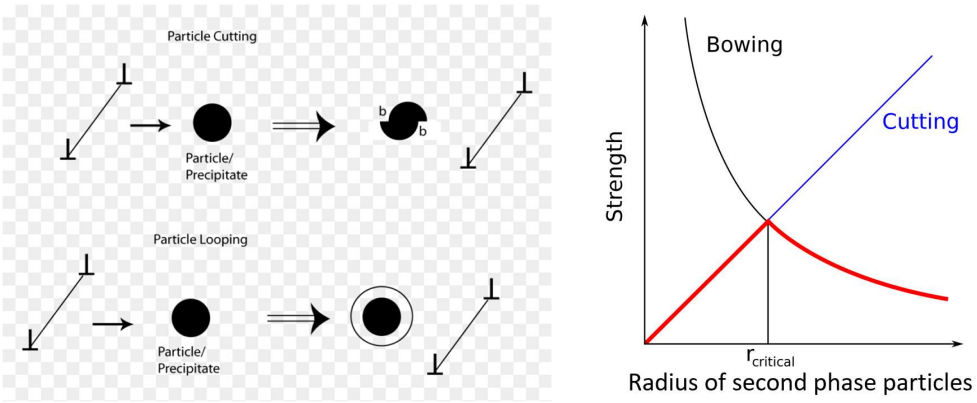

Figure 1.4 Two models of the passage of dislocation.

As the representative precipitation strengthened Cu alloys, CuCrZr is the baseline for heat sink material of IETR. The heat treatment of CuCrZr-IG (ITER grade) is that solution annealing at 980~1000 °C for 1 h, followed by water quenching, then aging at 450~480 °C for 2~3 hours [35, 36]. CuCrZr-IG has unique comprehensive properties, including excellent thermal conductivity, higher strength at target temperature, better ductility and toughness. However, the severe environment will challenge the CuCrZr as the heat sink materials. Over aging is easier occurred for CuCrZr at relative high temperature, significantly coarsening the precipitates and grain structure. Therefore, CuCrZr cannot be joint through conventional furnace brazing or welding techniques [37]. Besides, the ultimate tensile strength of CuCrZr-IG reduces from 270 MPa to 170 MPa with the temperature increase from room temperature to 400 °C. Moreover, CuCrZr-IG suffered plastic fatigue at the high heat flux of 20 MW/m^2 [38, 39]. The irradiation caused by fast neutrons with high energy and flux is expected another serious issue. The irradiation damage can cause embrittlement below 250 °C with the uniform elongation of 1~2 %, swelling at 300 °C similar with pure copper, and irradiation enhanced creep above 350 °C for CuCrZr-IG [26]. Even so, the CuCrZr-IG was selected as the heat sink

material for ITER, but the narrow window of operation temperature limits its application in future [40].

For the dispersion strengthening (DS), the dispersive particles can act as the pinning of the movement of dislocations, can prevent the recrystallization and the grain coarsening at high temperature, and also is useful to maintain high mechanical strength even at elevated temperature. Furthermore, the dispersion strengthened materials have better irradiation resistance. The DS-Cu maintained high tensile strength, high thermal conductivity, and small irradiation swelling, compared to pure Cu. However, the DS-Cu also showed linear decreases of tensile strength and 30% swelling under harder neutron irradiation condition at 400 °C with 150 dpa [41]. Compared to the other strengthened Cu alloys, the DS-Cu alloys are more promising because of their excellent strength, lower decrease of thermal conductivity, and much better irradiation stability [42-45].

The thermal and mechanical properties of oxide dispersion strengthening (ODS) -Cu alloys were great influenced by the oxide dispersive particles. Glidcop® developed by North American Höganäs is Cu-based metal strengthened by Al_2O_3 particles [46], which is easier to coarsen compared to other dispersive particles, leading to the deterioration of the strength at elevated temperature shown as in Figure 1.5 [47]. Besides, the fracture toughness of Glidcop® decreased very fast with the increased temperature. A larger reduction with a factor of 2-3 from room temperature to 350 °C after irradiation are reported [48]. Therefore, in order to satisfy the design requirements of DEMO and future fusion reactors, the other dispersive particles to improve high temperature performance of ODS-Cu alloys should be developed.

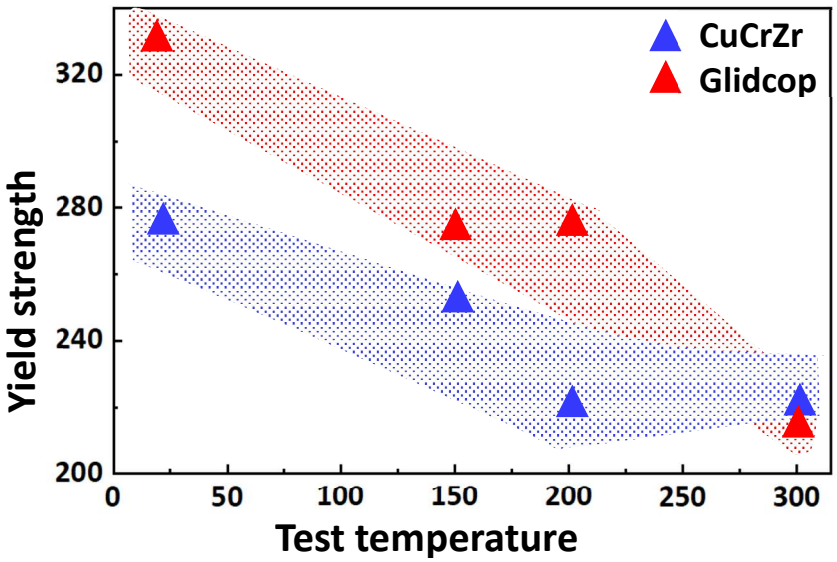

Figure 1.5 Yield strength versus test temperature for Cu alloys. [47]

1.6 Selection of the dispersive particle

The principles of particle selection should be considered from the points of thermodynamic stability, coarsening resistance, mechanical stability and interface stability.

(1) Thermodynamic stability: The peak operation temperature for the heat sink materials is typically in the range of 700-1300 K [35], and the anticipated operation temperature is significantly higher. So, the candidate dispersive particles should have better thermodynamic stability without phase transformation even at elevated temperature around 1300 K [35]. Low enthalpy of formation at high temperature and high melting point contribute to the thermodynamic stability of the dispersive particles. Table 1.1 shows the enthalpy of formation of the candidate dispersive particles at 1300 K, and the corresponded melting points. Compared to Al_2O_3 used in the Glidcop®, the Y_2O_3 has higher thermodynamic stability because of the lower enthalpy of formation and higher melting point.

(2) Coarsening resistance: Low solubility and diffusivity of the dispersive elements in the Cu matrix are required to prevent the coarsening during service temperature, contributing to the maintenance of high strength and high thermal conductivity at elevated temperature [35]. Besides, the purity of Cu matrix plays a more important role on the thermal conductivity than the dispersive particles. The dissolution of dispersive particles and formation of solid solution atoms can severely deteriorate the thermal conductivity. Therefore, coarsening resistance is the primary factor for dispersive particles to achieve excellent strength and thermal conductivity without deterioration. The coarsening kinetic of dispersive particles can be described by Lifshitz-Slyozov-Wagner law shown as follows [49]:

$$r^3 - r_0^3 = \frac{8\gamma C_\infty \mathrm{D}\Omega^2}{9RT} t \tag{1.10}$$

Where, r is the radius of dispersive particles, r_o is the initial radius of dispersive particles, γ is the particle surface tension, D is the diffusion coefficient of corresponded elements, C_∞ is the solubility of the solute elements. Ω is the partial molar volume. R, T and t are the ideal gas constant, absolute temperature and time, respectively. So, low diffusivity and solubility are necessary for the coarsening resistance. Compared to the Al_2O_3 used in the Glidcop, the Y_2O_3 has better coarsening resistance because of much lower solubility of Y element (0.005 at. %) than Al element (16.2 at. %) in Cu matrix.

(3) Mechanical stability: Minor difference in thermal expansion coefficient between Cu matrix and dispersive particles can avoid the fatigue micro cracks around the interface and

providing excellent thermal fatigue resistance. Table 1.2 shows the physical properties of the candidate ceramic phases for DS-Cu. It can be found that the mismatch of thermal expansion ($\Delta\alpha$) between ceramic and copper is lower for Y_2O_3 than that for Al_2O_3.

Table 1.1 Enthalpy of formation and melting point of the candidate dispersive particles [35].

	Enthalpy of formation (KJ/mol)	Melting point (K)
Y_2O_3	-1905.3	2703
Al_2O_3	-1667	2323
Cr_2O_3	-1140	2708
CeO_2	-1088.7	2873
TiO_2	-944.7	2113
Si_3N_4	-744.8	2173
CaO	-635.1	2845
MgO	-601.2	3073
Be_3N_2	-588.3	2513
SiC	-67	2700

Table 1.2 Physical properties of the candidate ceramic phase for DS-Cu. [35]

	Modulus of elasticity (GPa)	Density (g/cm^{-3})	$\Delta\alpha$ (10^{-6} /℃)
Y_2O_3	120	5.03	7.3
Al_2O_3	380	3.97	7.8
Cr_2O_3	103	5.21	8.2
TiO_2	283	4.25	7.2
SiC	207	3.18	11.9

(4) Interface stability: the interface of dispersive particles and Cu matrix play an important role on the mechanical properties of ODS-Cu alloys. The commercial Glidcop® contains Al_2O_3 nano dispersoids with high disordered spinel type structure and incoherent $\{111\}_{Al_2O_3}$ / $\{111\}_{Cu}$ interface with Cu matrix [50, 51]. The incoherent interface can induce the stress concentration because of the accumulation of the tripped dislocations, leading to the premature initiation of micro cracks [52]. Different from Al_2O_3 interface, the Y_2O_3 has semi-coherent interface of $\{001\}_{Y_2O_3}$ / $\{001\}_{Cu}$ with Cu matrix. For semi-coherent interfaces, some of

dislocations can enter the interior of the dispersive particles [51, 53]. The semi-coherent interface can balance the pinning effect and the inhibition of the micro cracks caused by the dislocations' accumulation, thereby improving the mechanical performance [54].

Therefore, Y_2O_3 is a very competitive dispersive particle for ODS-Cu alloys compared to Al_2O_3 because of better comprehensive properties: lower enthalpy of formation and higher melting point, insolubility and lower diffusivity into Cu matrix, smaller difference of thermal expansion coefficient, and semi-coherent interface with Cu matrix [48, 50, 51, 53, 55-71].

1.7 Thermal conduction mechanisms

As one of the important factors for the heat sink material, thermal conductivity can be simply described by electrical conductivity through Wiedmann-Franz law shown as follows [72]:

$$\frac{k}{\sigma} = LT \tag{1.11}$$

Where k is the thermal conductivity, σ is the electrical conductivity, L is the Lorenz number and T is also the temperature.

For non-pure metals, which means some impurities are included, called contamination if unintentional, while called dopants if intentional, the electrical resistivity, which is the inverse of electrical conductivity, can be divided by Matthiessen's rule shown as follow [73, 74]:

$$\rho^{met}(T) = \rho^{pure}(T) + \sum_i^n \Delta\rho^i(T) + \Delta\rho^{dis}(T) + \Delta\rho^{GB}(T) + \Delta\rho^{poro}(T) \tag{1.12}$$

Where $\rho^{met}(T)$ is the resistivity of metal at temperature of T; $\rho^{pure}(T)$ is the resistivity of pure metal without any defects at temperature of T. The electrical resistivity of pure copper ρ^{pure-} at room temperature is 16.7 nΩm; $\Delta\rho^i(T)$ is the resistivity contributed by the solid solute elements i; $\Delta\rho^{di}(T), \Delta\rho^{GB}(T)$ and $\Delta\rho^{poro}(T)$ are the resistivity contributed by dislocation, grain boundary and porosity, respectively.

For the precipitation strengthened or dispersion strengthened Cu alloys, which include other phases except the Cu matrix, the contribution of those phases to resistivity should be considered as follows:

$$\rho^{multi}(T) = \rho^{meta}(T) + \Delta\rho^{sec}(T) \tag{1.13}$$

Where, the $\Delta\rho^{sec}(T)$ is the electrical resistivity of the multi-phase materials, and $\Delta\rho^{sec}(T)$ is also the contribution of second phases on electrical resistivity.

The effect of impurities on electrical resistivity $\Delta\rho^i$ can be calculated according to [75]:

$$\Delta\rho^i(T) = \beta f \tag{1.14}$$

Where β is the unit contribution of specific solute impurity to the electrical resistivity, for Fe impurity in Cu matrix, $\beta = 115 \times 10^{-9}\Omega m$ and the f is also the concentration of solute element [30]. The contamination has great influence on the resistivity of ODS-Cu alloys. Trace solute elements can severely deteriorate the thermal conductivity of Cu based materials. The effect of much smaller content of solid solute Fe with 0.13 wt. % on electrical resistivity is 15 nΩm, much larger than the contribution of dispersive particles (0.33 nΩm) and the ground boundary (2.5 nΩm) [30].

The effect of dislocations on the electrical resistivity $\Delta\rho^{dis}(T)$ can be calculated as follows [48]:

$$\Delta\rho^{dis}(T) = \rho \times r^{dis}(T) \tag{1.15}$$

ρ is the density of dislocations, and $r^{dis}(T)$ is the specific resistivity of dislocation, and have a value of $0.8\times 10^{-2}\ \Omega m^{-3}$ for copper at room temperature [76].

The contribution of grain boundary to the electrical resistivity is defined as follows [77]:

$$\Delta\rho^{GB}(T) = \frac{2}{3}\rho^{gb}(T) \times \left(\frac{S}{V}\right) \tag{1.16}$$

Where, the $\rho^{gb}(T)$ is the specific electrical resistivity by grain boundary. $\rho^{gb} = 3.12 \times 10^{-16}\Omega m$ for Cu matrix at room temperature [77]. The ratio of *S*/*V* is the grain boundary area per unit volume, approximated to be $2.37/d_G$ [77], where the d_G is the mean diameter of grain.

The precipitates and dispersive particles also contribute to the resistivity by scattering the free elections. The contribution of Y_2O_3 particles or porosity on electrical resistivity can be calculated using the modified Schroeder equation for the second phase with higher resistivity [78]:

$$\Delta\rho^{sec}(T) = \Delta\rho^{m}(T) \times \frac{3f}{(1-f)} \tag{1.17}$$

Where $\Delta\rho_m(T) = \rho^{pure}(T) + \Delta\rho^{disl}(T) + \Delta\rho^{GB}(T)$. The $\rho^{pure}(T)$, $\Delta\rho^{disl}(T)$ and $\Delta\rho^{GB}(T)$ mean resistivity of based matrix, the contribution of dislocation, and the contribution of grain boundary, respectively. f is the volume fraction of second phases. The contribution of porosity

on the resistivity can be calculated based on the same equation, in that case the vacancy was recognized as the second phase.

1.8 The non-equilibrium processing for ODS-Cu

The lower solubility of oxide dispersive particles in Cu matrix prevents the fabrication of ODS-Cu alloys by equilibrium processing. The lower density of dispersive particles ($\rho_{Y_2O_3}$ being 5.03 g/cm^3, and $\rho_{Al_2O_3}$ being 3.97 g/cm^3) and higher melting points lead to the rapid formation of the oxide slag on the surface of molten Cu [48]. Therefore, the non-equilibrium solid state processing is necessary for the fabrication of ODS-Cu alloys.

Non-equilibrium processing is a novel technique fabricating the desired materials by thermodynamic non-equilibrium system. There are several factors can be regulated to obtain the non-equilibrium condition, such as temperature, mechanical stress, light, pressure, and so on. The corresponded techniques are rapid solidification process, mechanical alloying, laser process, and thermal plasma process shown as follows.

1.8.1 Rapid solidification processing

Rapid solidification processing developed by Pol Duwez at 1960s can form non-equilibrium phases and increase the solid solubility limit. During rapid solidification processing, the thermal energy is rapidly extracted during the transition process from the melted liquid to solid condition. Different from conventional casting, where the usual cooling rate is about 1 K/s or less, the cooling rate in rapid solidification process can be faster than 10^3 K/s [79]. The process of metals remained in liquid phase form with higher temperature is limited in milliseconds, followed by quenching with water or liquid nitrogen to room temperature, resulting in non-equilibrium condition. The rapid solidification process has three methods. First is droplets method as shown in Figure 1.6, in which atomization process by using spray method to fragment or atomize the melt stream into droplets. This droplet technique is more popular to fabricate large quantities of rapid solidified materials. But the cooling rate in the normal atomization process is lower with rate of $10^2 - 10^3$ K/s [79]. Second is spinning method, in which the melt stream was casted onto a lean metal wheel by foil casting process, forming orifice in the forms of thin strip or ribbon without fragmentation. The cooling rate in this kind of method is typically about $10^5 - 10^6$ K/s [80], depending on the thermal conductivity of substrate, the section thickness and so on. Third is surface melting method, which is in-situ

melting a thin layer followed by rapid solidification on the surface of heat sink. The cooling rate in this process can reach very high level of 10^{14} K/s [81].

The commercial Glidcop® is fabricated mainly based on rapid solidification process through droplet method [46]. Supersaturated solid solute Al are internal oxidized by air and then reduced by hydrogen, finally consolidation by extrusion. However, the oxides bonds consisted of coarse Al_2O_3 particles with different size and shape are first formed, which can highly suppress the internal oxidation process. The inhomogeneous microstructure significantly degrades the performance of Glidcop® [82]. For the Y_2O_3 dispersion strengthened copper, it is very difficult to form supersaturated solid solute Y in Cu matrix by rapid solidification process because of the extremely low solubility of Y in the Cu matrix. Aggregation and precipitation occurred even in the high-speed solidification process [55].

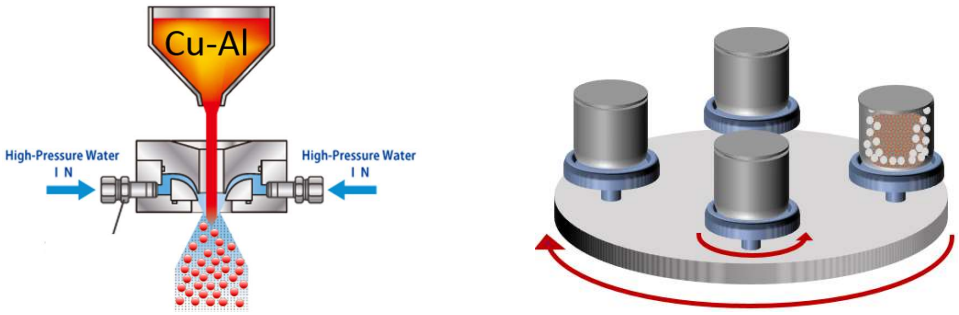

Figure 1.6 The schematic diagrams of rapid solidification processing (left) and mechanical alloying (right).

1.8.2 Mechanical alloying

Mechanical alloying (MA) is a novel technique as shown in Figure 1.6, which can great breakthrough the limitation of the solid solubility of solute in the solvent matrix, used to fabricate the ODS materials. In this solid-state process, the blend powders are repeated fractured and cold welded by ball milling in high speed to fabricate the homogeneous distributed composite materials. Both the blend powders and pre alloyed powders can be used as the initial powders [83, 84].

During MA process, the ductile powders were severe plastic deformation with the increase in surface-to-volume ratio, and the brittle powders such as intermetallic compounds will fracture and comminute more severely for refinement. The MA powders are subjected compression and high shear by high-speed collision, resulting in mixing, shaping and bonding each other, balancing the fracture and welding, all of which greatly accelerate the diffusion rate

of dispersive elements. In microscopic level, the defects such as solid solute atoms, vacancies, and dislocations are introduced and accumulated, causing the destabilization of the crystalline phases, resulting in the decrease of grain size, and contributing to the increase in free energy of the alloyed powders. The nanocrystal powders contain plenty of atoms at the grain boundaries, thereby the diffusivity of solute atoms is greatly accelerated, and the solid solubility is therefore increased compared to the phase diagram [85].

For Cu, which is ductile material, adding several weight percent of process control agent (PCA) is one of the popular methods during mechanical alloying [86]. PCA is covered on the surfaces of the MA powders, including the new surfaces formed by fracture. PCA can effectively minimize the severe cold welding among the powders and the grinding mediums. But PCA addition unavoidably introduce contamination into the alloyed powders. Because the most of the PCA are organic materials, such as stearic acid, ethanol and so on, and include carbon, oxygen, nitrogen and hydrogen elements. Some of the PCA can be removed by the followed heat treatment due to their low melting and boiling points. But some of them decompose during MA process and react with the alloyed powders, forming undesirable carbides, oxides, nitrides and so on. Another method to avoid the severe sticking is cryogenic milling, which is a mechanical alloying process at lower temperature (< 123 K) cooled by liquid nitrogen, liquid carbon dioxide or other coolant [58, 87-89]. During cryogenic milling, which is the extremely low alloying temperature, can suppress the recovery and the recrystallization, resulting in rapid grain refinement and finer MA powders. The low temperature avoids the severe sticking in some degree and make the soft materials grindable. Cryogenic milling can avoid the PCA addition and decrease the contamination. However, considering that there is no ductile brittle transition temperature (DBTT) for Cu, which is FCC crystal structure, the suppression for sticking is limited. Besides, the complex mechanical alloying process limit the industrial scale. There are some other methods used to suppress the growth and stick of alloyed powders. Intermittent milling to prevent the sharp increase of temperature is a useful method to suppress the growth of alloyed powders [37, 89]. Another method is adding more brittle blend powders [71]. Some of targeted pure metal powders are ductile because of their crystal structure. While the corresponded intermetallic compounds are brittle. Using the intermetallic compounds, instead of blended pure metal powders, as the source of MA powder is an effective method to suppress the growth of MA powders, example of minimizing the sticking of MA powders, and to prevent the introduction of contamination.

1.8.3 In-situ fabrication method in MA process

During the conventional MA process, the reinforced dispersive particles are introduced from the outside directly, in which the dispersive particles always keep larger size, thermodynamic instability, low interface bonding strength and so on. Besides, the lower number density of dispersive particles limits the contribution of dispersion strengthening [33, 34].

In-situ fabrication method is an innovative MA process by adding precursor of dispersive particles to form the reinforced dispersive particles by in-situ chemical reaction [90-96]. In-situ fabrication method by mechanical alloying is a promising technique to produce the composite with strengthened dispersive particles. During MA process, the reactant is subjected compression, high shear by high-speed collision, result in mixing and dissolving into the based matrix, forming 2-D dispersive nucleus. The reinforced dispersive particles are in-situ formed by chemical reaction in the following consolidation treatment, and the size of in-situ formed particles can be adjusted by the consolidation parameters, such as temperature, time and so on [91].

There are many obvious advantages for the in-situ formed dispersive particles. Compared to the ex-situ nano particles, the size of in-situ formed particles can easier be refined to be nano-class with coherent or semi-coherent particle/matrix interface. The coherent or semi-coherent interface can reduce the interfacial energy between the matrix and dispersive particles, beneficial to the stability of the dispersive particles [91]. Besides, the in-situ formed dispersive particles is beneficial to the overall mechanical performance because some dislocations can enter the interior of dispersive particles along the coherent or semi-coherent interface due to the low mismatch and lattice distortion, contributing to the reduction of dislocations accumulation and the improvement of macroscopic performance [91].

There are several kinds of materials act as the source of Y_2O_3 during in-situ fabrication process. One is pure metal Y, which is oxidized by the dissolved O impurity in the matrix or the added oxidant, forming Y_2O_3 particles.

$$Y + O \rightarrow Y_2O_3 \tag{1.18}$$

Second is Y contained intermetallic compound. In order to minimize the introduction of contamination into the Cu matrix, only Cu-Y can be expected as the source of Y_2O_3. The in-situ reaction during fabrication process is shown as follows:

$$Cu - Y + O \rightarrow Y_2O_3 + Cu \tag{1.19}$$

Third is Y containing organics, such as yttrium acetate ($Y(CH_3CO)_3 \cdot 4H_2O$), which can play the roles of both the PCA and the source of Y_2O_3. While the introduction of contamination is inevitable [71].

1.8.4 Other non-equilibrium processing

Laser processing is that melting or changing the characteristics of the surface of work piece by high energy laser beams. The laser process is conducted in a smaller range with very high speed. Rapid heating and cooling rate during laser process can be used to fabricate non-equilibrium materials with supersaturated solid solute phases. The materials fabricated by laser usually exceed the limit of solid solubility shown in the equilibrium phase diagram. The common cooling rate in this method is 10^5 K/s, and faster cooling rate up to 10^{14} K/s is also reported [98]. While this method only popular in modifying the surface of materials, named laser surface modification (LSM)**.**

Thermal plasma processing is widely used from spray coating to metallurgy. This method can be divided into process metallurgy and plasma spray coating. For process metallurgy, plasma with high temperature can faster melt, refine and cast the metals or alloys, compared to conventional methods. High melt and quench rates can shorten the fabrication process into milliseconds, result in non-equilibrium condition, forming supersaturated solid solute phases [99]. Plasma spray coating is one of the prime candidate methods to produce coating for base material in the forms of wear, thermal barriers and so on. The materials used for coating are supplied in the form of wires as the arc electrodes. The gas jet melts the electrodes and coats the substrate. However, the industrial application of thermal plasma processing is limited because of the slow development of this technology [100, 101].

Ion beam mixing is an effective method to mix and alloy the different materials in the atomic level. During ion irradiation, the ions with high energy collide with the matrix and transfer the energy to the target atoms. The atoms move during collision cascade, and the mixing at atomic level occurred. This processing can exceed the limit of solid solubility and produce the non-equilibrium phases by using lower amounts of irradiation. While the disadvantage of the ion beam mixing is uncontrolled beam direction, forming undesirable disorder in the samples [102].

Vapor deposition is a process to deposit layers on the substrate. Vapor depositions are divided into physical vapor deposition, which use liquid or solid as the deposition source, and chemical vapor deposition, which use chemical vapor as the deposition source [103]. The

plasma chemical vapor deposition is one of the famous film deposition techniques, which can deposit high quality films in the effective deposition rates. The high dense plasma has very high temperature and exceeds 10^4 K near the torch nozzle, the materials used for deposition is rapidly vaporized when inject into the plasma, and the plasma jet with high velocity accelerate the precursor toward the substrate to form film.

It should be noted that except the rapid solidification and mechanical alloying, other non-equilibrium methods (laser processing, thermal plasma processing, ion beam mixing and vapor deposition) are only suitable for producing functional layers, such as wears, thermal barriers and so on.

1.9 Consolidation methods

All the non-equilibrium particulates must be consolidated into fully dense bulk materials before used. The consolidation process requires the application of heat, accompanied with the pressure. There are several popular consolidation methods: spark plasma sintering, hot pressing, and hot isostatic pressing as shown in Figure 1.7.

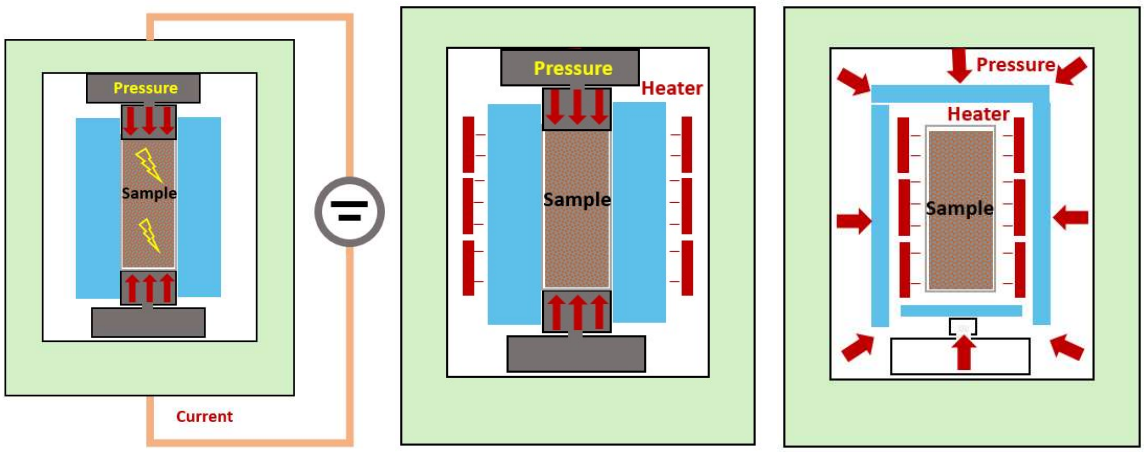

Figure 1.7 The schematic diagrams of spark plasma sintering (left), hot pressing (center) and hot isostatic pressing (right).

1.9.1 Spark plasma sintering

Spark plasma sintering (SPS) is a sintering technology using pulsed electrical current and uniaxial pressure to consolidate the powders. This technique can heat and cool the materials in high-speed rate reaching to 1000 °C/min, resulting in the densification before grain growth, maintaining the initial properties of the powders [104, 105]. During the SPS, the electrical spark discharge is occurred with high energy spark plasma generated by spark electrical current,

resulting in high localized temperature in the contact points of powders. In the microscopic scale, more energy exactly dissipates at the contact points of powders, where more energy is needed for consolidation. There are some advantages compared to conventional consolidation methods, such as ease operation, high sintering speed, high reproducibility and safety.

However, there is a problem of non-homogenous distribution of temperature during SPS process, because of its specific heat transformation [104]. The temperature gradients in the powders should be regulated through controlling the intensity and waveform of the electrical current. Besides, the spark plasma can generate very high localized temperature, resulting in the localized vaporization and melting at the contact point of powders, leading to the aggregation of dispersive particles [104].

1.9.2 Hot pressing (HP)

Hot pressing (HP) is a major sintering process with simultaneous pressing, in which the powders are placed in the graphite stamper for consolidation. Plastic deformation and thermal creep occur for powders during HP to form the bulk metals with high density. The sinter process clearly shortens the densification time compared to the ordinary cold pressing. The HP process is unbalance, the alloy elements do not have enough time to dissolve homogenously. As to the HP parameters, the higher sintering temperature and larger pressure, the more intense of the metals. There are some advantages for HP method, such as the high density and good performance of the products, and smaller pressing pressure requirement compared to cold pressing. But the large free surface of the loose powder increases the possibility of oxidation during HP at elevated temperature. Besides, the bonding and welding of the powders on the tool cavity will influence the flow of powders, deteriorating the density of the consolidated materials [106].

1.9.3 Hot isostatic pressing (HIP)

Hot isostatic pressing (HIP) is one of popular manufacturing method for sintering and densifying the powders to reduce the porosity of metals by both elevated temperature from 500 to 2000 °C and isostatic pressure gas with high pressure from 50 MPa to 1000 MPa [107, 108]. The consolidation mode for HIP is different from HP. In HIP, the materials are pressed by the isostatic force and deform in all direction, keeping the near net shape with isotopic properties. The heat transfer mechanism is different from SPS. During the HIP, the powders are heated by heat radiation from the furnace, and the heat moves from the external surface to the internal powders. The most popular isostatic pressure gas is argon (Ar) to avoid the chemical reaction

during HIP process. The powders can be consolidated because of the plastic deformation and thermal creep, eliminating the void among the powders, and reducing the porosity.

HIP has many advantages compared to conventional process, such as the isotropic microstructures, reduction of the welds, and densification without segregation. Besides, the material design is flexible to densify the composite materials with freedom compositions and size. Moreover, the lean manufacturing route also reduces the cost by simplifying the welding process and nondestructive testing (NDT). The HIP technique also can reduce the impact on environment because of the high efficiency material output due to the near net shape production [109]. HIP has become a viable and effective alternative to the conventional consolidation process.

1.10 Outline of this doctoral thesis

In this doctoral thesis, in order to modify the Y_2O_3 dispersive particles strengthened Cu alloys, the innovative MA-HIP fabrication process based on in-situ fabrication method was investigated. Several Y precursors, especially the brittle Cu_6Y intermetallic compound with lower Y enrichment was firstly proposed as the source of Y_2O_3. The objective of this doctoral thesis is the exploring the innovative MA-HIP process, and various Y precursors to refine the Y_2O_3 dispersive particles.

First, several fabrication parameters based on the pure metal Y soured samples through MA-HIP process by in-situ fabrication method were explored. In chapter 2, the effect of HIP temperature from 850 °C to 950 °C on the crystal structure, porosity, distribution of Y and O elements, mechanical properties, and thermal conductivity were explored. In chapter 3, as to the non-uniform distribution of Y element for all samples consolidated at different HIP temperatures, the effect of MA time on the crystal structure, microscope, Y distribution, and the contamination were further investigated through extending the MA time from 32 hours to 96 hours. In chapter 4, considering the formation of multiscale powders during MA process, the MA powders were classified into four group based on their size <46 μm, 46~100 μm, 100~212 μm and >212 μm. influence of powders size on microstructure and several properties of ODS-Cu alloys were explored.

In chapter 5.1, in order to further enhance the Y distribution, based on the same MA-HIP process by in-situ fabrication method, the Y precursor were modified from pure metal Y to Cu-Y intermetallic compounds. The possibility of Cu-Y intermetallic compounds (Cu_2Y and Cu_6Y)

as the source of Y_2O_3 were investigated without the oxidant addition for the purity of the Cu matrix. The comparison between Cu_2Y sourced samples and Cu_6Y sourced samples with various content from 0.39 wt. % Y to 2.36 wt. % Y was also carried out to obtain the optimum representative of Cu-Y compounds.

In chapter 5.2, considering aggregation of Y elements occurred for the Cu-Y soured samples with high amount of the Y addition, based on the representative of Cu-Y compounds, Cu_6Y sourced samples with and without oxidant material were fabricated. The influence of oxidant on the amount of the in-situ formed Y_2O_3, the distribution of Y elements, and the mechanical properties were investigated. The in-situ fabrication mechanism was also discussed.

In chapter 5.3, a comparison among the ODS-Cu with 1.5 wt. % Y_2O_3 by adding different kinds of Y_2O_3 sources was carried out for comparison, direct Y_2O_3 source by conventional MA-HIP process, pure metal Y source and Cu-Y compound representative (Cu_6Y) source through innovative MA-HIP process by in-situ fabrication method. The influence of Y_2O_3 sources on the MA powders such as morphology, Y distribution, Y_2O_3 particle size, and contamination were investigated.

In chapter 6, in order to suppress the introduction of contamination during MA-HIP processing by in-situ fabrication method for Cu_6Y sourced sample, the effects of reduction of the Y_2O_3 content from 1.5 wt. % to 0.5 wt. % to reduce the Cu_2O addition was investigated. The influence of Y_2O_3 content on the particle boundary of the MA powder, Y_2O_3 particle structure and distribution, contamination, mechanical properties and thermal conductivity were investigated in detail.

In chapter 7, based on the investigation in this doctoral thesis, some suggestions for further improvement were given, including how to further reduce the contamination, how to further suppress the growth of MA powders, and how to further increase the number density of finer Y_2O_3.

In chapter 8, the main conclusions of all the research in this doctoral thesis were summarized.

References:

[1] D. Ahuja, M. Tatsutani. Sustainable energy for developing countries. Surveys and Perspectives Integrating Environment and Society. Volume 2 Issue 1 2009.

[2] S. F. Lincoln. Fossil Fuels in the 21st Century. Ambio Vol. 34, No. 8 (Dec. 2005), pp. 621-627.

[3] V. V. Klimenko and A. G. Tereshin. World Energy and Climate in the Twenty-First Century in the Context of Historical Trends: Clear Constraints to the Future Growth. Journal of Globalization Studies, Vol. 1, Num. 2, November 2010, pp. 27–40.

[4] G. Berndes, B. Abt, A. Asikainen, A. Cowie, V. Dale, G. Egnell, M. Lindner, L. Marelli, D. Paré, K. Pingoud and S. Yeh. Forest biomass, carbon neutrality and climate change mitigation. From Science to Policy 3. European Forest Institute. 2016.

[5] A. Michaelowa, M. Allen & F. Sha. Policy instruments for limiting global temperature rise to 1.5°C – can humanity rise to the challenge? Climate Policy, 2018 Vol. 18, No. 3, 275–286.

[6] S. E. Wurzel, S. C. Hsu. Progress toward Fusion Energy Breakeven and Gain as Measured against the Lawson Criterion. arXiv preprint arXiv:2105.10954, 2021 - arxiv.org.

[7] P. Kite and A. Richardson. The Promise of Nuclear Fusion. Pam review. Vol 1 (2014).

[8] R. V. V. Petrescu, A. Raffaella, S. Kozaitis, A. Antonio and F. I. T. Petrescu. Some Basic Reactions in Nuclear Fusion. American Journal of Engineering and Applied Sciences Volume 10, Issue 3, (2017).

[9] Mitsuru Kikuchi, Masafumi Azumi. Frontiers in Fusion Research II. Springer International Publishing Switzerland 2015.

[10] J. Ongena & G. V. Oost. Energy for Future Centuries: Will Fusion Be an Inexhaustible, Safe, and Clean Energy Source? Fusion Science and Technology. Vol. 45 Mar. 2004.

[11] S. M. Friedman. Three Mile Island, Chernobyl, and Fukushima: An analysis of traditional and new media coverage of nuclear accidents and radiation. Bulletin of the Atomic Scientists. 67(5) 55–65.

[12] H. Azechi1, K. Mima1, Y. Fujimoto1, S. Fujioka1, H. Homma et al. Plasma physics and laser development for the Fast-Ignition Realization Experiment (FIREX) Project. Nucl. Fusion 49 (2009) 104024 (6pp).

[13] A. Pironti and M.Walker. Control of tokamak plasmas. IEEE Control Systems Magazine. October 2005.

[14] K. Okano. Review of Strategy Toward DEMO in Japan and Required Innovations. Journal of Fusion Energy (2019) 38:138–146.

[15] K. Tobita, G. Federici, K. Okano, the BA DEMO Design Activity Unit. Research and development status on fusion DEMO reactor design under the Broader Approach. Fusion Engineering and Design 89 (2014) 1870–1874.

[16] A. Komori, H. Yamada, S. Imagawa, O. Kaneko, K. Kawahata et al. Goal and Achievements of Large Helical Device Project. Fusion Science and Technology Vol. 58 July/ Aug. 2010.

[17] R. Aymar, P. Barabaschi and Y. Shimomura (for the ITER Team). The ITER design. Plasma Phys. Control. Fusion 44 (2002) 519–565.

[18] D. M. Yao, G. N. Luo, Z. B. Zhou, L. Cao, Q. Li, W. J. Wang, L. Li, S. G. Qin, Y. L. Shi, G. H. Liu and J. G. Li. Design, R&D and commissioning of EAST tungsten divertor. Phys. Scr. T167 (2016) 014003 (7pp).

[19] S. Suzuki, M. Akiba, M. Araki, K. Satoh, K. Yokoyama, M. Dairaku. High heat flux experiments of saddle type divertor module. Journal of Nuclear Materials 212-21.5 (1994) 1365-136.

[20] Y. Kubota, N. Noda, A. Sagara, R. Sakamoto, O. Motojima, I. Fujita, T. Hino, T. Yamashina, K. Tokunaga, N. Yoshida. Developments and high heat flux tests of divertor components for LHD. Fusion Engineering and Design 39 – 40 (1998) 247 – 252.

[21] R. A. Pitts, A. Kukushkin, A. Loarte, A. Martin, M. Merola, C. E. Kessel, V. Komarov1 and M. Shimada. Status and physics basis of the ITER divertor. Phys. Scr. T138 (2009) 014001 (10pp).

[22] H. Bolta, V. Barabash, G. Federici, J. Linke, A. Loarte, J. Roth, K. Sato. Plasma facing and high heat flux materials – needs for ITER and beyond. Journal of Nuclear Materials 307–311 (2002) 43–52.

[23] T. Hirai, F. Escourbiac, S. Carpentiern Chouchana, A. Durocher. ITER full tungsten divertor qualification program and progress. Phys. Scr. T159 (2014) 014006 (5pp).

[24] G. Pintsuk, M. Bednarek, P. Gavila, S. Gerzoskovitz, J. Linke, P. Lorenzetto, B. Riccardi, F. Escourbiac. Characterization of ITER tungsten qualification mock-ups exposed to high cyclic thermal loads. Fusion Engineering and Design 98–99 (2015) 1384–1388.

[25] G. J. Butterworth, C. B. A. Forty. A survey of the properties of copper alloys for use as fusion reactor materials. Journal of Nuclear Materials 189 (1992) 237-276.

[26] J. H. You. Copper matrix composites as heat sink materials for water-cooled divertor target. Nuclear Materials and Energy 5(2015) 7–18.

[27] L. Fang, L. H. Friedman. Analytic treatment of metallic multilayer strength at all length scales: Influence of dislocation sources. Acta Materialia 55 (2007) 1505–1514.

[28] Y. Z. Tian, S. D. Wu, Z. F. Zhang, R. B. Figueiredo, N. Gao, T.G. Langdon. Comparison of microstructures and mechanical properties of a Cu–Ag alloy processed using different severe plastic deformation modes. Materials Science and Engineering A528 (2011) 4331–4336.
[29] S. Lefebvre, B. Devincre, T.Hoc. Simulation of the Hall–Petch effect in ultra-fine grained copper. Materials Science and Engineering A 400–401 (2005) 150–153.
[30] S. Nachum, N.A. Fleck, M.F. Ashby, A. Colella, P. Matteazzi. The microstructural basis for the mechanical properties and electrical resistivity of nanocrystalline Cu–Al_2O_3. Materials Science and Engineering A 527 (2010) 5065–5071.
[31] S. A. Fabritsiev, S. J. Zinkle and B. N. Singh. Evaluation of copper alloys for fusion reactor divertor and first wall components. Journal of Nuclear Materials, 233-237, (1996), 127-137.
[32] G. Kalinin, V. Barabash, A. Cardella, J. Dietz, K. Ioki, R. Matera, R. T. Santoro, R. Tivey and The ITER teams. Assessment and selection of materials for ITER in-vessel components. Journal of Nuclear Materials, 283-287, (2000), 10-19.
[33] J. F. Nie, B. C. Muddle, I. J. Polmear. The Effect of Precipitate Shape and Orientation on Dispersion Strengthening in High Strength Aluminium Alloys. Materials Science Forum (Volumes 217-222) May 1996 257-1262.
[34] T. Gladman. Precipitation hardening in metals. Materials Science and Technology Volume 15, 1999 - Issue 1.
[35] J. R. Groza, and J. C. Gibeling. Principles of particle selection for dispersion-strengthened copper materials. Materials Science and Engineering: A, 171, (1993), 115-125.
[36] M. M. li, S. J. Zinkle. Radiation effects in copper and copper alloys for fusion application. Comprehensive nuclear material 2nd edition volume 6 2020.
[37] G. Carro, A. Muñoz, B. Savoini, M. A. Monge. Fabrication and characterization of dispersion strengthened Cu-0.8%Y. Fusion Engineering and Design 154 (2020) 111548.
[38] I. S. Batra, G. K. Dey, U. D. Kulkarni, S. Banerjee. Microstructure and properties of a Cu-Cr-Zr alloy. Journal of Nuclear Materials 299 (2001) 91-100.
[39] G. M. Kalinin, S. A. Fabritziev, B. N. Singh, S. Tahtinen, S. J. Zinkle. Specification of properties and design allowable for copper alloys used in HHF components of ITER. Journal of Nuclear Materials 307–311 (2002) 668–672.
[40] S. J. Zinkle. Applicability of copper alloys for DEMO high heat flux components. Phys. Scr. T167 (2016) 014004 (10pp).
[41] S. J. Zinkle. A Brief Review of Cavity Swelling and Hardening in Irradiated Copper and Copper Alloys. 15th Intern. Symp. on Effects of Radiation on Materials.

[42] A. Fathy, O. Elkady, A. A. Oqail. Synthesis and characterization of CueZrO$_2$ nanocomposite produced by thermochemical process. Journal of Alloys and Compounds 719 (2017) 411-419.

[43] F. L. Wang, Y. P. Li, X. Y. Wang, Y. Koizumi, Y. Kenta, A. Chiba. In-situ fabrication and characterization of ultrafine structured Cu-TiC composites with high strength and high conductivity by mechanical milling. Journal of Alloys and Compounds 657 (2016) 122-132.

[44] S. Z. Han, H. Joh, J. H. Ahn, J. Lee, S. M. Kim, S. H. Lim, Y. G. Son. Ti-added alumina dispersion-strengthened Cu alloy fabricated by oxidation. Journal of Alloys and Compounds 622 (2015) 384–387.

[45] S. B. Chandrasekhar, S. S. Sarma, M. Ramakrishna, P. S. Babu, T. N. Rao, B. P. Kashyap. Microstructure and properties of hot extruded Cu-1 wt% Al_2O_3 nano-composites synthesized by various techniques. Materials Science & Engineering A 591 (2014) 46–53.

[46] https://www.hoganas.com/en/powder-technologies/glidcop/.

[47] S. A. Fabritsiev, A. S. Pokrovsky, D. J. Edwards, S. J. Zinkle, A. F. Rowcliffe. Effect of high-dose neutron irradiation on the mechanical properties and structure of copper alloys and Cu/SS joints for ITER applications. Journal of Nuclear Materials 283-287 (2000) 523-527.

[48] A. Morrison. Powder based processing of novel dispersion strengthened copper alloys for fusion applications [D]. University of Oxford, 2017.

[49] P. Laurençot. The Lifshitz-Slyozov-Wagner Equation with Conserved Total Volume. SIAM J. Math. Anal., 34(2), 257–272. (16 pages).

[50] D. S. Zhou, H. W. Geng, W. Zeng, D. Q. Zheng, H. C. Pan, C. Kong, P. Munroe, G. Sha, C. Suryanarayana, D. Zhang. High temperature stabilization of a nanostructured Cu-Y_2O_3 composite through microalloying with Ti. Materials Science & Engineering A 712 (2018) 80-87.

[51] D. S. Zhou, X. K. Wang, W Zeng, C. Yang, H. C. Pan, C. G. Li, Y. J. Liu, D. L. Zhang. Doping Ti to achieve microstructural refinement and strength enhancement in a high volume fraction Y_2O_3 dispersion strengthened Cu. Journal of Alloys and Compounds 753 (2018) 18-27.

[52] J. Groza. Heat-Resistant Dispersion-Strengthened Copper Alloys. Journal of Materials Engineering and Performance, Volume 1(1), February 1992, 113.

[53] S. M. S. Aghamiri, N. Oono, S. Ukai, R. Kasada, H. Noto, Y. Hishinuma, T. Muroga. Microstructure development and high tensile properties of He/H_2 milled oxide dispersion strengthened copper. Journal of Alloys and Compounds, 783, (2019), 674-679.

[54] S. W. Pan, X. L. Zhou, K. X. Chen, M. Yang, Y. D. Cao, X. H. Chen, Z. D. Wang. In-Situ Nanoparticles: A New Strengthening Method for Metallic Structural Material. Appl. Sci. 2018, 8, 2479.

[55] M. S. Nagorka, C. G. Levi and G. E. Lucas. The potential of rapid solidification in oxide-dispersion-strengthened copper alloy development. Materials Science and Engineering, A 142 (1991) 277-289.

[56] M. S. Nagorka, C. G. Levi, and G. E. Lucas. Novel Oxide-Dispersion-Strengthened Copper Alloys from Rapidly Solidified Precursors: Part 1. Microstructural Development. Metallurgical and Materials Transactions A., Volume 26A, April 1995, 859.

[57] M. S. Nagorka, G. E. Lucas, and C. G. Levi. Novel Oxide-Dispersion-Strengthened Copper Alloys from Rapidly Solidified Precursors: Part 2. Creep Behavior. Metallurgical and Materials Transactions A. Volume 26A 1995—873.

[58] D. V. Kudashov, H. Baum, U. Martin, M. Heilmaier, H. Oettel. Microstructure and room temperature hardening of ultra-fine-grained oxide-dispersion strengthened copper prepared by cryomilling. Materials Science and Engineering A 387–389 (2004) 768–771.

[59] U. Martin, D. V. Kudashov, M. Heilmaier & H. Oettel. Microstructure and deformation behavior of ultra-fine-grained ODS copper prepared by mechanical alloying. High Performance Structures and Materials II. 2004.

[60] J. P. Stobrawa, Z. M. Rdzawski. Dispersion – strengthened nanocrystalline copper. Journal of Achievements in Materials and Manufacturing Engineering. Volume 24 Issue 2 October 2007.

[61] L. Commin, S. Antusch, S. Baumgärtner, D. Bolich, B. Dafferner, W. Goldacker, M. Hoffmann, P. Lukits, M. Rieth, H. Zimmermann. Assessment of Copper based Materials for the Water-Cooled Divertor Concept of the DEMO European Fusion Reactor. IEEE, 10-14 June 2013.

[62] G. Carro, A. Muñoz, B. Savoini, M. A. Monge, R. Pareja. Processing, microstructure and mechanical characterization of dispersion strengthened Cu-1%Y. Fusion Engineering and Design 138 (2019) 321–331.

[63] G. Carro, A. Muñoz, M. A. Monge, B. Savoini, R. Pareja, C. Ballesteros and P. Adeva. Fabrication and characterization of Y_2O_3 dispersion strengthened copper alloys. Journal of Nuclear Materials, 455, (2014), 655-659.

[64] G. Carro, A. Mu˜noz, M.A. Monge, B. Savoini, R. Pareja. Microstructural and mechanical characterization of Cu-0.8 wt. %Y. Fusion Engineering and Design 98–99 (2015) 1941–1944.

[65] G. Carro, A. Mu˜noz, M.A. Monge, B. Savoini, A. Galatanu, M. Galatanu, R. Pareja. Thermal conductivity and diffusivity of Cu-Y alloys produced by different powder metallurgy routes. Fusion Engineering and Design 124 (2017) 1156–1160.

[66] Z. Xiao, H. R. Geng, C. Y. Sun, P. Jia, H. Luo. Effect of yttrium on properties of copper prepared by powder metallurgy. Advanced Powder Technology 26 (2015) 1079–1086.

[67] R. Shabadi, M. N. Avettand-Fènoël, A. Simar, R. Taillard, P.K. Jain, R. Johnson. Thermal conductivity in yttria dispersed copper. Materials and Design 65 (2015) 869–877.

[68] F. Huang, H. Wang, B. Yang, T. Liao and Z. Y. Wang. Pinning effect of Y_2O_3 network on copper grain growth during high temperature annealing. Mater. Res. Express 5 (2018) 056520.

[69] H. N. Oono, S. M. S. Ahgamiri, S. Ukai, R. Kasaka, H. Noto, Y. Hishinuma and T. Muroga. Development of Oxide Dispersion Strengthened (ODS) Copper for the Divertor of Nuclear Fusion Reactors. J. Plasma Fusion Res. Vol.95, No.8 (2019)370-373.

[70] Y. Liu, S. Kondo, H. Yu, K. Yabuuchi and R. Kasada. Statistical Approach for Understanding the Effect of Specimen Size on the Yield Stress and Its Scattering in Mechanically-Alloyed Cu and ODS-Cu Obtained by Micro-Pillar Compression Test. Materials Transactions, Vol. 61, No. 5 (2020) pp. 955-962.

[71] A. Muñoz, B. Savoini, M.A. Monge, M. Eddahbi, O.J. Dura. Microstructure and mechanical properties of hot rolled ODS copper. Nuclear Materials and Energy 24 (2020) 100754.

[72] B. G. V. Chester, A. Thellung. The Law of Wiedemann and Franz. Proceedings of the Physical Society. 1961 77 1005.

[73] R. Li, E. G. Wang, and X. W. Zuo. Co-Precipitation, Strength and Electrical Resistivity of Cu–26wt. %Ag–0.1wt. %Fe Alloy. Materials 2017, 10, 1383.

[74] P. S. Phani, V. Vishnukanthan, G. Sundararajan. Effect of heat treatment on properties of cold sprayed nanocrystalline copper alumina coatings. Acta Materialia 55 (2007) 4741–4751.

[75] P. L. Rossiter. The electrical resistivity of metals and alloys. Cambridge university press. Cambridge, UK, 1987.

[76] E. Schafler, G. Steiner, E. Korznikova, M. Kerber, M. J. Zehetbauer. Lattice defect investigation of ECAP-Cu by means of X-ray line profile analysis, calorimetry and electrical resistometry. Mater Sci Eng A 2005; 410–411:169.

[77] E. Botcharova, J. Freudenberger, L. Schultz. Mechanical and electrical properties of mechanically alloyed nanocrystalline Cu–Nb alloys. Acta Mater. 54 (2006)3333-3341.

[78] P. S. Phani, V. Vishinukanthan, G. Sundararajan. Effect of heat treatment on properties of cold sprayed nanocrystalline copper alumina coatings. Acta Mater. 55 (2007) 4741-4751.

[79] E. J. Lavernia, T. S. Srivatsan. The rapid solidification processing of materials: science, principles, technology, advances, and applications. J Mater Sci (2010) 45:287–325.

[80] M. Sherif El-Eskandarany. Mechanical Alloying Energy Storage, Protective Coatings, and Medical Applications. Third Edition. 2020.

[81] M. Sherif El-Eskandarany. Mechanical Alloying: Nanotechnology, Materials Science and Powder Metallurgy. 2015.

[82] X. Y. Zhou, D. Q. Yi, L. Nyborg, Z. Hu, J. Huang, Y. Cao. Influence of Ag addition on the microstructure and properties of copper-alumina composites prepared by internal oxidation. Journal of Alloys and Compounds 722 (2017) 962-969.

[83] C. Suryanarayana. Mechanical Alloying: A Novel Technique to Synthesize Advanced Materials. Research Volume 2019, Article ID 4219812.

[84] C. Suryanarayana. Mechanical alloying and milling, Progress in Mater Sci, 2001 1-168.

[85] L. Shan, X. L. Wang and Y. P. Wang. Extension of Solid Solubility and Structural Evolution in Nano-Structured Cu-Cr Solid Solution Induced by High-Energy Milling. Materials 2020, 13, 5532.

[86] R. Rahmanifard, S. M. Javidan, and M. A. Asadabad. Effects of Process Control Agents on Characteristics of Cu-Ta Nanocomposite during Milling and Subsequent Sintering. Journal of Materials Engineering and Performance. Volume 28 (7) July 2019 4102-4110.

[87] K. Barai, C. S. Tiwary, P. P. Chattopadhyay, K. Chattopadhyay. Synthesis of free standing nanocrystalline Cu by ball milling at cryogenic temperature. Materials Science & Engineering A 558 (2012) 52–58.

[88] M. A. Atwater, D. Roy, K. A. Darling, B. G. Butler, R. O. Scattergood, C. C. Koch. The thermal stability of nanocrystalline copper cryogenically milled with tungsten. Materials Science & Engineering A 558 (2012) 226–233.

[89] B. Huang, Y. Hishinuma, H. Noto and T. Muroga. Mechanochemical processing of Cu-Y_2O_3 alloy by MA-HIP for heat sink materials application. Fusion Engineering and Design, 140, (2019), 33-40.

[90] D. D. Gu, Z. Y. Wang, Y. F. Shen, Q. Li, Y. F. Li. In-situ TiC particle reinforced Ti–Al matrix composites: Powder preparation by mechanical alloying and Selective Laser Melting behavior. Applied Surface Science 255 (2009) 9230–924.

[91] S. W. Pan, X. L. Zhou, K. X. Chen, M. Yang, Y. D. Cao, X. H. Chen, Z. D. Wang. In-Situ Nanoparticles: A New Strengthening Method for Metallic Structural Material. Appl. Sci. 2018, 8, 2479.

[92] B. Huang, Y. Hishinuma, H. Noto, R. Kasada, N. Oono, S. Ukai and T. Muroga. In-situ fabrication of yttria dispersed copper alloys through MA-HIP process. Nuclear Materials and Energy, 16, (2018), 168-174.

[93] H. Arami, A. Simchi, S.M. Seyed Reihani. Mechanical induced reaction in Al–CuO system for in-situ fabrication of Al based nanocomposites. Journal of Alloys and Compounds 465 (2008) 151–156.

[94] S. Sheibani, A. Ataie, and S. H. Manesh. In-Situ Synthesis of Cu/Cr-Al_2O_3 Nanocomposite by Mechanical Alloying and Heat Treatment. Metallurgical and Materials Transactions A. Volume 41A, October 2010.

[95] M. Elmahdy, G. Abouelmagd, A. A. E. Mazen. Microstructure and Properties of Cu-ZrO_2 Nanocomposites Synthesized by in Situ Processing. Materials Research. 2018; 21(1): 20170387.

[96] T. X. Lu, C. G. Chen, P. Li, C. Z. Zhang, W. H. Han, Y. Zhou, C. Suryanarayana, Z. M. Guo. Enhanced mechanical and electrical properties of in situ synthesized nano-tungsten dispersion-strengthened copper alloy. Materials Science & Engineering A 799 (2021) 140161.

[98] J. Mazumder, O. Conde, R. Villar and W. Steen. Laser Processing: Surface Treatment and Film Deposition. Series E: Applied Sciences Vol.307.

[99] M. I. Boulos. Thermal plasma processing. IEEE Transactions on Plasma Science. Volume: 19, Issue: 6, Dec 1991.

[100] E. Pfender. Thermal Plasma Technology: Where Do We Stand and Where Are We Going. Plasma Chemistry and Plasma Processing, Vol. 19, No. 1, 1999.

[101] P. R. Taylor, and S. A. Pirzada. Thermal Plasma Processing of Materials: A Review. Advanced Performance Materials, 1, 35-50 (1994).

[102] J. K. Hirvonen. Ion beam assisted thin film deposition. Materials Science Reports 6 (1991) 215-274.

[103] D. M. Mattox. Handbook of Physical Vapor Deposition (PVD) Processing. Elsevier 2010.

[104] M. Suárez, A. Fernández, J. L. Menéndez, R. Torrecillas, H. U. Kessel, J. Hennicke, R. Kirchner and T. Kessel. Challenges and Opportunities for Spark Plasma Sintering: A Key Technology for a New Generation of Materials. Sintering Applications. 2013.

[105] Z. H. Zhang, Z. F. Liu, J. F. Lu, X. B. Shen, F. C. Wang, Y. D. Wang. The sintering mechanism in spark plasma sintering – Proof of the occurrence of spark discharge. Scripta Materialia 81 (2014) 56–59.

[106] https://www.slideshare.net/DonakhiLps/hot-pressing.

[107] A. S. Helle, K. E. Easterling, M. F. Ashby. Hot-isostatic pressing diagrams: New developments. ACTA metal. Vol. 33, No. 12. pp. 2163-2174, 1985.

[108] H. V. Atkinson and S. Davies, Fundamental Aspects of Hot Isostatic Pressing: An Overview. Metallurgical and Materials Transactions A. Volume 31A, December 2000—2983.

[109] Introduction to Hot Isostatic Pressing Technology. https://www.epma.com/epma-free-publications/product/introduction-to-hot-isostatic-pressing-brochure.

Chapter 2. Effect of HIP temperature on in-situ fabricated ODS-Cu alloys

2.1 Introduction

Dispersion strengthened copper alloys are attractive for the heat sink material of divertor in fusion devices because of their better irradiation resistance, thermal stability and inhabitation of recrystallization at higher temperature [1, 2]. Compared to oxide dispersion strengthened copper (ODS-Cu) with Al_2O_3 particles (Glidcop®), the ODS-Cu with Y_2O_3 has potential advantages because of the lower solubility of Y in Cu matrix, beneficial to thermal conductivity, and the higher enthalpy of formation for Y_2O_3, beneficial to thermal stability [3-11]. Considering that the conventional mechanical alloying process forms the large, thermodynamic instable and aggregated Y_2O_3 particles original from outside directly, the in-situ fabrication method based on MA process by adding Y precursor is more attractive because of the finer, thermodynamic stable, in-situ formed dispersive particles [12-17]. In this chapter, the pure metal Y was used as the source of Y_2O_3 and oxidized by the mid added CuO to fabricate the ODS-Cu with nominal content of 3 wt. % Y_2O_3.

As an effective powder metallurgy (PM) technology, hot isostatic pressing (HIP) is used to consolidate the supersaturated solid solute powders fabricated by atomization or mechanical alloying. The performance of the consolidated materials is strictly controlled by the HIP parameters, including HIP pressure, HIP temperature, and HIP duration. Among them, the HIP temperature is a very important fabrication parameter to determine the microstructure of materials, including porosity, density, grain size distribution, number density of defects, and the diffusivity of alloyed elements. Besides, elevated HIP temperature also has influence on the morphology of dispersive particles in some degree. Furthermore, the properties of particle boundaries (PPB) also have relationship with the HIP temperature. PPB consist of many impurities such as oxide, carbon, nitrogen, iron impurities from mechanical alloying process. As the special area for powders metallurgy materials, the PPB particularly determines the mechanical properties of consolidated materials, such as tensile strength, ductility, fatigue and so on. Increasing the HIP temperature is reported to dissolve the impurities elements at the PPB [18, 19]. The previous HIP temperature and pressure were applied during the HIP process to

fabricate ODS-Cu alloys as shown in Table 2.1. It is found that various consolidated temperatures were conducted to fabricate the ODS-Cu without obvious guidance. It is necessary to explore the influence of HIP temperature on the microstructure and macro performance of ODS-Cu alloys and obtain the optimum HIP temperature for in-situ fabrication process.

Table 2.1 summary of the fabrication parameters by global peers.

Authors	Temperature	Time	Pressure	References
G. Carro and A. Muñoz et al.	900 °C	3 hours	180 MPa	[7, 9]
Yuchen Liu et al.	800 °C	45 min	45 MPa	[8]
Alasdair Morrison	850 °C	2 hours	150 MPa	[11]
Tianxing Lu et al.	1000 °C	2 hours	50 MPa	[12]
Xueliang Wang.	950 °C	3 hours	300 MPa	[20]
Adel Fathy et al.	950 °C	2 hours	700 MPa	[21]
D.V. Kudashov et al.	650 °C	20 min	650 MPa	[10]

Besides, for the in-situ fabrication method adopted in this chapter, the pure metal Y and oxidant were added out of synchronous during MA process. The enhanced diffusivity of Y and O in Cu matrix at optimum HIP temperature is necessary to enhance the combination and in-situ reaction between Y and O elements. In this research, the influence of HIP temperature from 850 °C to 950 °C on the microstructure and physical properties of ODS-Cu with Y_2O_3 through innovative MA-HIP process by in-situ fabrication method were investigated.

2.2 Experimental procedure

2.2.1 Samples preparation

In this work, the stoichiometric ratio of raw powders Cu-2.36 wt. %Y-3.17 wt. % CuO were prepared to fabricate ODS-Cu with 3wt. % of Y_2O_3 particles. Cu-Y solid solute powders were formed during MA process, and then the middle added CuO was reduced by Y, forming Y_2O_3 at HIP process with high temperature and high pressure. The reaction was shown as follows:

$$3\,CuO + 2\,Y = 3\,Cu + Y_2O_3 \tag{2.1}$$

In MA process, the pure Cu (99.9% purity, 50 μm) and the Y (99.9% purity, 300 μm) were first milled for 16 hours with the speed of 250 rotation per minute (rpm). In the second stage of MA, the mechanically alloyed Cu-Y powders were further milled with CuO (99.9% purity, 1 μm) powders for additional 16 hours with the same parameters. The mechanical alloying was conducted by planetary-type ball mill machine (Pulverisetee 5, Fritsch) placed in the glove box

filled with high purity Ar gas shown in Figure 2.1. The oxygen content in the glove box was adjusted to below 1 ppm (parts per million) by the oxygen removal machine. The milling was conducted in stainless steel pots and balls with the composition shown in Table 2.2. The diameter of the MA balls made by the stainless steel is 5 mm and the ball-powder ratio is 7:3. In order to slow down the growth of MA powders without introduce contamination at the same time, the intermittent milling, in which short milling period (1 hour) alternated with longer natural cooling period (3 hours), was conducted.

Figure 2.1 The pictures of milling machine, glove box, NIFS-Sealing device, NIFS-HIP devices.

Table 2.2 Composition of milling pot and milling ball. (wt. %)

Element	Fe	Cr	Ni	Mn	Si	C
AISI 304	Bal	17.5-19.5	8-10.5	2	1	0.07

The HIP was conducted in National Institute for Fusion Science (NIFS) by NIFS-HIP facility with a maximum temperature being 2000 °C and maximum pressure being 196 MPa. The HIP unit consists of heating system, compression system by Ar gas and pressure vessel. The dimensions of the processing space are 240 mm in height and 120 mm in diameter, covered by

ceramic fibers to protect the steel pressure vessel against the high temperature. During HIP process, the steel capsules, filled with milled powders, were respectively kept in pressure of 150 MPa with temperature of 850 °C, 900 °C and 950 °C for 1 hour. It should be noted that the heat and cooling rate is 7.5 °C/min for all three samples, and the HIP pressure is also loaded and unloaded synchronously with the rate of 1.22 MPa/min shown in Figure 2.2.

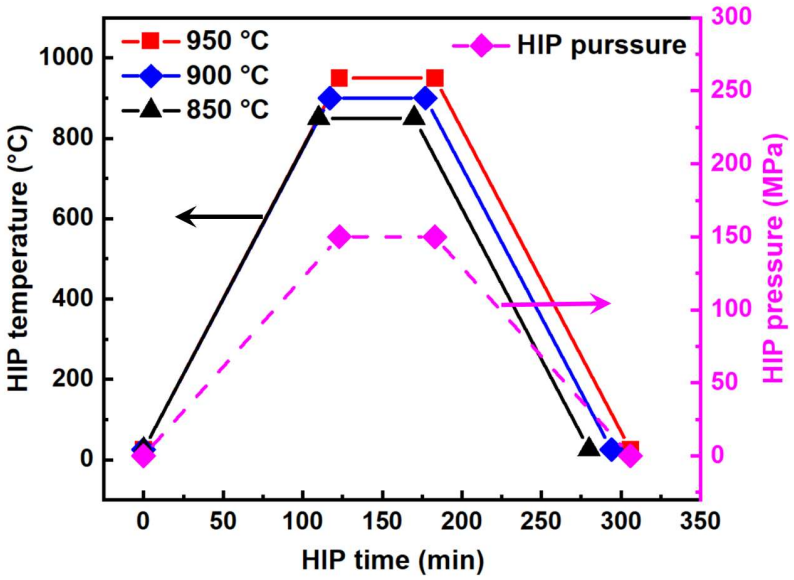

Figure 2.2 The parameters during HIP process.

2.2.2 Characterization

The XRD analyses were conducted on the Rigaku RINT-2200 diffractometer shown in Figure 2.3 with Cu Ka radiation at the parameters of 40kV and 40 mA. The scanning speed was 0.5 °/min and the diffraction angle (2θ) range was restricted to 10-100°. Furthermore, the variation of lattice parameter and crystallite size were analyzed based on the XRD spectrum. The diffraction of X-ray by crystal obeys the famous Bragg's law:

$$2d \sin\theta = n\lambda \tag{2.1}$$

Where d is the inter-planner distance, θ is the scattering angle, n is the integer, and λ is the wavelength of X-ray. The lattice parameter (a_{hkl}) is extremely parameter for evaluating the solid solution state. It can be calculated as follows:

$$a_{hkl} = d\sqrt{h^2 + k^2 + l^2} \tag{2.2}$$

Where h, k, l are the miller indices of the Bragg plane. The lattice parameter can be obtained if know the scattering angle θ. Moreover, the α calculated by Formula 2.2 includes various

factors, and can be divided based on Cohen-wagner rules [22], which can eliminate the instrumental aberrations:

$$a_{hkl} = a_0 + S_1(hkl)a_0\sigma + D\chi_{hkl}a_0 + s\cos\theta\cot\theta \quad (2.4)$$

Wherea_{hkl} is the lattice parameter corresponding to the *hkl* peak, a_0 is the stress-free lattice parameter for the ideal crystal. The second part on right is associated with the influence of first kind stress, the third parts is caused by the lattice defects, and the last part is caused by the instrumental aberrations, which should be delated for the true lattice parameter. The grain size can be calculated by Williamson-Hall equation [22]:

$$\frac{\beta\cos\theta}{\lambda} = \frac{K}{D} + \frac{2\varepsilon\sin\theta}{\lambda} \quad (2.5)$$

Where β is the integral widths that can be obtained by eliminating the instrumental broadening, K is the Scherrer constant, D is the grain size and ε is the strain of matrix.

Scanning electron microscope (SEM) analyses were conducted by SEM (JEOL JSM-5600) equipped with an energy-dispersive X-ray spectroscope (EDS) in NIFS shown in Figure 2.3, and the EDS data was analyzed by Oxford Instruments Aztec software. The accelerating voltage is 15 keV, with a probe current of 72 μA. It should be noted that the working distance for all analyses is 10 mm.

Figure 2.3 The images of XRD and SEM machines.

Vickers hardness was tested at room temperature by micro indenter with a Vickers indenter diamond tip with interfacial angle of 136 °. The indenter was loaded with 100 gf/mm^2 for 30 seconds. The 30 times indentations with space of 0.2 mm between each other were conducted

for all the samples. After Vickers hardness test, the indentations caused by the indenter were measured to calculate the Vickers hardness based on the formula shown as follows:

$$\mathrm{HV} = 0.1891 \times F/d^2 \tag{2.6}$$

$$d = \frac{d_1+d_2}{2} \tag{2.7}$$

Where F is the load, d_1 and d_2 are the diagonal length of the indentation.

The densities of bulk samples after HIP were tested by electronica densimeter shown in Figure 2.4 (Alfa Mirage MDS-300) based on:

$$\rho_s = \frac{m_s}{V_s} \tag{2.8}$$

Where ρ_s is the density of sample, m_s is the mass of sample measured when the sample out of pure water, and V_s is the volume of the sample, calculated based on the Archimedes principle:

$$m_s\mathrm{g} - m_i\mathrm{g} = \rho_w V_w \mathrm{g} \tag{2.9}$$

$$V_s = V_w \tag{2.10}$$

Where g is the gravity constant (9.8 m/s^2), m_i is the mass of sample completely submerged in pure water, ρ_w is the density of water and V_w is the volume of water. During test, zero adjustment was conducted, followed by measuring the mass of samples out of water m_s, then slowly put the samples in the water and measured the mass of samples submerged in pure water m_i, and the density was calculated by densimeter automatically based on the Formula 2.8. It should be ensured that no float on the samples' surface and no water droplets on the tweezer when put the samples in the water.

Figure 2.4 The pictures of Vickers hardness machine and densimeter.

Considering that the free conductive electrons make the main contribution to the thermal conductivity for metals, the thermal conductivity can be evaluated by electrical conductivity based on the Wiedemann-Franz law [23]:

$$\frac{k}{\sigma} = LT \tag{2.11}$$

Where k is the thermal conductivity, σ is the electrical conductivity, L is the Lorenz number ($2.44 \times 10^{-8} W\Omega K^{-2}$), and T is the measurement temperature. Therefore, the electrical conductivity of the sample was estimated from the electrical resistance in this study. The electrical resistance under various temperature was measured by the four-probe methods. The rectangular samples with size of $20 \times 5 \times 2.5$ mm were cut by low speed cutting machine. The three temperatures were chosen (room temperature, 0 °C by the mixing with ice and water, and -196 °C in liquid nitrogen), and then three kinds of the currents (1, 3 and 5 A) were supplied to the sample. After the current supply, the waiting for five minutes needed to collect the data under the stabilities of the sample temperature and the voltage signal.

2.3 Results and discussion

2.3.1 X-Ray diffraction

In order to investigate the influence of HIP temperature on the crystalline structure, XRD tests were conducted on the bulk samples consolidated at different HIP temperatures. As shown in Figure 2.5, there is neither Y peak nor CuO peak in the XRD spectrum, while the peak of Y_2O_3 was appeared for all samples, indicating that Y_2O_3 particles were successfully formed by the in-situ fabrication method. The peak of Y_2O_3 gradually increased with the HIP temperature, indicating that the content of Y_2O_3 particles increased with the HIP temperature in the range investigated as shown in Figure 2.7. Besides, the increase in the amounts of Y_2O_3 particles between 900 °C and 950 °C is not as much as that between 850 °C and 900 °C, probably because the amounts of Y_2O_3 particles approached saturation from 900 °C.

Figure 2.6 shows the plot of lattice parameters versus cos 2θ/sin θ based on the Cohen-Wagner rules, and the plot of Williamson-Hall equation for the consolidated samples with various HIP temperatures. The influence of HIP temperature on the lattice parameter of the samples calculated based on Figure 2.6 (a) were shown in Figure 2.7, and the lattice parameters of the samples consolidated at 850 °C, 900 °C and 950 °C are 3.6162 Å, 3.6159 Å and 3.6157 Å, respectively. The difference of lattice parameters from 850 °C to 900 °C is larger than that from 900°C to 950 °C. During the HIP process at elevated temperature, the Y elements

precipitate from the supersaturate solid solution state, resulting in the decrease in lattice parameter. The more precipitation of Y element, the more formation of dispersive Y_2O_3 particles. The increase in precipitation from 850 °C to 900 °C is larger than that from 900 °C to 950 °C, indicating that the contents of Y_2O_3 particles gradually reach saturation with the HIP temperature.

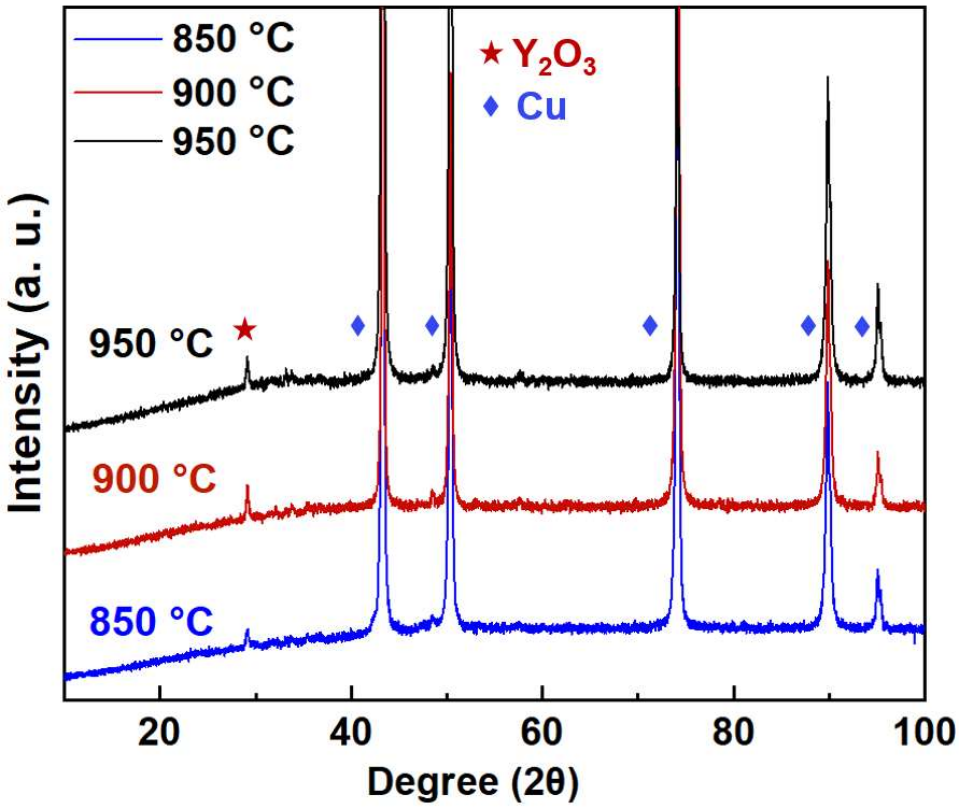

Figure 2.5 XRD spectrum of the Cu-3.0 wt. % Y_2O_3 samples with different HIP temperatures (850 °C, 900 °C, 950 °C)

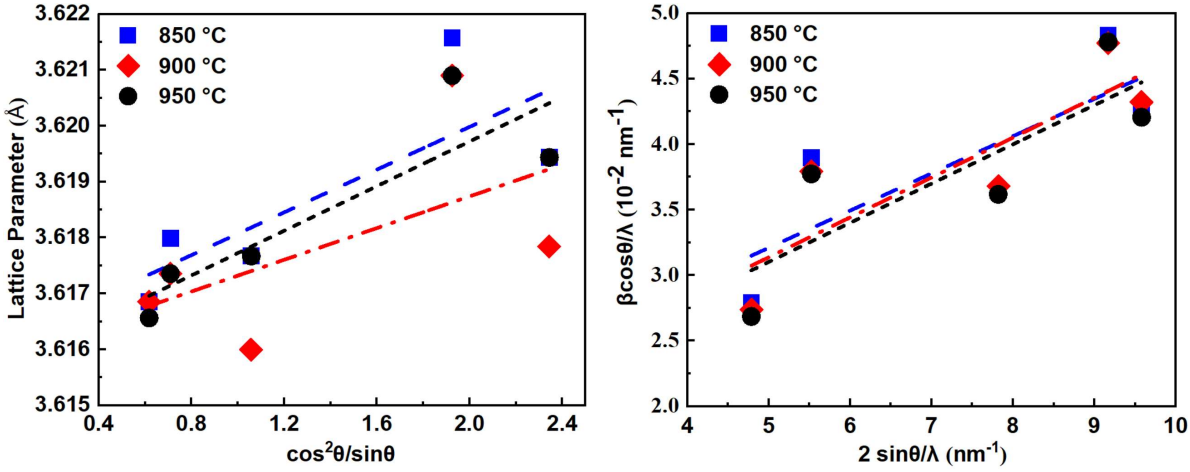

(a) (b)

Figure 2.6 Plot of lattice parameter versus cos2θ/sinθ (a), plot of Williamson-Hall equation (b).

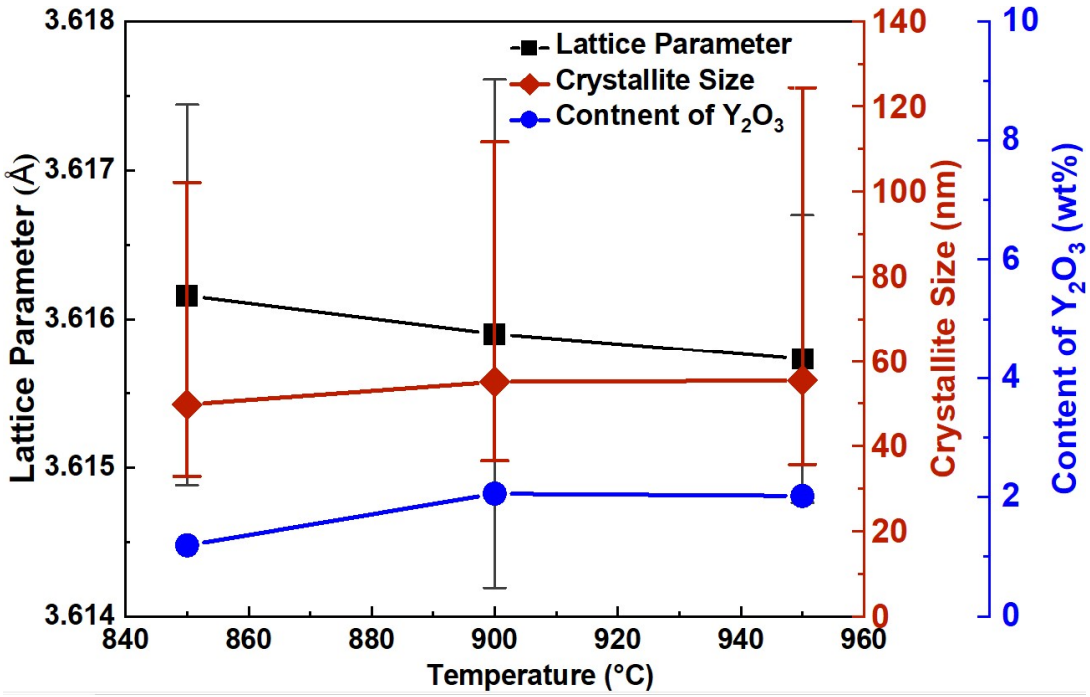

Figure 2.7 Development of lattice parameters, crystallite size and Y_2O_3 content with HIP temperatures.

Figure 2.7 also shows the crystallite size derived from the plot of Williamson-Hall equation shown in Figure 2.6 (b). The crystallite sizes of samples consolidated at 850 °C, 900 °C and 950 °C are 47.72 nm, 55.08 nm and 55.45 nm, respectively. The grains grow up faster with the increase in HIP temperature. The increase rate became stable from 900 °C mainly because of the suppression of recrystallization caused by the in-situ formed particles. In MA process, the collisions between balls and powders result in plastic deformation, fatigue, and fracture of the powders. Under long time dynamic loading, high-density dislocations are produced inside the copper-based materials, resulting in the decrease in crystallite size. In HIP process at high temperature, the crystallite size grows up in some degree because of the recovery of the internal defects.

2.3.2 Microstructures

To achieve a better understanding of the microstructure, SEM images in BSE mode for samples with different HIP temperatures are shown in Figure 2.8. For the sample consolidated at 850 °C, the alloyed powders were pressed with plastic deformation, forming irregular shape with obvious boundaries. There were some macro holes (> 10 μm) on the powder boundaries and micro holes (1< μm) in the powders. The clear stripes in the powders indicated that the MA powders were fully mechanically alloyed. On the other hand, the stripes also indicated that the element distribution were still not uniform. Figure 2.8 also show the typical microstructures

of samples consolidated at 900 °C and 950 °C, respectively. The stripes in the MA powders of these two samples were not as clear as those at 850 °C, implying that the element distribution in the powders were relative more uniform. It should be emphasized that all samples exhibited a morphology corresponding to the original MA powders, and no sample shows fully homogeneous microstructure. The fabrication process should be modified, such as extending the MA process before consolidation, to enhance the uniform distribution of elements.

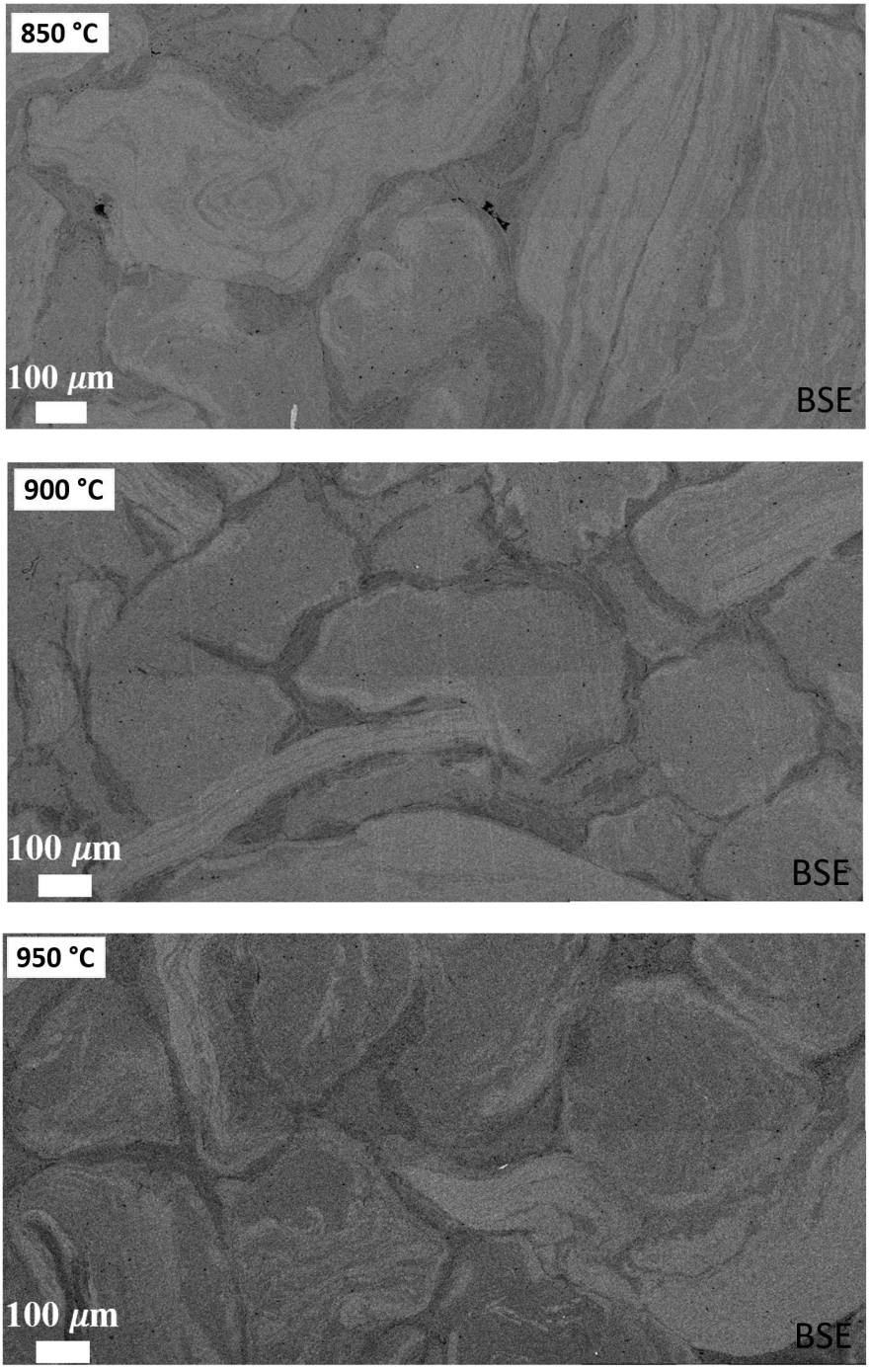

Figure 2.8 SEM-BSE images of samples with the HIP temperatures of 850 °C, 900 °C and 950 °C.

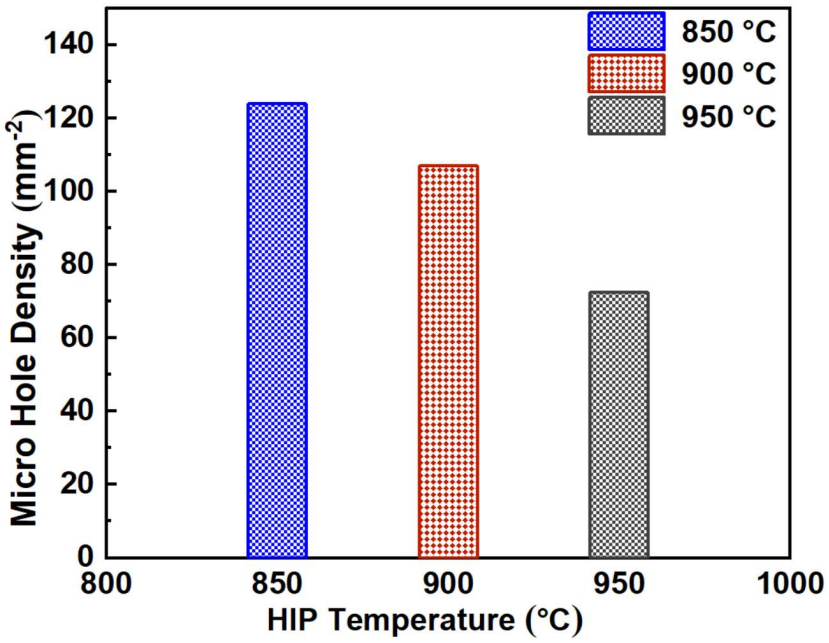

Figure 2.9 The number density of surface holes for consolidated samples with different HIP *T*.

Compared to the sample consolidated at 850 °C, the macro holes on the powder boundary disappeared, only the micro holes were left for the samples consolidated at 900 °C and 950 °C. The number densities of the micro holes were counted and shown in Figure 2.9. It was found that the number density of micro holes decreased with the increase in HIP temperature and that the decrease rate became larger with the temperature increasing. Relative higher temperature is beneficial to the porosity of consolidated materials. The alloyed MA powders can be softened at elevated temperature, inducing the easier plastic deformation during consolidation process, thereby contributing to the reduction of porosity.

The EDS mappings of the samples consolidated at 850 °C and 950 °C are shown in Figure 2.10. The higher magnify images of the sample consolidated at 850 °C clearly showed the higher dense micro holes. The EDS mappings in Figure 2.10 (a) shows that there were many Y rich particles with size of 30 μm left for the sample consolidated at 850 °C. Besides, the distribution of oxygen and yttrium did not perfectly correspond with each other, marked by the color arrows. Combining with the XRD results with low peak of Y_2O_3 for the sample consolidated at 850 °C shown in Figure 2.5, it was found that the yttrium element did not fully transfer to Y_2O_3.

Figure 2.10 (b) shows the SEM-BSE image and the corresponded EDS mappings of the sample consolidated at 950 °C. It is found that the distribution of yttrium was much more uniform compared to the sample consolidated at 850 °C. Furthermore, it was found that the

distribution of yttrium and oxygen were more consistent. Combing with the XRD results with higher peak of Y_2O_3 for the sample consolidated at 950 °C shown in Figure 2.5, it was found that more amount of pure yttrium was transferred to Y_2O_3. According to the diffusivity mechanism in the bulk materials, the high temperature can enhance the diffusivity of Y and O in the Cu matrix, which contribute the more uniform distribution and more agreement of Y and O elements.

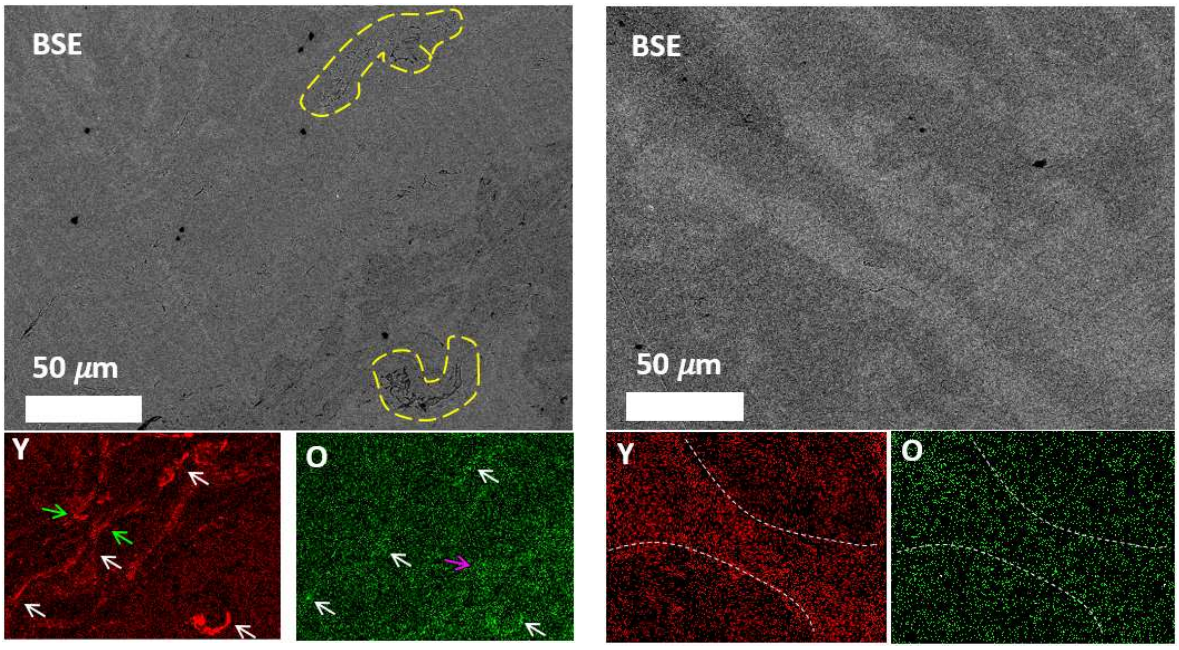

(a) (b)

Figure 2.10 SEM images and the corresponded EDS mappings of samples with the HIP temperature of 850 °C (a) and 950 °C (b). Y and O respectively mean the distribution of yttrium and oxygen.

2.3.3 Physical properties

The relative density and Vickers hardness were measured as shown in Table 2.3. The relative densities were calculated based on the ratio of the measured density and the calculated ideal density of ODS-Cu alloys, which were obtained through dividing the mass of 97.0 wt. % Cu and 3.0 wt. % Y_2O_3 by the volume of Cu and Y_2O_3. From Table 2.3 we can find that the relative density increases with the HIP temperature, in agreement with the amounted number density of macro and micro holes. The Vickers hardness decreases with the increase in HIP temperature. Recovery of the internal defects introduced in MA process and the precipitation of Y_2O_3 particles from the solid solution state can be enhanced with the increase in HIP temperature, both of which can decrease the Vickers hardness and thus modifying the comprehensive mechanical properties.

Table 2.3 Relative density and Vickers hardness of samples consolidated at different HIP *T*.

Conditions	Relative density (%)	Vickers hardness
850°C	95.83	181
900°C	96.36	161
950°C	98.94	151

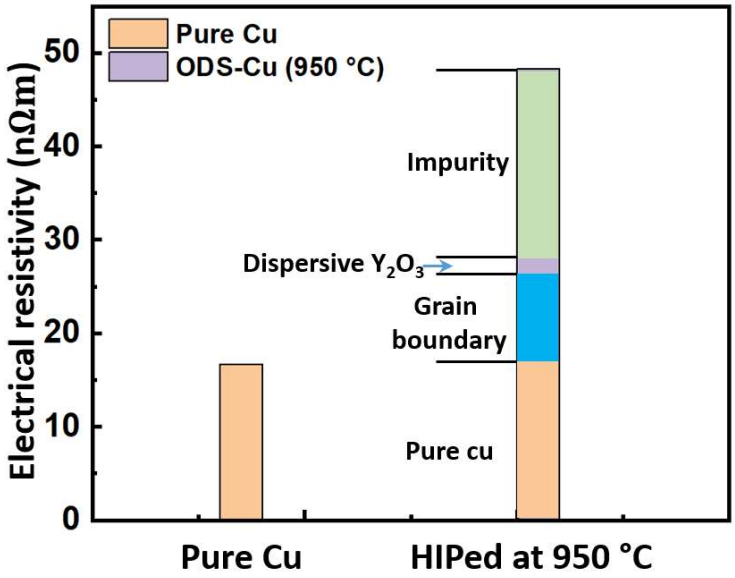

Figure 2.11 The electrical resistivity of Cu and ODS-Cu

Considering the relative more uniform distribution of the Y elements and higher density of the sample consolidated at 950 °C, electrical resistivity measurement was conducted only for ODS-Cu consolidated at 950 °C shown in Figure 2.11. The electrical resistivity of pure Cu (16.7 nΩm) was shown as a comparison. The electrical resistivity of ODS-Cu alloy can be divided based on the Matthiessen's rule shown in chapter 1. According to the grain size of sample consolidated at 950 °C being 55.45 nm, the contribution of grain boundary on electrical conductivity is 8.96 nΩm. Based on the Y_2O_3 addition of 3 wt. %, the contribution of the dispersive particles on the electrical resistivity is 1.20 nΩm. The rest of electrical resistivity (21 nΩm) is mainly caused by the contamination introduced during the MA process. For the major contamination, Fe contributes to 115 nΩm electrical resistivity per 1wt. %, which means that only 0.18 wt. % Fe can result in the remaining increase in electrical resistivity. Therefore, the solid solute contamination has great influence on the electrical resistivity and should be suppressed during mechanical alloying process.

2.4 Conclusions

Cu-3.0 wt. % Y_2O_3 were produced through innovative MA-HIP process by the in-situ fabrication method with a various HIP temperature from 850 °C to 950 °C. The influence of HIP temperature on the microstructure and physical properties were investigated. The main results were summarized as follows:

(1) Y_2O_3 particles were successfully formed through this innovative MA-HIP process by in-situ fabrication method, whose relative density increased with the HIP temperature increasing from 850 °C to 950 °C.

(2) The distribution of oxygen and yttrium did not match with each other at 850 °C perfectly, and the correspondence increased with the increase in HIP temperature. Besides, higher HIP temperature enhanced the more uniform distribution of Y and O elements.

(3) Relative higher HIP temperature can reduce the porosity of the consolidated samples, thereby increasing the density. Besides, the increase in HIP temperature decreased the Vickers hardness and was expected to modify the comprehensive mechanical properties.

(4) The clear stripes in the MA powders observed at all HIP temperatures indicated that the powders were fully mechanically alloyed during the MA process and that the distribution of elements were not yet uniform. The homogeneity of the MA powders needs to be further improved during the MA process.

References:

[1] G. J. Butterworth, C. B. A. Forty. A survey of the properties of copper alloys for use as fusion reactor materials. Journal of Nuclear Materials 189 (1992) 237-276.

[2] J. Groza. Heat-Resistant Dispersion-Strengthened Copper Alloys. Journal of Materials Engineering and Performance Volume 1(1) February 1992—113.

[3] L. Commin, S. Antusch, S. Baumgärtner, D. Bolich, B. Dafferner, W. Goldacker, M. Hoffmann, P. Lukits, M. Rieth, H. Zimmermann. Assessment of Copper based Materials for the Water-Cooled Divertor Concept of the DEMO European Fusion Reactor. IEEE, 10-14 June 2013.

[4] M. S. Nagorka, C. G. Levi, G. E. Lucas and S. D. Ridder. The potential of rapid solidification in oxide-dispersion-strengthened copper alloy development. Materials Science and Engineering: A, 142, (1991), 277-289.

[5] M. S. Nagorka, C. G. Levi, and G. E. Lucas. Novel Oxide-Dispersion-Strengthened Copper Alloys from Rapidly Solidified Precursors: Part 1. Microstructural Development. Metallurgical and Materials Transactions A. Volume 26A, April 1995—859.

[6] M. S. Nagorka, G. E. Lucas, and C. G. Levi. Novel Oxide-Dispersion-Strengthened Copper Alloys from Rapidly Solidified Precursors: Part 2. Creep Behavior. Metallurgical and Materials Transactions A. Volume 26A 1995—873.

[7] G. Carro, A. Muñoz, B. Savoini, M.A. Monge. Fabrication and characterization of dispersion strengthened Cu-0.8%Y. Fusion Engineering and Design 154 (2020) 111548.

[8] Y. Liu, S. Kondo, H. Yu, K. Yabuuchi and R. Kasada. Statistical Approach for Understanding the Effect of Specimen Size on the Yield Stress and Its Scattering in Mechanically-Alloyed Cu and ODS-Cu Obtained by Micro-Pillar Compression Test. Materials Transactions, Vol. 61, No. 5 (2020) pp. 955-962.

[9] A. Muñoz, B. Savoini, M.A. Monge, M. Eddahbi, O.J. Dura. Microstructure and mechanical properties of hot rolled ODS copper. Nuclear Materials and Energy. 24 (2020) 100754.

[10] D. V. Kudashov, H. Baum, U. Martin, M. Heilmaier, H. Oettel. Microstructure and room temperature hardening of ultra-fine-grained oxide-dispersion strengthened copper prepared by cryomilling. Materials Science and Engineering A 387–389 (2004) 768–771.

[11] A. Morrison. Powder based processing of novel dispersion strengthened copper alloys for fusion applications [D]. University of Oxford, 2017.

[12] T. X. Lu, C. G. Chen, P. Li, C. Z. Zhang, W. H. Han, Y. Zhou, C. Suryanarayana, Z. M. Guo. Enhanced mechanical and electrical properties of in situ synthesized nano-tungsten dispersion-strengthened copper alloy. Materials Science & Engineering A 799 (2021) 140161.
[13] S. W. Pan, X. L. Zhou, K. X. Chen, M. Yang, Y. D. Cao, X. H. Chen, Z. D. Wang. In-Situ Nanoparticles: A New Strengthening Method for Metallic Structural Material. Appl. Sci. 2018, 8, 2479.
[14] S. Sheibani, A. Ataie, and S. H. Manesh. In-Situ Synthesis of Cu/Cr-Al_2O_3 Nanocomposite by Mechanical Alloying and Heat Treatment. Metallurgical and Materials Transactions A. Volume 41A, October 2010.
[15] M. Elmahdy, G. Abouelmagd, A. A. E. Mazen. Microstructure and Properties of Cu-ZrO_2 Nanocomposites Synthesized by in Situ Processing. Materials Research. 2018; 21(1): 20170387.
[16] F. L. Wang, Y. P. Li, X. Y. Wang, Y. Koizumi, Y. Kenta, A. Chiba. In-situ fabrication and characterization of ultrafine structured Cu-TiC composites with high strength and high conductivity by mechanical milling. Journal of Alloys and Compounds 657 (2016) 122-132.
[17] V. A. Popov, M. Burghammer, M. Rosenthal, A. Kotov. In situ synthesis of TiC nano-reinforcements in aluminum matrix composites during mechanical alloying. Composites Part B: Engineering Volume 145, 15 July 2018, Pages 57-6.
[18] L. T. Chang, W. R. Sun, Y. Y. Cui, R. Yang. Development of prior particle boundary free hot isostatic pressing process for Inconel 718 powder. TMS (The Minerals, Metals & Materials Society), 2014.
[19] Y. L. Kuo, K. Kakehi. Effect of the Prior Particle Boundary on the Microstructure and Mechanical Properties of Hot-Isostatic-Pressed IN718 Alloy. Materials Transactions, Vol. 58, No. 7 (2017) pp. 1042-048.
[20] X. L. Wang, J. R. Li, Y. Zhang, Y. P. Wang. Improvement of interfacial bonding and mechanical properties of Cu-Al_2O_3 composite by Cr-nanoparticle-induced interfacial modification. Journal of Alloys and Compounds 695 (2017) 2124-2130.
[21] A. Fathy, O. Elkady and A. A. Oqail. Production and properties of Cu-ZrO_2 nanocomposites. Journal of Composite Materials 2018, Vol. 52(11) 1519–1529.
[22] G. K. Williamson, W. H. Hall. X-ray line broadening from filed aluminum and wolfram. Acta Metallurgica. Volume 1, Issue 1, January 1953, Pages 22-31.
[23] G. V. Chester, A. Thellung. The Law of Wiedemann and Franz. Proceedings of the Physical Society. 1961 77 1005.

Chapter 3. Influence of MA time on in-situ fabricated ODS-Cu alloys

3.1 Introduction

As the mainstream to fabricate the dispersion strengthened materials, the mechanical alloying (MA) is a solid-state powder processing technology, in which the materials are repeated fracture, cold welding. The supersaturated solid solution state can be formed during MA, and the solubility limit shown in the phase diagram can be exceeded. MA is a complex fabrication process, and there are many parameters need to be optimization to achieve the desired materials, such as MA speed, ball to powder weight ratio, process control agent, MA time and so on. The performance of consolidated materials is great influenced by MA alloyed powders. MA time, as one of the key parameters, has great influence on the MA powders. Extending the MA time can sufficiently mix MA powders, enhance the distribution of alloyed elements, and form higher supersaturated solid solution state. But longer MA time increase the contamination and form undesirable phases. Various MA time were applied to fabricate ODS-Cu alloys as shown in Table 3.1. It is found that various milling parameters were conducted to fabricate the Y_2O_3 dispersion strengthened Cu alloys without obvious guidance. It is necessary to explore the influence of MA time on the microstructure and macro performance of ODS-Cu alloys.

Table 3.1 summary of the MA parameters by global peers. (rpm: rotation per min)

Authors	MA time	Speed	References
A. Muñoz et al.	72 hours	150 rpm	[1]
Alasdair Morrison	36 hours	250 rpm	[2]
G. Carro et al.	40 hours	100 rpm	[3]
Yuchen Liu et al.	20 hours	500 rpm	[4]
S.M.S. Aghamiri et al.	48 hours	470 rpm	[5]
Dengshan Zhou et al.	12 hours	500 rpm	[6]
D.V. Kudashov et al.	20 hours	200 rpm	[7]

For the innovative MA-HIP process by in-situ fabrication method developed in this doctoral thesis, the oxidant was added at the middle of MA process in order to avoid the premature formation of Y-O clusters. Considering the unsynchronized Y and O element additions, the

investigation about the influence of MA time on the properties of MA powders and the followed bulk sample after HIP is especially crucial. In the previous topic about the influence of HIP temperature on the properties, all samples after 32 hours MA showed the non-uniform distribution of elements. In this topic, The MA time was extended from 32 h to 96 h, and the elements distribution, crystal lattice evolution, morphology development, and the contamination content were investigated. The objective of this topic is to explore the optimum MA time for ODS-Cu through innovative MA-HIP process by in-situ fabrication method.

3.2 Experimental procedure

In this work, ODS-Cu with 3.0 wt. % Y_2O_3 after various MA time from 32 hours to 96 hours were fabricated shown in Table 3.2. In the first stage. Y (99.9% purity, 20 mesh) was first milled with Cu (99.9% purity, 300mesh) for 16 hours with a speed of 250 rpm in planetary-type ball mill machine, which was in a glove box with Ar atmosphere. The diameter of stainless-steel ball used for MA is 5 mm and the ball to powder weight ratio is 7:3 based on previous works. In the second stage, CuO (99.9% purity, 300 mesh) was added into the half-milled powders, and further milled for another 16, 48 and 80 hours with same parameters. The total MA time are 32, 64 and 96 hours, respectively.

Table 3.2 Summary of ODS-Cu alloys with different MA time (Total:100 g)

Samples	Cu	Y	CuO	MA time
Cu-3.0 wt. %Y_2O_3 (32 h)	94.47	2.36	3.17	32 h
Cu-3.0 wt. %Y_2O_3 (64 h)	94.47	2.36	3.17	64 h
Cu-3.0 wt. % Y_2O_3 (96 h)	94.47	2.36	3.17	96 h

The alloyed powders were transferred to the capsule fabricated by mild steel, which is easier deformation during HIP. In order to avoid the sucking away of the powders in the following evacuation, metal mesh was used to enclose the capsule. Then the capsules were transferred into the NIFS-Sealing Device filled with Ar atmosphere for sealing operation. The capsules were evacuated by mechanical vacuum pump for one hour to make sure the vacuum condition with pressure less than 0.1 MPa. The capsules were finally sealed by gas tungsten arc melting method. During the HIP process, the steel capsules, filled with milled powders, were kept in the pressure of 150 MPa and temperature of 950 °C for 1 hour. It should be noted that the heat and cooling rate was 7.5 °C/min, and the HIP pressure was also loaded and unloaded

synchronously with the rate of 1.22 MPa/min. The specimens after HIP were mounted in the conductive mosaic cement, followed by ground using silicon carbide papers with grids order of 150, 400, 800, 1200 and 2400, and finally polished by alumina powders with diameters of 0.3 and 0.05 μm.

The milled powders with different MA time and the bulk samples after HIP were analysed in terms of crystal structure, morphology, Vickers hardness and electrical conductivity. The crystal structure was analysed by XRD based on the Rigaku RINT-2200 diffractometer with Cu Kα radiation with the parameters of 40 kV and 40 mA. Microstructures were examined by scanning electron microscopy (SEM, JEOL JSM-5600) equipped with energy dispersive X-ray spectroscope (EDS). The Vickers Hardness was tested at room temperature with a loading of 100 gf/mm^2 for 30 seconds. The detail description about the procedures were shown in chapter 2.

3.3 Results and discussion

3.3.1 For MA powders

XRD is an effective analysis method to conform the structure, lattice parameter, and content of the target phase, all of which are the important parameters to characterize the influence of MA time on the analysed sample during MA process. Figure 3.1 shows the XRD spectrum of the MA powders after 32h, 64h and 96h MA. It was found that there was no significant difference in the spectrum for powders with different MA time, excepting of a superficial peak of Cu_2O in the 32 hours' sample, which meant that CuO was converted to Cu_2O during MA process. The similar formation of the intermediate product was observed in the previous research [8] shown in Figure 3.2. The in-situ reaction during MA-HIP process do not occur directly, and the intermediate phase is always formed. In this MA process, the CuO were gradually converted to Cu_2O, finally to the pure Cu.

From Figure 3.3 it is found that the lattice parameter of the powders after 32 hours' MA is obviously lower than that of pure Cu. With the MA continuing, the lattice parameter simultaneously increased. During MA process, crystal deformation due to grinding and solid solution are the two main mechanisms to influence the lattice parameter. Lattice distortion caused by cold welding play the main role in the preliminary stage of MA, causing the decrease of lattice parameter, resulting in the lower lattice parameter for the powder after 32 hours' MA than pure Cu. With the MA time increasing, solid solution mechanism gradually plays the main role, stretching the crystal of MA powders and causing the increase in lattice parameter.

As to crystallite size, it gradually decreased with the MA continuing, and trended to be stable after 64 hours' MA. During MA process, the MA powders experience plastic deformation in the form of fatigue and fracture because of the collision between MA powders and balls, introducing dislocations with high density and finally leading to very fine crystallite size. From the perspective of crystallite size, 64 hours of MA is enough to form fine size of grains.

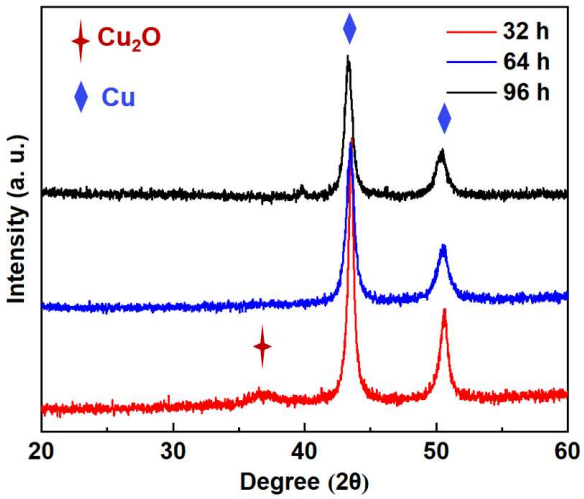

Figure 3.1 XRD spectrum of the samples with different MA time (32 h, 64 h, 96 h)

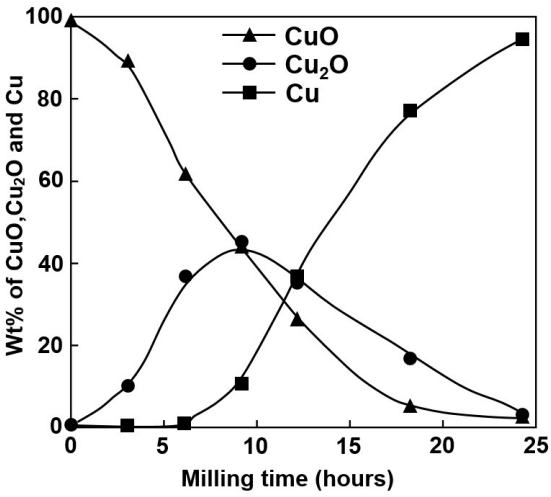

Figure 3.2 Effect of MA time on the CuO [8].

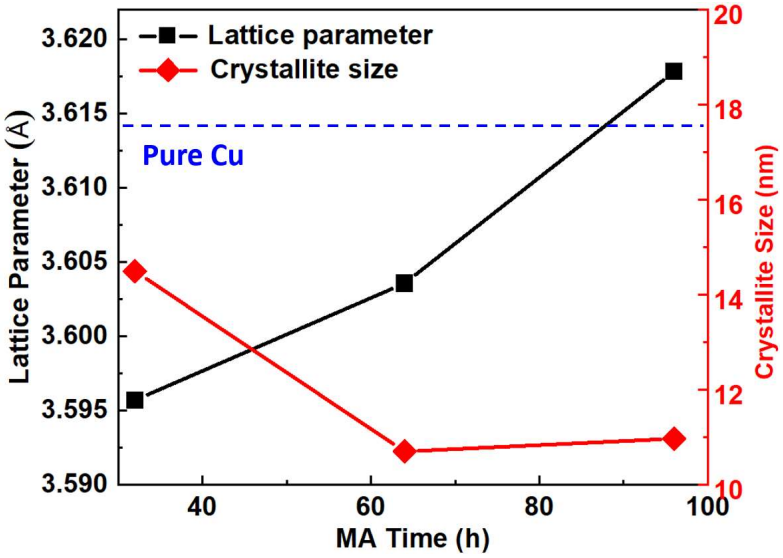

Figure 3.3 Development of lattice parameter and crystallite size.

Figure 3.4 shows the size distribution of MA powders, including the corresponded SEM images. Considering that the most of powders are not sphere, they were amounted by average of length and width. The size distribution of powders covered the range from initial size to 1800 μm. The mode, which represents the particle size of MA powders increased from 80 μm after 32 hours' MA to 220 μm after 96 hours' MA. As an FCC material, Cu matrix has large

ductility because of its 12 glide systems, leading to plastic deformation and adhesion, thereby enhancing the increase in powder size with the MA time extending.

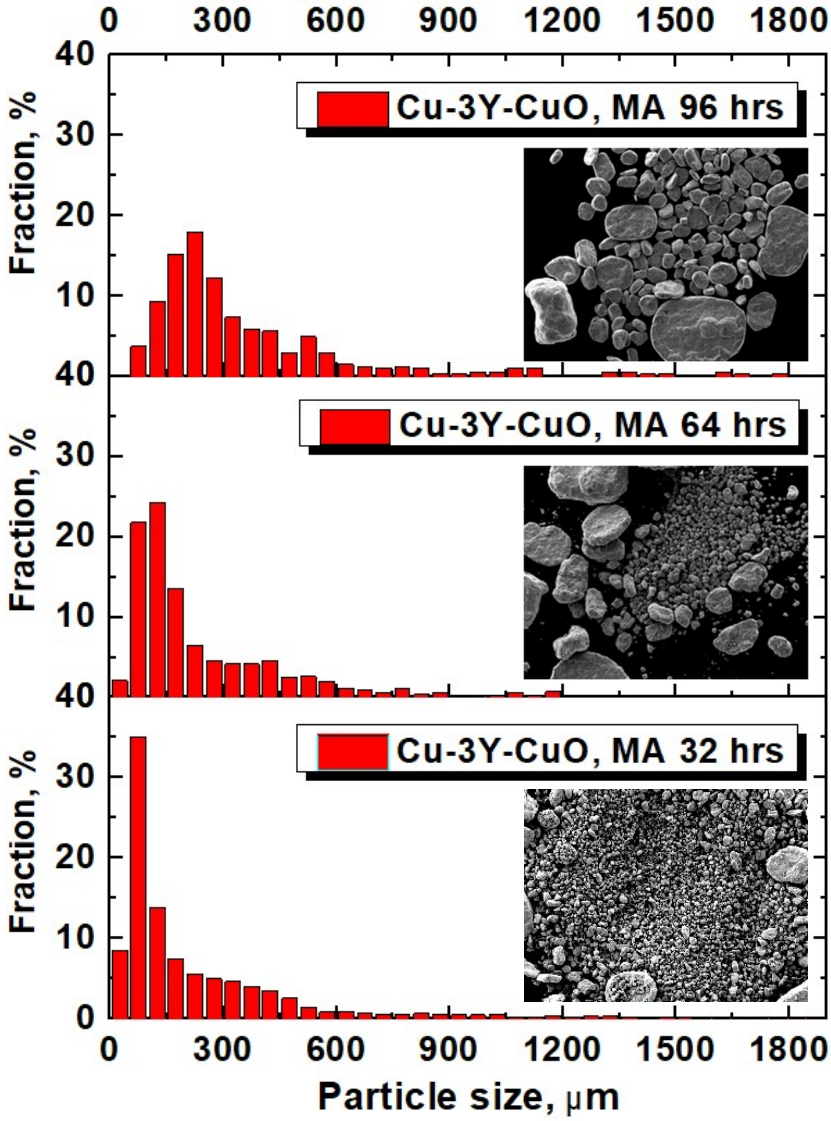

Figure 3.4 Size distribution of MA powders with MA time.

Considering the fine MA powders (<80 μm) disappeared after 96 hours' MA, the surface evolution of powders during MA process from 32 h to 96 h were characterized and shown in Figure 3.5. It is found that after 32 hours' MA, many of smaller particles attached on the surface of larger MA powders due to cold welding and adhesion, forming coarse surface. With the MA continuing, the smaller particles attached on the larger powders changed their shape because of plastic deformation. Along with the increase in MA time, the surface state trended to stable, only became more and more smooth. The adhesion of fine MA powders on the coarse MA powder's surface was the reason of growth with the MA extending.

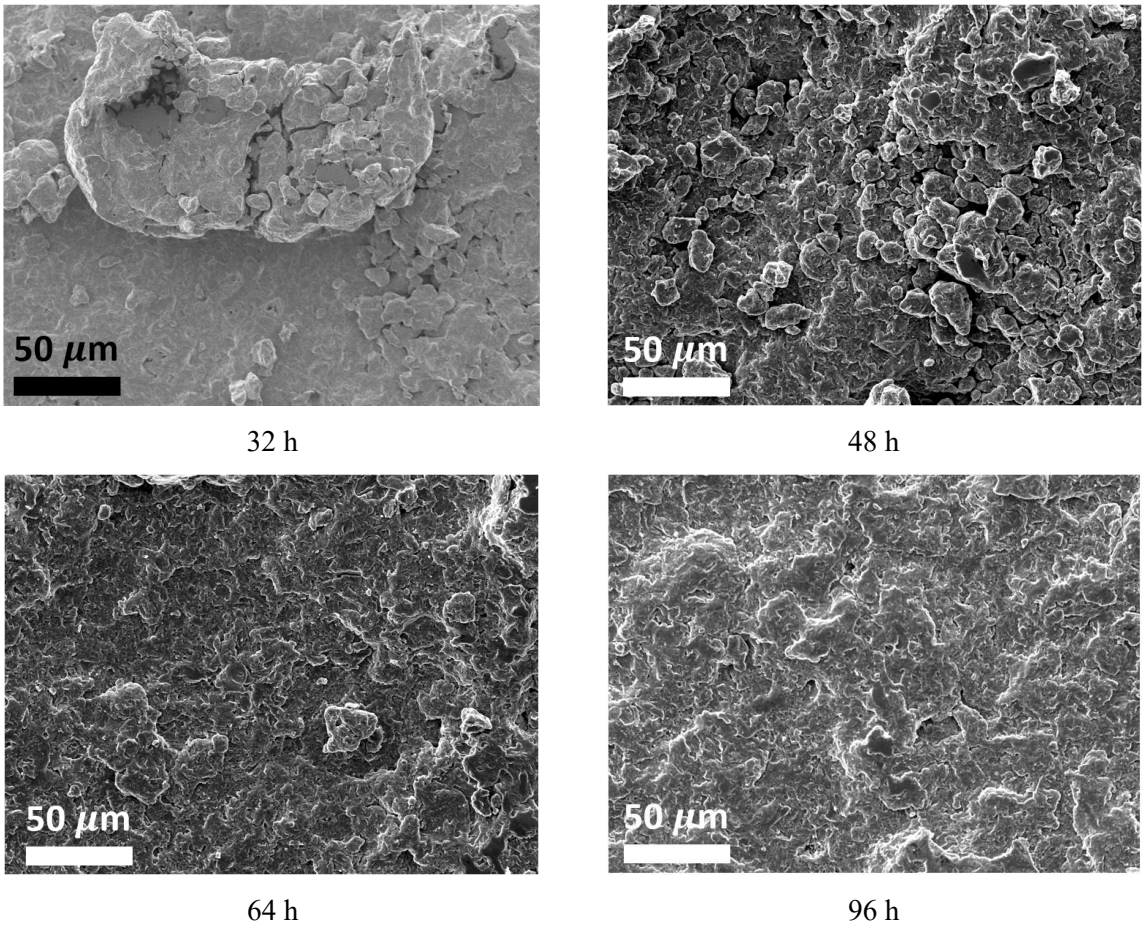

32 h 48 h

64 h 96 h

Figure 3.5 The evolution of coarse MA powers' surface with the MA time.

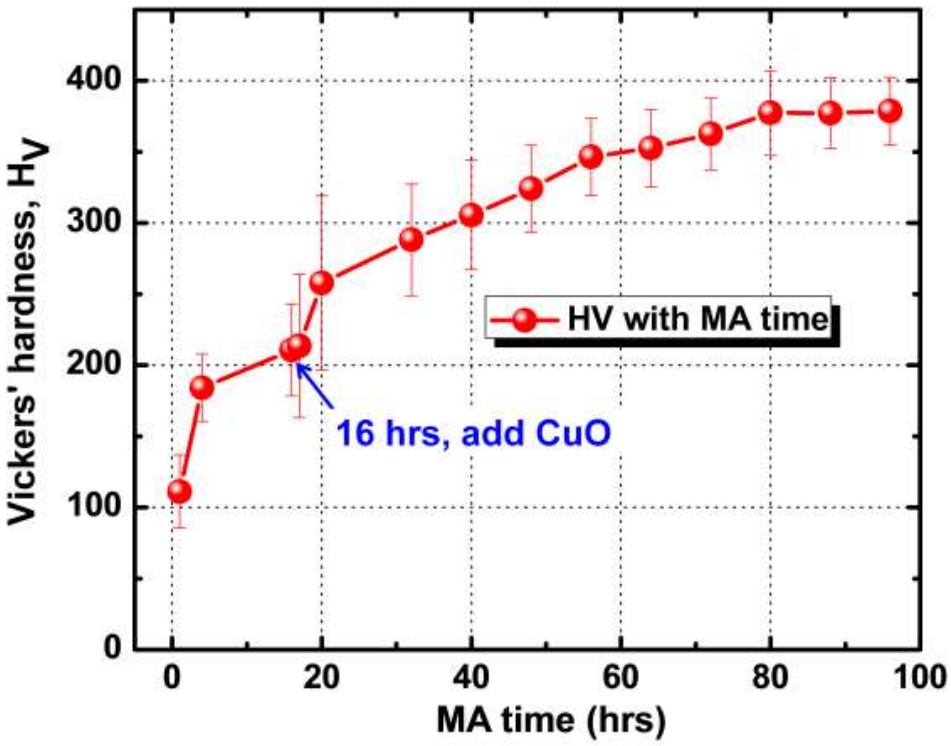

Figure 3.6 Vickers hardness development of MA powders with MA time.

Vickers hardness is a based parameter to explore the mechanical properties. Figure 3.6 shows the Vickers hardness of powders with different MA time. It was found that Vickers hardness increased sharply at first 4 hours and trended to smooth until 16 hours. Vickers hardness increased sharply again with the CuO addition, a relatively brittle materials, and weakly grew up until 64 hours, reaching to stable value at 80 hours. It is worth emphasizing that the error bar increased sharply when added CuO, caused by the non-uniform distribution of elements, and gradually decreased with the MA continuing, indicating the elements distribution was gradually uniform. During MA process, both the introduction of dislocation and the solid solute atoms caused by collision can increase the Vickers hardness.

3.3.2 For consolidated samples

In order to investigate the influence of MA time on the crystalline structure, XRD tests were conducted on the bulk samples consolidated by the powders with different MA time. As shown in Figure 3.7, the peak of Y_2O_3, which didn't exist in the XRD spectrum of MA powders, directly indicated that Y_2O_3 were successfully formed during HIP process by in-situ reaction. Besides, the constant peak of Y_2O_3 in different MA time indicated that in-situ reaction can easily occur in the HIP process with temperature of 950 °C, and 32 hours' MA was enough for fully reaction. While the influence of MA time on Y_2O_3 particle size need be further explored in future.

The influence of MA time on the lattice parameter and crystallite size of the consolidated samples is shown in Figure 3.8, which was also gotten from XRD spectrum by Bragg's law and Scherrer equation shown in chapter 2. The lattice parameters of bulk samples consolidated after 32 h, 64 h, and 96 h MA are 3.6128 Å, 3.6161 Å and 3.6162 Å, respectively. The lattice parameter of bulk samples increased sharply first with the MA time from 32 hours to 64 hours and trended to stable from 64 hours to 96 hours. Compared to the lattice parameters of MA powders, it was found that all the sample's lattice parameter increased in some degree after HIP. During the HIP process, recovery of lattice distortion introduced by MA made a greater contribution to the increase in lattice parameter. The crystallite sizes of bulk samples consolidated by 32 hours', 64 hours' and 96 hours' MA powders are 42.6 nm, 41.55 nm and 41.45 nm, respectively. Compared to the MA powders, the crystallite sizes of all samples grew up during HIP process. The elevated temperature enhances the recrystallization, resulting in the growth of grain for the consolidated samples.

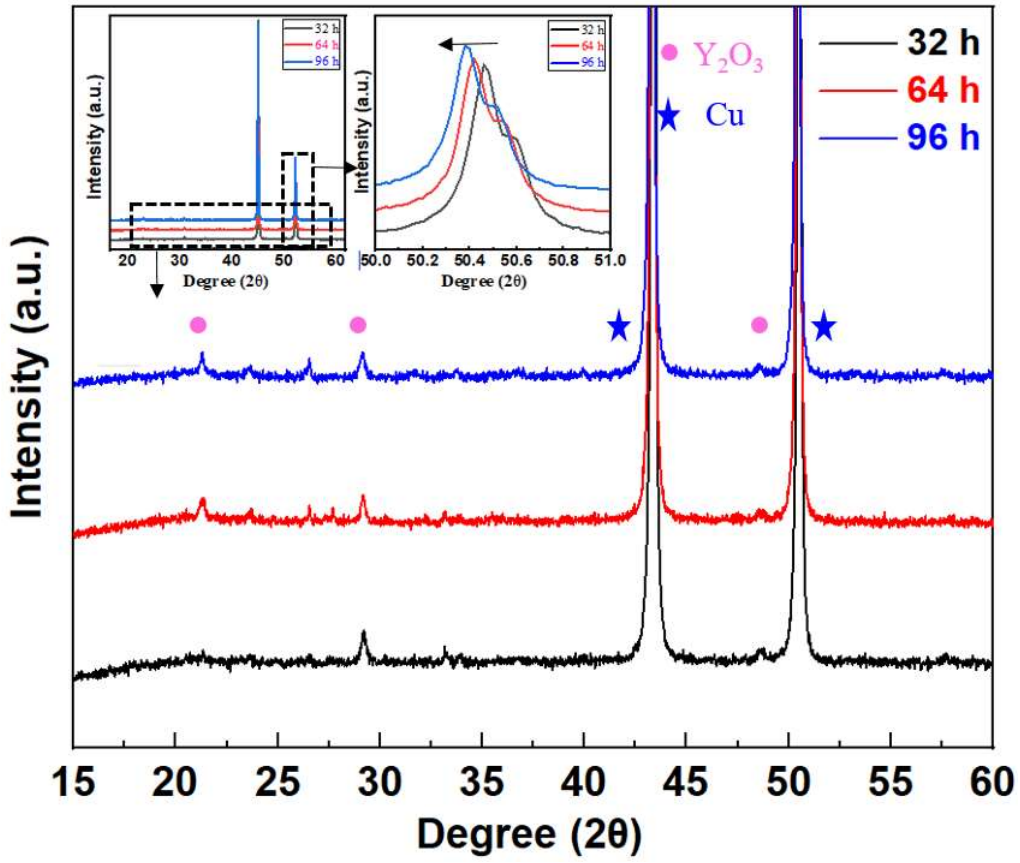

Figure 3.7 XRD spectrum of consolidated samples with different MA time.

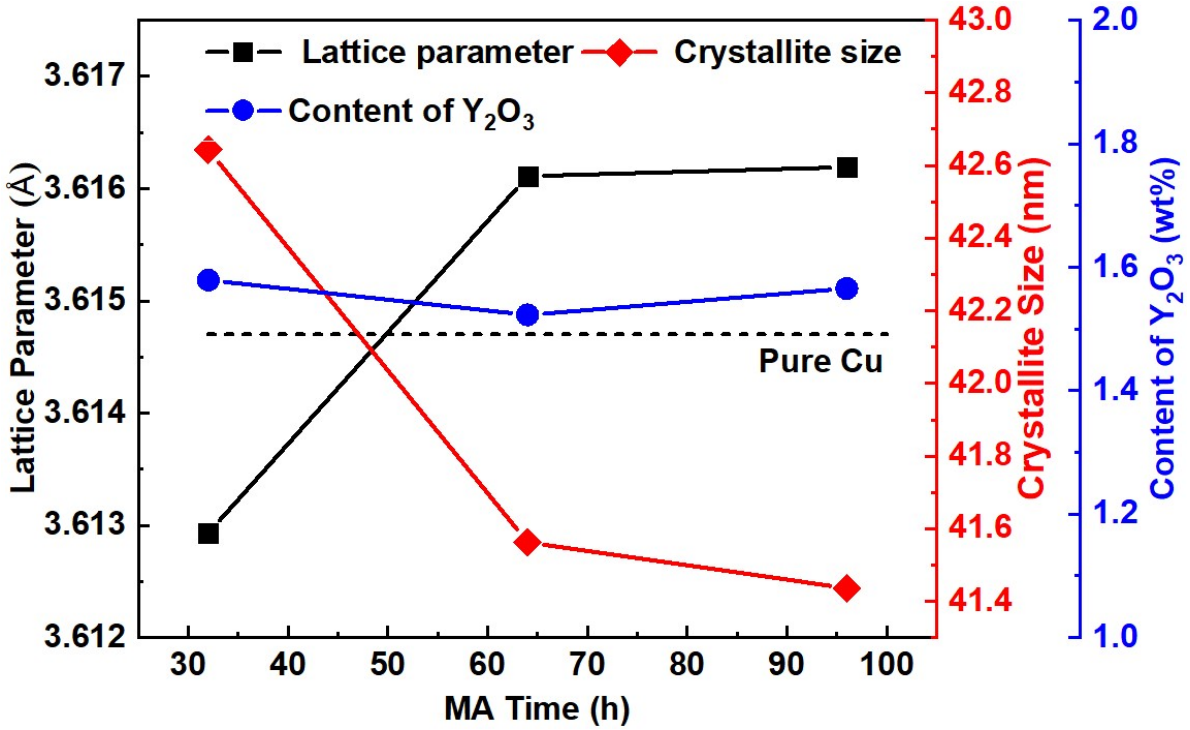

Figure 3.8 Development of lattice parameter, crystallite size and Y_2O_3 content of consolidated samples with different MA time.

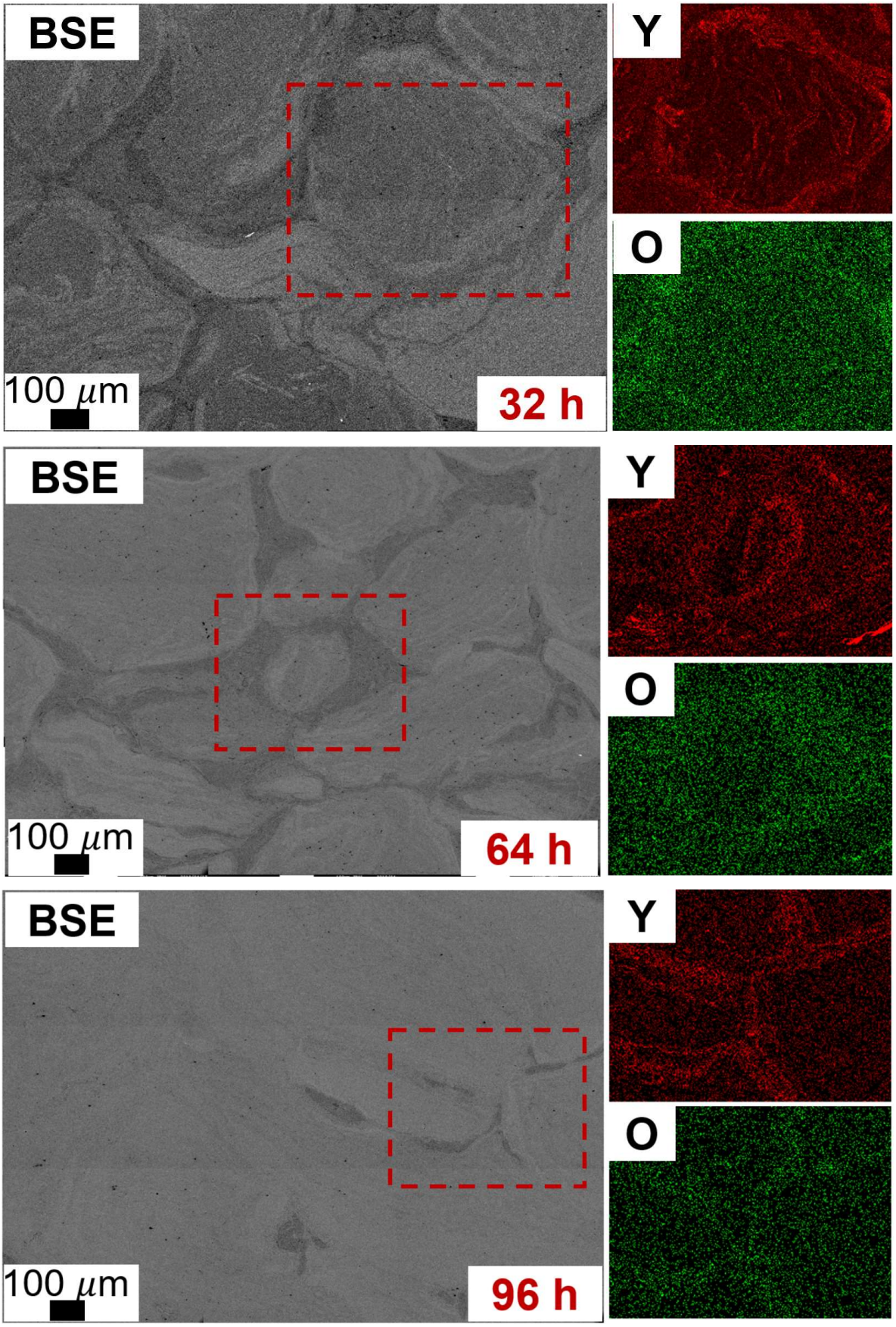

Figure 3.9 The SEM images and the corresponded EDS mappings for the consolidated samples with different MA time.

In order to explore the morphology and the elements distribution, SEM images in BSE mode and the corresponded EDS mappings were conducted based on the bulk samples with different MA time. As shown in Figure 3.9, the oxygen distribution, labelled O, and the yttrium distribution, labelled Y, corresponded to the red box area in the SEM-BSE images. It was found that there was a good match between O and Y distribution for all samples, indicating the formation of Y_2O_3 particles, corresponding to the similar Y_2O_3 content calculated from the XRD spectrum. The MA powders were pressed with irregular shape caused by the plastic deformation, showing the obvious particles boundaries. From the EDS mappings it was found that Y and O are rich on the particle boundaries. The blurry lines in the particles indicated that the particles had been fully mechanical alloyed during MA process. While the obvious particles boundaries meant that the element distribution were still not uniform. For the bulk sample with 64 hours' MA, the powder boundaries are not as prominent as that of 32 hours' sample and the elements distribution were more uniform. For the bulk sample after 96 hours' MA, the prominent boundary disappeared, and all elements distribution were uniform except seldom areas. Actually, the extending of the MA time can enhance the uniform distribution of Y and O elements, but introduce more contamination, which can induce the great deterioration of the thermal conductivity of ODS-Cu alloys. Therefore, other methods except for extending MA time need to be explored to enhance the uniform of Y elements.

3.4 Conclusions

ODS-Cu alloys with 3 wt. % Y_2O_3 was produced through innovative MA-HIP process by in-situ fabrication method. The influence of MA time from 32 hours to 96 hours on the microstructure and physical properties were investigated. The main results were shown as follows:

(1) The cold welding played the main role in the early stage of MA, causing the lattice contraction. With the MA continuing, the solid solution process dominated the lattice distortion. The introduction of defects during MA process such as dislocations and solid solute Y contributed to the increase in Vickers hardness. Besides, the MA powders had the trend to grow up and become smoother due to cold welding and continuous collision.

(2) There was a good match between O and Y distribution for all samples, forming Y_2O_3 particles, corresponded to the similar Y_2O_3 content calculated from the XRD spectrum. 32 hours' MA is enough for the fully in-situ reaction to form dispersive Y_2O_3.

(3) The extending the MA time enhanced the uniform distribution of Y and O elements, but introduced more contamination, which can induce the great deterioration of the thermal conductivity for ODS-Cu alloys. Therefore, other methods except for extending MA time need to be explored to enhance the uniform of Y elements.

References:

[1] A. Muñoz, B. Savoini, M.A. Monge, M. Eddahbi, O.J. Dura. Microstructure and mechanical properties of hot rolled ODS copper. Nuclear Materials and Energy 24 (2020) 100754.

[2] A. Morrison. Powder based processing of novel dispersion strengthened copper alloys for fusion applications [D]. University of Oxford, 2017.

[3] G. Carro, A. Muñoz, B. Savoini, M.A. Monge. Fabrication and characterization of dispersion strengthened Cu-0.8%Y. Fusion Engineering and Design 154 (2020) 111548.

[4] Y. Liu, S. Kondo, H. Yu, K. Yabuuchi and R. Kasada. Statistical Approach for Understanding the Effect of Specimen Size on the Yield Stress and Its Scattering in Mechanically-Alloyed Cu and ODS-Cu Obtained by Micro-Pillar Compression Test. Materials Transactions, Vol. 61, No. 5 (2020) pp. 955-962.

[5] S. M. S. Aghamiri, N. Oono, S. Ukai, R. Kasada, H. Noto, Y. Hishinuma, T. Muroga. Microstructure development and high tensile properties of He/H_2 milled oxide dispersion strengthened copper. Journal of Alloys and Compounds 783 (2019) 674-679.

[6] D. S. Zhou, X. K. Wang, W Zeng, C. Yang, H. C. Pan, C. G. Li, Y. J. Liu, D. L. Zhang. Doping Ti to achieve microstructural refinement and strength enhancement in a high volume fraction Y_2O_3 dispersion strengthened Cu. Journal of Alloys and Compounds 753 (2018) 18-27.

[7] D. V. Kudashov, H. Baum, U. Martin, M. Heilmaier, H. Oettel. Microstructure and room temperature hardening of ultra-fine-grained oxide-dispersion strengthened copper prepared by cryomilling. Materials Science and Engineering A 387–389 (2004) 768–771.

[8] C. Suryanarayana. Mechanical alloying and milling. Progress in Materials Science 46 (2001) 1-184.

Chapter 4. Size distribution of MA powders

4.1 Introduction

Mechanical alloying is a solid-state process in which fracture and cold welding are repeated, and the structure of MA powders is changed as a result, including size, shape, composition, morphology and so on. Cold welding enlarges the size of MA powders, and fracture reduce the size of MA powders. Cu with face centered cubic (FCC) structure, is more ductile, and cold welding is more frequently occurred compared to fracture, leading to the continued growth and severe sticking [1-3]. There are some methods to prohibit the growth of MA powders. One method is to add some organic compounds such as stearic acid and ethanol into the MA system as the process control agent (PCA). PCA can avoid the growth of MA powders by covering on the surface of MA powders, including the new surface formed by fracture, to decrease the surface activity [4, 5]. But the PCA addition inevitably introduces contamination and pollutes the Cu matrix. Another method is cryogenic milling, which is a low temperature (< 123 K) mechanical alloying process cooled by liquid nitrogen [6-10]. But there is no ductile brittle transition temperature (DBTT) for Cu, which is FCC crystal structure. The inhibition of sticking is limited. The expensive and difficult fabrication process also limit the application in industrial scale. In this thesis, the intermittent milling, in which short milling period (1 hour) alternated with longer natural cooling period (3 hours), was conducted to suppress the severe sticking.

The purpose of the methods shown above is just to balance the fracturing and cold welding, adjusting the MA powders in macro scale. The detail information about the micro mechanism of MA powders evolution needs further exploration. The fracture mode, whether passing through the MA powders or along the powders' surface, has great influence on the structure and element distribution of MA powders. The structure of MA powders also needs to be explored, whether uniform structure or shell structure. Besides, considering multi modal size distribution of the MA powders, it is necessary to investigate the relationship between powder size and element distribution. The similarities and differences among the MA powders with different sizes can characterize the evolution of powders during MA process, contributing to better understanding on the mechanism during MA process.

In this topic, the MA powders after 32 hours MA were classified into four parts (<46 μm, 46 ~ 100 μm, 100 ~ 212 μm, >212 μm) based on their size, and the detail information of every

group was analyzed, including the proportion, morphology, composition, hardness and so on. The analysis on the size distribution of MA powders is beneficial to detailed understand the mechanism of mechanical alloying process and provide the guidance to optimize the innovative MA-HIP process.

4.2 Experimental procedure

As shown in Table 4.1, the materials with nominal composition of Cu-1wt. % Y_2O_3, Cu-3wt. % Y_2O_3 and Cu-5wt. % Y_2O_3 were produced through innovative MA-HIP process by in-situ fabrication method. Metal Y powder (99.9% purity, 20 mesh) and metal Cu powder (99.9% purity, 300 mesh), supplied by Furuuchi Chemical Co. Ltd in Japan, were mechanical milled with stainless steel balls (5 mm) by planetary-type ball-milling machine (Pulverisetee 5, Fritsch) with a ball-powder ratio of 7:3 and a speed of 250 rpm for 32 hours. CuO (99.9% purity, 300 mesh) as the oxidant material was added at the middle of MA process. It should be noted that the rotation was repeated by an automated program (1h milling + 3h pause) to avoid excess temperature increase.

Table 4.1 Summary of ODS-Cu with different Y_2O_3 content (Total:100 g)

Sample ID	Samples	Cu	Y	CuO
#1	Cu-1.0 wt. %Y_2O_3	98.15	0.79	1.06
#3	Cu-3.0 wt. %Y_2O_3	94.47	2.36	3.17
#5	Cu-5.0 wt. %Y_2O_3	90.79	3.93	5.28

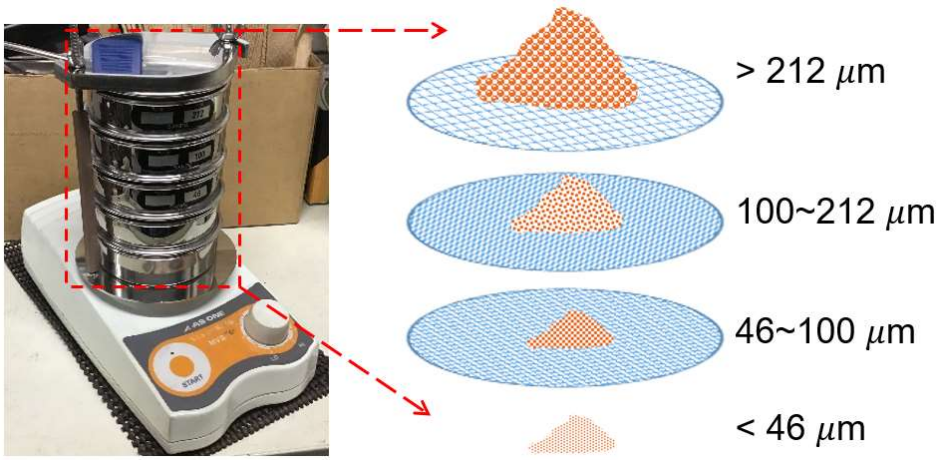

Figure 4.1 Images of the screening machine.

The mechanical alloyed powders were separated by their size using a screening machine shown in Figure 4.1 and were divided into four categories (<46 μm, 46 ~ 100 μm, 100 ~ 212 μm, >212 μm). All the operations were conducted in a glove box with pure Ar atmosphere to prevent oxidation and contamination. The screened powders were put into the steel capsules. Before clamping, the capsules were degassed for 1 hour in 0.1 Pa vacuum, followed by welding. During the HIP process, the steel capsules, filled with classified powders, were kept in the pressure of 150 MPa at temperature of 950 °C for 1 hour. For the cross-sectional area observations, the classified MA powders were mounted on the conductive mosaic cement, followed by grinding using silicon carbide papers with grids order of 150, 400, 800, 1200 and 2400, and finally polished by alumina powders with diameters of 0.3 and 0.05mm.

Figure 4.2 Images of the FIB and TEM machines.

The screened samples were characterized by various techniques. Vickers hardness measurements were conducted at room temperature with a load of 10 gf for 30 seconds. The morphology and local composition of the particles were examined by scanning electron microscopy (SEM, JEOL JSM-5600) equipped with energy dispersive X-ray spectroscope (EDS) and wavelength-dispersive spectroscopy (WDS), whose images was shown in chapter 2. The sectioning with focused ion beam (FIB) (Hitachi nano DUE'T NB5000) machine was carried out to prepare transmission electron microscope (TEM) samples. Microstructures were analysed by JEOL JEM-2800 TEM shown in Figure 4.2.

4.3 Results and discussion

4.3.1 The influence of Y_2O_3 content on alloyed powders

Figure 4.3 shows the SEM images of the MA powders with various Y_2O_3 content. The sample with 1 wt. % Y_2O_3 had large powders with size of several hundred micrometer. While

there were plenty of fine particles among the coarse MA powders for the sample with 3 wt. % and 5 wt. % Y_2O_3. Besides, the surface of the MA powder also became rougher with the increase in Y_2O_3 content. Figure 4.4 and Table 4.2 show the size distribution of the MA powders after classification. It was found that the occupation of fine MA powders gradually increased with the Y_2O_3 content. It was indicated that the Y and CuO additions played not only the role of Y_2O_3 sources but also the process control agent to suppress the growth of MA powders. Compared to the ductile Cu, Y and CuO being relative brittle, which can suppress the cold welding during MA process, resulting in both the roughness of the surface of the MA powder and the fine MA powder formation. It seems that the fine MA powders came from the exfoliation of the coarse powders' surface, resulting in the rough surfaces and the reduced size of coarse powders. More evidence needs to be investigated to support this hypothesis.

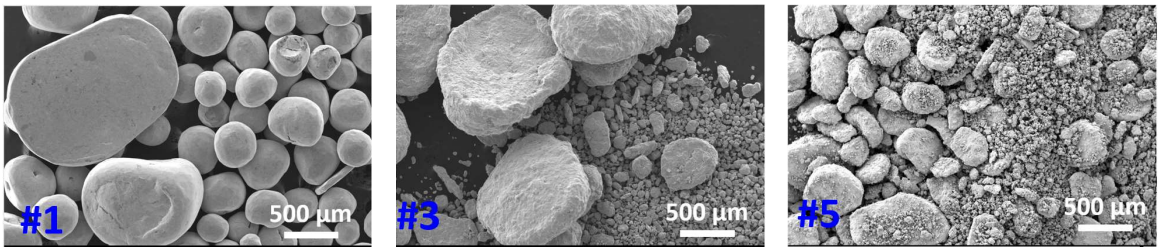

Figure 4.3 Morphology of the MA powders with different Y_2O_3 content after 32 hours MA.

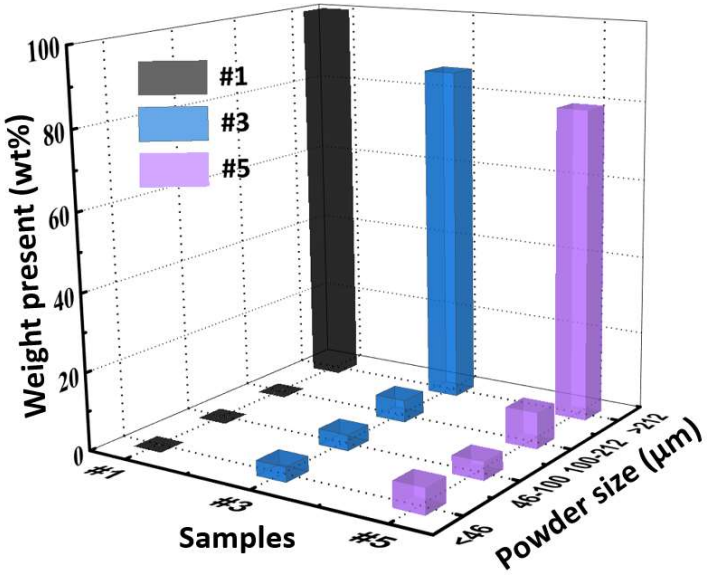

Figure 4.4 Particle size distribution of MA powders with different Y_2O_3 content.

Table 4.2 Size distribution of MA powders with different Y_2O_3 content. (wt. %)

Samples	< 46 μm	46-100 μm	100-212 μm	>212 μm
#1	0	0	0	100
#3	3.79	4.11	5.73	86.37
#5	6.52	4.64	9.24	79.60

4.3.2 Characterization of classified MA powders of sample #3

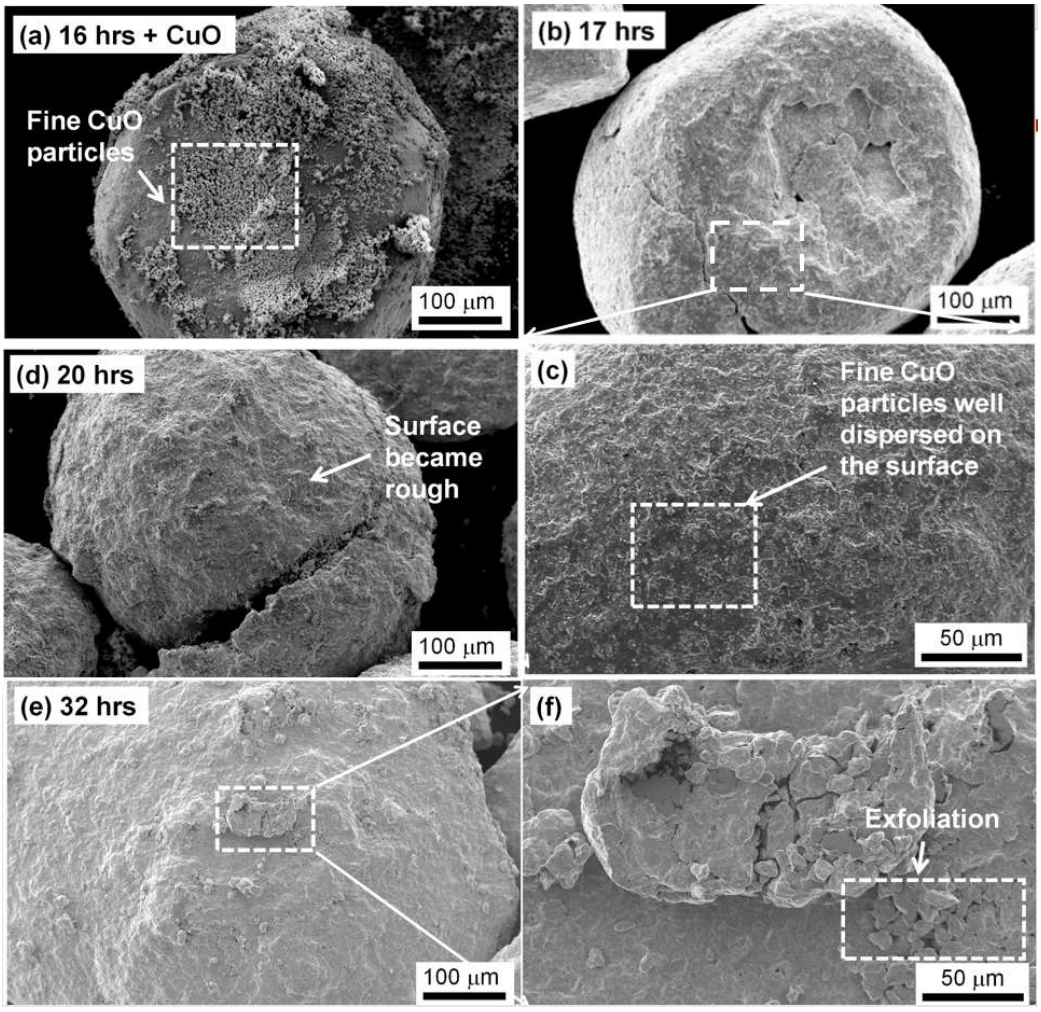

Figure 4.5 Microstructure evolution of the surface of the coarse MA powder in the sample #3 during MA process from 16 h to 32 h.

Figure 4.5 shows the microstructure evolution of the surface of the coarse MA powder from 16 hours to 32 hours for the sample #3. It was found that the middle added CuO was first attached on the surface of middle alloyed coarse MA powders. With MA continuing, the CuO particles were grinded and uniform distributed on the coarse powders' surface. After 20 hours' MA, the surface of the coarse MA powder became rough, then some fine MA powders were exfoliated from the surface of coarse MA powders after 32 hours MA. Therefore, the fine MA powders came from the surface of coarse MA powders based on the morphology evolution.

In order to further verify the viewpoint shown above, the cross section of fine (< 46 μm) and coarse (> 212 μm) MA powders of sample #3 were investigated respectively, as shown in Figure 4.6. Fine MA powders had irregular shape with bright layered structures, which were caused by the uneven distribution of elements. The bright layered structure inside the fine powders not only demonstrated that the powders were fully alloyed, but also meant that the

elements distribution were still not uniform. The arrow in Figure 4.6 (a) indicates a boundary where two small powders were merging, corresponding to the growth tendency of fine MA powders with the increase in MA time shown above. The coarse MA powders in Figs 4.6 (b) showed nearly circular shape with discrete dark surface layers, and the lack parts had been peeled off during ball milling. It should be emphasized that the fracture of surface layers of the coarse powders, accompanied with cold welding during MA, kept the size of coarse powders in a dynamic balance.

Considering the significantly different morphologies of the central and outer area for coarse MA powders, EDS and WDS were conducted based on three kinds of areas, fine MA powders, central and outer areas of coarse MA powders, as shown in Table 4.3. For both fine and coarse MA powders, Y had a relatively uniform distribution. In the central region of coarse MA powders, the atomic ratio of Y and O was around 2:3, same as the atomic ratio of Y_2O_3. Oxygen content was enriched in fine MA powders and the outer layer of coarse MA powders. Furthermore, Vickers hardness test were conducted based on those three areas, as shown in Figure 4.7. Compared to pure Cu, the Vickers hardness of central region of coarse MA powders was higher. Vickers hardness of the fine MA powders was comparable with that of outer area of the coarse MA powders, slightly larger than the central area.

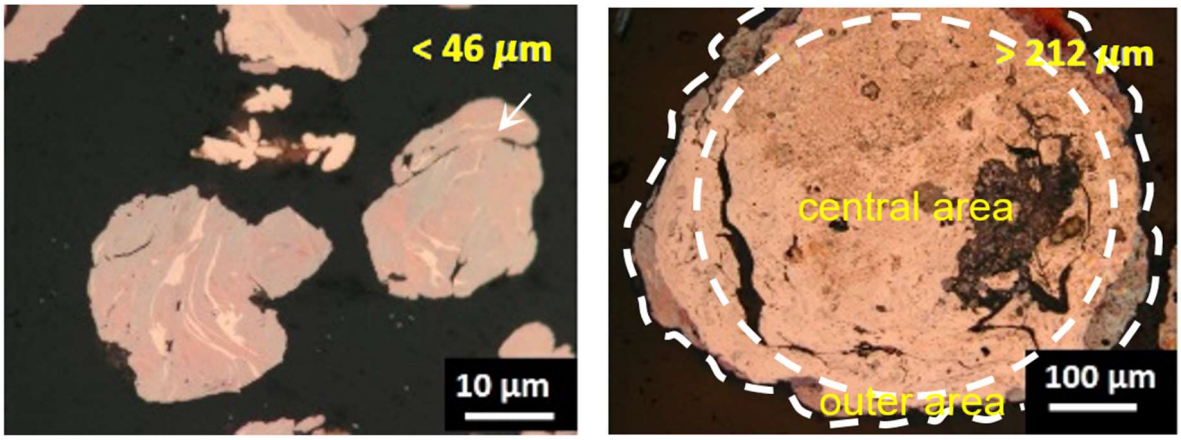

(a) (b)

Figure 4.6 Optical image of fine MA powder less than 46 μm (a) and coarse powders larger than 212 μm (b) after 32 hours of MA.

Table 4.3 Element distribution of fine and coarse MA powders with 32 hours of MA. (at %)

Particle size	Area region	Cu	Y	O
< 46 μm		79.08	1.82	19.10
> 212 μm	Center	95.57	1.85	2.58
	Outer	78.17	1.80	20.03

At the first stage of MA, the pure Y and Cu powders were mechanical alloyed to form Cu-Y phase, and Y were uniformly dissolved into the copper matrix. Meanwhile, higher degree of cold welding than fracture occurred, inducing the growth of MA powders with multi modal size distribution. At the second stage of MA, CuO was added into the middle-alloyed powders, forming oxygen-enriched layers on the surface of MA powders. With the MA continuing, some of oxygen diffused into the central area region and in-situ reacted with Y to form Y_2O_3 particles. The extra oxygen still kept at the outer region to form the oxygen-enriched coating, which were peeled off by mutual collision. Considering the similar composition and Vickers hardness of the fine MA powders and the layer of coarse MA powders, companied with the morphology development of MA powders during MA process shown above, the peeled O rich fragments were the main source of the fine MA powders. Compared to pure Cu, the exact atomic ratio of Y and O in the central area of coarse powders contributed to the formation of Y_2O_3, which had great influence on Vickers hardness. While the redundant O at outer region of coarse powders and fine powders only slightly improved the Vickers hardness.

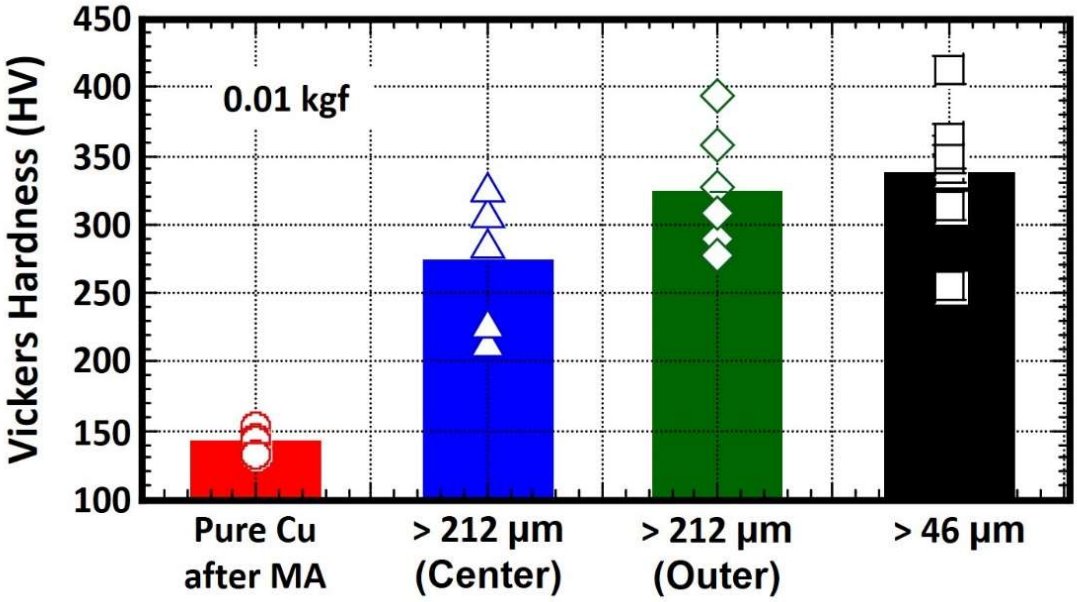

Figure 4.7 Vickers hardness of different areas of MA powder after 32 hour milling.

Figures 4.8 and 4.9 show the TEM images of fine and coarse MA powders after 32hours' MA, respectively. The selected area electron diffraction (SAED) patterns in Figure 4.8 and Figure 4.9 showed that Cu_2O (1 1 0) and Y_2O_3 (2 2 2) were overlapped near the central diffraction ring, and Cu_2O (1 1 1) ring with the maximum diffraction intensity was also confirmed. In addition, another diffraction ring of Y_2O_3 (6 4 0) was only shown in the diffraction patterns of fine MA powders in Figure 4.8. The SAED proved the existence of

copper matrix, Cu-O phase and Y_2O_3. The fine powders in Figure 4.8 consisted of fine-sized and redundant Cu-O particles with size of 5 nm, and fine grains with size of 40 nm. Most of O was kept in the form of Cu-O, and the content of Y_2O_3 phase was very low, corresponding to the XRD results in chapter 3. In Figure 4.9, there were larger Y_2O_3 particles with size of 30 nm both in grains and on crystalline boundary regions, in addition to the smaller redundant Cu-O particles with size of 5 nm. The grains were shown in form of long strip with a length of 250 nm in average, probably because of the extrusion during the MA process.

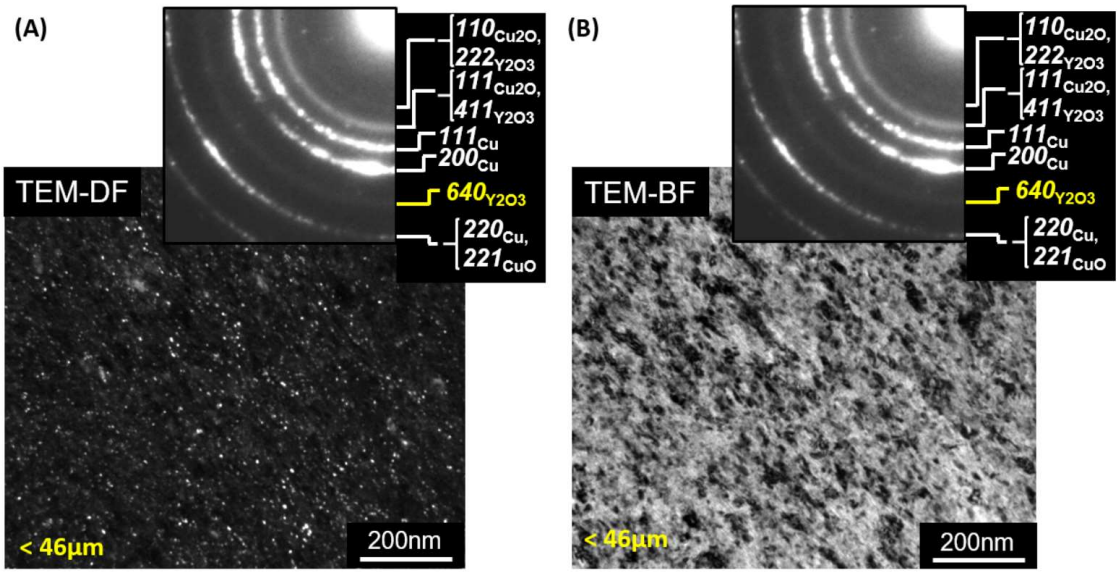

Figure 4.8 TEM dark field (a) and bright field (b) images of the fine MA powder (< 46 µm) after 32 hours; MA.

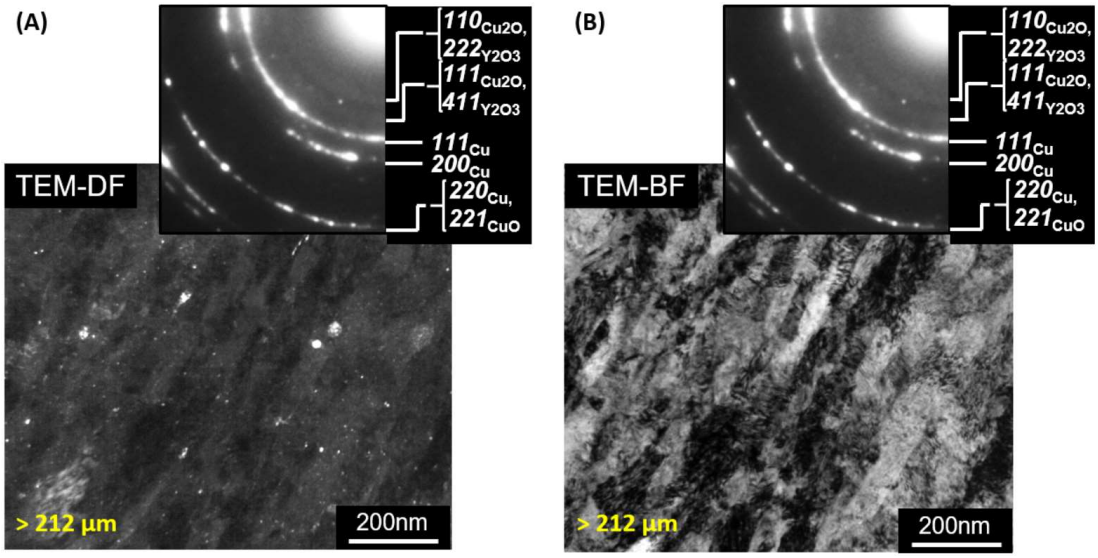

Figure 4.9 TEM dark field (A) and bright field (B) images of the coarse MA powder (> 212 µm) after 32 hours' MA.

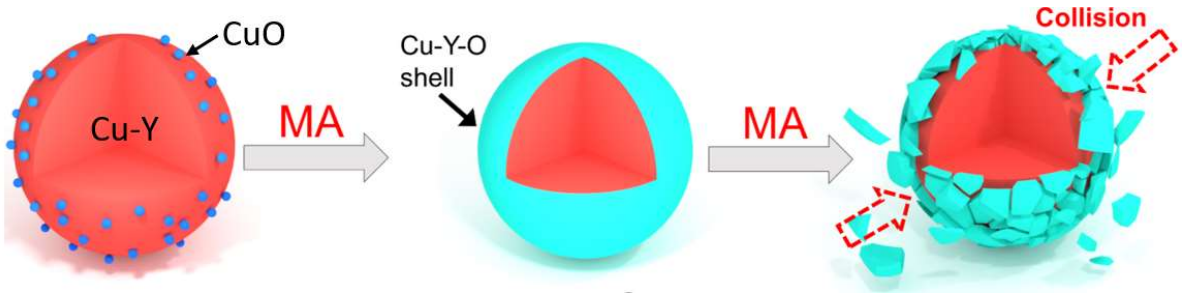

Figure 4.10 The schematic diagram of MA process after CuO being added into the Cu-Y powders.

Combing the morphology evolution of the MA powders, the similar element distribution, similar Vickers hardness, and similar redundant Cu-O phases for fine MA powders and the surface of coarse MA powders, a mechanism about the MA powders evolution was proposed, as shown in Figure 4.10. The MA powders were first mixed and attached on the surface of the alloyed MA powders. With the MA continuing, the CuO particles were grinded and formed a hard and brittle O rich shell on the surface of coarse MA powders. With further MA, the brittle shell was fractured into pieces, forming the fine MA powders.

4.3.3 Characterization of #3 consolidated samples by classified MA powders

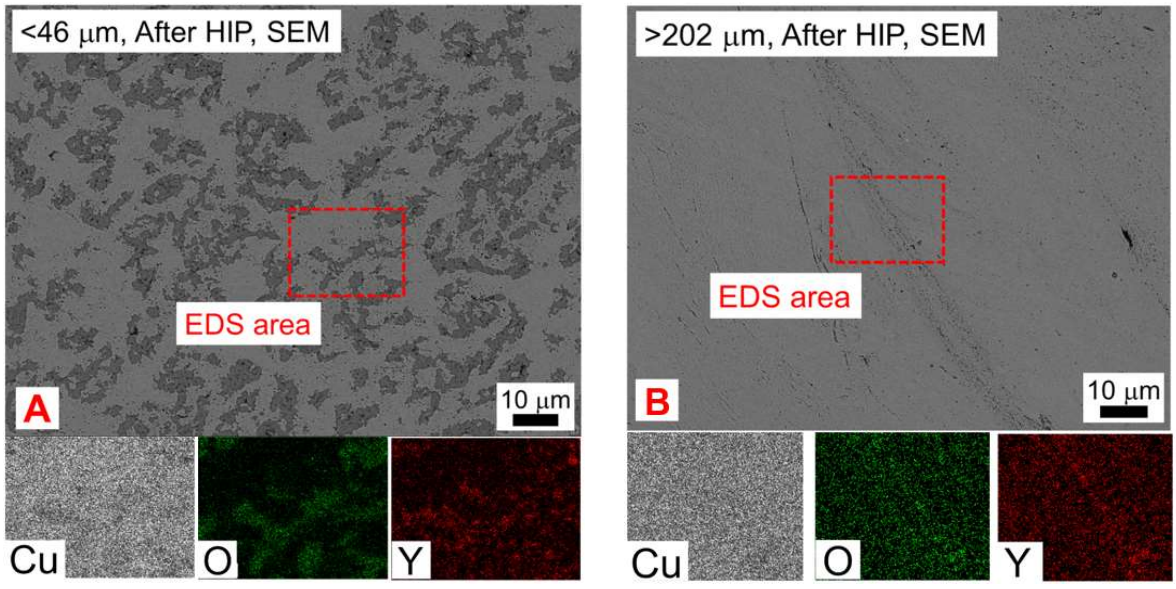

Figure 4.11 SEM and EDS mappings for bulk samples consolidated by fine powders (A) and coarse powders (B).

Figure 4.11 shows the SEM-BSE images and the corresponded EDS mappings of the consolidated samples by the fine MA powders and by the coarse MA powders. It was found that there were plenty of Y and O rich areas with dark colour in the sample consolidated by the fine MA powders. For the sample consolidated by coarse MA powders, the element distributions were uniform except for a few areas. Thereby, screening of the MA powders

before consolidation is beneficial to form the consolidated samples with uniform elements distribution. Besides, fine MA powders (< 46 μm) had redundant Cu-O phases, which have poor thermal conductivity compared to Cu [12], and the redundant oxide ceramics had great influence on the thermal conductivity of ODS-Cu alloys [13-15]. In addition, the small grains in fine MA powders are also bad for the thermal conductivity [16]. Therefore, filtering out the fine MA powders before HIP, removing the peroxide component, is expected to improve the properties of the consolidated materials.

4.4 Conclusions

For the characterization of the difference among the multi scale size of MA powders, the alloyed powders were classified based on their size. The detail information of every group was analyzed, including the proportion, morphology, composition, hardness and so on. The main results were shown as follows:

(1) The Y and CuO additions played not only the role of Y_2O_3 sources but also the process control agent to suppress the growth of MA powders.

(2) The peeled peroxide Cu fragments from the surface of coarse MA powders are the main source of fine MA powders (< 46 μm).

(3) Y had a uniform distribution in all kinds of MA powders, while O had a non-uniform distribution and was rich at the surface of coarse powders, because of the half-way addition of CuO. In contrast to the central area of coarse MA powders with an atomic ratio of Y and O being 2:3, same as the atomic ratio of Y_2O_3, fine MA powders and the surface of coarse MA powders consisted of redundant Cu-O particles and fine grains, which can deteriorate the uniform distribution of elements and the thermal conductivity of ODS-Cu alloys.

(4) Filtering out the fine MA powders before HIP and removing the O-enriched fragments were expected to improve the properties of the consolidated materials after HIP.

References:

[1] C. Suryanarayana. Mechanical alloying and milling, Progress in Mater Sci, 2001 1-168.

[2] C. Suryanarayana. Mechanical Alloying: A Novel Technique to Synthesize Advanced Materials. Research Volume 2019, Article ID 4219812.

[3] L. Lv and M. O. Lai. Mechanical Alloying. Springer Science Business Media, Llc. 1998.

[4] N. S. Anas, M. Ramakrishna, R. K. Dash, T. N. Rao, R. Vijay. Influence of process control agents on microstructure and mechanical properties of Al alloy produced by mechanical alloying. Materials Science & Engineering A 751 (2019) 171–182.

[5] R. Rahmanifard, S. M. Javidan, and M. A. Asadabad. Effects of Process Control Agents on Characteristics of Cu-Ta Nanocomposite during Milling and Subsequent Sintering. Journal of Materials Engineering and Performance. Volume 28(7) July 2019 4102-4110.

[6] M. A. Atwater, D. Roy, K. A. Darling, B. G. Butler, R. O. Scattergood, C. C. Kocha. The thermal stability of nanocrystalline copper cryogenically milled with tungsten. Materials Science & Engineering A 558 (2012) 226–233.

[7] K. Barai, C. S. Tiwary, P. P. Chattopadhyay, K. Chattopadhyay. Synthesis of free standing nanocrystalline Cu by ball milling at cryogenic temperature. Materials Science & Engineering A 558 (2012) 52–58.

[8] D. V. Kudashov, H. Baum, U. Martin, M. Heilmaier, H. Oettel. Microstructure and room temperature hardening of ultra-fine-grained oxide-dispersion strengthened copper prepared by cryomilling. Materials Science and Engineering A 387–389 (2004) 768–771.

[9] J. C. Liu, H. Cui, X. L. Zhou and J. S. Zhang. Microstructure Characterization and Thermal Stability of Nanocrystalline Cu Powders Processed via Cryomilling. Materials Transactions, Vol. 53, No. 4 (2012) pp. 766 to 769.

[10] J. H. Kim, J. H. Lee, J. Y. Min, S. W. Kim, C. H. Park, J. T. Yeom, T. S. Byun. Cryomilling effect on the mechanical alloying behaviour of ferritic oxide dispersion strengthened powder with Y_2O_3. Journal of Alloys and Compounds 580 (2013) 125–130.

[11] B. Huang, Y. Hishinuma, H. Noto and T. Muroga. Mechanochemical processing of Cu-Y_2O_3 alloy by MA-HIP for heat sink materials application. Fusion Engineering and Design, 140, (2019), 33-40.

[12] K. D. Sattler. Handbook of Nanophysics: Nanoparticles and Quantum Dots. CRC Press. 32-1.

[13] A. Fathy, A. Wagih, A. Abu-Oqail. Effect of ZrO_2 content on properties of Cu-ZrO_2 nanocomposites synthesized by optimized high energy ball milling. Ceramics International. 45 (2019) 2319-2329.

[14] A. Fathy, O. E. Kady. Thermal expansion and thermal conductivity characteristics of Cu–Al_2O_3 nanocomposites. Materials and Design 46 (2013) 355–359.

[15] J. Groza. Heat-Resistant Dispersion-Strengthened Copper Alloys. Journal of Materials Engineering and Performance. 1 (1992) 113-121.

[16] M. Elmahdy, G. Abouelmagd, A. A. E. Mazen. Microstructure and Properties of Cu-ZrO_2 Nanocomposites Synthesized by in Situ Processing. Materials Research. 21 (2018) 1.

Chapter 5. Exploring the Y_2O_3 sources for in-situ fabricated ODS-Cu alloys

5.1 The possibility of using Cu-Y compounds as the sources of Y_2O_3 for ODS-Cu alloys.

5.1.1 Introduction

Compared to the mainstream of fabricating ODS-Cu with Y_2O_3 by conventional MA process, in which the Y_2O_3 is directly added and milled with Cu powders, resulting in larger dispersive particles with low number density [1-3], this doctoral thesis adopted innovative MA-HIP process by in-situ fabrication method, in which Y precursor was added and milled with pure Cu. 2-D dispersive nucleus can be formed in the MA process [4]. The Y contained nucleus can in-situ react with oxygen impurity in the Cu matrix, or the oxidant originated from the external addition, forming fine dispersive Y_2O_3 particles.

The properties of Y precursors have great influence on the dispersion of Y element, and the in-situ formed Y_2O_3 particles. There are several kinds of Y precursors. First, the yttrium acetate ($Y(CH_3CO)_3 \cdot 4H_2O$), which can play the roles of both process control agent (PCA) and the source of Y_2O_3 [5]. While the introduction of contamination is inevitable by this Y precursor. Second, pure metal Y, which was used as the source of Y_2O_3 in the previous topics. There are many advantages compared to the Y contained organics. Pure metal Y can be oxidized by O impurity in the Cu matrix without introducing contamination, which is beneficial to the purity of Cu matrix. Besides, there are experiences of using pure metal Y as the source of Y_2O_3 to fabricate ODS materials [6-8]. However, there are still some remain issues when used pure metal Y. Since both Y and Cu are ductile materials, severe sticking of MA powders on the surface of grind balls and pots frequently occurred, which influenced the productivity of MA powders, and the reusing of grind mediums. The peeled of materials from the grind mediums in the next MA process will pollute the MA system. Besides, compared to the target ODS-Cu with the uniform Y enrichment of around 1 wt. %, the Y enrichment of pure metal Y is 100%. Several huge pure Y powders still remained after 32 hours' MA as shown in chapter 2, while extending MA time introduced more contamination as shown in chapter 3.

Considering the Cu-Y compounds can be formed in the mid-term of MA process for pure Cu and pure Y MA system [9], the preliminary addition of pre-alloyed Cu-Y compounds was

expected to reduce the MA time, thereby decreasing the contamination. There are many advantages for the application of Cu-Y compounds as the source of Y_2O_3. First, compared to the ductile pure metal Y, the Cu-Y compounds are more brittle, and they can easily break during milling process, which is beneficial to the dispersion of Cu-Y powders. Second, Cu-Y compounds have lower Y enrichment compared to pure metal Y, which is beneficial to reaching the target ODS-Cu with Y enrichment of around 1 wt. %. Besides, the more amount of Cu-Y compound addition compared to pure metal Y when fabricate the same ODS-Cu can play the roles of both Y_2O_3 source and process control agent without introduction of contamination [5]. There were some relevant precedents to use the Y contained compounds to fabricate the ODS alloys with Y_2O_3. T. Graning et al demonstrated that Fe_3Y was easier to dissolve and distribute in the steel matrix than Y_2O_3, and the Fe_3Y addition can reduce the MA time and decrease the oxygen impurity [10, 11].

There are several Cu-Y compounds in the Cu-Y phase diagram shown in Figure 5.1.1, CuY, Cu_2Y, Cu_7Y_2, Cu_4Y, and Cu_6Y, in which Cu_2Y and Cu_6Y intermetallic compounds were chosen as two extreme representatives considering that the CuY is relative ductile shown in Table 5.1.1. In this topic, the possibility that using Cu-Y intermetallic compounds (C_2Y and Cu_6Y) as the source of Y_2O_3 to fabricate ODS-Cu were firstly investigated. The comparison between Cu_2Y sourced sample and Cu_6Y sourced samples with various content from 0.39 wt. % to 2.36 wt. % Y were also conducted to obtain the optimum representative of Cu-Y compounds.

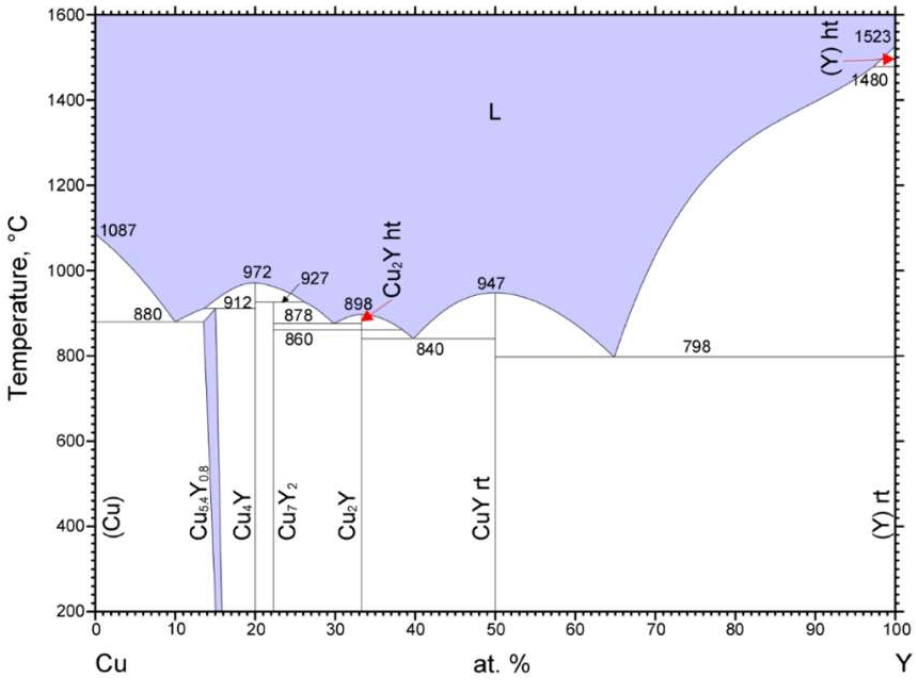

Figure 5.1.1 Cu-Y phase diagram.

Table 5.1.1 Properties of Y, Cu-Y compounds, and ODS-Cu.

Properties	Y	CuY	Cu_2Y	Cu_6Y	ODS-Cu
Ductility	ductile	ductile	brittle	brittle	ductile
Y enrichment (wt. %)	100	58	41	19	～1

5.1.2 Experimental procedure

Cu_2Y and Cu_6Y intermetallic compounds were fabricated by the arc melting, which is a useful technique to fabricate intermetallic compounds. Before melting, the chamber was evacuated by mechanical vacuum pump followed by molecular pump to reach 10^{-4} Pa, then back filled by high purity Ar gas (99.99%) to make the arc melting was conducted in Ar atmosphere. For the fabrication of Cu_2Y, small amount of pure Cu (8.56 g) and pure Y (6 g) in the atomic ratio of 2:1 were placed on the cooper hearth waiting to be remelted. The electrode is brought close to the blended metal powders to melting with gradually increased power. The copper hearth is surrounded by a water jacket used to cool the melt and control the solidification rate. The solidified metals were turn over by the tweezer without break the vacuum. These processes such as arc-melting and remelting was repeated for three times in order to perform the homogeneous arc-casting of the Cu_2Y ingot. The Cu_6Y ingot was also made by pure Cu (12.84 g) and pure Y (3 g) in the atomic ratio of 6:1 during the same procedures. The arc melted ingots were heat-treated at the temperature of 500 °C for 20 hours in the vacuum heat treatment furnace to make sure the homogeneous Cu-Y compounds formation due to the solution treatment. Finally, these Cu-Y compounds were hand crushed to form the fine powders before the mechanical alloying.

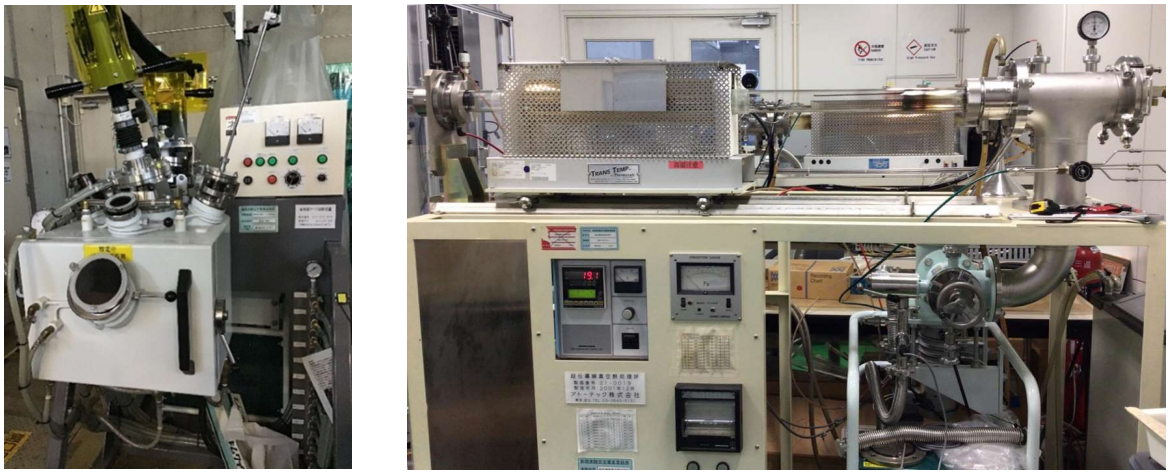

Figure 5.1.2 The images of arc melting machine and the heat treatment machine.

Table 5.1.2 The composition of ODS-Cu having *x* wt % Y. (Total: 100 g)

	Cu (g)	Cu_2Y (g)	Cu_6Y (g)
Cu-0.39 wt. %Y (Cu_2Y)	99.04	0.96	-
Cu-0.39 wt. %Y (Cu_6Y)	97.92	-	2.08
Cu-1.18 wt. %Y (Cu_2Y)	97.13	2.87	-
Cu-1.18 wt. %Y (Cu_6Y)	93.75	-	6.25
Cu-2.36 wt. %Y (Cu_2Y)	94.26	5.74	-
Cu-2.36 wt. %Y (Cu_6Y)	87.51	-	12.49

ODS-Cu alloys with various Y content from 0.39 wt. % to 2.36 wt. % were prepared, and the stoichiometric ratio were shown in Table 5.1.2. The mixed powders were milled for 32 hours with the speed of 250 rpm through planetary-type ball mill machine (Pulverisetee 5, Fritsch) in Ar atmosphere. The diameter of stainless-steel ball used for the MA was 5 mm and the ball-powder ratio was 7:3 based on previous works. The milled powders were put into the steel capsules. Before clamping, the capsules were degassed for 1 hour to less than 0.1 Pa, followed by welding in the vacuum condition. During the HIP process, the steel capsules, filled with milled powders, were kept in the pressure of 150 MPa at temperature of 1000 °C for 2 hours.

Figure 5.1.3 The images of TG-DTA machine.

The thermal behaviour and microstructure of the Cu_2Y and Cu_6Y intermetallic compounds powders were evaluated by the differential thermal analysis (DTA) and X-ray diffraction (XRD) method. The milled powders with different MA time and the bulk samples after HIP were analyzed by XRD, morphological observation and DTA. Finally, the bulk samples after HIP were evaluated in the terms of thermal conductivity and mechanical properties, which are very

important for the heat sink materials. As to thermal conductivity, it is mainly dominated by electron conduction, and there is a close relationship between the electronic and thermal conductivity. The thermal conductivity can be evaluated by electrical conductivity based on the Wiedemann-Franz law shown in chapter 1. As to the mechanical property, Vickers hardness test was chosen because it is an important mean for rapid quality assessment.

The XRD analysis were conducted on the Rigaku RINT-2200 diffractometer with Cu Kα radiation with the parameters of 40 kV and 40 mA. Microstructures were examined by scanning electron microscopy (SEM, JEOL JSM-5600) equipped with energy dispersive X-ray spectroscope (EDS). DTA was conducted by Rigaku TG 8110 shown in Figure 5.1.3, using Al_2O_3 as the reference. 50 mg sample and reference were prepared and put into the DTA crucible. It should be noted that the crucible with reference materials is placed in the left side of the balance, and crucible with sample put in the right side of the balance. High purity Ar gas (99.999%) with the flow of 0.5 L/min was used as the purge gas. The Ar gas was turn on 1 hour before the test starting to make Ar gas atmosphere into the vessel. The heat rate was 10 °C/min from room temperature to 800 °C and slowed down to be 2 °C/min from 800 °C to 1100 °C, keeping 1 hour at 1100 °C, and cooling down in the same procedures. The Vickers hardness was tested at room temperature with a loading of 100 gf for 30 seconds. The electrical conductivity was estimated from the electrical resistance measured by the four-probe method from -196 ℃ to room temperature with current of 1, 3, and 5 A.

5.1.3 Results and discussion

5.1.3.1 Characterization of the Cu-Y compounds

Figure 5.1.4 shows the SEM images of Cu_2Y compound and Cu_6Y compound after crush in same process. The average size of Cu_2Y is around 150 μm, and the average size of Cu_6Y is around 100 μm. Besides, there are plenty of fragments except the large powders for Cu_6Y compound, which indicate that the Cu_6Y is more brittle than Cu_2Y, and fracture was easier occurred during the crush process. In the larger magnified image of Cu_2Y, the fracture surfaces show the layered structure, which indicate some ductile fracture. In the larger magnified image of Cu_6Y, all the powders show very smooth fracture surface, which demonstrate that Cu_6Y compounds is more brittle. Therefore, compared to Cu_2Y, Cu_6Y is more brittle and expected to break more easily during the mechanical alloying process, thereby accelerating the MA process.

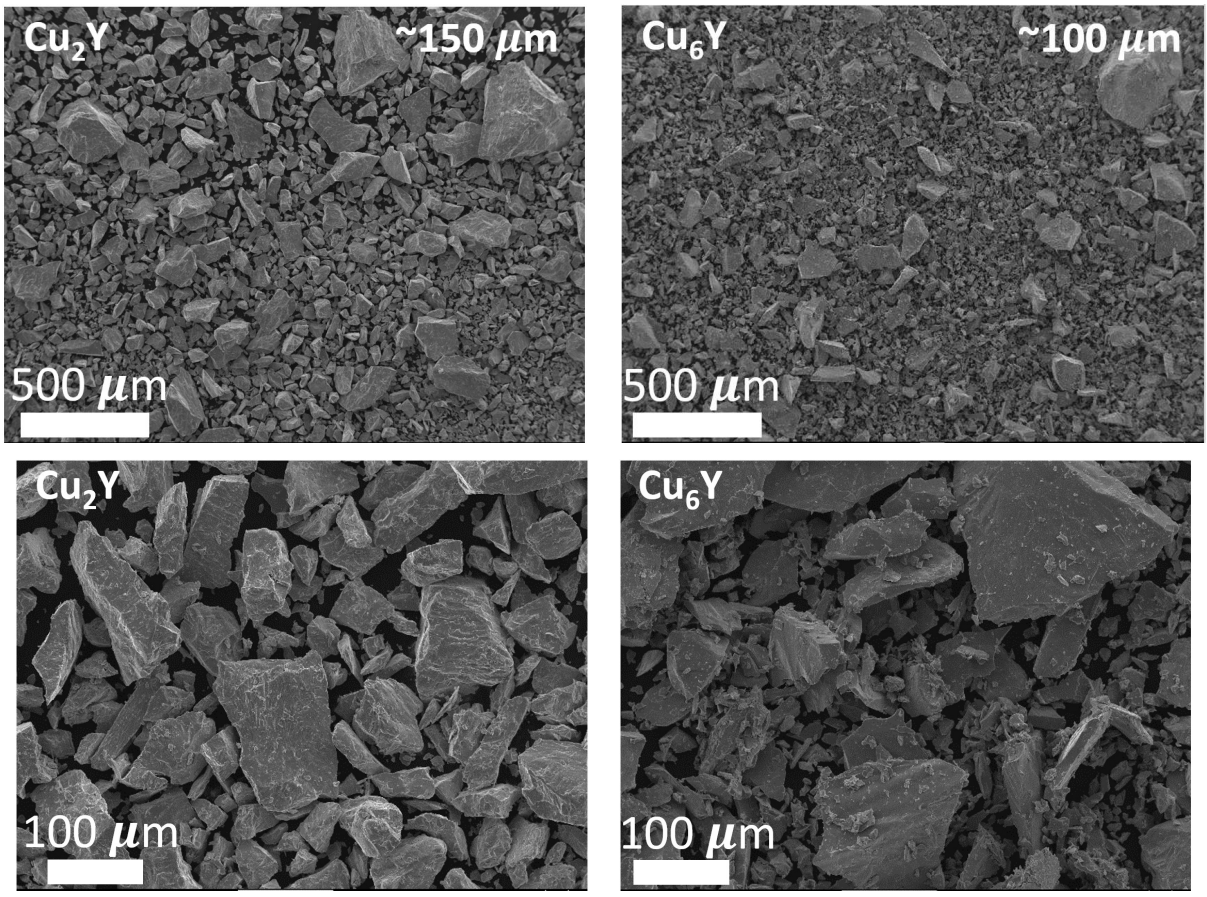

Figure 5.1.4 The morphologies of Cu_2Y (left) and Cu_6Y (right) compounds.

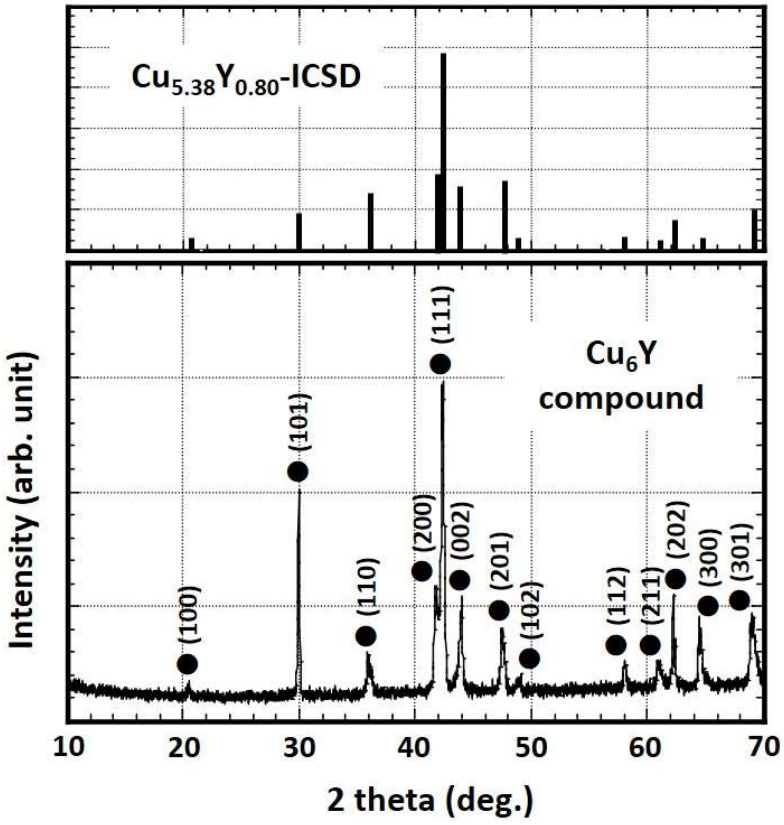

Figure 5.1.5 XRD spectrum of $Cu_{5.38}Y_{0.80}$ (up) and Cu_6Y pre-alloy powder (down).

Figure 5.1.5 shows the typical XRD spectra of the Cu_6Y intermetallic compound powders and the standard XRD spectra of the $Cu_{5.38}Y_{0.80}$ intermetallic compound from the ICSD database. The X-ray diffraction peaks of Cu_6Y powders almost completely correspond to the powder diffraction data of $Cu_{5.38}Y_{0.80}$ compound. The only differences between Cu_6Y and $Cu_{5.38}Y_{0.80}$ are the relative intensity of (1 0 1) peak and (1 1 0) peak, because of preferred orientation caused by the anisotropy of grain growth. In addition, the peak broadening of Cu_6Y is caused by the decrease in grain size during the hand crush process based on Sherrer equation. The slight variation of the Cu/Y ratio around 6/1 is because the hexagonal structured Cu_6Y phase could accommodate phases of various Cu:Y ratio [12]. It was conformed that the Cu_6Y compound powder was mainly obtained in the form of the $Cu_{5.38}Y_{0.80}$ single phase. The Cu_2Y compound was also confirmed by XRD analysis.

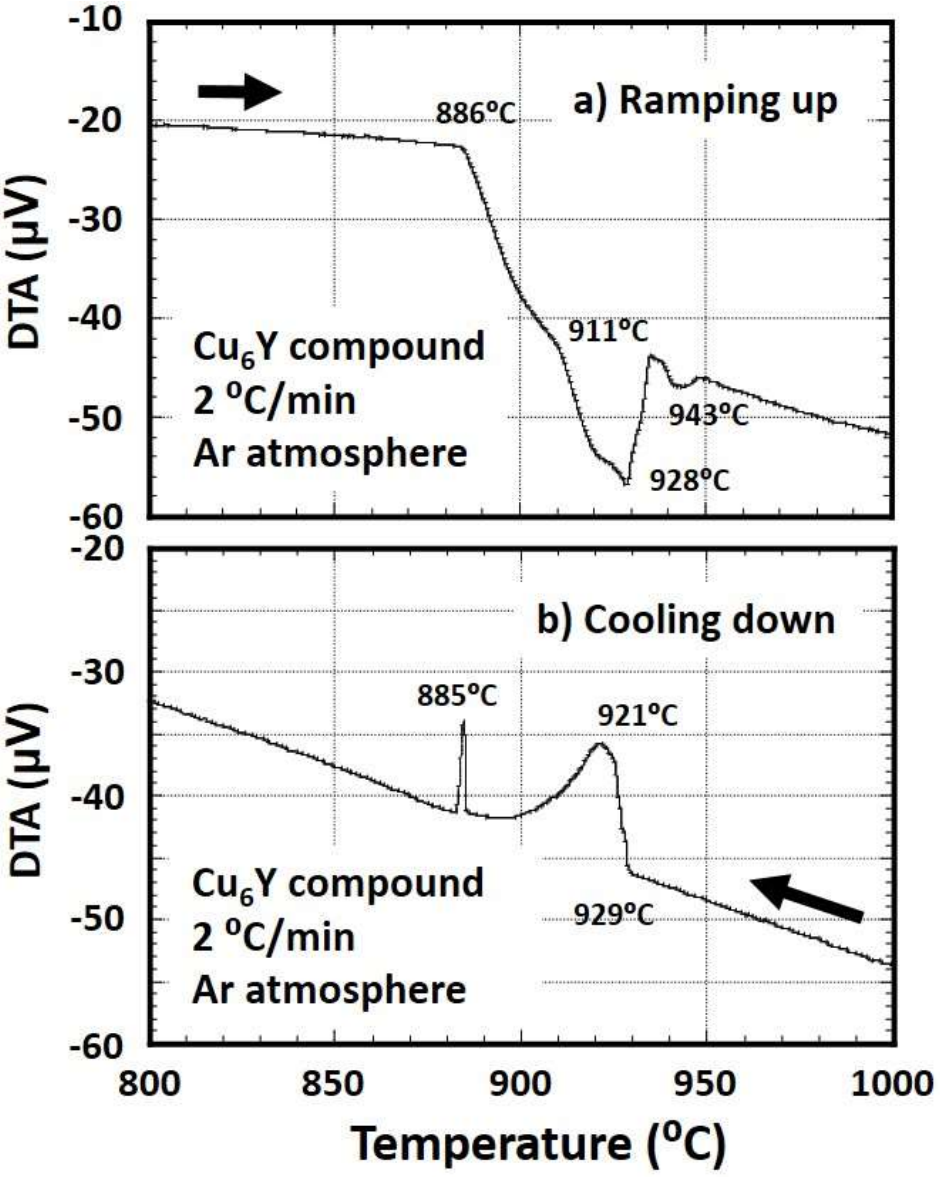

Figure 5.1.6 DTA curves of Cu_6Y powders in heating up process (a) and cooling down process (b).

Figure 5.1.6 shows the DTA curves of the Cu_6Y compound powders during the ramping up and cooling down process. In the temperature ramping process, the first endothermic transition of the DTA curve was observed at 886℃, which indicated that the phase changed was occurred for Cu_6Y compound at around 886℃. The endothermic transition of the DTA curve was also observed at 928℃ after the second endothermic transitions at 911℃, which meant that the Cu_6Y compound powder was melted completely at 928℃. The small endothermic transition at 943℃ is believed to be caused by the disturbance of composition. In the temperature dropping process, the first exothermic transition of the DTA curve was observed at 929 ℃, which indicated that the solidification was conducted at this temperature. The final exothermic transition of the DTA curve was observed at 885 ℃, corresponding to the phase transformation.

It was found that these endothermic and exothermic transition behaviors corresponded to the Cu-Y system binary phase equilibrium diagram shown in Figure 5.1.1, in which the eutectic temperature between Cu and Cu_6Y phases is at 880℃, and the eutectic temperature between Cu_6Y and Cu_4Y phase is 910 ℃. Combing the DTA curves and the Cu-Y phase diagram, it was found that the thermal peak of 885 ℃ and 886 ℃ in DTA curve is located in the interval of phase transformation point from 880 ℃ to 910 ℃, corresponding to the Cu_6Y phase. Besides, the endothermic and exothermic transition of 928℃ and 929℃ in DTA curves showed the melting point of the Cu_6Y compound, corresponding to the melting point of Cu_6Y in the Cu-Y phase diagram. Therefore, the Cu_6Y were successfully fabricated, and the Cu_2Y was also confirmed by the DTA analyses process.

5.1.3.2 Characterization of the MA powders

Figure 5.1.7 shows the SEM-BSE images and corresponded EDS mappings of Y element after 4 hours MA and after 32 hours MA. It was found that there were still plenty of Cu-Y compound powders remained after 4 hours MA. For Cu_2Y sourced samples, the remained Cu-Y compound powders with larger size of 30 μm is smaller than the initial powder size of 150 μm. For Cu_6Y sourced sample, most of the Cu_6Y were easy to form fine Cu_6Y powders with size of less than 10 μm, which is much smaller than the initial average size of 100 μm. The Cu_6Y compound powders broke more easily during the MA process because of its brittleness, forming fine Y rich powders. For the Cu-Y sourced samples after 32 hours MA, Y was uniformly distributed for the Cu_6Y sourced sample compared to the Cu_2Y sourced sample, in which there were still some fine Y rich particles left.

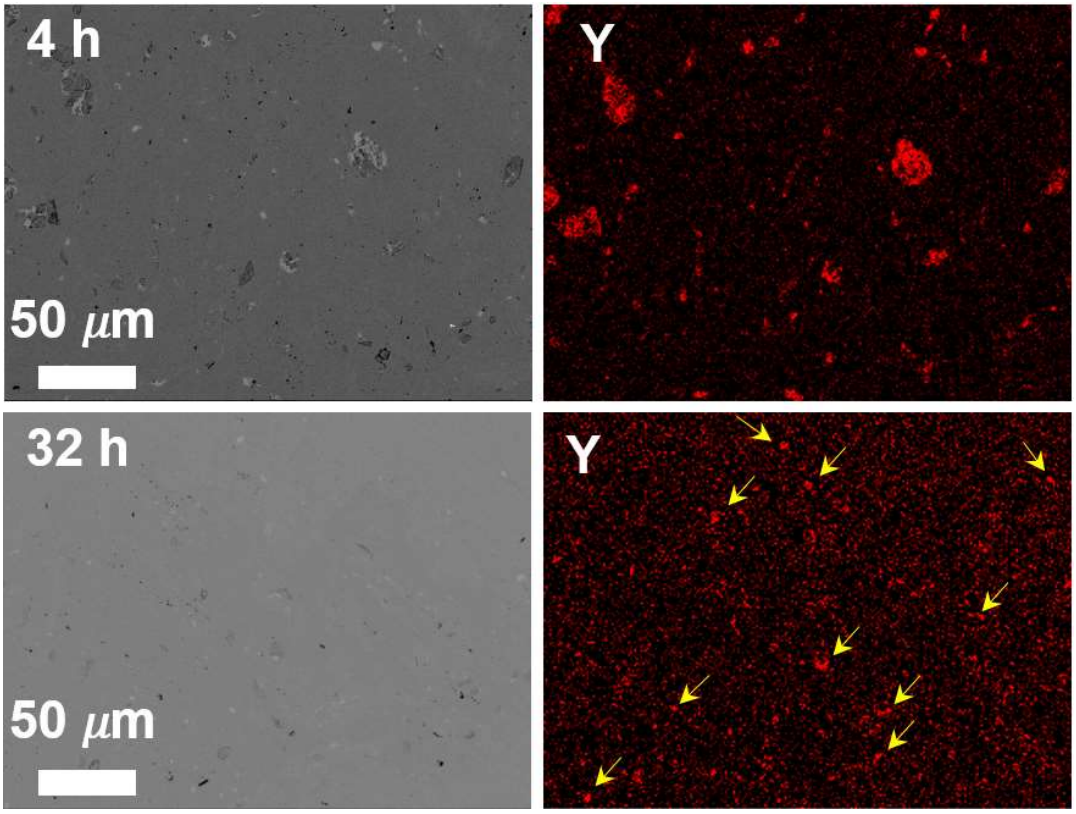

(a) Cu_2Y

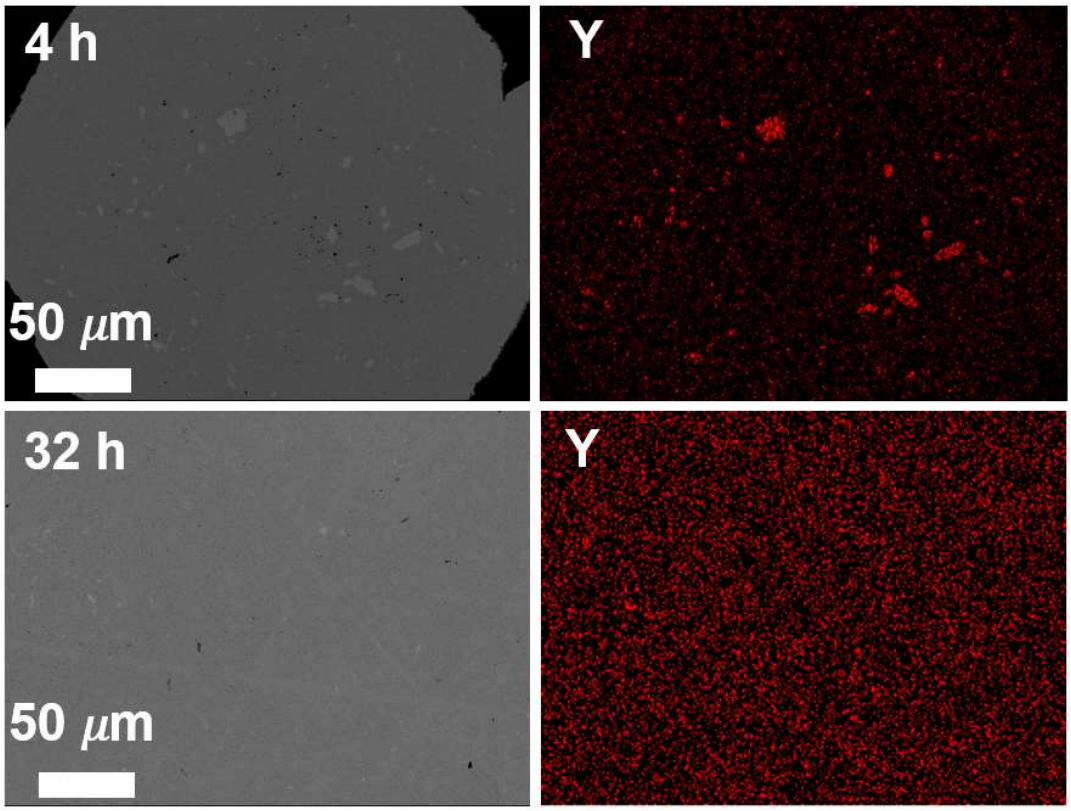

(b) Cu_6Y

Figure 5.1.7 The development of Y element with the MA time from 4 to 32 h for Cu_2Y sourced samples (a) and Cu_6Y sourced samples (b).

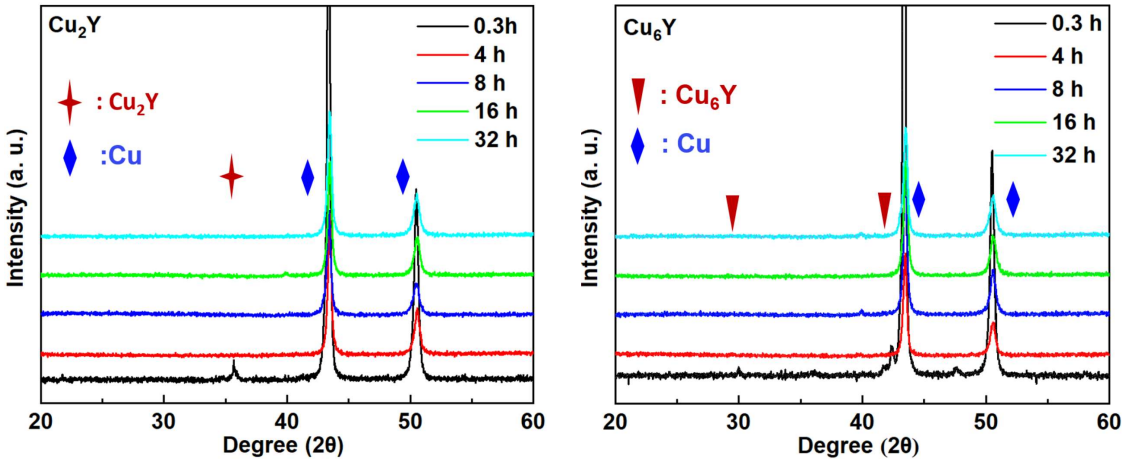

Figure 5.1.8 Development of XRD spectrum with MA time for the samples with 1.18 wt. % Y (Left: Cu_2Y, Right: Cu_6Y)

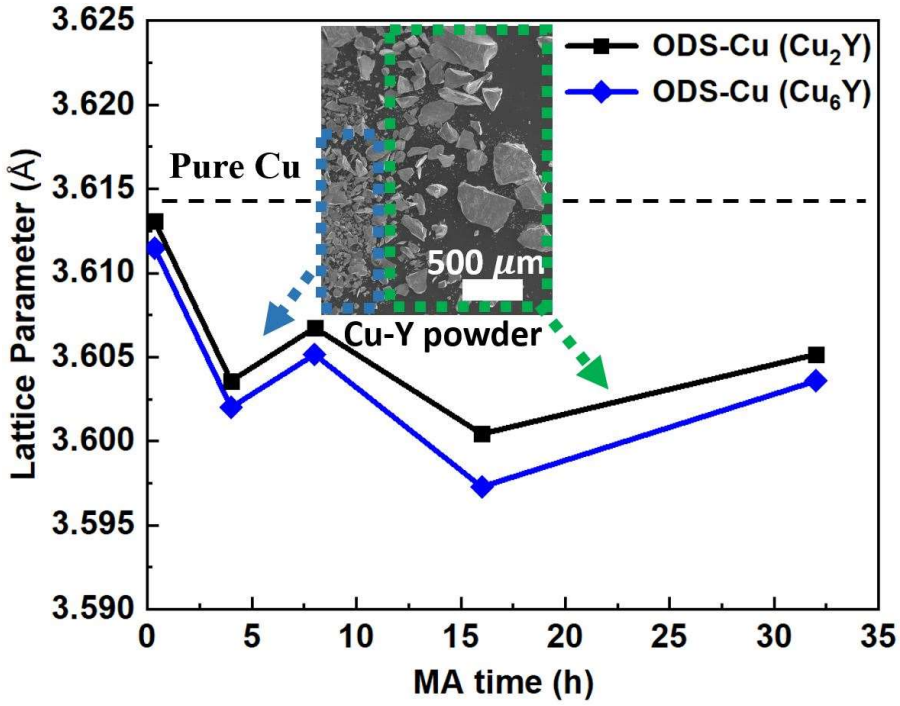

Figure 5.1.9 Lattice parameter development with MA time for the samples with 1.18 wt. % Y.

Figure 5.1.8 shows XRD spectrum of Cu_2Y sourced MA powders and Cu_6Y sourced MA powders with different MA time from 0.3 h to 32 h. it was found that there were specific peaks of Cu_2Y and Cu_6Y compounds after 0.3 hours MA but disappeared after 4 hours' MA. Combing the SEM-BSE images and the EDS mappings, it was found that the disappearance of Cu_2Y and Cu_6Y specific spectrum was not caused by the dissolution of all the Cu-Y compounds, but because of the covering of Cu-Y compounds by ductile Cu powders. The development of lattice parameter of Cu as a function of MA time, calculated by Bragg's law based on XRD spectrum, for the Cu_2Y sourced and Cu_6Y coursed samples are shown in Figure 5.1.9. It was found that the lattice parameters of Cu for both samples had similar macro trends, first decreasing from

the original lattice parameter (3.6147 Å) of pure Cu, then increasing from the middle of MA process. The decrease during first half process was mainly due to the dominance of crystal distortion caused by the collision between MA powders and steel balls, and the subsequent increase during latter half process mainly because the dominance of solid solution mechanism. It was worth noted that there was a small fluctuation during the first half process. It was probably caused by the preferential solid solution of the fine Cu-Y powders. Most of the coarse Cu-Y powders were fractured into fine powders during the early MA process, then dissolved into the Cu matrix during the latter MA process.

5.1.3.3 Characterization of the consolidated samples

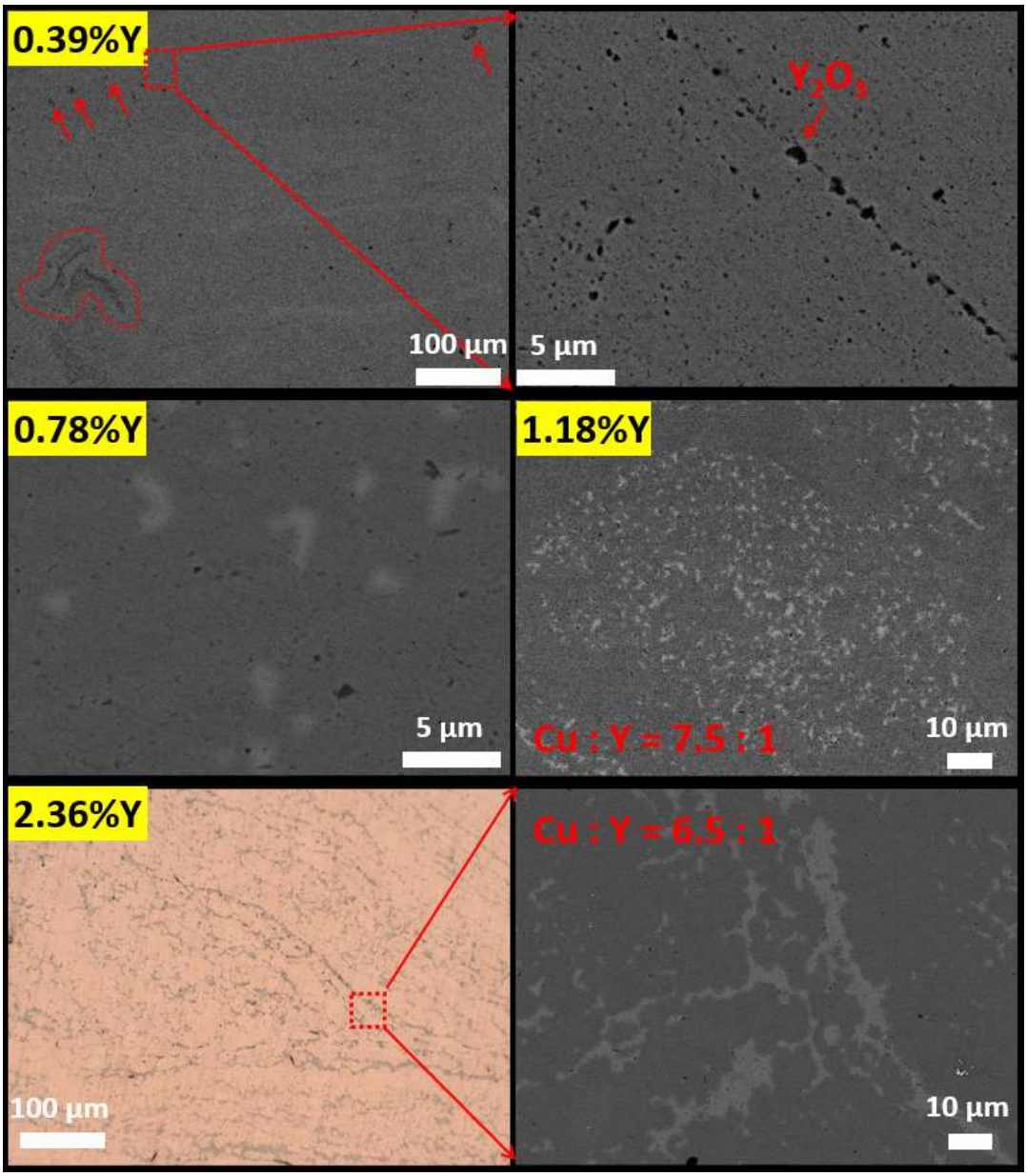

Figure 5.1.10 SEM-BSE and optical images of the Cu_2Y sourced bulk samples with various Y content.

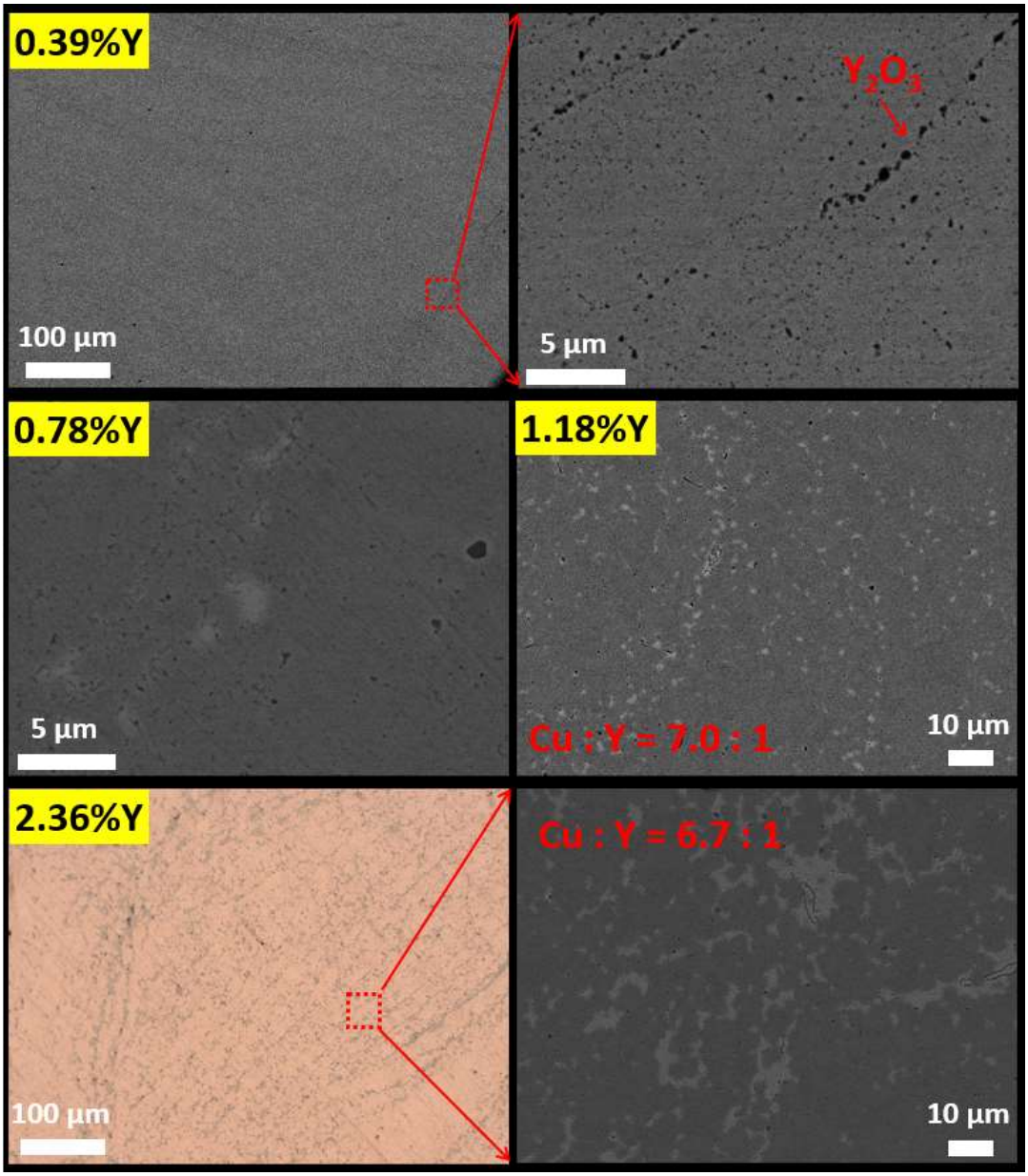

Figure 5.1.11 SEM-BSE and optical images of the Cu_6Y sourced bulk sample with various Y content.

Microstructures of the bulk samples after HIP with various Y content (from 0.39 wt. % to 2.36 wt. %) are shown in Figure 5.1.10 by using Cu_2Y and Figure 5.1.11 by using Cu_6Y. For the Cu_2Y sourced sample with lower content of Y, the Y_2O_3 particles with largest size of 1 μm were formed after HIP. Considering no oxidant was introduced and Ar gas protection was conducted during fabrication process, the oxygen element in sintered materials possibly came from the inherent O impurity in the initial raw materials. It should be highlighted that there still had some Y enrichment areas labeled by red circle and arrows. For the samples with 1.18 wt. % and 2.36 wt. % Y, there are plenty of phases with light color in the SEM images, and it was found that these phases showed a aggregated state with Cu:Y ratio of 6.5:1 confirmed by EDS.

In the case of Cu_6Y sourced bulk sample with lower Y content, Y_2O_3 particles with smaller size were also formed after HIP. Difference from the Cu_2Y sourced sample, the sample with Cu_6Y was much more uniform, and there were no Y enriched phases, which were observed in the Cu_2Y sourced sample. Cu_6Y is beneficial to form the uniform Y distribution. For the samples with higher content of Y, the similar aggregation was observed for both samples, and there is no clear difference between the Cu_2Y sourced and Cu_6Y sourced samples for higher Y content.

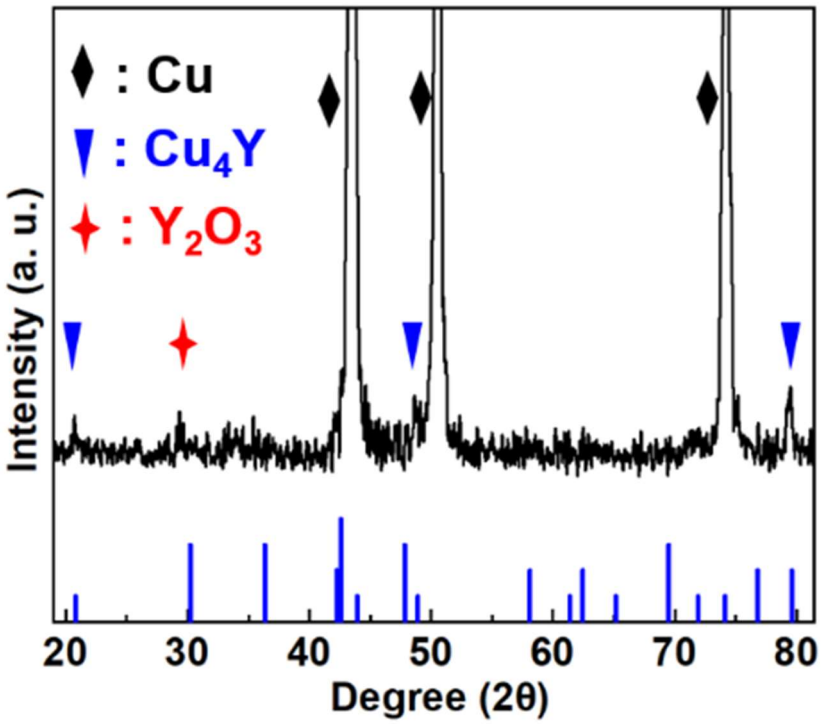

Figure 5.1.12 XRD spectra of the sample with 1.18 wt. % Y (Cu_6Y).

Figure 5.1.12 shows the XRD spectra of the Cu_6Y sourced sample with 1.18 wt. % Y after consolidation. The main peaks labelled by black diamond are the characteristic peaks of Cu, the small specific peak of Y_2O_3 corresponds to the fine Y_2O_3 particles shown in the SEM-BSE images. The series of blue peaks are the spectrum of Cu_4Y compound. The specific peaks of Cu_4Y for the bulk samples indicated that the aggregated phases shown in the SEM images are Cu_4Y compounds. The mismatch of the major peaks of Cu_4Y were caused by the influence of adjacent Cu peaks and the different grain orientation of Cu_4Y compound. The higher ratio of Cu:Y (~6.5:1) than Cu_4Y obtained by EDS was caused by the influence of Cu background.

Based on the Cu-Y phase diagram, phase transformation occurred for Cu_6Y compound at 886 °C and it was melted at 927 °C. The MA powders had uniform Y distribution after ball milling. During HIP process at 1000 °C, the Cu-Y phases were melted, forming liquid phase,

and then aggregated to increase the ratio of Y:Cu, followed by precipitation initiated at 971 °C in the form of Cu_4Y compound during the cooling process.

5.1.3.4 Thermodynamic verification

As the binary stoichiometric phase, the Gibbs free energy of CuY, Cu_2Y, Cu_4Y and Cu_7Y_2 can be described by:

$$G^{Cu_xY} = x_{Cu}G^{Cu} + x_YG^Y + \Delta G_f \quad (5.1.1)$$

Where x_{Cu} and x_Y represent the mole fraction of copper and yttrium, G^{Cu} and G^Y are the Gibbs free energy of copper and yttrium. ΔG_f represent the Gibbs free energy of formation, which can be described:

$$\Delta G_f = a + bT \quad (5.1.2)$$

The parameters *a* and *b* were obtained by optimization using experimental data. The *a* and *b* of CuY, Cu_2Y, Cu_4Y and Cu_7Y_2 were shown in Table 5.1.3 based on the references [13-15].

Table 5.1.3 The *a* and *b* of formula 5.1.2.

Compound	*a*	*b*
CuY	-44616.68	4.12
Cu_2Y	-65324.22	6.03
Cu_4Y	-89328.50	8.25
Cu_7Y_2	-168519.60	15.57

Therefore, the Gibbs energy of formation of the Cu_2Y is shown in Table 5.1.4. The Gibbs free energy of formation for CuO, Cu_2O, and Y_2O_3 can gotten in the similar way.

Table 5.1.4 The Gibbs energy of formation ΔG (KJ/mol) for Cu_2Y, CuO, Cu_2O and Y_2O_3

T(K)	Cu_2Y	CuO	Cu_2O	Y_2O_3
298	-63.52	-129.50	-147.89	-1816.65
400	-62.91	-120.10	-140.09	-1786.51
600	-61.70	-102.10	-124.94	-1728.41
800	-60.50	-84.67	-110.09	-1671.47
1000	-59.29	-67.68	-95.52	-1615.28
1200	-58.08	-51.06	-81.21	-1559.57

As the terminal solid solution materials, the Gibbs free energy of Cu_6Y can be described by:

$$G^{Cu_6Y} = x_{Cu}G^{Cu} + x_YG^Y + \Delta G_f \quad (5.1.3)$$

Where x_{Cu} and x_Y represent the mole fraction of copper and yttrium, G^{Cu} and G^Y are the Gibbs free energy of copper and yttrium, ΔG_f represents Gibbs's energy of formation of the terminal solid solution, and can be described as follows:

$$\Delta G_f = x_{Cu}RT\ln x_{Cu} + x_YRT\ln x_Y + \Delta G^E \quad (5.1.4)$$

Where R is the universal gas constant (8.31 J/K^{-1}mol^{-1}), T is the temperature in K. ΔG^E is the excess Gibbs energy, which can be described by the Redlich-Kister polynomial model:

$$\Delta G^E = x_{Cu}x_Y\sum_{v=0}^{n}(x_{Cu}-x_Y)^vL^{(v)}(T) \quad (5.1.5)$$

With:

$$L^{(v)}(T) = A^{(v)} + B^{(v)}T + C^{(v)}T\ln T \quad (5.1.6)$$

The $A^{(v)}$, $B^{(v)}$, $C^{(v)}$ for Cu_6Y can be found in references [13-15] and shown in Table 5.1.5.

Table 5.1.5 The parameters of formula 5.1.6 for Cu_6Y.

Phase	v	$A^{(v)}$	$B^{(v)}$	$C^{(v)}$
Cu_6Y	0	-5722.8	5.10651	0
	1	-173110.0	34.10269	0
	2	91791.8	0	0
	3	930.5	0	0
	4	1196.7	0	0

Therefore, the Gibbs energy of formation of the Cu_6Y is shown in Table 5.1.6:

Table 5.1.6 The Gibbs energy of formation for Cu_6Y.

T(K)	ΔG (KJ/mol)
298	-23.46
600	-19.71
1000	-14.73
1300	-10.99

Based on the Gibbs free energy of the reactants in the in-situ reaction, the Gibbs free energy of Cu_2Y precipitated reaction ΔG_{Cu_2Y} and Cu_6Y precipitated reaction ΔG_{Cu_6Y} were shown in Table 5.1.7

$$2\ Cu_2Y + 3\ Cu_2O = Y_2O_3 + 10\ Cu \quad (5.1.7)$$

$$2\ Cu_6Y + 3\ Cu_2O = Y_2O_3 + 18\ Cu \quad (5.1.8)$$

Table 5.1.7 The Gibbs energy of Cu_2Y precipitated reaction and Cu_6Y precipitated reaction

T(K)	ΔG_{Cu_2Y} (KJ/mol)	ΔG_{Cu_6Y} (KJ/mol)
298	-1321.02	-1326.07
300	-1320.96	-1325.99
400	-1317.88	-1321.85
500	-1314.68	-1317.94
600	-1311.38	-1314.17
700	-1307.94	-1310.47
800	-1304.35	-1306.78
900	-1300.62	-1303.06
1000	-1296.73	-1299.27
1100	-1292.68	-1295.42
1200	-1288.49	-1291.468
1300	-1284.16	-1287.42

Table 5.1.7 shows the Gibbs free energy of the in-situ reaction occurred during the innovative MA-HIP process. It was found that the Gibbs free energy of formation is much lower than zero, which demonstrated that the in-situ reaction can occurred during MA-HIP process, and it was feasible to use the Cu-Y compounds as the sources of Y_2O_3 to fabrication ODS-Cu alloys.

5.1.3.5 Performance evaluation

Figure 5.1.12 shows the influence of Y content on the Vickers hardness for the Cu_2Y sourced and Cu_6Y sourced samples. Compared to pure Cu, Vickers hardness was greatly improved by adding Cu-Y compounds, because of the formation of Y_2O_3 particles. For the samples with Cu-Y compound, the Vickers hardness gradually decreased and reached saturation with the increase in Y content. The inherent interstitial O have great influence on the Vickers hardness of ODS-Cu, and the decrease of Vickers hardness with the increase in Y content is possibly

because the redundant of Cu-Y consumed all the interstitial O impurity. Besides, the precipitated macro phases distributed in the Cu matrix had small influence on the Vickers hardness. That is also the reason that Vickers hardness does not change with the increase in Y content from 1 wt. %. The sample with 0.39 wt. % Y (Cu_6Y) has higher Vickers hardness than the sample with 0.39 wt. % Y (Cu_2Y) because of more evenly distribution of Y as shown in the SEM-BSE images. For the samples with higher Y content, there is no difference in Vickers hardness between Cu_2Y sourced sample and Cu_6Y sourced sample, corresponding to the similar microstructure shown in the SEM-BSE images above.

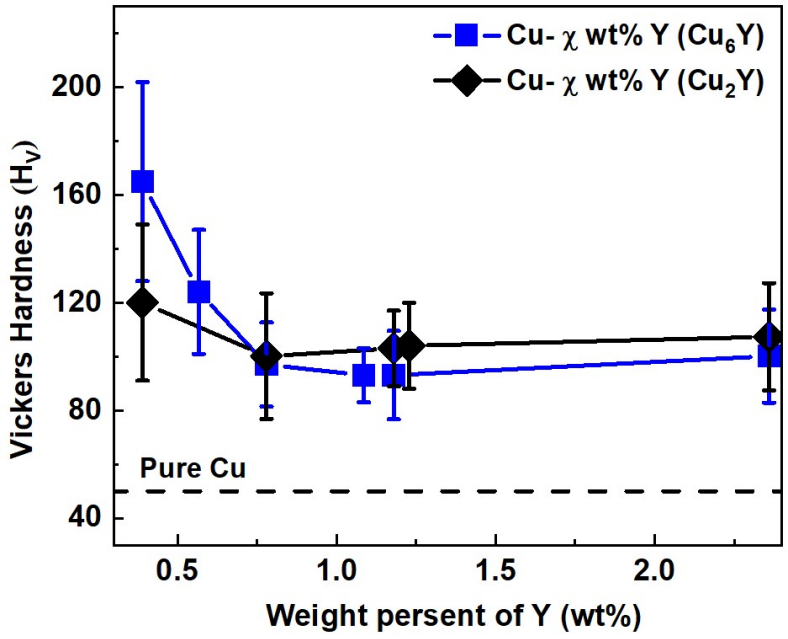

Figure 5.1.12 Vickers hardness of Cu- ***x*** wt. % Y (Cu_2Y or Cu_6Y).

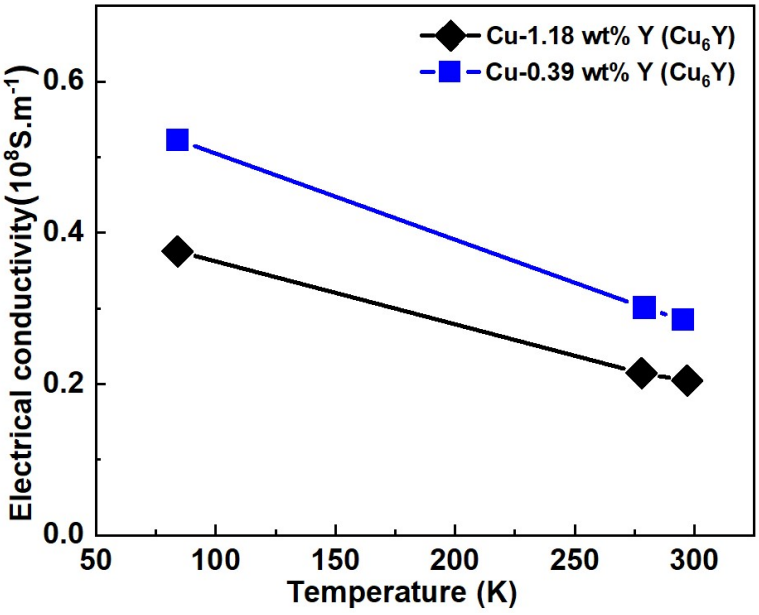

Figure 5.1.13 Electrical conductivity of Cu- ***x*** wt. % Y (Cu_6Y).

Considering the better performance of the Cu_6Y sourced samples. The electrical conductivity evaluated for the Cu_6Y sourced samples with different amount of the Y addition. As shown in Figure 5.1.13, compared to the sample with 1.18 wt. % Y, which has a large amount of Cu_4Y precipitation phase, the sample with 0.39 wt. % has better electrical conductivity, phase possibly because of the more uniform formation of Y_2O_3 and the absence of precipitation phases. Combing with the Vickers hardness, the Cu_6Y sourced sample with lower content of Y has better comprehensive performance.

5.1.4 Conclusions

ODS-Cu alloys with various content of Y by adding Cu_2Y and Cu_6Y were fabricated through innovative MA-HIP process by in-situ fabrication method. Comparative analyses were conducted for the Cu_2Y sourced and Cu_6Y sourced samples, and the influence of Y content was also explored. The main results were shown as follows:

(1) Cu_2Y and Cu_6Y were produced by arc melting method and the single phase formation was confirmed by the crystal structure and thermodynamic analyses.

(2) Few Y_2O_3 were successfully formed by in-situ reaction between Y element and intrinsic O impurities in the Cu matrix.

(3) Cu_6Y was easier to form evenly distribution Y compared to Cu_2Y for the samples with lower amount of the Y addition, because of lower Y enrichment and higher brittleness of Cu_6Y.

(4) The Cu_6Y sourced sample with 0.39 wt. % Y had higher Vickers hardness possibly because of the higher content of interstitial O, and also better electrical conductivity. Cu_6Y was a better choice as the representative of Cu-Y compounds to fabricate ODS-Cu alloys.

(5) The most of the unoxidized Y were aggregated and precipitated during HIP for both Cu-Y sourced samples with higher amount of the Y addition. The methods to prohibit the aggregation and precipitation of Y element during in-situ fabrication process need to be investigated.

5.2 Influence of oxidant addition on the Cu_6Y sourced sample

5.2.1 Introduction

In the previous topics, the feasibility of using Cu-Y compounds as the source of Y_2O_3 to fabricate the ODS-Cu with Y_2O_3 was demonstrated. Low content of Y_2O_3 were successfully formed from the Cu-Y compounds oxidized by oxygen impurity in the Cu matrix. In the case of lower Y content, Cu_6Y can form more uniform Y distribution compared to Cu_2Y compound, which still had some Y rich phases in the consolidated sample. However, with the Y content increasing, Y rich phases with aggregated morphology were appeared for both Cu_2Y sourced and Cu_6Y sourced samples. The alloyed MA powders formed supersaturated solid solute state after MA. While during HIP at elevated temperature, except for the few Y that had been transformed to Y_2O_3, most of the unoxidized Y elements transferred from non-equilibrium condition to the equilibrium condition through precipitation. Oxidization of the Y element before precipitation is necessary to avoid the large Y rich phases. There are some oxidization methods. First, using air flow to oxide the supersaturated solid solute powders, forming the dispersive oxide particles. But the flow rate and oxidation progress are difficult to control. Therefore, some heat treatments needed to reduce the copper oxide formation, such as hydrogen purge in higher temperature [16]. Besides, this oxidation method leads to the peroxidation of the powders' surface, and under-oxidation of the inside [17, 18]. Another method is moderate oxidant addition based on the stoichiometric ratio during the MA process. The oxidant can be milled, accelerating the dissolution of O element into the MA powders. In this topic the oxidant addition was conducted to oxidize the Y before precipitation. The Cu_2O was chosen as the oxidant instead of CuO used in the previous research, because Cu_2O has low O enrichment compared to the CuO. Besides, the CuO used in the previous research (chapter 3) transferred to Cu_2O during the MA process. The oxidant addition time is also a very important parameter during the fabrication process. The initial oxidant addition with the Cu_6Y is beneficial to the synchronous distribution of Y and O element. However, this addition can easily form the Y-O clusters [19-22], leading to the premature formation of Y_2O_3 and deteriorate the dispersion of the Y element.

In this topic, the Cu_2O was used as the oxidant and added at the middle of MA process. Based on the ODS-Cu with nominal content of 1.38 wt. % Y_2O_3, the comparison between the samples with Cu_2O and without Cu_2O was conducted. The influence of oxidant on the content

and morphology of Y_2O_3 particles, and the macro properties of ODS-Cu were carried out. The mechanism of in-situ reaction was also analysed.

5.2.2 Experimental procedure

Figure 5.2.1 shows the SEM images of the initial Cu_2O powders and Cu_6Y powders. Cu_6Y intermetallic compound was fabricated by the arc melting, followed by heat treatment and hand crush, and the detail procedure was described in chapter 5.1. The Cu_6Y fine powders were confirmed by Differential Thermal Analyzer (DTA) and XRD in chapter 5.1. Two samples shown in Table 5.2.1 were prepared by the innovative MA-HIP process through in-situ fabrication method.

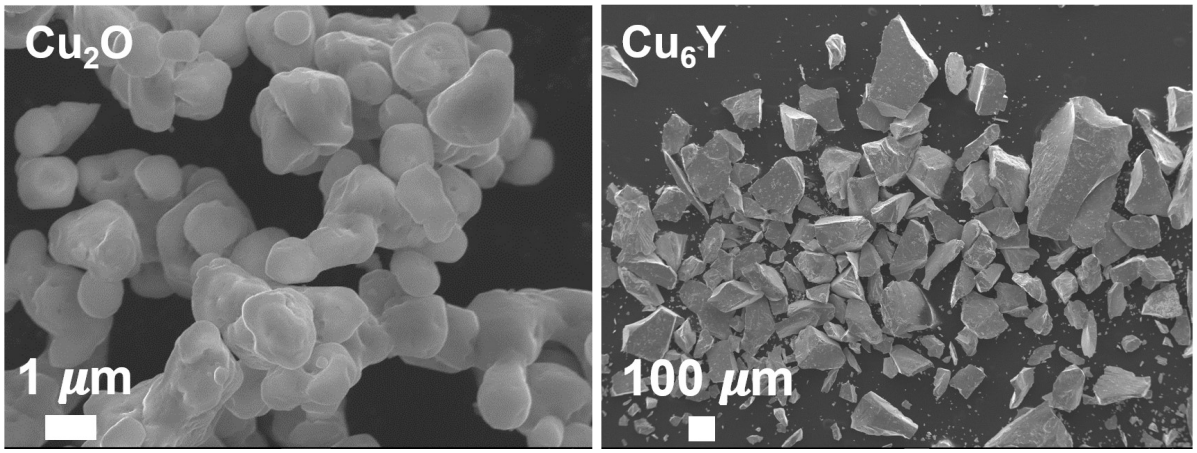

Figure 5.2.1 The SEM images of the initial Cu_2O powders and Cu_6Y powders.

Table 5.2.1 Composition of Cu_6Y sourced ODS-Cu alloys with or without Cu_2O. (Total: 100 g)

Samples	Cu	Cu_6Y	Cu_2O
Cu-1.38 wt. %Y_2O_3(Cu_6Y, Cu_2O)	91.64	5.74	2.62
Cu-1.38 wt. %Y_2O_3(Cu_6Y)	94.26	5.74	0

For the sample without oxidant, the Cu_6Y powder as the Y precursor was milled with Cu (99.99%, purity, 300 mesh) powder for 32 hours with a speed of 250 rpm by the planetary-type ball milling machine (Pulverisetee-5, Fritsch) in the high purity Ar atmosphere glove box at NIFS. For the sample with oxidant, 2.62 wt. % of Cu_2O (99.9%, purity, 300 mesh) powder was added into the half-milled powders at the middle of MA process. The milled powders were put into the iron capsules and transferred into the NIFS-Sealing Device filled with high purity Ar atmosphere for the sealing operation. The capsules were degassed for 1 hour to reach the pressure of 0.1 Pa, followed by welding to keep the powders in a vacuum condition. During

the HIP process, the tube capsules were consolidated under the pressure of 150 MPa and at the temperature of 1000 ºC for 2 hours.

Microstructures and morphologies of the MA-HIP processed samples without and with Cu_2O addition were evaluated by XRD on the Rigaku RINT-2200 diffractometer with Cu Kα radiation with the parameters of 40 kV and 40 mA apparatus and scanning electron microscope (SEM, JEOL JSM-5600) equipped with energy dispersive X-ray spectroscopy (EDS). In addition, thin sampling from a part of the MA-HIP processed Cu alloy bulk samples was carried out using the focused ion beam (FIB, Hitachi nano DUE'T NB5000) machine. After that, nanostructure of the thin FIB sample was observed using electron backscatter diffraction (EBSD) and scanning transmission electron microscope (TEM, JEOL JEM-2800) equipped with EDS. The Vickers hardness of the MA-HIP processed samples were evaluated at room temperature with a loading of 100 gf/mm^2 for 30 seconds.

In order to explore the in-situ reaction mechanism, DTA measurements for the Cu_6Y powders and the blend powders of Cu_6Y and Cu_2O were carried out using Rigaku TG8110 from 600℃ to 1000℃ with a rate of 2℃/min in pure Ar gas flow. Alumina powders were chosen as standard reference sample during the DTA measurements.

5.2.3 Results and discussion

5.2.3.1 XRD spectrum of the consolidated samples

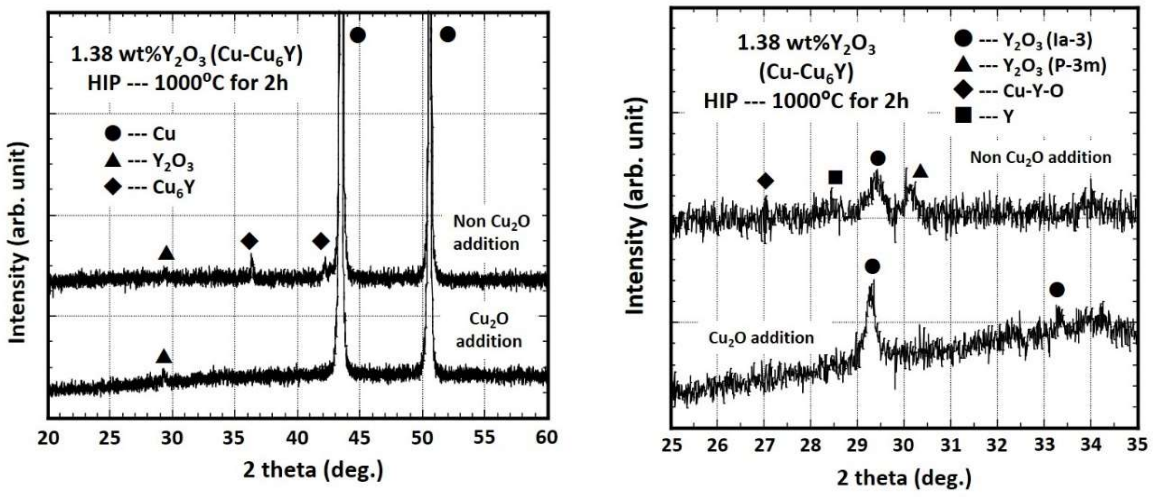

(a) (b)

Figure 5.2.2 XRD spectrum(a) and the enlargement (b) of samples without Cu_2O and with Cu_2O.

Figure 5.2.2 (a) shows the XRD spectrum of ODS-Cu alloys with 1.38 wt. % Y_2O_3 (without Cu_2O and with Cu_2O) after consolidated by HIP. For the sample without Cu_2O, there was a

small Y_2O_3 peak, which demonstrated that the Y_2O_3 particles were successfully formed. Besides, there were still relatively higher Cu_6Y peaks which demonstrate that most of Cu_6Y was remained into the Cu matrix. As to the spectra of the sample with Cu_2O, the obvious differences from the sample without Cu_2O were the disappearance of Cu_6Y peaks and the increase of Y_2O_3 peak, which demonstrated that all Cu_6Y has been oxidized by Cu_2O and fully transformed to Y_2O_3.

In order to obtain detailed information of Y_2O_3, we tested the samples with lower scanning speed of 0.01 º/min in the angle range from 25 º to 35º, where Y_2O_3 characteristic peak located, as shown in Figure 5.2.2 (b). For the sample without Cu_2O, the Cu_6Y compound transformed to various forms of Cu-Y-O, Y_2O_3 in different crystal structure, and so on. For the sample with Cu_2O, only Y_2O_3 peaks with higher intensity were shown. From the XRD results, it was found that the lower content of Y_2O_3 in the sample without Cu_2O was formed from the reaction between Y and the oxygen impurity in the Cu matrix. The trace O impurity, however, was not enough to oxidize all the Cu-Y compound, and most of Cu_6Y still kept in its original form. When adding the Cu_2O, all Y in the alloyed Cu matrix was transformed to Y_2O_3 particles.

5.2.3.2 Morphologies of the consolidated samples

Figure 5.2.3 shows SEM images of the samples without Cu_2O (up) and with Cu_2O (down) addition in backscattered electron (BSE) mode and the corresponded EDS mappings. For the sample without Cu_2O, there were plenty of light color phases with aggregated morphology. The EDS results showed that the atomic ratio of Cu, Y and O was 18.0:2.8:1.0. Considering that there were no those aggregated Y rich phases for the MA powders after 32 hours MA shown in the previous topic, where Y was evenly distributed into the Cu matrix, those Y rich phases were aggregated during HIP process. The metastable solid solution of Y in Cu matrix was formed during MA. Once the MA powders were activated during HIP at higher temperature, the solid solute Y was reconstituted, shown aggregated phase.

For the sample with Cu_2O, the obvious difference was the dark color phases, whose atomic number ratio of Cu, Y and O detected by EDS was 1.0:1.5:3.2. The ratio of Y to O was larger than 2:3, even though the Cu_2O was added based on the reaction ratio shown above. Presumably additional oxygen, such as the inherent impurity in the Cu powders, enhanced the Y:O ratio. Adjusting the amount of the oxidant in this innovative MA-HIP process is valuable to reach the target composition, where oxygen impurity, which has great influence on the thermal conductivity of Cu matrix, and oxidant added from outside fully oxidize Cu_6Y, forming

Y_2O_3 nano-particles. It needs to be noted that the dark phases with size of 3 μm were consisted of smaller Y_2O_3 particles with size of 0.5 μm, and were aggregated around the particle boundaries, where the Cu_2O is rich because of its hysteresis addition. The similar morphology of the dark phases and the Cu_2O particles indicated that the distribution of oxidant was still not uniform.

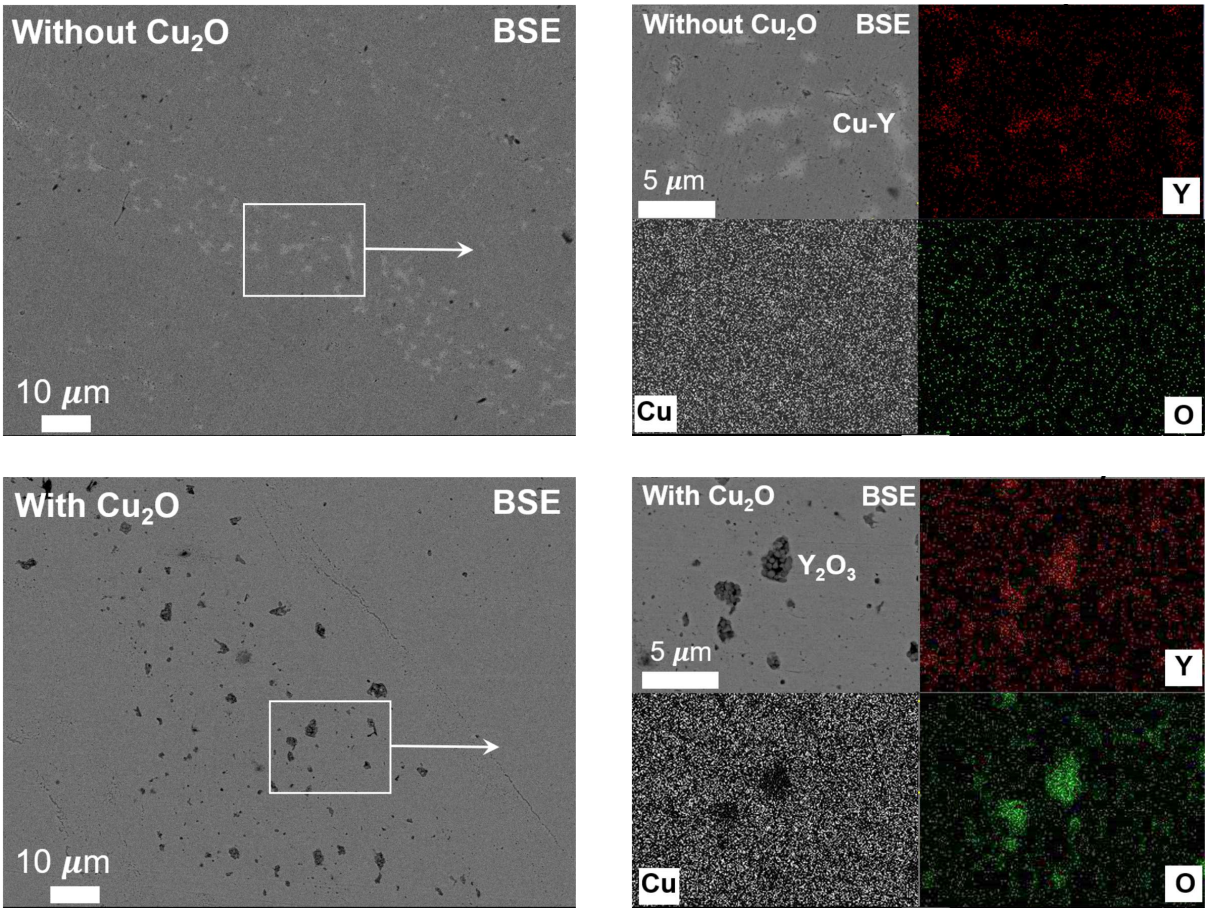

Figure 5.2.3 SEM-BSE images and EDS mappings of samples without Cu_2O (up) and with Cu_2O (down) addition.

5.2.3.3 TEM observation

Figure 5.2.4 shows the STEM images, statistic of the corresponded grain size distribution and the EDS mappings of the sample without Cu_2O. The grains were accounted, and it was found that the average grain size is 1.8 μm. EDS mappings were conducted for the red box area, and the elements distribution of Cu, Y, and O were shown in Figure 5.2.4. It was found that the aggregated phases around the grain boundary were the Y rich phases. Considering the Y was uniformly dissolved into the Cu matrix during MA process, the aggregation of Y occurred during the HIP process, in which the high temperature broke the non-equilibrium condition of the solid solute Y. Precipitation and aggregation of Y occurred, leading to the solid solute Y in

the Cu matrix aggregated on the grain boundary, forming Y rich phases. The small amount of O element indicated that only a few of Y were successfully oxidized by O, forming Y_2O_3. Considering no oxidant was added during the MA process under Ar atmosphere. The most of the O were supplied from the originated impurity into the Cu matrix. The in-situ reaction of Y and O impurity gathered the O to the grain boundaries, purifying the Cu matrix, thereby beneficial to the thermal conductivity of the Cu alloys.

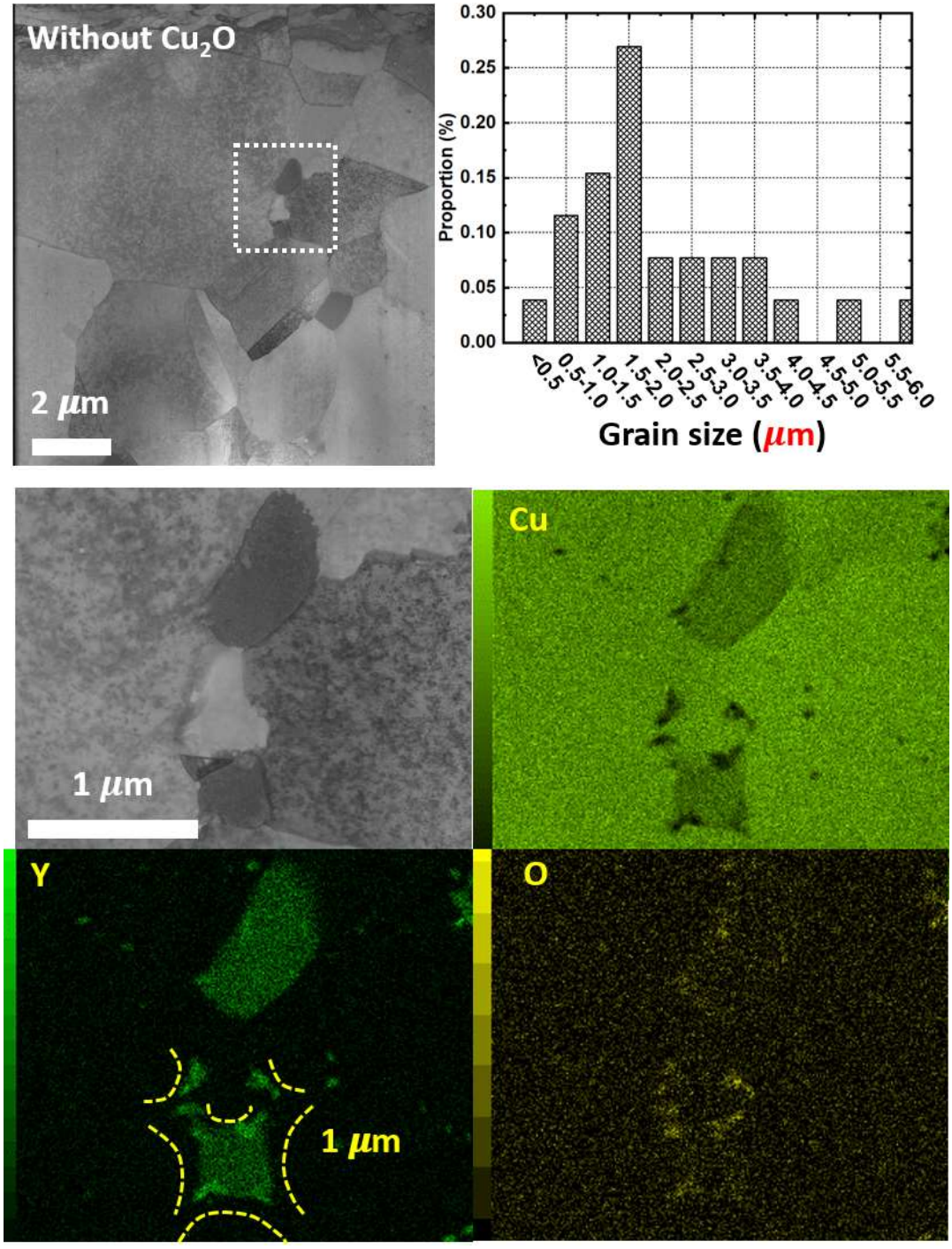

Figure 5.2.4 STEM images, grain size statistics and EDS mappings of sample without Cu_2O.

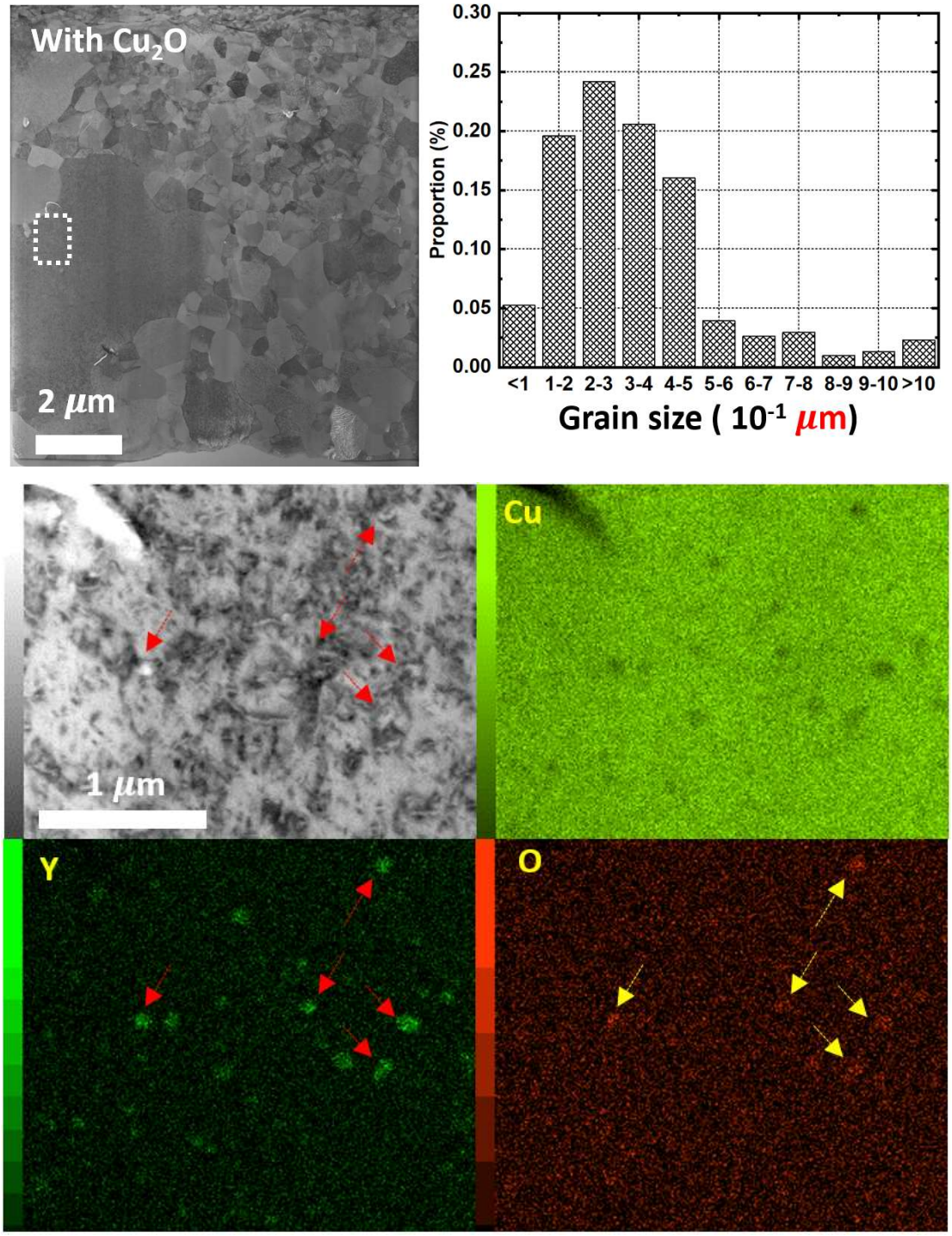

Figure 5.2.5 STEM images, grain size statistics and EDS mappings of sample with Cu_2O.

Figure 5.2.5 shows the STEM images, statistic of the corresponded grain size distribution and the EDS mappings of the sample with Cu_2O. The grains were accounted, and it was found that most of the grains kept smaller size less than 1 μm, except for a huge grain with size of around 5 μm. The average grain size of the sample with Cu_2O is 480 nm, smaller than the average grain size of 1 μm for the Glidcop® Al-15 [23], and much smaller than the sample without Cu_2O addition. EDS mappings were conducted for the red box area, and the elements

distribution of Cu, Y, and O were shown in Figure 5.2.5. It was found that different from the sample without Cu_2O, in which aggregation occurred, the Y_2O_3 nano-particles for the sample with Cu_2O were observed in the grain with high number density of $1.7 \times 10^{21}/m^3$ and average size of 15 nm. In-situ reaction between Y and O occurred during HIP, forming fine Y_2O_3 dispersive particles. The in-situ formed Y_2O_3 particles suppressed the growth of MA powders, contributing to the formation of finer grains compared to the sample without Cu_2O. Therefore, adding oxidant is necessary for the fabrication of ODS-Cu with Y_2O_3 through the innovative MA-HIP process by in-situ fabrication method.

5.2.3.4 Vickers hardness of the consolidated samples

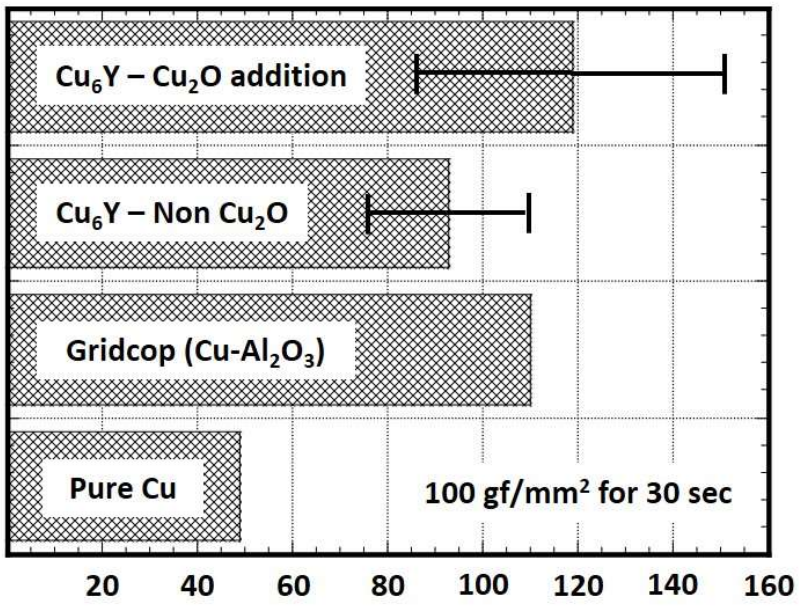

Figure 5.2.6 Comparison of Vickers hardness for the Cu alloys.

Vickers hardness test is an effective and convenient method to characterize the mechanical property of material. The Vickers hardness of the samples without Cu_2O and with Cu_2O were conducted, and pure Cu and Glidcop® Al-15 were also tested for compassion, as shown in Figure 5.2.6. Compared to pure Cu with a Vickers hardness of 50, the sample without Cu_2O has a Vickers hardness of 93±16.46, mainly because of the lower content of Y_2O_3, fine grain size and the precipitation of Cu-Y phases. With the Cu_2O addition, the Vickers hardness increase to be 120±31.80, even larger than the Glidcop® Al-15 with Vickers hardness of 110. The introduction of Cu_2O promotes the formation of Y_2O_3, which has great influence on the mechanical property. The increased error bar of Vickers hardness for ODS-Cu with Cu_2O was mainly caused by the non-uniform Y_2O_3 particle distribution.

5.2.3.5 DTA analyses on Cu_6Y and $Cu_6Y + Cu_2O$

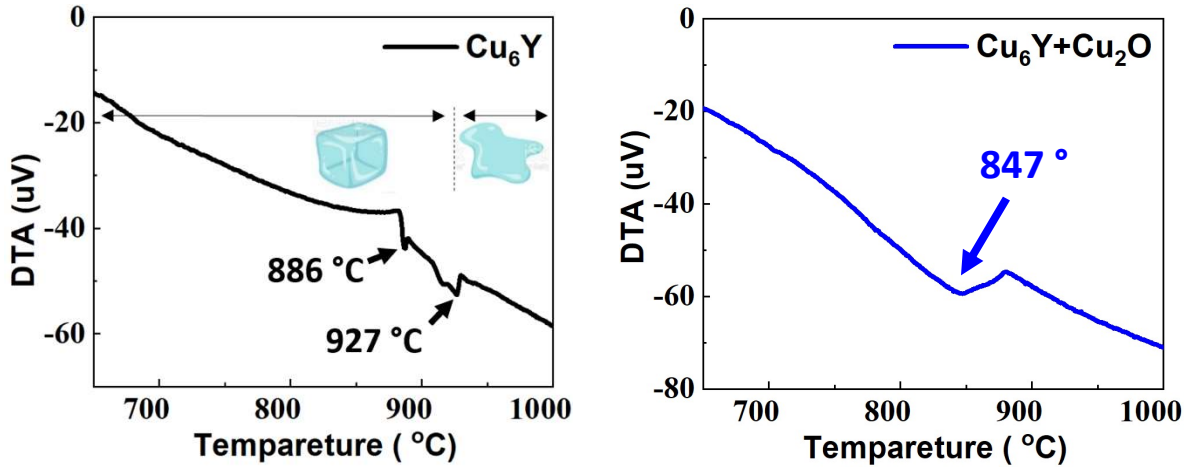

Figure 5.2.7 DTA curves of Cu_6Y powders (left), $Cu_6Y + Cu_2O$ powder (right).

In order to explore the reaction mechanism of the sample without Cu_2O and the sample added Cu_2O, DTA analyses on Cu_6Y powders and $Cu_6Y + Cu_2O$ blended powders were conducted and the DTA curves are shown in Figure 5.2.7. For the Cu_6Y powders, it was found that endothermic transition of the DTA curve was observed at 886 ℃ and 927 ℃, corresponding to the phase transformation point and the melting point shown in the Cu-Y phase diagram, and the detail description was shown in chapter 5.1. For the Cu_2O and Cu_6Y blended powders, the endothermic transition of the DTA curve was only observed at 847 ℃. Combining the XRD spectrum and the EDS mappings, it was found that 847 ℃ is the in-situ reaction point of Cu_6Y and Cu_2O. Considering the in-situ reaction point is lower than the Cu_6Y melting point of 927 ℃, the in-situ reaction can be occurred before Cu_6Y melting. That is the reason that adding oxidant can suppress the aggregation of Y, forming fine Y_2O_3 dispersive particles.

Based on the analyses shown above, the in-situ reaction mechanism of the samples without Cu_2O and with Cu_2O are shown in Figure 5.2.8. For the sample without Cu_2O, the Cu_6Y compounds were gradually dissolved into the Cu matrix caused by the repeated fracture and cold welding, forming the supersaturated solid solute Y in non-equilibrium condition. During HIP at elevated temperature, the non-equilibrium Y transformed into the equilibrium condition, and aggregation and precipitation occurred during the cooling process, only a few Y were oxidized by the inherent O impurity in the Cu matrix. For the sample with Cu_2O, the Cu_6Y were first dissolved into the Cu matrix during the preliminary MA process, forming the supersaturated solid solute Y. The Cu_2O was added as the oxidant at the middle of MA process. The O was dissolved into the alloyed MA powders in the following MA process. During HIP at elevated temperature, the reaction between Y and O occurred before the aggregation and

precipitation of the molten Y, forming fine dispersive Y_2O_3 particles. Therefore, adding oxidant during the innovative MA-HIP process by in-situ fabrication method is useful to suppress the aggregation of Y elements and form fine dispersive particles.

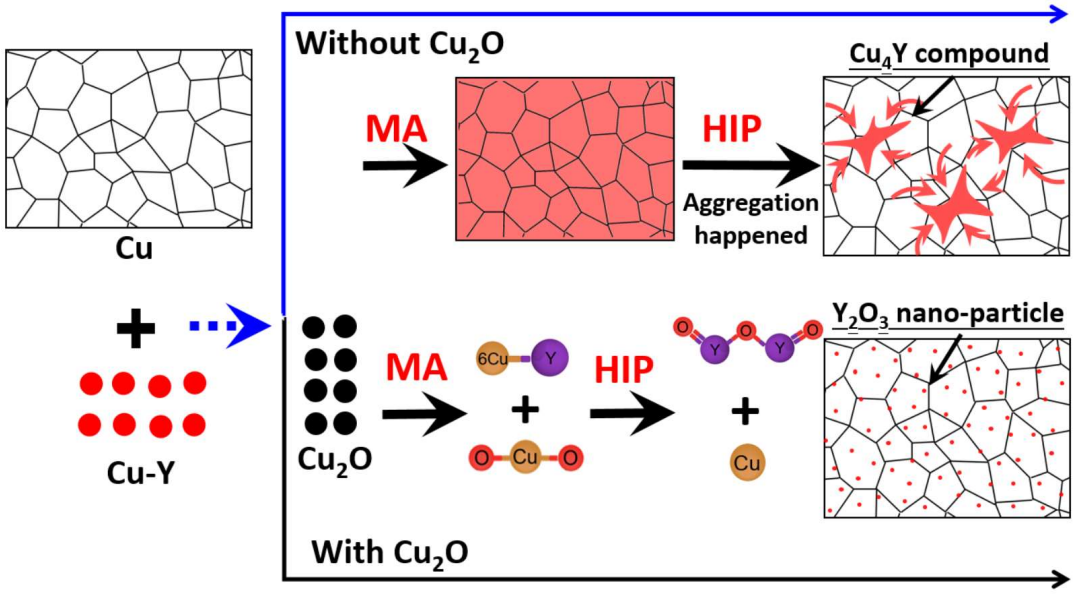

Figure 5.2.8 The in-situ reaction mechanism of the samples without and with Cu_2O.

5.2.4 Conclusions

Based on the Cu_6Y sourced ODS-Cu alloys with nominal content of 1.38 wt. % Y_2O_3, samples without Cu_2O and with Cu_2O were fabricated through innovative MA-HIP process by in-situ fabrication method, and the effects of Cu_2O as the oxidant were also investigated. The main results were shown as follow:

(1) For the sample without Cu_2O, except for a small amount of Y were oxidized by the O impurity in the Cu matrix, forming a low content of Y_2O_3, most of the Cu_6Y compounds were melted during the HIP process, resulting in the aggregation phases during cooling process.

(2) For the sample with Cu_2O, the Cu_6Y compounds were oxidized at 847 ℃ before melt by the oxidant, forming fine dispersive Y_2O_3 particles with typical size of 15 nm and higher number density of $1.7 \times 10^{21}/m^3$.

(3) The formation of fine dispersive Y_2O_3 particles and fine grains contributed to the improvement of Vickers hardness. Therefore, adding oxidant (Cu_2O) is necessary for the ODS-Cu by in-situ fabrication method.

5.3 Effect of Y_2O_3 sources on the ODS-Cu alloys

5.3.1 Introduction

In Chapters 2 ~ 4, ODS-Cu alloys with Y_2O_3 fabricated by adding pure metal Y through innovative MA-HIP process by in-situ fabrication method were investigated. The optimum fabrication parameters (HIP temperature, MA time), and the powder size classification were carried out. In Chapter 5.1, the possibility of using Cu-Y intermetallic compounds as the source of Y_2O_3 to fabricate the ODS-Cu alloys through innovative MA-HIP process by in-situ fabrication method was investigated. In chapter 5.2, the influence of oxidant on the microstructure and physical properties of Cu_6Y sourced samples was investigated. It was found that both using pure metal Y and Cu-Y intermetallic compounds as the Y_2O_3 source were feasible. The comparisons among the ODS-Cu alloys with same content of Y_2O_3 and same fabrication parameters, but different Y_2O_3 sources should be conducted for comparison.

In this topic, three kinds of ODS-Cu alloys with 1.5 wt. % Y_2O_3 were fabricated in same MA-HIP parameters with different Y_2O_3 sources. One sample added Y_2O_3 directly through conventional MA-HIP process, the other two added pure metal Y and Cu_6Y intermetallic compound separately through innovative MA-HIP process by in-situ fabrication method. The morphology evolution of MA powders, the distribution of Y_2O_3, and the macro properties such as strength and thermal conductivity were evaluated.

5.3.2 Experimental procedure

In this topic, the ODS-Cu alloys with the nominal content of 1.5 wt. % Y_2O_3 were fabricated by adding different Y_2O_3 sources, direct Y_2O_3 powders, pure metal Y, and Cu_6Y intermetallic compounds. The Cu (99.9% purity, 50 μm), Y_2O_3 (99.9% purity, 5 μm) , Y (99.9% purity, 300 μm) and Cu_2O (99.9% purity, 1 μm) were purchased from Furuuchi Chemical Co., Ltd in Japan, and the Cu_6Y intermetallic compound with average size of 150 μm was fabricated by arc melting described in chapter 5.1. All the initial MA powders and the size distribution of the homemade Cu_6Y are shown in Figure 5.3.1.

The compositions of prepared samples are shown in Table 5.3.1. For the Y_2O_3 sourced sample, the Cu and Y_2O_3 blended powders were direct mechanical alloyed for 32 hours with speed of 250 rpm. For the pure metal Y sourced and Cu_6Y intermetallic compound sourced samples, the Cu and Y blended powders, Cu and Cu_6Y blended powders were mechanical alloyed for 16 hours with speed of 250 rpm, followed by adding Cu_2O. The mechanically

alloyed Cu-Y powders were further milled with Cu_2O powders for additional 16 hours with the same speed. The milled powders of three samples were put into the steel capsules. Before clamping, the capsules were degassed for 1 hour in 0.1 Pa vacuum, followed by welding in the vacuum condition. During the HIP process, the steel capsules, filled with milled powders, were kept in the pressure of 150 MPa at temperature of 1000 °C for 2 hours.

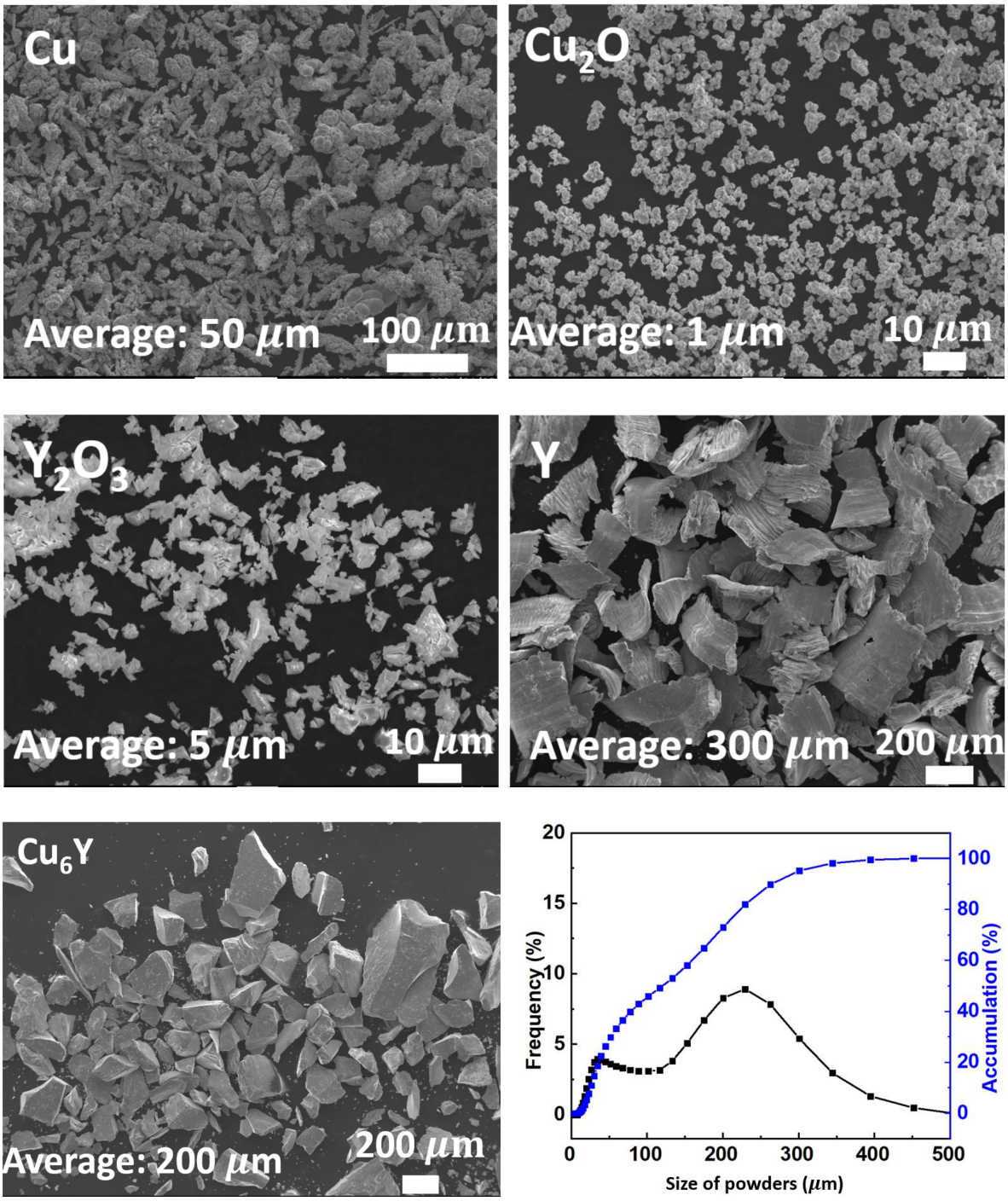

Figure 5.3.1 The SEM images of initial blend powders (Cu, Cu_2O, Y_2O_3, Y, Cu_6Y), and the size distribution of Cu_6Y compound.

Table 5.3.1 Composition of ODS-Cu alloys by different Y_2O_3 sources.

Samples	Cu	Y_2O_3	Y	Cu_6Y	Cu_2O
Cu-1.5 wt. % Y_2O_3(Y_2O_3)	98.50	1.50	/	/	/
Cu-1.5 wt. % Y_2O_3(Y, Cu_2O)	95.97	/	1.18	/	2.85
Cu-1.5 wt. % Y_2O_3(Cu_6Y, Cu_2O)	90.91	/	/	6.24	2.85

Microstructures and morphologies of the MA powders and consolidated samples with different Y_2O_3 sources were evaluated by XRD apparatus and scanning electron microscope (SEM, JEOL JSM-5600) equipped with energy dispersive X-ray spectroscopy (EDS). In addition, thin sampling from a part of the MA-HIP processed Cu alloy bulk samples was carried out using the focused ion beam (FIB, Hitachi nano DUE'T NB5000) machine. After that, nanostructure of the thin FIB sample was observed using electron backscatter diffraction (EBSD) and scanning transmission electron microscope (TEM, JEOL JEM-2800) equipped with EDS.

Figure 5.3.2 images of the tensile machine, tensile test fixture and the tensile sample.

The tensile tests were conducted by universal testing machine (Shimadzu, AGS-X 10 kNG) in Kobe material testing laboratory. The size of miniature specimens for tensile test was shown in Figure 5.3.2. The tests were conducted in a strain rate of 0.06 mm/min until fracture at room temperature (23±2 ℃) and relative humidity of 50±5 %RH (Relative Humidity). According to the load-displacement curve of the tensile test, the tensile strength and strain of bulk sample were estimated by the sample dimension and the cross-sectional area of fractured surface.

5.3.3 Results and discussion

5.3.3.1 Characterization of MA powders

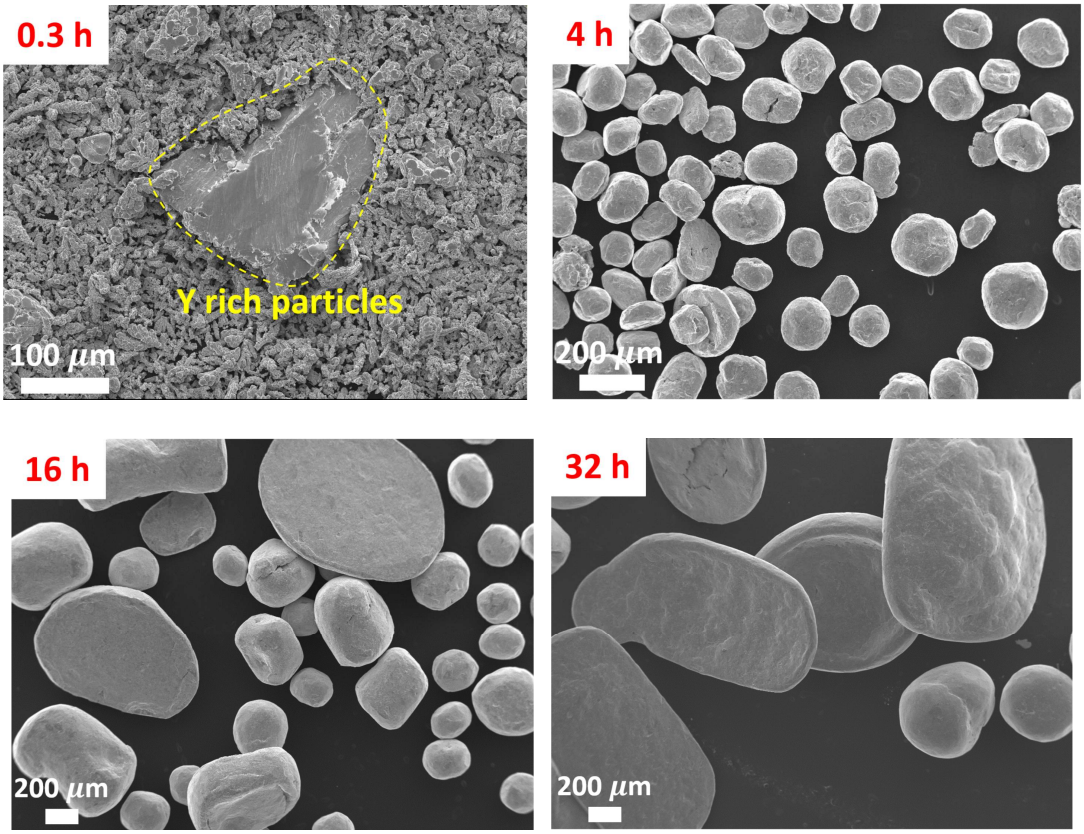

Figure 5.3.3 The MA powders evolution with the MA process for the pure Y sourced sample.

Figure 5.3.3 shows the development of MA powders during MA process for the pure Y sourced sample. At 0.3 h, some of pure Cu powders started to stick with each other, and pure Y powders still maintained the initial morphology with the size of 200 μm. Those two kinds of powder clearly distinguished with each other. With the MA continuing, the pure Y powders were fractured and mixed with pure Cu powders, growing up to 150 μm with spherical shape. After 16 hours' MA, the MA powders further grew up to 300 μm, and the surface of MA powders became smoother. The phenomenon of sticking happened in the MA time of 16 hour shown in Figure 5.3.3, which demonstrated that the sticking not only occurred between fragments and MA powders but also between two MA powders. But considering that the surface of the MA powder is brittle and hard, this sticking mode is not tight. Besides, the particularly obvious change was the formation of huge flat powders. During MA process, some MA powders were sticked and coated on the grind steel balls. Those sticked MA powders were peeled off during the followed MA process by collision, showing the spherical shells, and then were grinded to flat shape. After 32 hours MA, the proportion of flat MA powders became

larger with smoother surface. The more MA powders in flat shape, the more sticking occurred. The development of other sourced MA powders showed the similar tendency.

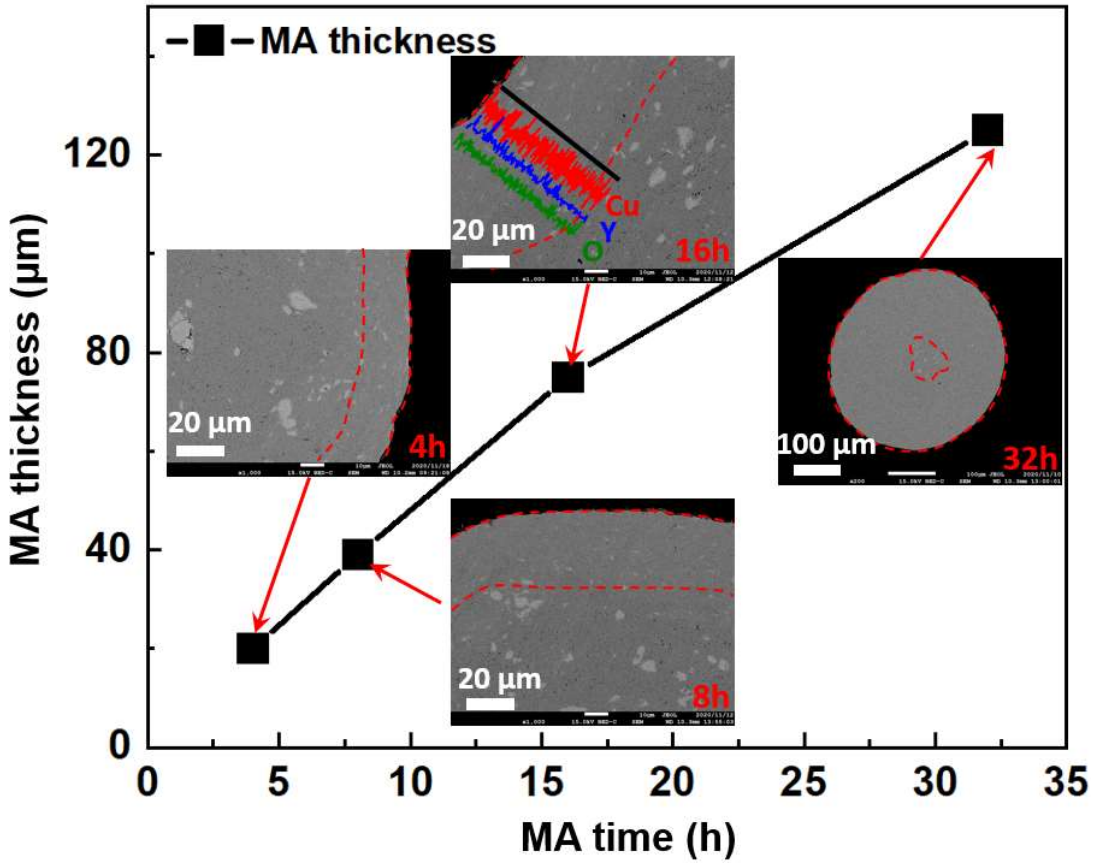

Figure 5.3.4 The development of alloyed thickness of MA powders with MA process for Cu_6Y sourced sample.

Figure 5.3.4 shows the development of alloyed thickness of MA powders with MA time for the Cu_6Y sourced sample. The thickness of the alloyed layer was confirmed by the statistics of SEM–BSE images. In the SEM-BSE images, the light color phases are Cu-Y compounds, which were crushed during the ball milling. The blurred border indicated the dissolved state of Y elements into the Cu matrix. The EDS in the form of line scanning showed that the Y element was uniformly distributed in the alloyed layers except for some local areas. The thickness of MA powders was increased from 20 μm to 120 μm with the MA time from 4 hours to 32 hours, and the relationship between thickness of alloyed layer and MA time is approximately proportional. The increase of the alloyed layer demonstrated that the mechanical alloying not only occurred on the surface of MA powder but also the inside areas. The extrusion during collision between grind balls and MA powders caused large deformation of the MA powders, this isotropic large deformation enhanced the dissolution of Y into the Cu matrix. It indicated that in addition to the common consensus that the supersaturated solid solution state is caused

by fracture and cold welding, large deformation caused by collision also contribute to the dissolution to form supersaturated solid solution state.

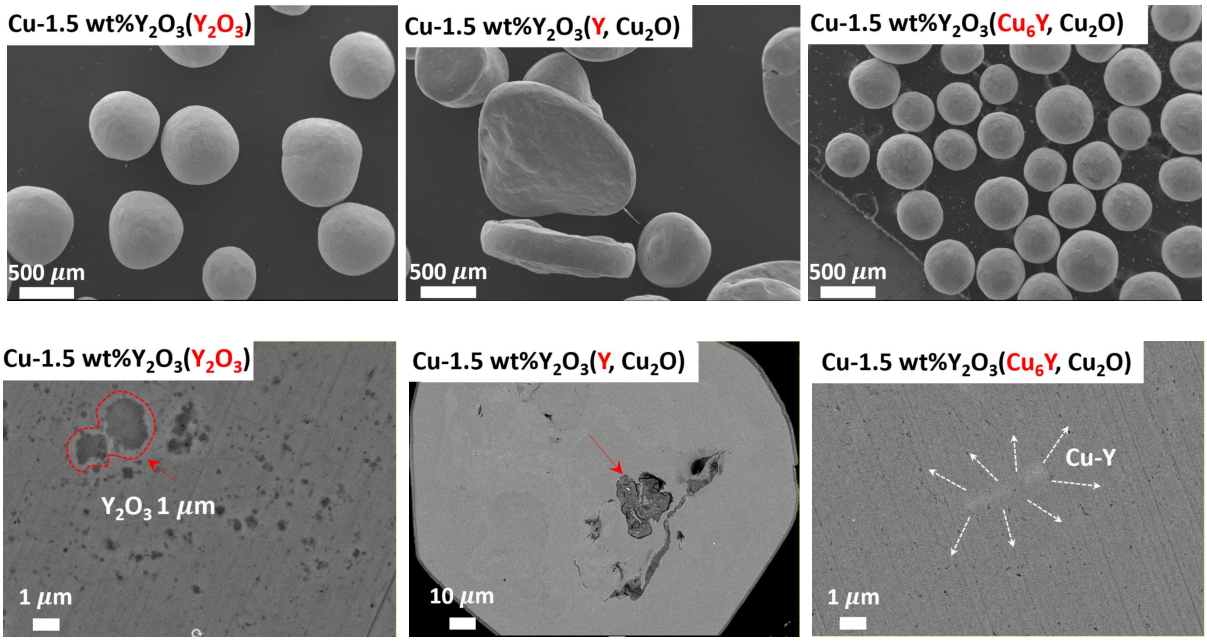

Figure 5.3.5 Morphlogies and the corss sections of the MA powders after 32 hours MA for different Y_2O_3 sourced samples.

The morphologies of MA pwoders after MA were compared among the direct Y_2O_3 sourced sample, pure metal Y sourced sample, and Cu_6Y sourced sample, as shown in Figure 5.3.5. MA powders of direct Y_2O_3 sourced sample and Cu_6Y sourced sample showed spherical shape with size of 500 μm and 300 μm, respectively. However, the MA powders of pure metal Y sourced sample showed flat shape with typical size of 800 μm, which indicated that severe sticking occurred for the pure Cu and pure metal Y MA system, because of the ductility of both blend powders. The smallest MA powders for Cu_6Y sourced sample confirmed that more amount of brittle Cu_6Y intermetallic compound played not only the role of Y_2O_3 source but also the role of PCA to supress the growth of MA powders in some degree. Figure 5.3.5 shows the cross section of the alloyed powders with different Y_2O_3 sources. For the direct Y_2O_3 sourced sample, some relatively large Y_2O_3 particles (2 μm) with half size of the initial Y_2O_3 powders remained after MA. Some larger Y rich powder with one tenth size of the initial pure powders also remained after MA for pure metal Y sourced sample, which indicated that the pure metal Y had relative higher dissolution ability compared to the Y_2O_3. For the Cu_6Y sourced sample, all Y rich particles were disappeared and fully dissolved into the Cu matrix, only left a fuzzy light color area, reflecting the ongoing dissolution. Therefore, from the MA powder level, the Cu_6Y intermetallic compound had better performance to suppress the growth of MA powders and enhance the dissolution of Y element.

5.3.3.2 Characterization of the consolidated samples

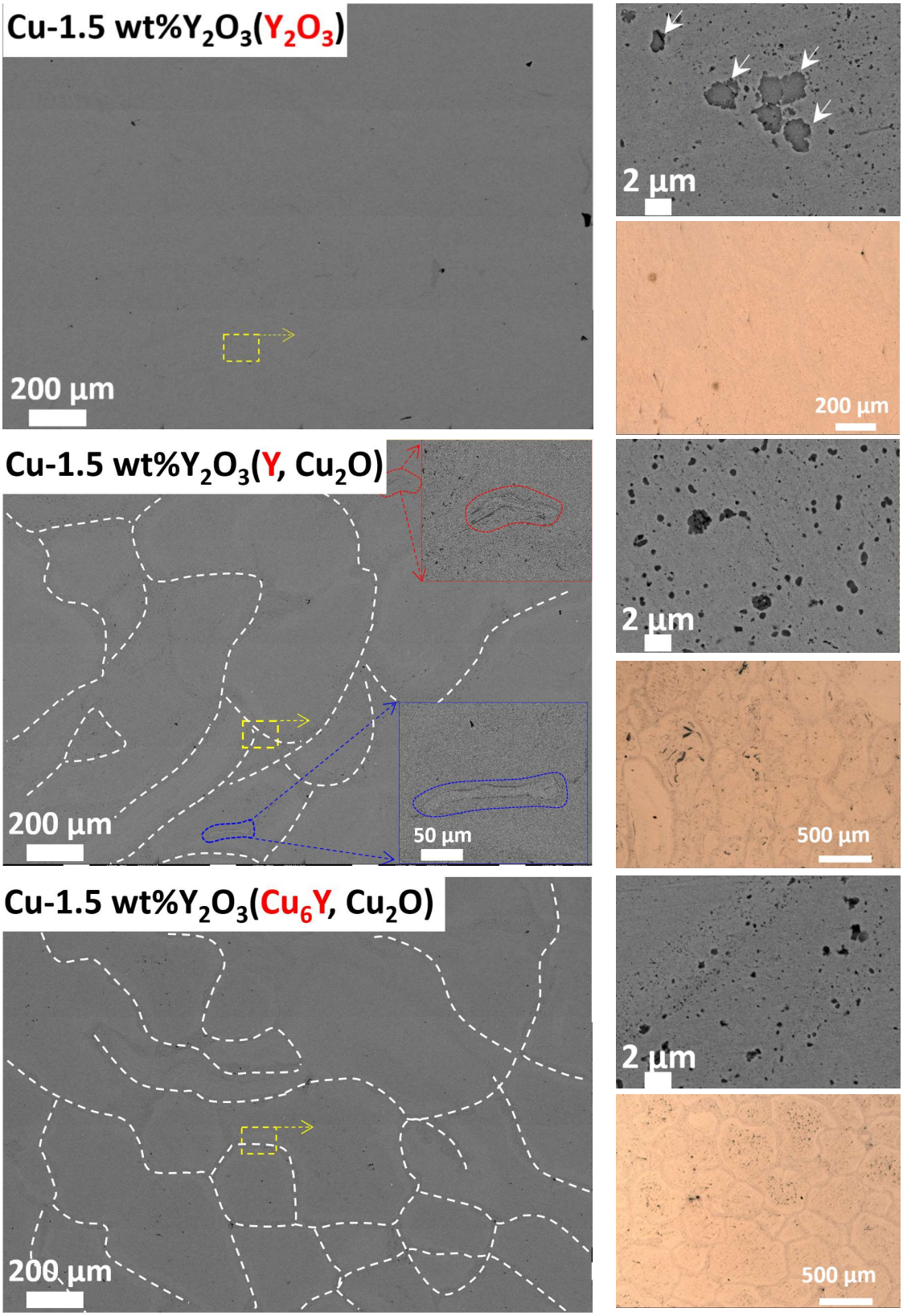

Figure 5.3.6 The SEM-BSE images and the optical images for the consolidated samples after HIP with three different kinds of Y_2O_3 sources.

Figure 5.3.6 shows the morphologies of consolidated samples with three different kinds of Y_2O_3 in the form of SEM images and optical images. The clear particle boundaries were formed for the two in-situ formed ODS-Cu samples, compared to the direct Y_2O_3 sourced sample by conventional MA-HIP process. The larger magnified images about the particle boundaries show that plenty of contamination contained particles with average size of 0.5 μm were existed. Considering that the contamination contained particles did not existed in the alloyed MA powders, the introduced contamination in the supersaturate solid solution state during MA process were precipitated during HIP process, forming the contamination contained particles. Besides, the larger Y rich particles existed in the alloyed MA powders for the direct Y_2O_3 sourced sample and pure metal Y sourced sample remained after consolidation at elevated HIP temperature. Combining the facts shown in Chapter 2 that high HIP temperature can enhance the diffusivity of Y elements in some degree, it was found that the HIP process can only fine-tune the distribution of Y elements, and the MA process play the dominate role in the distribution of Y element.

Figure 5.3.7 shows the XRD spectrum and the enlargement of the consolidated samples with different Y_2O_3 sources. The existed Y_2O_3 peaks for all three samples demonstrated that the Y_2O_3 was formed by the in-situ reaction between Y precursors and O element. The lowest content of Y_2O_3 in pure metal Y sourced sample indicated that the in-situ reaction was not efficient, and some of Y reacted with contamination. The existed impure peaks showed that there were $YCrO_3$, Fe_2O_3, or CrO_2, corresponding to the contamination contained particles shown in the SEM images. During in-situ fabrication process, the oxidant was added at the middle of MA process, which induced the formation of O rich layers. During collision between MA powders and grind balls, the O element not only oxidized the Y element in the MA powders, but also oxidized the grind steel mediums, accelerating the introduction of contamination into the particle boundary. For in-situ fabricated samples, the higher Y_2O_3 peak and lower impure peaks for Cu_6Y sourced sample compared to pure metal Y sourced sample indicated that Cu-Y compound can suppress the introduction of contamination in some degree. The oxidation of the grind mediums was confirmed by the thermodynamic analysis that the Gibbs free energy of formation for Fe participated compound is lower than Gibbs free energy of formation for Cu_2O. Therefore, the existed problems of O rich layers for the in-situ fabricated samples indicated that the oxidant form, content, and oxidation method need to be further improved.

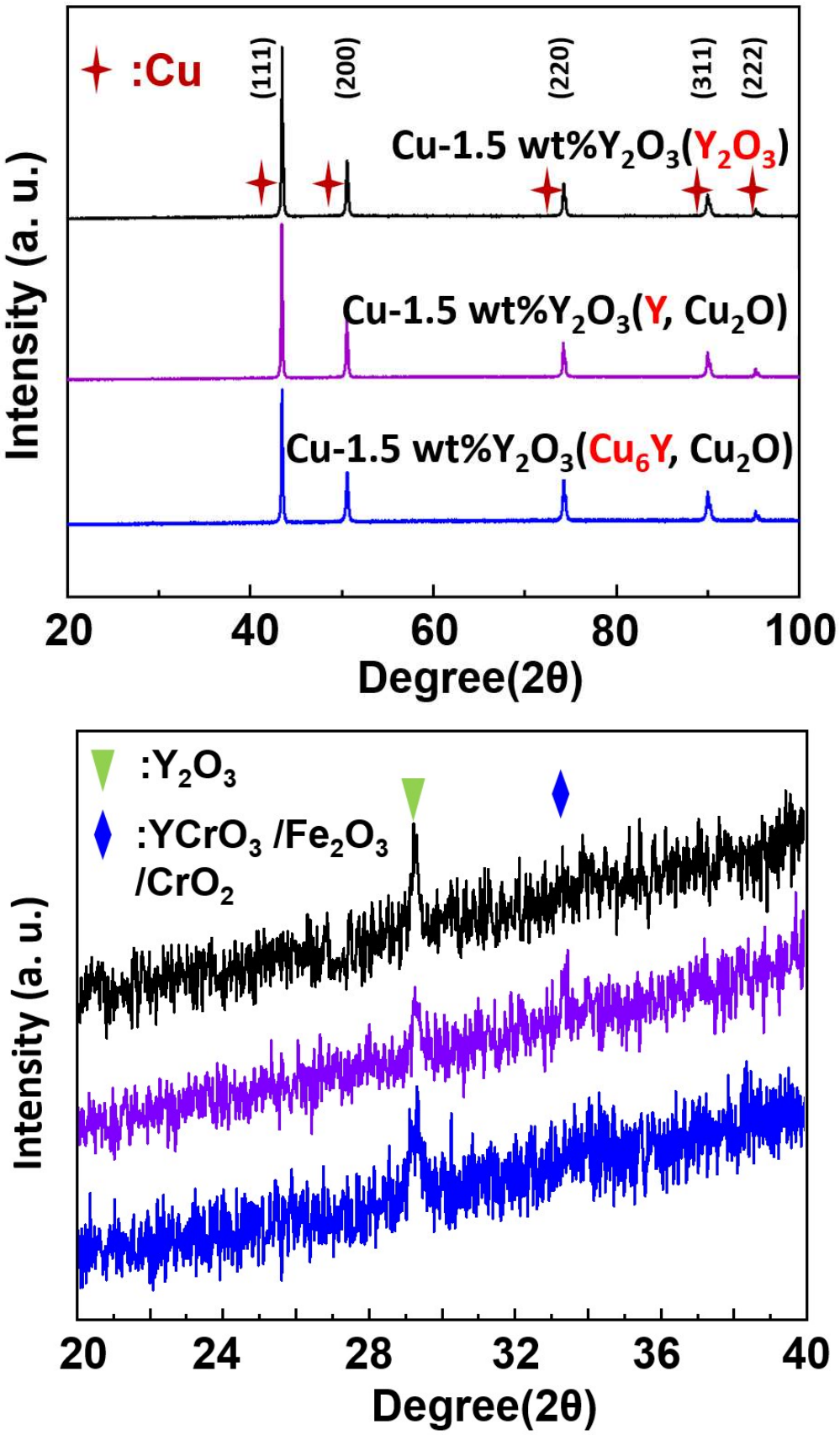

Figure 5.3.7 XRD spectrum (up) and the enlargement (down) of the consolidated samples with different Y_2O_3 sources.

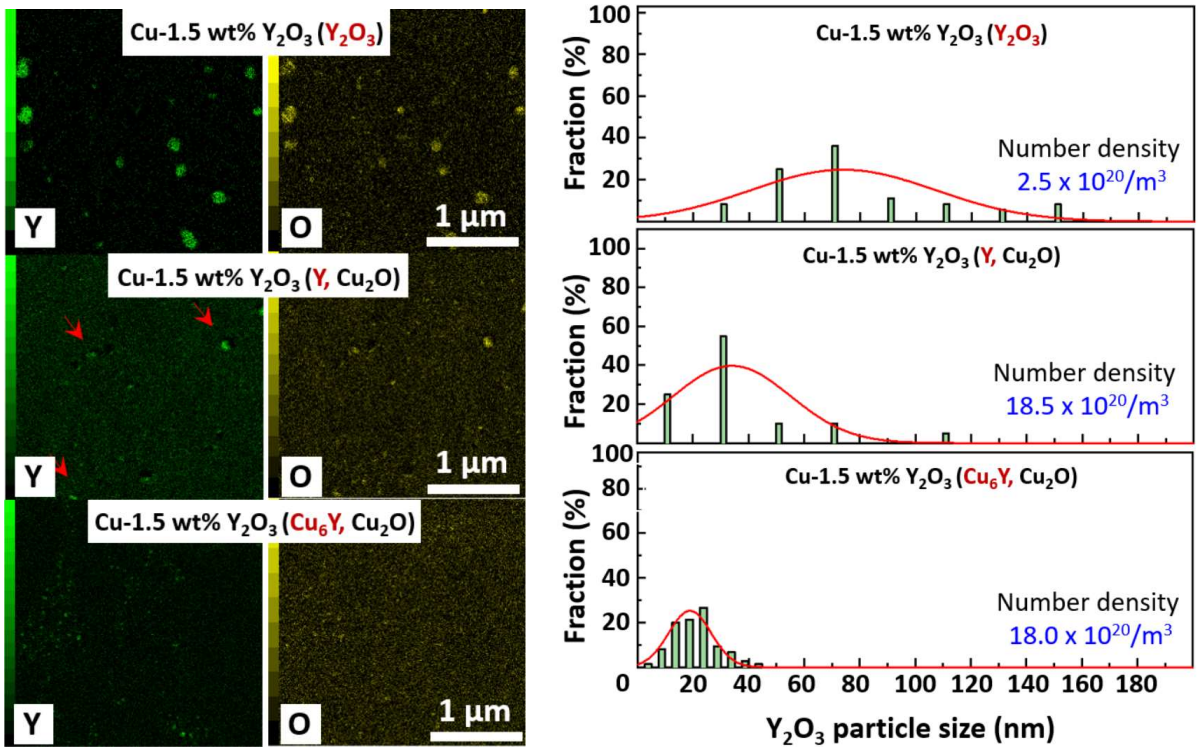

Figure 5.3.8 TEM-EDS mappings and the statistical size distribution of Y_2O_3 particle for the samples with different Y_2O_3 sources.

Figure 5.3.8 shows the TEM-EDS mappings and the statistical size distribution of Y_2O_3 particles for the samples with different Y_2O_3 sources. From the EDS mappings, it was found that the Y element fitted the O element very well for all three samples. Compared to the larger Y_2O_3 particles with average size of 73±33 nm and number density of $2.5\times 10^{20}/m^3$ for the direct Y_2O_3 sourced sample by conventional MA-HIP process, the samples by in-situ fabrication method have much smaller Y_2O_3 particles with size of 34±21 nm and number density of $18.5\times 10^{20}/m^3$ for pure metal Y addition, and much smaller Y_2O_3 particles with size of 19±7 nm and number density of $18.0\times 10^{20}/m^3$ for Cu_6Y compound addition. For the Y_2O_3 sourced sample, the fine Y_2O_3 particles came from the break of the initial large Y_2O_3 powders during the grinding. The fracture of Y_2O_3 particles was suppressed gradually with the MA continuing, because the Y_2O_3 powders were easily coved by the ductile of Cu during MA process as shown in chapter 5.1. The ex-situ Y_2O_3 particles are thermodynamic instable, and with low interface boding strength. For the in-situ formed Y_2O_3 particles, the Y precursor were dissolved into the Cu matrix by the compression and shear during the grinding, forming supersaturate solid solute Y and O elements. The fine dispersive Y_2O_3 particles were in-situ formed by chemical reaction during HIP process at high temperature and have the characteristics of thermodynamic stability and coherent or semi-coherent interface [24]. For the in-situ fabricated samples, it should be noted that different from the Cu_6Y sourced sample,

there were some larger Y_2O_3 particles with size of 110 nm remained for the pure metal Y sourced sample. Compared to the Cu_6Y intermetallic compound, the pure metal Y has relative ductility and high Y enrichment, which are not conducive to the solubility and uniform distribution of Y element, resulting in the existence of large Y rich particles. That is the reason of larger Y_2O_3 particles in the pure metal Y sourced sample.

According to the dispersion strengthening mechanism, the particles size and number density of dispersive particles play an important role to improve the strength. Too large dispersive particles with incoherent interface can induce the concentration of the dislocations, resulting in the premature micro cracks, thereby deteriorating the mechanical performance [25]. Too small dispersive particles have weak block effect for the movement of dislocation. The dislocations can move through the dispersive particles, deteriorating the dispersion strengthening [25]. The in-situ formed dispersive Y_2O_3 particles had an average size of 19 nm for the Cu_6Y sourced sample, very closed to the optimum particle size with the range of 8~18 nm for Y_2O_3 strengthened Cu alloys [26].

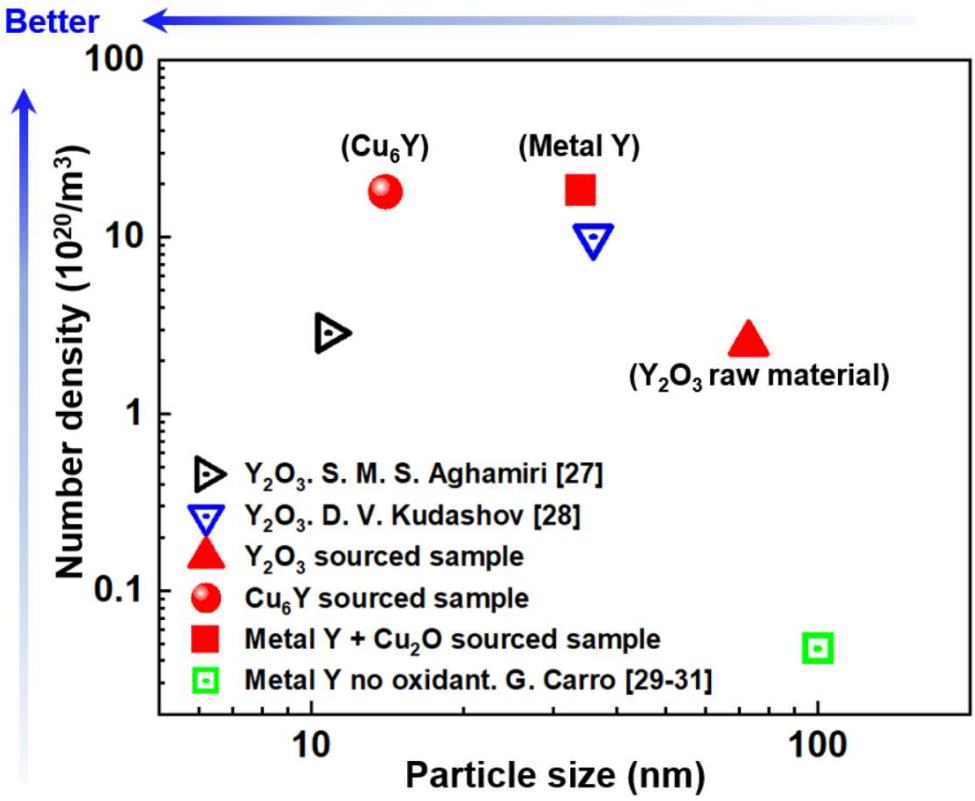

Figure 5.3.9 Summary the particle size and number density of the Y_2O_3 particles for ODS-Cu by global peers [27-31].

Figure 5.3.9 shows the summary the particle size and number density of the Y_2O_3 particles for ODS-Cu fabricated by the various methods in the world. It was found that most of ODS-Cu alloys had the Y_2O_3 particles with size of 10~100 nm and number density in the order of $10^{20}/m^3$, it was similar to the direct Y_2O_3 sourced sample fabricated by conventional MA-HIP process. The particle size and number density of the Y_2O_3 particle were much improved in the Cu_6Y sourced samples through innovative MA-HIP process by in-situ fabrication method. Besides, compared to the Y sourced sample by G. Carro et al, Cu_2O is an effective material to refine the dispersive Y_2O_3 particles and increase of the number density.

5.3.3.3.3 Properties evolution

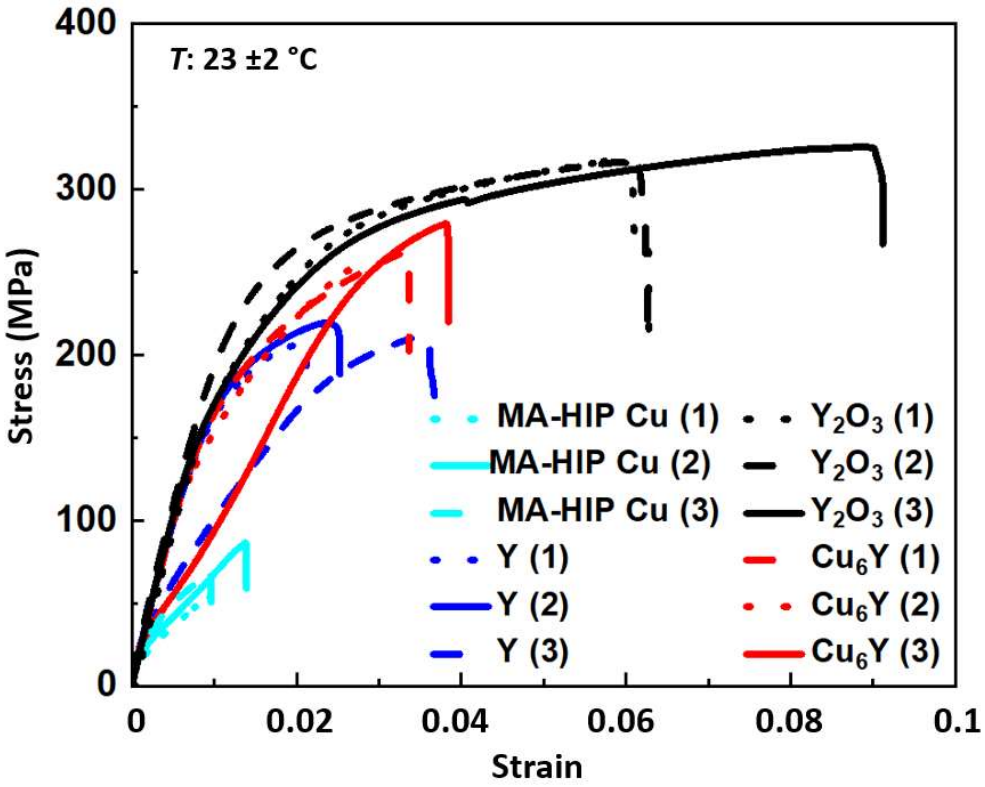

Figure 5.3.10 The strain-stress curves for pure Cu and ODS-Cu alloys with the same MA-HIP parameters.

Figure 5.3.10 shows the strain-stress curves of ODS-Cu alloys by tensile test. The pure Cu fabricated by the MA-HIP process with the same parameters (32h MA with speed of 250 rpm, and 2 hours for HIP at 1000 °C with pressure of 150 MPa) was also tested for comparison. Compared to pure Cu, all the ODS-Cu alloys had much better tensile strength and larger elongation. For the ODS-Cu alloys, the direct Y_2O_3 sourced sample fabricated by conventional MA-HIP process had better tensile strength and elongation compared to the in-situ fabricated

samples. For the in-situ fabricated ODS-Cu alloys, the Cu_6Y sourced sample had higher tensile strength compared to the pure metal Y sourced sample.

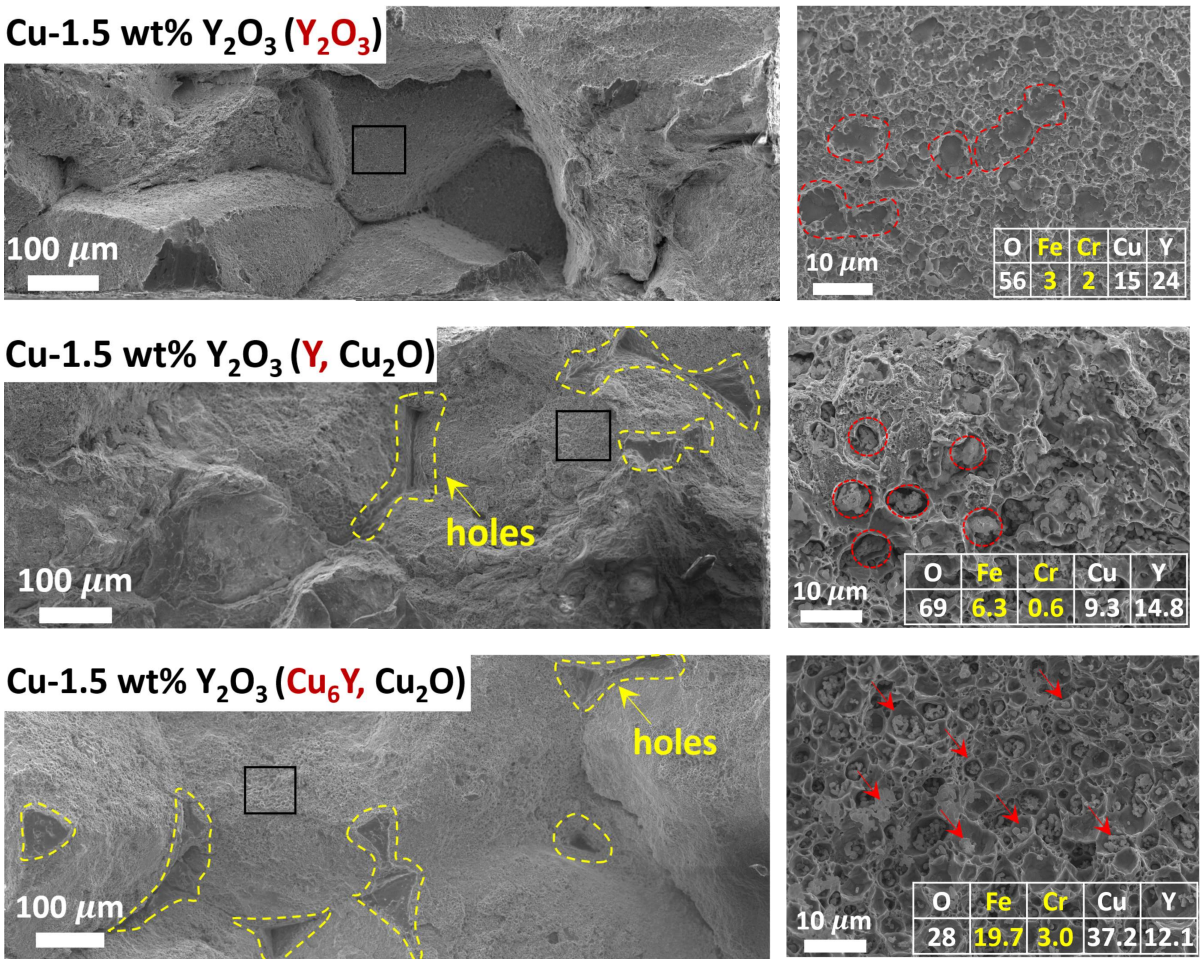

Figure 5.3.11 The cross sections of the ODS-Cu alloys with different Y_2O_3 sources after tensile fracture.

In order to analyse the fracture mechanism, the cross sections of all samples after tensile fracture were observed by SEM, as shown in Figure 5.3.11. All the samples were fractured around the particle boundary, where more large particles existed, and they were too large to play the role of dispersion strengthening. Besides, there were plenty of larger dimples surrounding the large particles on the fracture surfaces for in-situ fabricated samples. The interface of large particles and Cu matrix concentrated plenty of dislocation during tensile test, inducing the premature initiation of micro cracks. Compared to the large particles in direct Y_2O_3 sourced sample with lower contamination, the large particles in in-situ fabricated samples had more contamination introduced from the grind mediums. The concentrated contamination hardened around the particle boundaries, which regions were more difficult in deformation during HIP process, resulting in the increase in porosity. Both the higher porosity and the existed large particles deteriorated the tensile strength and ductility. Therefore, suppressing the

introduction of contaminations during MA process is a key issue for developing high strengthened ODS-Cu alloys in future. Considering that the in-situ fabrication method can form the fine dispersive Y_2O_3 particles with high number density confirmed by TEM-EDS mappings, which play very important role in dispersion strengthening mechanism, the Cu_6Y sourced sample had larger potential for improvement once the means to reduce contamination and porosity are developed.

5.3.4 Conclusions

In this topic, the comparison among three different kinds of Y_2O_3 sourced samples (direct Y_2O_3 by conventional MA-HIP process, pure metal Y and Cu_6Y compound by in-situ fabrication method) were investigated. The main results were shown as follows:

(1) Compared to Y_2O_3 or pure metal Y, Cu_6Y played the roles of both suitable Y precursor and process control agent in some degree, to enhance Y dissolution and suppresses the growth of MA powders.

(2) Compared to direct Y_2O_3 sourced sample, the samples by in-situ fabrication method (Y and Cu_6Y sourced) had more contamination, because of the oxidation of milling balls by O-rich layers, which were formed when adding oxidant at the middle of MA process. The contamination contributed to the weak layers where fracture took place during the tensile tests.

(3) Compared to the direct Y_2O_3 sourced sample with the large and sparse dispersive Y_2O_3 particles, the samples by in-situ fabrication method (Y and Cu_6Y sourced) formed fine and high dense dispersive Y_2O_3 particles, especially for Cu_6Y sourced sample with Y_2O_3 particles size of 19±7 nm, very close to the optimum size, and high number density of $1.8\times 10^{21}/m^3$.

(4) Considering smallest Y_2O_3 particles were formed by in-situ fabrication method, the Cu_6Y sourced sample has larger potential for improvement once the means to reduce Fe impurities and holes are developed.

References:

[1] Y. Liu, S. Kondo, H. Yu, K. Yabuuchi and R. Kasada. Statistical Approach for Understanding the Effect of Specimen Size on the Yield Stress and Its Scattering in Mechanically-Alloyed Cu and ODS-Cu Obtained by Micro-Pillar Compression Test. Materials Transactions, Vol. 61, No. 5 (2020) pp. 955-962.

[2] D. S. Zhou, H. W. Geng, W. Zeng, D. Q. Zheng, H. C. Pan, C. Kong, P. Munroe, G. Sha, C. Suryanarayana, D. Zhang. High temperature stabilization of a nanostructured Cu-Y_2O_3 composite through microalloying with Ti. Materials Science & Engineering A 712 (2018) 80–87.

[3] D. S. Zhou, X. K. Wang, W Zeng, C. Yang, H. C. Pan, C. G. Li, Y. J. Liu, D. L. Zhang. Doping Ti to achieve microstructural refinement and strength enhancement in a high volume fraction Y_2O_3 dispersion strengthened Cu. Journal of Alloys and Compounds 753 (2018) 18-27.

[4] S. W. Pan, X. L. Zhou, K. X. Chen, M. Yang, Y. D. Cao, X. H. Chen, Z. D. Wang. In-Situ Nanoparticles: A New Strengthening Method for Metallic Structural Material. Appl. Sci. 2018, 8, 2479.

[5] A. Muñoz, B. Savoini, M.A. Monge, M. Eddahbi, O.J. Dura. Microstructure and mechanical properties of hot rolled ODS copper. Nuclear Materials and Energy 24 (2020) 100754.

[6] Tim Graning, Michael Rieth, Jan Hoffmann, Sascha Seils, Philip D. Edmondson, Anton Moslang. Microstructural investigation of an extruded austenitic oxide dispersion strengthened steel containing a carbon-containing process control agent. Journal of Nuclear Materials 516 (2019) 335-346.

[7] Zhiyuan Hong, Xiaoxin Zhang, Qingzhi Yan, Yingxue Chen. A new method for preparing 9Cr-ODS steel using elemental yttrium and Fe_2O_3 oxygen carrier. Journal of Alloys and Compounds 770 (2019) 831-839.

[8] SeungHyeok Chunga, Bin Lee b, Soo Yeol Leec, Changwoo Do d, Ho Jin Ryu. The effects of Y pre-alloying on the in-situ dispersoids of ODS CoCrFeMnNi high-entropy alloy. Journal of Materials Science & Technology 85 (2021) 62–75.

[9] L.K. Tan, Y. Li, S.C. Ng, L. Lu. Structures, properties and responses to heat treatment of Cu–Y alloys prepared by mechanical alloying. Journal of Alloys and Compounds 278 (1998) 201–208.

[10] T. Graning, M. Rieth, J. Hoffmann, A. Maoslang. Production, microstructure and mechanical properties of two different austenitic ODS steels. Journal of Nuclear Materials 487 (2017) 348-361.

[11] T. Graning, M. Rieth, J. Hoffmann. Microstructural investigation of an extruded austenitic oxide dispersion strengthened steel containing a carbon-containing process control agent. Journal of Nuclear Materials 516 (2019) 335-346.

[12] I. Kimio, Q. Guojun, S. Mey. P. J. Spencer. Evaluation of the phase diagram and thermochemistry of the Cu-Y system. Calphad, 14 (1990), 377-384.

[13] K. Itagaki. Evaluation of the phase diagram and thermochemistry of the Cu-Y system. Calphad Vol.14, No 4, pp.377-384.1990.

[14] S. Mey, K. Hack, K. Itagaki, P. J. Spencer, D. Neuschiitz. A thermodynamic evaluation of the Ba-Cu-Y system. Calphali Vol. 14, No. 2, pp. 175183, 1990.

[15] V. A. Davydov, L. S. Kashevarova, O. G. Revin. The kinetics of the initial step of pyrolytic transformation of naphthalene under high pressure. Russian journal of physical chemistry. Vol. 70. No. 6. 1996.

[16] A. Daoud, J. B. Vogt, E. Charkaluk, J.Bouquerel, L. Zhang, J. C. Biasci. Anisotropy effects on the tensile and fatigue behavior of an oxide dispersion strengthened copper alloy. Materials Science and Engineering A 534 (2012) 640– 648.

[17] S. B. Chandrasekhar, S. SudhakaraSarma, M. Ramakrishna, P. SureshBabu, T. N. Rao, B. P. Kashyap. Microstructure and properties of hot extruded Cu–1 wt%Al_2O_3 nano-composites synthesized by various techniques. Materials Science & Engineering A 591 (2014) 46–53.

[18] X. Y. Zhou, D. Q. Yi, L. Nyborg, Z. Hu, J. Huang, Y. Cao. Influence of Ag addition on the microstructure and properties of copper-alumina composites prepared by internal oxidation. Journal of Alloys and Compounds 722 (2017) 962-969.

[19] T. Graning, M. Rieth, J. Hoffmann, A. Moslang. Production, microstructure and mechanical properties of two different austenitic ODS steels. Journal of Nuclear Materials 487 (2017) 348-361.

[20] G. B. Schaffer and P. G. Mccormick. Displacement Reactions during Mechanical Alloying. Metallurgical Transactions A Volume 21A, October 1990-2789.

[21] S. Zohari, Z. Sadeghian, B. Lotfi, C. Broeckmann. Application of spark plasma sintering (SPS) for the fabrication of in situ Ni–TiC nanocomposite clad layer. Journal of Alloys and Compounds 633 (2015) 479–48.

[22] B. Huang, Y. Hishinuma, H. Noto and T. Muroga. Mechanochemical processing of Cu-Y_2O_3 alloy by MA-HIP for heat sink materials application. Fusion Engineering and Design, 140, (2019), 33-40.

[23] N. Simos, Z. Kotsina, E. Dooryhee et al. 200 MeV proton irradiation of the oxide-dispersion-strengthened copper alloy (GlidCop-Al15). Journal of Nuclear Materials 516 (2019) 360-372.

[24] M. S. Nagorka, C. G. Levi and G. E. Lucas. The potential of rapid solidification in oxide-dispersion-strengthened copper alloy development. Materials Science and Engineering, A 142 (1991) 277-289.

[25] P. Susila, D. Sturm, M. Heilmaier, B. S. Murty, V. S. Sarma. Effect of yttria particle size on the microstructure and compression creep properties of nanostructured oxide dispersion strengthened ferritic (Fe–12Cr–2W–0.5Y_2O_3) alloy. Materials Science and Engineering A528 (2011) 4579–4584.

[26] J. R. Groza, and J. C. Gibeling. Principles of particle selection for dispersion-strengthened copper materials. Materials Science and Engineering: A, 171, (1993), 115-125.

[27] D. V. Kudashov, H. Baum, U. Martin, M. Heilmaier and H. Oettel. Microstructure and room temperature hardening of ultra-fine-grained oxide-dispersion strengthened copper prepared by cryomilling. Materials Science and Engineering: A, 387-389, (2004), 768-771.

[28] S. M. S. Aghamiri, N. Oono, S. Ukai, R. Kasada, H. Noto, Y Hishinuma and T. Muroga. Microstructure and mechanical properties of mechanically alloyed ODS copper alloy for fusion material application. Nuclear Materials and Energy, 15, (2018), 17-22.

[29] G. Carro, A. Muñoz, B. Savoini, M.A. Monge. Fabrication and characterization of dispersion strengthened Cu-0.8%Y. Fusion Engineering and Design 154 (2020) 111548.

[30] G. Carro, A. Muñoz, B. Savoini, M.A. Monge, R. Pareja, Processing, microstructure and mechanical characterization of dispersion strengthened Cu-1%Y, Fusion Engineering and Design, 138 (2019) 321-331.

[31] G. Carro, A. Muñoz, M. A. Monge, B. Savoini, R. Pareja, C. Ballesteros and P. Adeva. Fabrication and characterization of Y_2O_3 dispersion strengthened copper alloys. Journal of Nuclear Materials, 455, (2014), 655-659.

Chapter 6. Effect of Y_2O_3 content on the Cu_6Y sourced sample

6.1 Introduction

In previous chapters, compared to the direct Y_2O_3 sourced ODS-Cu alloy, the obvious advantage for Cu_6Y sourced ODS-Cu alloys was the much smaller Y_2O_3 particles with higher number density, which is the key parameter during the development of dispersion strengthened materials. However, the higher porosity around the particle boundaries in in-situ formed samples increase the true stress to prematurely reach the critical fracture stress, resulting in the deterioration of performance during the tensile test. Different from the direct Y_2O_3 sourced ODS-Cu alloy, the in-situ formed samples added the Cu_2O at the middle of MA process in order to avoid the premature formation of Y_2O_3. However, the middle added Cu_2O leaded to the non-homogenous distribution of O element, forming O enriched shells on the surface of MA powders. The O enriched shells are harder and more brittle, and difficult in deformation during consolidation, leading to the higher porosity. Besides, the O enriched shells reacted with the grind mediums through oxidation during milling, accelerating the introduction of contamination into the MA powders. The contamination not only contributed to the brittleness of shells through solid solution strengthening, but also resulted in the significantly deterioration of the thermal conductivity. Therefore, reducing the O enriched shells on the particle boundaries is an essential issue to improve the performance of in-situ formed ODS-Cu alloys.

Further decreasing the dispersive Y_2O_3 particle size on the premise of keeping high number density is a promising method to improve the comprehensive performance of dispersion strengthening materials. There are many kinds of parameters which can influence the in-situ formed Y_2O_3 particle size, such as HIP temperature, HIP time, and the concentration of Y element. Controlling the in-situ formed particle size by adjusting the HIP parameters can also influence the other properties of materials, such as density, grain size, number density of defects and so on [1, 2]. The concentration of Y in the Cu matrix can influence the size and distribution of in-situ formed particles. The higher concentration of Y result in the higher diffusivity of Y during HIP process, leading to the larger Y enriched nucleus [3]. Therefore, as a potential method to refine the in-situ formed dispersive particles, optimizing the Y content is expected to modify the comprehensive performance of ODS-Cu alloys.

Furthermore, the commercial ODS-Cu alloys with Al_2O_3 (Glidcop®) have various content of dispersive particles from 0.15 wt. % to 0.6 wt. % [4]. The mechanical strength was further improved with little sacrificing of thermal conductivity for the Glidcop® with 0.15 wt. % Al_2O_3, which demonstrate that the optimum size and number density have much more influence on the mechanical strength than just roughly increase the content of particles.

Therefore, adjusting the Y_2O_3 content was expected an effective method to decrease the contamination and porosity, and further refine the dispersive Y_2O_3 particles, thereby improving the comprehensive performance of in-situ formed ODS-Cu alloys. Because decreasing the content of Y_2O_3 not only can reduce the O enriched shells, including more O and introduced contamination, but also decrease the concentration of Y, thereby refining dispersive particles. In this topic, the Y_2O_3 content for Cu_6Y sourced ODS-Cu was decreased from 1.5 wt. % to 0.5 wt. % under the guidance of Glidcop® with much lower content of particles. The microstructures of consolidated samples, such as thickness of the particle boundary and porosity, the morphology of in-situ dispersive particles, including particle size and number density, and the macro performance of consolidated samples, including tensile strength, elongation and thermal conductivity, were evaluated.

6.2 Experimental procedure

In this topic, the Cu_6Y sourced ODS-Cu alloys with various content of Y_2O_3 from 1.5 wt. % to 0.5 wt. % were fabrication through innovative MA-HIP process by in-situ fabrication method. The compositions of prepared samples are shown in Table 6.1. The blended Cu and Cu_6Y powders were mechanical alloyed for 16 hours with speed of 250 rpm, followed by adding Cu_2O. The mechanically alloyed Cu-Y powders were further milled with Cu_2O powders for additional 16 hours with the same parameters. The milled powders were pulled into the iron capsules. Before clamping, the capsules were degassed for 1 hour to less than 0.1 Pa, followed by welding in the vacuum condition. During the HIP process, the steel capsules, filled with milled powders, were consolidated in the pressure of 150 MPa at temperature of 1000 °C for 2 hours.

Microstructures and morphologies of the consolidated samples with different Y_2O_3 addition were evaluated by XRD apparatus, lase flash apparatuses and scanning electron microscope (SEM, JEOL JSM-5600) equipped with energy dispersive X-ray spectroscopy (EDS). In addition, thin sampling from a part of the MA-HIP processed Cu alloy bulk samples was carried out using the focused ion beam (FIB, Hitachi nano DUE'T NB5000) machine. After that,

nanostructure of the thin FIB samples was observed using scanning transmission electron microscope (TEM, JEOL JEM-2800) equipped with EDS.

Table 6.1 Composition of Cu_6Y sourced ODS-Cu with different Y_2O_3 content. (Total: 100 g)

Sample ID	Samples	Cu	Cu_6Y	Cu_2O
#1.5	Cu-1.5 wt. % Y_2O_3 (Cu_6Y, Middle Cu_2O)	90.91	6.24	2.85
#1.0	Cu-1.0 wt. % Y_2O_3 (Cu_6Y, Middle Cu_2O)	93.94	4.16	1.90
#0.5	Cu-0.5 wt. % Y_2O_3 (Cu_6Y, Middle Cu_2O)	96.97	2.08	0.95

Figure 6.1 The image of lase flash apparatuses.

Thermal conductivity is a key parameter for ODS-Cu alloys. Laser flash analysis is an effective and precise method to measure the thermal diffusivity. And the thermal conductivity can be calculated:

$$\lambda(\mathrm{T}) = a(T) \cdot \rho(T) \cdot C_P(T) \tag{6.1}$$

Where $\lambda(\mathrm{T})$ is the thermal conductivity at temperature of T, $a(T)$ is the thermal diffusivity at T, $\rho(T)$ is the bulk density at T, and $C_P(T)$ is the specific heat of the bulk at T. In this technique, the target samples were heated on bottom surface by the pulse laser, causing a gradient of temperature in the samples. The thermal conductivity was calculated based on the change in temperature with time on the top surface. The thermal conductivity of samples was conducted using Netzsch LFA 457 MicroFlash in NIFS, as shown in Figure 6.1. During this test, the disc

samples with diameter of 12 mm and thickness of 2 mm were coated with graphite paste for three times to ensure efficient observation of the laser energy, then placed in a sealed furnace filled with Ar atmosphere. The gas exchange was conducted for three times to make Ar atmosphere in the chamber. The change in temperature with time was recorded after each laser pulse in order to set the measure point. The four test temperatures (25 °C, 100 °C, 200 °C, and 300 °C) were selected, and three time of the laser-pulse per test temperature were conducted.

6.3 Results and discussion

6.3.1 Characterization of the particle boundaries

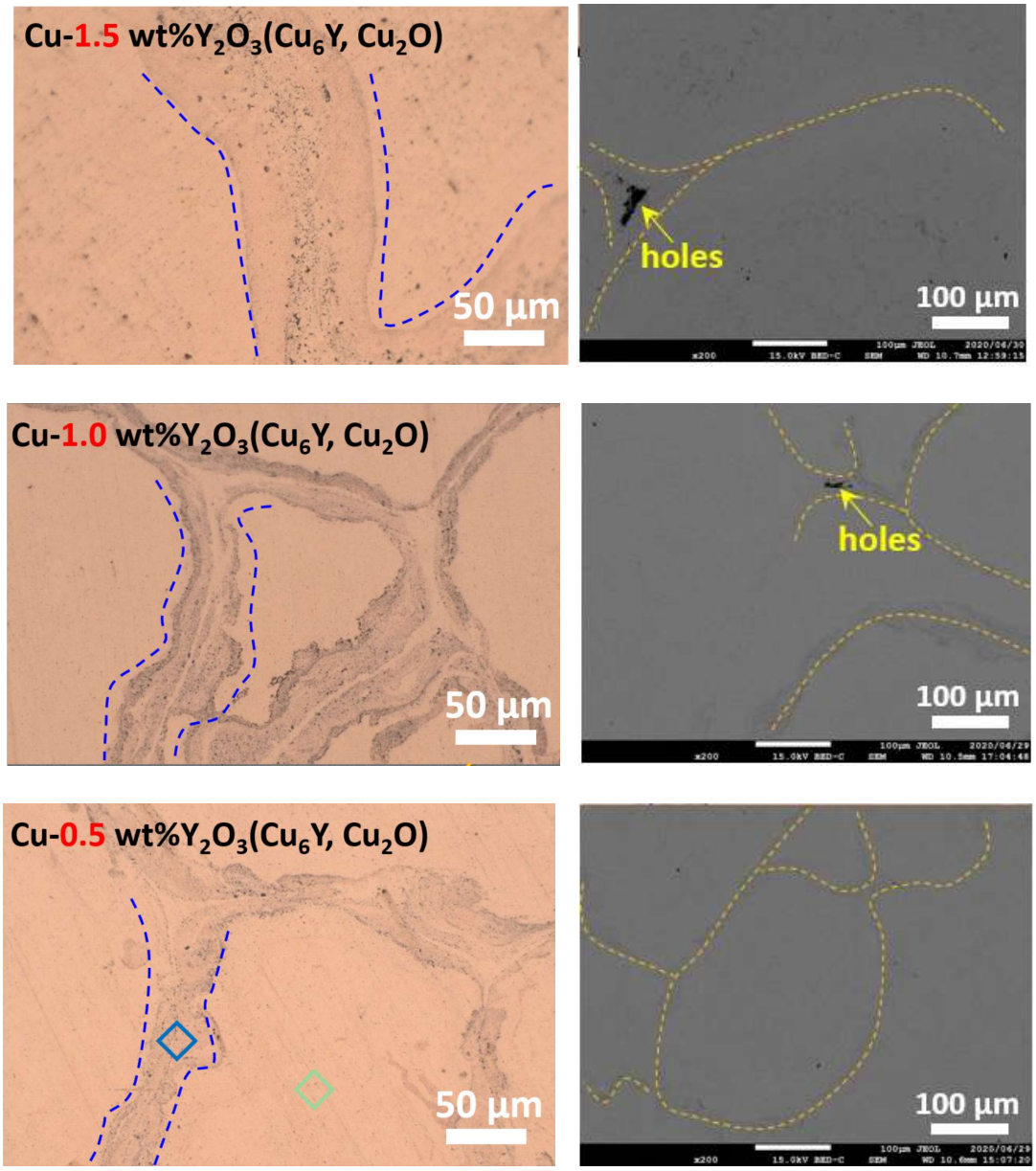

Figure 6.2 The optical images and the SEM images of the Cu_6Y sourced samples with different Y_2O_3 content.

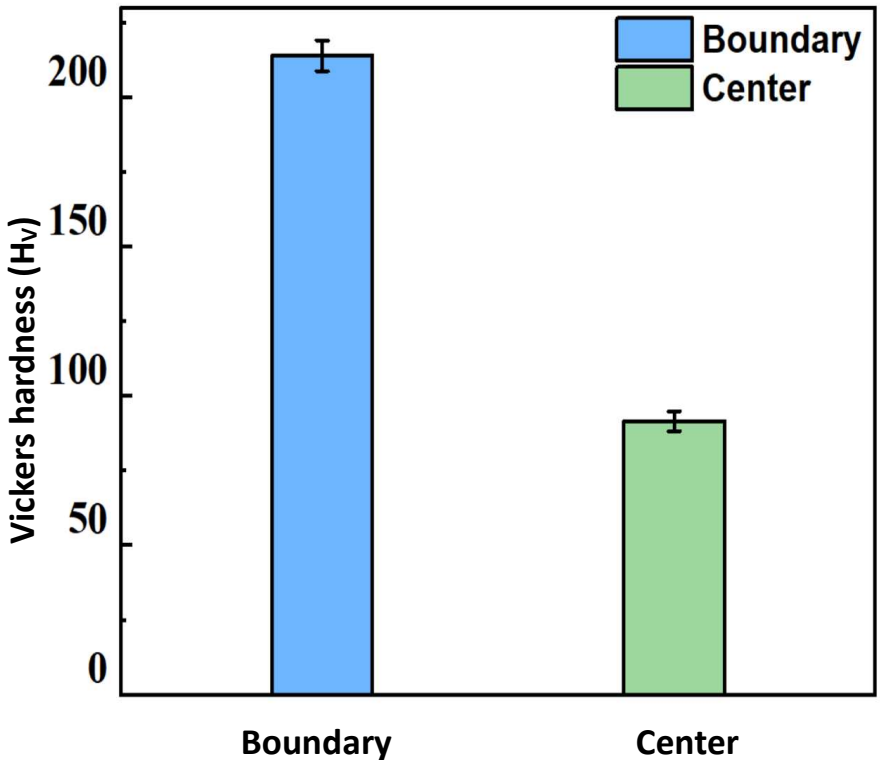

Figure 6.3 The Vickers hardness of 0.5 wt. % sample.

Figure 6.2 shows the morphologies of Cu_6Y sourced samples with decreasing content from 1.5 wt. % to 0.5 wt. % in optical images and SEM images. The clear boundaries in all samples surrounded the central area of the MA powders with more uniform morphologies, and the thickness of the boundaries decreased from 100 μm to 30 μm with the Y_2O_3 content reducing from 1.5 wt. % to 0.5 wt. %. There were holes around the boundaries for the higher content of Y_2O_3 as shown in the SEM images. With the Y_2O_3 content decreasing, the holes were compressed smaller. Figure 6.3 shows that the Vickers hardness of the boundaries was much higher than the central area of MA powders. The reasons of the formation of the O enriched boundaries have been shown in previous chapters. The boundaries were hard and brittle because of the rich O element and contamination. Decreasing the Y_2O_3 content reduced the Cu_2O addition at the middle of MA process, and thereby reducing the introduction of contamination. The layers became thinner, and the MA powders were easier deformed to reduce the holes around the boundary, thereby increasing the relative density. Therefore, reducing the Y_2O_3 content is one of the methods to decrease the boundary layer of MA powders, and reducing the porosity.

6.3.2 Characterization of the Y_2O_3 particles distribution

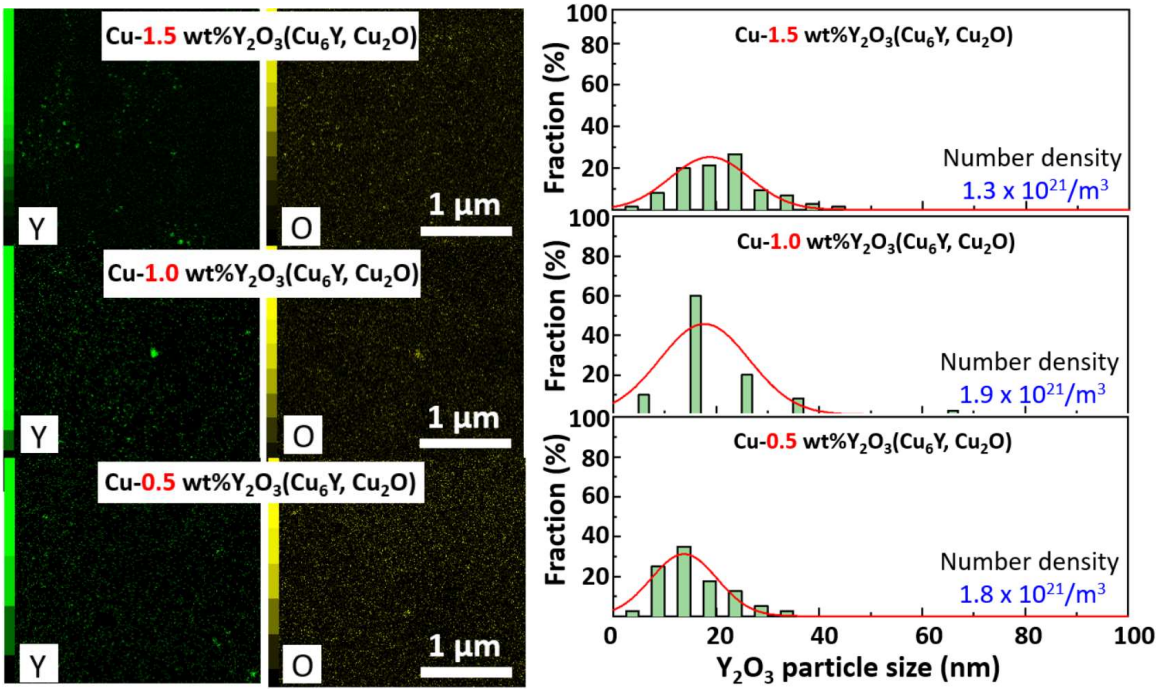

Figure 6.4 TEM-EDS mappings and the statistical size distribution of Y_2O_3 particle for the Cu_6Y sourced samples with different Y_2O_3 content.

Figure 6.4 shows the TEM-EDS mappings and the statistical size distribution of Y_2O_3 particle for the Cu_6Y sourced samples with different Y_2O_3 addition. It should be noted that all samples showed the similar number density of Y_2O_3 particles, and the reducing Y_2O_3 content had little influence on the number density. While the particle size of Y_2O_3 decreased from 19±7 nm to 14±6 nm with the Y_2O_3 content reducing from 1.5 wt. % to 0.5 wt. %. During MA process, the Cu_6Y intermetallic compounds were gradually dissolved into the Cu matrix, and more amount of Cu_6Y reached higher supersaturate solid solution state. Besides, plenty of defects such as dislocations were introduced into the MA powders, and the number density of defects are great influenced by the MA condition [1]. During HIP process, the supersaturate solid solute Y tended to precipitate and nucleate at the defects [2]. Therefore, the number density of in-situ formed dispersive Y_2O_3 particles is great influenced by the nucleation points, instead of the Y precursor content. Lower content of Y precursor formed lower Y concentration after MA process, resulting in the lower dissolubility during HIP process, which contributed to the refinement of Y_2O_3 dispersive particles [3]. That is the reason of Y_2O_3 particles reduced from 19±7 nm to 14±6 with the decrease of Y_2O_3 content from 1.5 wt. % to 0.5 wt. %. Therefore, modifying the MA process and adjusting the Y precursor addition can get the Y_2O_3 dispersive particles with optimum particles size and number density.

6.3.3 Properties evolution

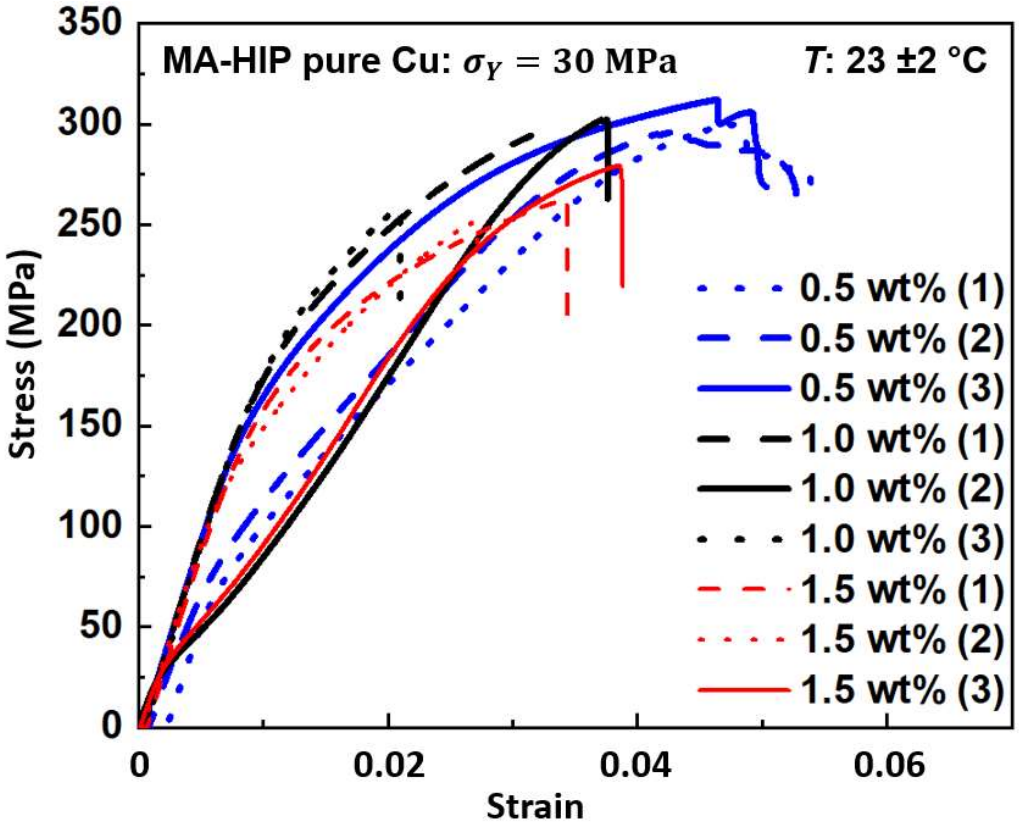

Figure 6.5 The strain-stress curves of Cu_6Y sourced samples with different Y_2O_3 content.

Figure 6.5 shows the strain-stress curves of Cu_6Y sourced ODS-Cu alloys with different Y_2O_3 content from 1.5 wt. % to 0.5 wt. %. All samples showed the similar tensile strength of around 290 MPa. As to the elongation, the samples with 1.5 wt. % and 1.0 wt. % of Y_2O_3 had the same elongation of 4 %, and the sample with 0.5 wt. % Y_2O_3 had better elongation of 5 %. With the decrease of Y_2O_3 from 1.5 wt. % to 0.5 wt. %, the tensile performance was improved. But it should be noted that the tensile test had a certain degree of dispersion, caused by the uneven structure and composition of the ODS-Cu alloys. Further improvement needs to be conducted in future.

In order to analyse the fracture mechanism, the fracture surface of the Cu_6Y sourced samples with different Y_2O_3 addition were observed by SEM, as shown in Figure 6.6. All samples were fractured around the grain boundaries. There were holes circled by yellow dashed lines on the fracture surface. With the increase in Y_2O_3 addition, the porosity decreased very fast, corresponding to the morphology shown in the cross section of bulk samples. Lower content of Y_2O_3 decreased the hard and brittle boundary, thereby easier plastic deformation reduced the porosity. From the larger magnified images, there were large dimples surrounding the large

particles, which contained contaminations. With the decreasing of Y_2O_3 content, the dimples gradually became smaller and lighter, accompanied with the gradually smaller particles with lower contaminations. Reducing the Y_2O_3 content can avoid the aggregation and formation of larger particles, which caused large dimples during tensile test, because of the concentration of dislocation and the mismatch of particles and Cu matrix. Therefore, the reduction of larger particles and porosity contributed the increasing of elongation.

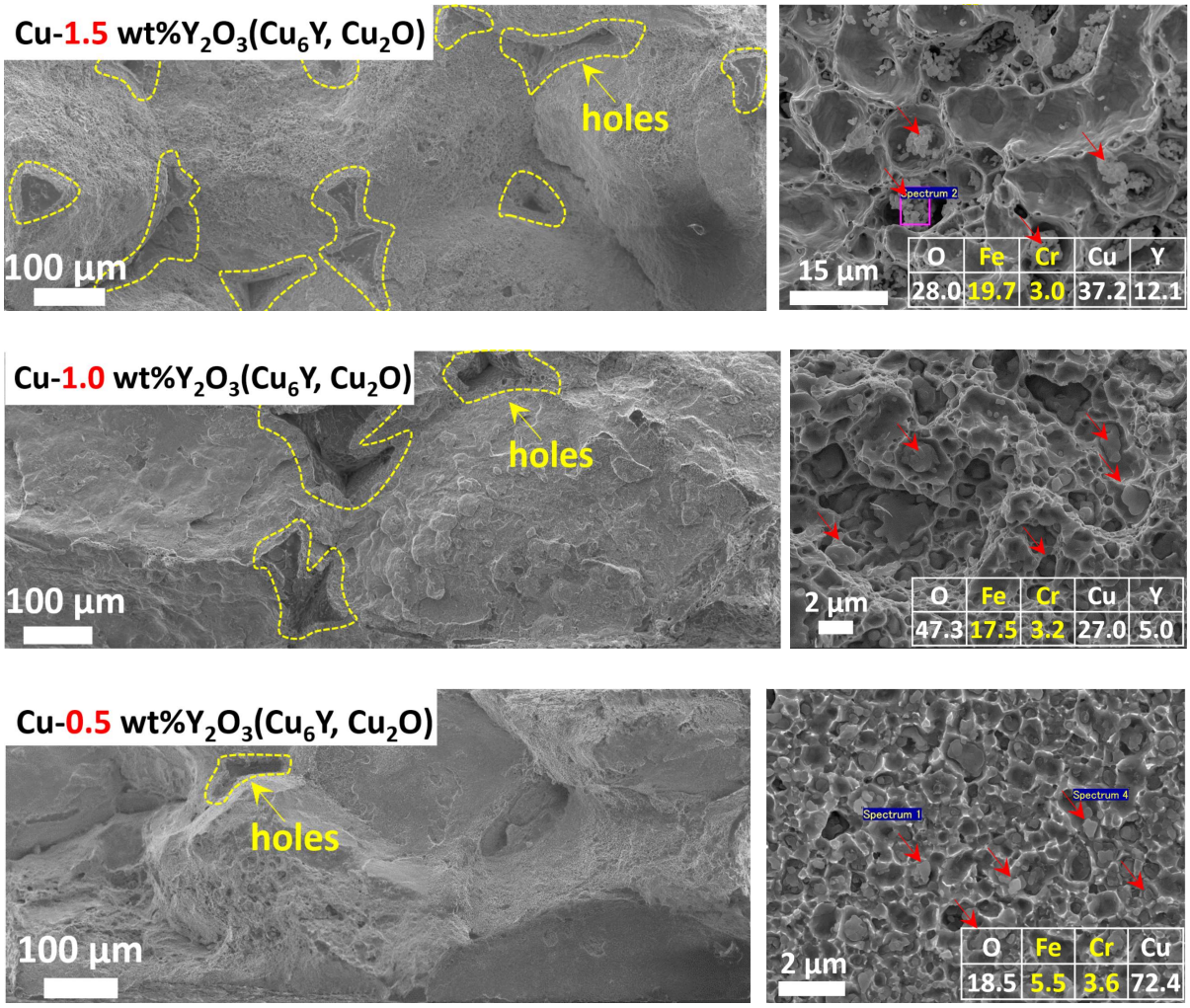

Figure 6.6 The fracture surfaces of the Cu_6Y sourced samples with different Y_2O_3 addition.

In order to explore the contribution of dispersion strengthening for the yield strength of Cu_6Y sourced ODS-Cu alloys, the pure Cu was fabricated by the same parameters (32 hours MA with speed of 250 rpm, and HIP at 150 MPa with temperature of 1000 °C for 2 hours) for comparison. The dispersion strengthening in ODS-Cu alloys follows Orowan by-passing mechanism shown in chapter 1 [5-7]. The formula for ODS-Cu can be describe:

$$\Delta\sigma = M\alpha Gb\lambda^{-1}$$

Where M is the Taylor factor (3.06), α is the coefficient of barrier strength and is estimated to be 0.84 in this case [8-11], G is the shear modulus of Cu (42 GPa), b is the burgers vector magnitude of Cu (0.256 nm), and λ is the average interbarrier distance, which can be described as [12]:

$$\lambda = 1.25\,(Nd)^{\frac{-1}{2}} - \pi d/4$$

Where N and d are the number density and average size of dispersive Y_2O_3 particles, respectively, and are shown in Table 6.2.

Table 6.2 the number density and average size of the dispersive Y_2O_3 particles.

	#1.5	#1.0	#0.5
σ_Y (MPa)	145±5	185±2	160±10
N (10^{21}/m^3)	1.3	1.9	1.8
d (nm)	19±7	17±8	14±6
Increment (Δσ, MPa)	105±20	120±30	107±24

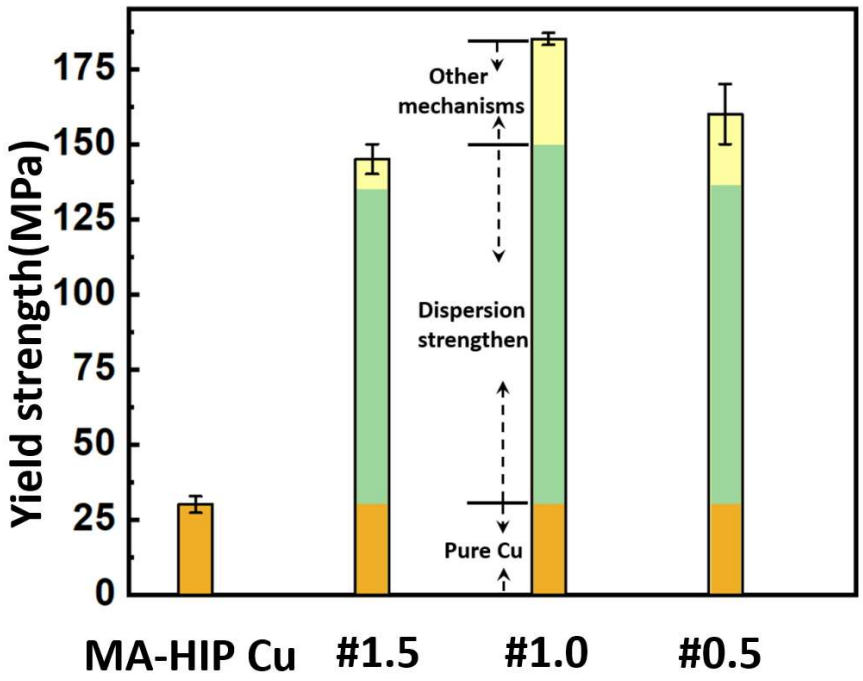

Figure 6.7 Comparison of the experimental yield strength and the calculated values of ODS-Cu alloys and the Pure Cu by same fabrication process.

Figure 6.7 shows the comparison of the experimental yield strength and the calculated values of ODS-Cu alloys and the pure Cu by same fabrication process. The yield strength of pure Cu by MA-HIP were gotten from the tensile test shown in Figure 5.3.10. It was found that the

dispersion strengthening made a great contribution to the improvement of yield strength. The calculated values had good agreement with the measured values, and there was small mismatch, possibly caused by the unoxidized Y and the contamination in the Cu matrix. It should be noted that the improved strength is expected to stable even under elevated temperature and neutron irradiation because of the stable Y_2O_3 particles and the effective sink ability of interfaces for irradiation defects, which have been demonstrated during the research experience of ODS steels. For the ODS-Cu alloys, the samples with 1 wt. % Y_2O_3 had higher strength because of the higher number density and the negligible reduced particles. Besides, the negligible reduced contamination compared to the samples with 1.5 wt. % Y_2O_3 also contribute the higher strength.

Table 6.3 The thermal conductivity of Cu alloys at different temperature (W/m·K).

	#1.5	#1.0	#0.5	Glidcop®	Pure Cu
25 °C	217.4±6.6	243.0±6.6	285.1±3.7	371.8±8.0	397.1±14.7
100 °C	228.1±0.6	251.9±0.7	288.3±0.3	366.5±0.6	386.1±0.4
200 °C	240.0±1.1	259.3±0.7	292.1±1.7	355.0±1.1	373.6±1.2
300 °C	245.7±1.1	262.6±0.6	290.1±0.5	345.4±1.0	357.2±1.9

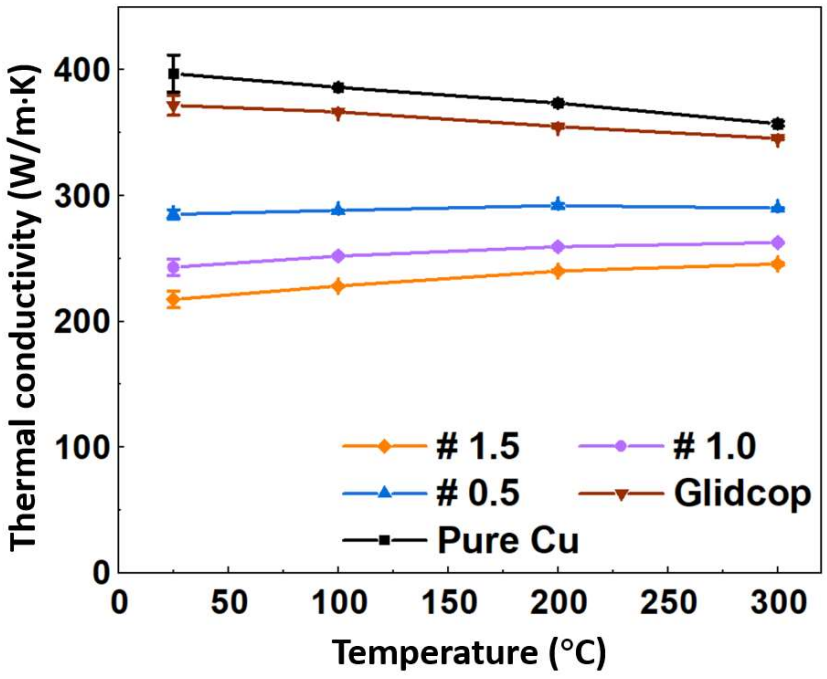

Figure 6.8 Thermal conductivities of pure Cu and ODS-Cu alloys as a function of temperature.

Table 6.3 and Figure 6.8 show the thermal conductivities as a function of temperature from 25 °C to 300 °C for the pure Cu, Glidcop® and Cu_6Y sourced samples with different Y_2O_3 content. As to the influence of test temperature on the thermal conductivity, the thermal

conductivity of pure Cu decreased with the increase in test temperature, because of the higher lattice scattering for free electron at elevated test temperature [13]. For the ODS-Cu alloys, the thermal conductivity increased with the test temperature. The gradient reduced with the decreasing of the dispersive particles content and reached the similar trend with pure Cu at 0.15 wt. % content for Glidcop®. The thermal conductivity of both pure Cu and pure dispersive particles decreased with the increase in test temperature. Considering the uptrend for the Cu and Y_2O_3 composites, the most possible reason is the impurities introduced during MA process. The more impurity, the greater the gradient. This phenomenon was also occurred in the GRCop-84, which is the CuCrNb alloys. Compared to the thermal conductivity of the GRCop-84 with Fe less than 20 ppm being down trend [19]. The thermal conductivity of GRCop-84 with Fe larger than 200 ppm has uptrend. For our samples, more impurity introduced during in-situ fabrication process. That is the reason of great up trend of the thermal conductivity with the test temperature. Compared to the pure Cu with 357 W/m·K and Glidcop® for 0.15 wt. % Al_2O_3 with 345 W/m·K at 300 °C, the Cu_6Y sourced samples had lower thermal conductivity of 290 W/m·K for 0.5 wt. % Y_2O_3, and 245 W/m·K for 1.5 wt. % Y_2O_3. Considering that the Fe impurities have great influence on the electrical resistivity of Cu matrix (115 nΩm/wt. %) [14], the deterioration of thermal conductivity for in-situ formed samples was mainly caused by the Fe impurities during MA process and the boundary of the MA powder. The prohibiting the introduction of Fe contamination through modifying the MA process is expected to much improve the thermal conductivity of Cu_6Y sourced ODS-Cu alloys.

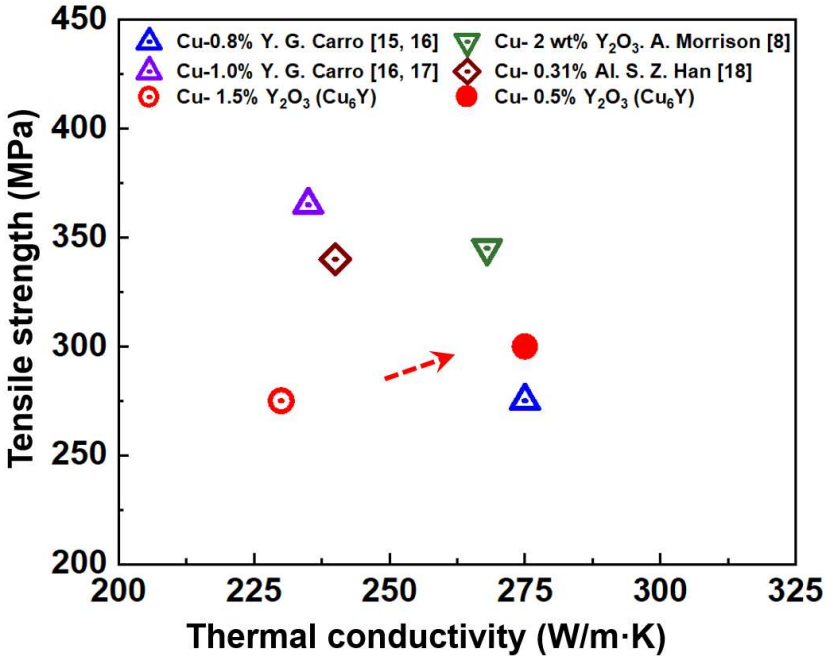

Figure 6.9 The tensile strength and the thermal conductivity of ODS-Cu alloys with Y_2O_3 [12-16].

Figure 6.9 summarizes the tensile strength and the thermal conductivity of ODS-Cu alloys developed in the worldwide. The bigger circle represent the Cu_6Y sourced ODS-Cu alloys fabricated by our laboratory through innovative MA-HIP process by in-situ fabrication method. It should be noted that the advantages of in-situ formed samples is not obvious, although much finer and higher density of dispersive Y_2O_3 particles were formed. This was because the plastic deformation and the followed fracture always started around the particle boundaries before the dispersion strengthening. Besides, extra contamination introduced by the oxidization of the oxidant great influenced the thermal conductivity of in-situ formed samples. Therefore, the Cu_6Y sourced ODS-Cu alloys by in-situ fabrication method have larger potential for improvement once further suppress the growth of MA powders and the introduction of contamination.

6.4 Conclusions

In order to reduce the introduction of contamination, and refine the dispersive Y_2O_3 particles, reducing the Y_2O_3 addition from 1.5 wt. % to 0.5 wt. % for Cu_6Y sourced ODS-Cu was investigated. The main results were shown as follows:

(1) Reducing the Y_2O_3 addition actually decreased the particle boundaries, thereby reducing the porosity.

(2) Reducing the Y_2O_3 addition had little influence on the number density of the Y_2O_3 but reduced the particle size.

(3) The large particles on the particle boundaries induced the dislocation concentration and the premature micro cracks, deteriorating the tensile performance. Reducing the Y_2O_3 content avoided the aggregation of larger particles around the boundary.

(4) Reducing Y_2O_3 content was also good for the thermal conductivity. The thermal conductivity and mechanical performance can be further improved for Cu_6Y sourced sample once reduce the introduction of contamination and suppress the growth of MA powders during MA process.

References:

[1] C. Suryanarayana. Mechanical alloying and milling, Progress in Mater Sci, 2001 1-168.

[2] C. Suryanarayana. Mechanical Alloying: A Novel Technique to Synthesize Advanced Materials. Research Volume 2019, Article ID 4219812.

[3] D. S. Zhou, X. K. Wang, W Zeng, C. Yang, H. C. Pan, C. G. Li, Y. J. Liu, D. L. Zhang. Doping Ti to achieve microstructural refinement and strength enhancement in a high volume fraction Y_2O_3 dispersion strengthened Cu. Journal of Alloys and Compounds 753 (2018) 18-27.

[4] https://www.hoganas.com/en/powder-technologies/glidcop/.

[5] Y. Liu, S. Kondo, H. Yu, K. Yabuuchi and R. Kasada. Statistical Approach for Understanding the Effect of Specimen Size on the Yield Stress and Its Scattering in Mechanically-Alloyed Cu and ODS-Cu Obtained by Micro-Pillar Compression Test. Materials Transactions, Vol. 61, No. 5 (2020) pp. 955-962.

[6] S. Nachum, N.A. Fleck, M.F. Ashby, A. Colella, P. Matteazzi. The microstructural basis for the mechanical properties and electrical resistivity of nanocrystalline Cu–Al_2O_3. Materials Science and Engineering A 527 (2010) 5065–5071.

[7] M. S. Nagorka, G. E. Lucas, and C. G. Levi. Novel Oxide-Dispersion-Strengthened Copper Alloys from Rapidly Solidified Precursors: Part 2. Creep Behavior. Metallurgical and Materials Transactions A. Volume 26A 1995—873.

[8] A. Morrison. Powder based processing of novel dispersion strengthened copper alloys for fusion applications [D]. Trinity, University of Oxford. 2017.

[9] S. M. S. Aghamiri, N. Oono, S. Ukai, R. Kasada, H. Noto, Y Hishinuma and T. Muroga. Microstructure and mechanical properties of mechanically alloyed ODS copper alloy for fusion material application. Nuclear Materials and Energy, 15, (2018), 17-22.

[10] H. O. Zhuo, J. C. Tang, N Ye. A novel approach for strengthening Cu–Y_2O_3 composites by in situ reaction at liquidus temperature. Materials Science & Engineering A 584 (2013) 1–6.

[11] J. Groza. Heat-Resistant Dispersion-Strengthened Copper Alloys. Journal of Materials Engineering and Performance Volume 1(1) February 1992—113.

[12] T. Muroga, H. Watanabe, N. Yoshida, H. Kurishita, M.L. Hamilton. Microstructure and tensile properties of neutron irradiated Cu and Cu-5Ni containing isotopically controlled boron. Journal of Nuclear Materials 225 (1995) 137-145.

[13] K. Frobose and J. Jackle. On the temperature dependence of the electrical resistivity of amorphous metals. J. Phys. F: Metal Phys. Vol. 7. No. 11. 1977.

[14] H. Pops. The role of the conductor in the manufacture and performance of magnet wire. IEEE Elec. Insul. Mag. 11 (5) (1995) 17–23.

[15] G. Carro, A. Muñoz, B. Savoini, M.A. Monge. Fabrication and characterization of dispersion strengthened Cu-0.8%Y. Fusion Engineering and Design 154 (2020) 111548.

[16] G. Carro, A. Mu˜noz, M.A. Monge, B. Savoini, A. Galatanu, M. Galatanu, R. Pareja. Thermal conductivity and diffusivity of Cu-Y alloys produced by different powder metallurgy routes. Fusion Engineering and Design 124 (2017) 1156–1160.

[17] G. Carro, A. Muñoz, B. Savoini, M.A. Monge, R. Pareja, Processing, microstructure and mechanical characterization of dispersion strengthened Cu-1%Y, Fusion Engineering and Design, 138 (2019) 321-331.

[18] S. Z. Han, H. Joh, J. H. Ahn, J. Lee, S. M. Kim, S. H. Lim, Y. G. Son. Ti-added alumina dispersion-strengthened Cu alloy fabricated by oxidation. Journal of Alloys and Compounds 622 (2015) 384–387.

[19] Robert P. Minneci, Eric A. Lass, Jeffrey R. Bunn, Hahn Choo & Claudia J. Rawn (2021) Copper-based alloys for structural high-heat-flux applications: a review of development, properties, and performance of Cu-rich Cu–Cr–Nb alloys, International Materials Reviews, 66:6, 394-425.

Chapter 7. Key issues for further improvement

In this doctoral thesis, ODS-Cu alloys with Y_2O_3 were fabricated through innovative MA-HIP process by in-situ fabrication method. The fabrication parameters, various Y precursors were investigated to enhance the uniform distribution of Y elements, refine the dispersive Y_2O_3 particles, and reduce the introduction of contamination. The in-situ fabrication method developed in this research can effective refine the dispersive Y_2O_3 particles. However, there are still some remain issues need to be improved, including further reducing the introduction of contamination, suppressing the growth of MA powders, and further increasing the number density of fine Y_2O_3 particles.

7.1 Further reducing the contamination

Mechanical alloying is an effective powder processing technology, in which the materials were repeated fracturing, cold welding. The supersaturated solid solution state can form, and break the solubility shown in the phase diagram. However, the contamination was inevitably introduced into the MA powders. There are two main sources of contamination during MA process. One is from atmosphere and can be prevented by inert gas applied in this research. The other is from the grind mediums. The contamination is introduced into the MA powders by abrasion through collision between MA powders and grind mediums, and by chemical reaction between grind mediums and the blend powders. During in-situ fabrication process, the middle added Cu_2O can form O rich layers on the surface of MA powders, this O rich layers can oxidize the grind mediums, accelerating the introduction of contamination. Even reducing the contamination through decrease the Y_2O_3 content, further improvements need to be developed.

7.1.1 Coating the grind mediums

Coating the grind mediums by Cu is an effective method to prevent the direct contact between grind mediums and MA powders [1]. This method can avoid both the abrasion and chemical reaction. There are several methods to coat the grind mediums by Cu.

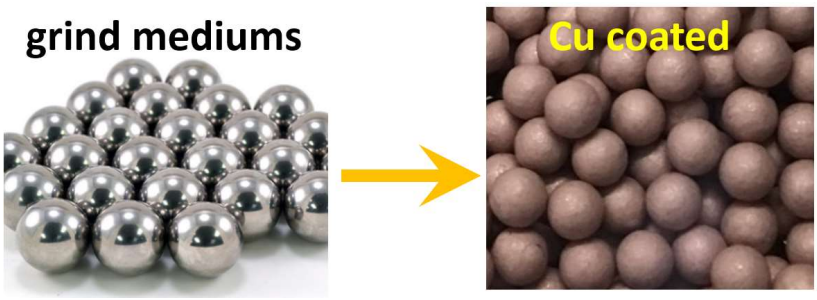

Figure 7.1 Coating the grind mediums by pre milling.

First, coating the grind mediums by pre milling before mechanical alloying using pure Cu to clean and coat the grind mediums. This is a sample method to coat the grind mediums by Cu. But this Cu coat can be peeled off from the grind mediums during the follow milling. This peeled Cu coat will be able to prevent the Fe contamination into the ODS-Cu. Therefore, how to avoid the Cu coat from peeling off is an important point need to be improved.

Second, coating the grind mediums by Cu through coating technology, such as spraying and deposition. The key parameter is the bendability of the coating to the grind mediums.

7.1.2 Novel grind mediums

Exploring novel material for grind mediums is also an effective method to suppress the introduction of contamination. Currently, the stainless steel was used as the grind mediums in this research. The Mohs hardens of steel is around 3.5~4.0. The materials with higher Mohs hardness have better abrasion resistance. Besides, from the Cu-Fe phase diagram, it can be found that Fe has larger solid solubility in Cu matrix at higher temperature (600 ~ 1080 °C). It is possible to form supersaturate solid solute condition during the actual smelting process, and the solid solute Fe in Cu matrix had huge influence on the electrical resistivity (115 nΩm/wt. %), thereby deteriorating the thermal conductivity.

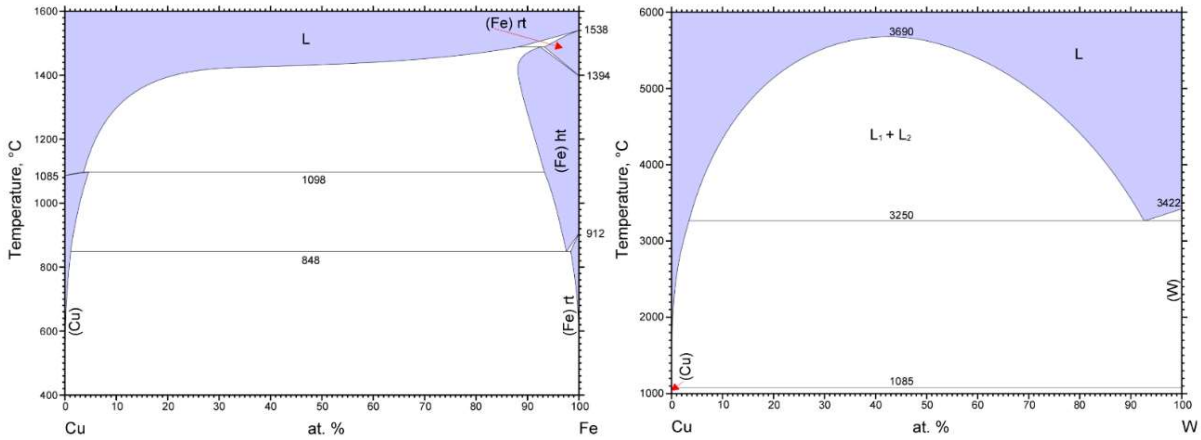

Figure 7.2 Cu-Fe phase diagram and Cu-Y phase diagram.

Compared to steel grind mediums, the tungsten (W) is more promising material of grind mediums because of the several obvious advantages following as, (1) compared to the steel with Mohs hardness of 4.0 ~ 5.4, the Mohs hardness of W is 9.0, which is the hardest metal in all metals. Hard grind mediums can suppress the introduction of contamination by abrasion, which is one of the mechanisms of the contamination, (2) it can be found that there is no solid solution state from the Cu-W phase diagram, and W is insoluble in Cu matrix. The insoluble W in Cu matrix is good for the purity of Cu matrix. There is little influence on the thermal conductivity of Cu even introduced trace W element, and also (3) high dense W can accelerate the MA process. During MA process, the kinetic energy of the grind balls transfer to MA powders through collision, resulting in the fracture and cold welding of MA powders. The higher kinetic energy per collision can accelerate the MA process. During MA process, the energy transfer from grind ball to MA powders can be calculated by the follow equation:

$$\mathrm{E} = \frac{1}{2} M_b V_c^2$$

Where M_b is the mass of grind balls, V_c is the relative velocity. Larger mass of grind ball can accelerate the MA process. W has the much higher density compared to steel. Therefore, choosing the tungsten as the grind ball material is expected to increase the efficiency of every collision and accurate the MA process.

7.1.3 Modifying the oxidation mode

Compared to the common phenomenon of abrasion, chemical reaction between grind mediums and oxidant is a special issue for the in-situ fabrication process, in which the O rich layer can not only oxidize the Y precursor in the MA powders, but also oxidize the grind mediums, accelerating the introduction of contamination. Therefore, changing the oxidation mode to suppress the chemical reaction is an effective method to reduce the introduction of contamination. There are several methods to modify the oxidation mode. Frist, optimizing the oxidant addition timing to reduce both the chemical reaction and prevent the premature formation of Y_2O_3. Second, modifying the oxidant from Cu_2O to oxygen gas. This method is expected to enhance the uniform distribution of O. Besides, as the potential oxidant for in-situ fabrication process, pure H_2O is expected to use as both oxidant and process control agent. During MA process, the H_2O can react with the Y precursors, while do not react with the Cu. The redundant H_2O can be removed by heat treatment with vacuum condition.

7.2 Suppressing the growth of MA powders

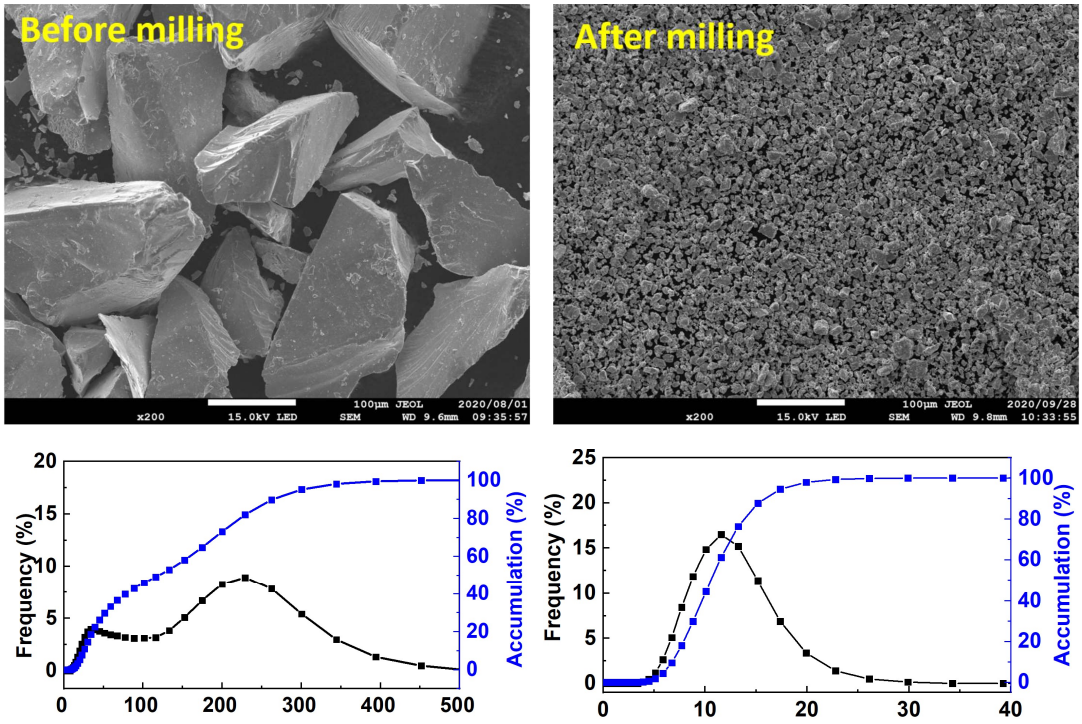

Figure 7.3 The morphologies and size distribution of Cu_6Y after hand crash (left) and after ball milling (right).

Suppressing the growth of MA powders is also an important issue need to be modified. There are several disadvantages of the growth of MA powders. First, the growth of MA powders is not conducive to the uniform distribution of Y and O elements. From the previous research, it was found that the consolidated samples even after 32 hours' high-speed milling still has clear strips in SEM-BSE images, which caused by the uneven distribution of Y and O elements. The middle added Cu_2O always formed the O rich layer on the surface of the MA powder. Second, the growth of MA powders is not conducive to the MA process. The outer area of the MA powders was over alloyed, but the inter area of the MA powders still under alloyed. Third, considering that all samples were fracture around the particle boundary during tensile test, suppressing the growth of MA powders and reduce the particle boundary is an effective method to improve the tensile performance. At the particle boundary, there are more contamination, and defects, which can harden the particles boundaries. The existence of macro holes at the contact corner and the non-dense junction between MA powders result in the premature fracture of samples around the particles boundaries. Considering that the MA powders grow up with the MA time, accelerating the MA process and shorten the MA time under the promise of full alloyed is an effective method to suppress the growth of MA powders. Besides, MA process is also the Y dissolution process. Cu_6Y compound is more fragile during milling

because of its brittleness. Figure 7.3 showed the Cu_6Y compound after hand crush, and the Cu_6Y compound after MA for 5 hours. From the size distribution, it can be found that the average size of Cu_6Y compound were refined easily from 200 μm to 10 μm. The pre-refining the Cu_6Y compound to reach nano scale is expected to promote the MA treatment and suppress the growth of MA powders.

7.3 Increasing the number density of finer Y_2O_3

The particles size number density of dispersive particles is the key parameter for the dispersion strengthening. The motivation of the research in this doctoral thesis is refine the dispersive Y_2O_3 particles through innovative MA-HIP process by in-situ fabrication method. Compared to the ODS-Cu alloy by conventional MA-HIP process, in which the dispersive particles size is around 73 nm, ODS-Cu alloys by in-situ fabrication method formed much smaller dispersive Y_2O_3 particles with size of 19 nm. The number density was increased one order of magnitude from 10^{20} /m^3 to 10^{21} /m^3. However, compared to the ODS-Cu alloy with Al_2O_3 by internal oxidation method, which formed Al_2O_3 particles with size of 6-9 nm and number density of 10^{22} /m^3, the ODS-Cu alloys with Y_2O_3 by in-situ fabrication method still need to be improved. There are several methods to refine the Y_2O_3 particles and increase the number density. First, considering that the formation of Y_2O_3 in in-situ fabrication method is relate to the nucleation points, increasing the nucleation points by enhance the mechanical alloying is one of the methods to improve the number density of Y_2O_3 dispersive particles. Second, the particles size also influenced by particle/matrix interfacial energy and the diffusivity of the alloying elements. Doping the Y_2O_3 with minor alloying elements is also an important method to refine the Y_2O_3 and increase the number density. Previous research on ODS materials with Y_2O_3 (including ODS steel, ODS-Cu and so on) found that the alloying elements can effectively refine the particle size and increase the number density, thereby improving the mechanical performance. That because the alloying elements can facilitate the precipitation of dispersive phase and modify the particle/matrix interface structure. Among the various doping alloying elements, Ti is an essential element to transfer the dispersive Y_2O_3 particle to the complex, stable and smaller Y_2TiO_5/$Y_2Ti_2O_7$ particles. Ti can promote the nucleation of Y containing oxide particles by increasing the coherency of the particle with the Cu matrix, forming lower energy interfaces, which are beneficial to the formation of smaller and semi-coherent Y-Ti-O nanoclusters [2]. Figure 7.4 showed the stress-strain curves of the ODS-Cu alloys with Y_2O_3 by conventional MA-HIP process with or without doping Ti element. It was found that compared to ODS-Cu alloys without doped Ti, the tensile strength of ODS-

Cu alloys with Ti were much improved. Therefore, the combination of in-situ fabrication and the doping method are expected to fabricate the finer dispersive Y-Ti-O particles with high number density similar with Glidcop®, and more stable than Al_2O_3 used in Glidcop® as shown in Figure 7.5.

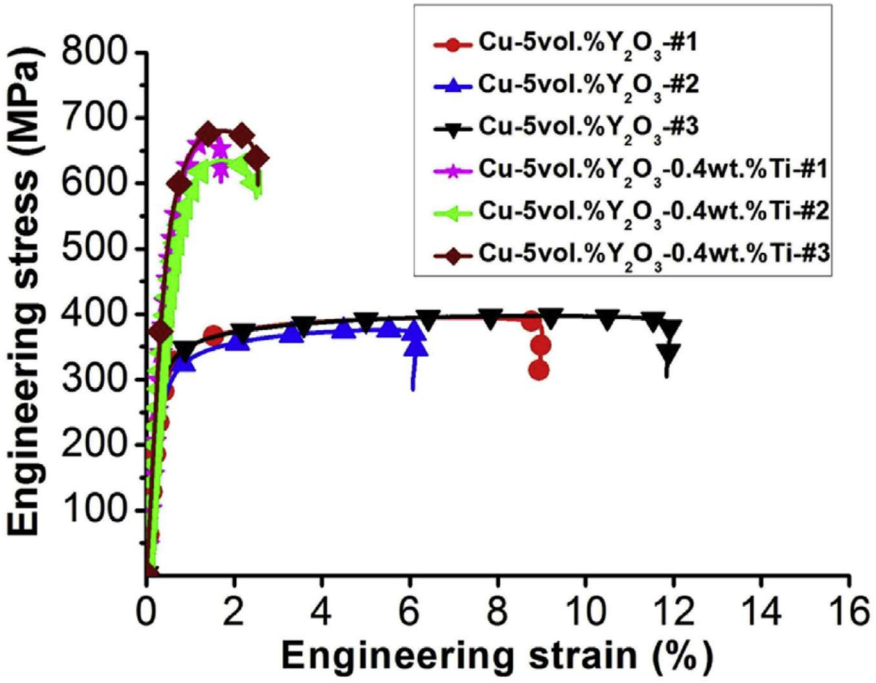

Figure 7.4 Tensile stress-strain curves of the extruded ODS-Cu alloys [2].

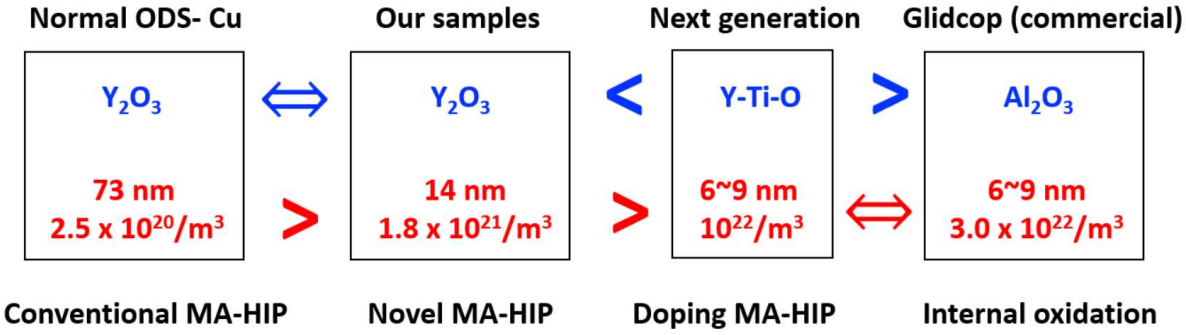

Figure 7.5 The development route of ODS-Cu alloys.

References:

[1] S. J. Hwang. Compressive yield strength of the nanocrystalline Cu with Al_2O_3 dispersoid. Journal of Alloys and Compounds 509 (2011) 2355–2359.

[2] D. S. Zhou, H. W. Geng, W. Zeng, D. Q. Zheng, H. C. Pan, C. Kong, P. Munroe, G. Sha, C. Suryanarayana, D. Zhang. High temperature stabilization of a nanostructured Cu-Y_2O_3 composite through microalloying with Ti. Materials Science & Engineering A 712 (2018) 80–87.

Chapter 8. Conclusions

In order to fabricate the high strengthened ODS-Cu alloys with fine dispersive Y_2O_3 particles with high density, an innovative MA-HIP process based on in-situ fabrication method was developed using the pure metal Y and the Cu-Y compounds as the Y source to form Y_2O_3 particles. Based on the Y distribution, morphology of the dispersive Y_2O_3 and the concentration of Fe impurities obtained, the influence of fabrication parameters (HIP temperature from 850 °C to 950 °C, MA time from 32 h to 96 h) on ODS-Cu alloys, and the mechanism of size distribution for MA powders was investigated based on the pure metal Y sourced samples. Then, the possibility of Cu-Y intermetallic compounds (Cu_2Y and Cu_6Y) as the source of Y_2O_3 and the influence of Cu_2O as the oxidant were investigated. Furthermore, comparison among the ODS-Cu with different kinds of Y_2O_3 sources was carried out for comparison. Finally, the effect of reduction of the Y_2O_3 content from 1.5 wt. % to 0.5 wt. % to suppress the introduction of contamination for Cu_6Y sourced sample was investigated. The main conclusions were shown as follows:

(1) Y_2O_3 was successfully formed by this innovative in-situ fabrication method. For the samples consolidated at different HIP temperatures, the enhanced diffusivity of Y and O in Cu matrix at elevated temperature improved the correspondence between Y and O, promoting the in-situ formation of Y_2O_3. Besides, the increase in HIP temperature decreased the number density of the micro holes, corresponding to the increase in relative density from 95.8 % to 98.9 %. Elevated HIP temperature is effective to enhance the in-situ formation of Y_2O_3 and decrease the porosity of ODS-Cu. While the clear stripe images observed in all samples indicated that distribution of elements was not yet uniform.

(2) The MA time were prolonged from 32 to 96 hours in order to enhance the uniform distribution of the elements. It was found that extending MA time enlarged the lattice parameter of MA powders from 3.596 Å to 3.6158 Å, because of the increase in Y solid solubility, resulting in the increase in Vickers hardness of MA powders from 100 Hv to 380 Hv. Extending MA time can enhance the uniform distribution of the elements, while introducing more Fe impurities because of the abrasion between MA powders and grind mediums.

(3) The analysis of the size evolution of MA powders during MA process showed that the Y and CuO addition can suppress the growth of MA powders. The coarse MA powders ($d > 200$ μm) with shell structure occupied 80 wt. % of all MA powders. The shell of coarse MA

powders had larger Vickers hardness of 325 Hv and higher oxygen content of 20 at. %, similar to the fine MA powders. On the other hand, the central area of coarse MA powders had an atomic ratio of Y and O being 2:3, same as the atomic ratio of Y_2O_3. Combing the morphology by SEM and diffraction patterns by TEM, the peeled Cu-Y-O fragments from the coarse MA powders were found to be the main source of finer MA powders, which had great influence on the thermal conductivity. Filtering out the fine MA powders before HIP, removing the O-enriched component, was expected to improve the properties of the consolidated materials after HIP.

(4) The possibility of using Cu-Y compounds (Cu_2Y or Cu_6Y) as the source of Y_2O_3 were investigated. For the Cu-Y compounds sourced ODS-Cu without oxidant, the Y distribution in Cu_6Y sourced sample was more uniform than that in Cu_2Y sourced sample at lower Y content (0.39 wt. %). The XRD results and thermodynamic analysis showed that Y_2O_3 were successfully formed because of the oxidation of Y by the desorbed O impurity in the Cu matrix. The Cu-Y compounds can purify the Cu matrix in some degree. This method can broaden the selection of dispersive particles during ODS-Cu fabrication using Cu-containing intermetallic compounds. On the other hand, most of the unoxidized Y were aggregated and precipitated during HIP for Cu-Y sourced samples with higher Y content (2.36 wt. %), because of the elevated HIP temperature being 1000 ℃ which was higher than the melting point of 927 ℃ for Cu_6Y, resulting in the aggregation phases during cooling process. For the sample with Cu_2O addition, the Cu_6Y compounds were oxidized at 847 ℃ before melting, forming fine dispersive Y_2O_3 particles with typical size of 15 nm and higher number density of $1.7 \times 10^{21}/\mathrm{m}^3$. Therefore, adding oxidant is feasible and necessary to oxidize all Cu_6Y before melting during in-situ fabrication process.

(5) For the ODS-Cu with 1.5 wt. % Y_2O_3, the comparison among direct Y_2O_3 sourced sample, pure metal Y sourced sample with oxidant, and Cu_6Y sourced sample with oxidant were conducted. The morphology and size evolution showed that the increase in the addition of the brittle Cu_6Y can enhance Y dissolution and suppress the growth of MA powders. Smaller (19±7 nm) with higher number density ($1.8 \times 10^{21}/m^3$) Y_2O_3 particles were formed in Cu_6Y sourced samples, compared to the direct Y_2O_3 sourced sample with larger Y_2O_3 particles (73±33 nm) in lower number density ($2.5 \times 10^{20}/m^3$) and the ODS-Cu fabricated by the worldwide peers. The finer Y_2O_3 particles formed by Cu_6Y contributed to about 100 MPa to the increase of yield strength calculated based on Orowan mechanism. The calculated value had good agreement with the measured value, and there was small mismatch, possibly caused by the unoxidized Y

and the contamination in the Cu matrix. It should be noted that the improved strength is expected to stable even under elevated temperature and neutron irradiation because of the stable Y_2O_3 particles and the effective sink ability of interfaces for irradiation defects. On the other hand, the Y and Cu_6Y sourced samples by in-situ fabrication method had more Fe impurities, because of the oxidation of milling balls by O-rich surface layers of MA powders, which were formed when added oxidant at the middle of MA process. More Fe impurities increased and harden the surface layer of MA powders, introducing holes, thereby deteriorating the elongation of the ODS-Cu alloys.

(6) Reducing the Y_2O_3 content from 1.5 wt. % to 0.5 wt. % were carried out, and it was found that lower Y_2O_3 content is beneficial to decrease Fe impurities, and to reduce the thickness of the Fe accumulated boundaries and porosity, and thus improving ductility. Besides, reducing Y_2O_3 content is also good for the thermal conductivity.

(7) It should be noted that Cu_6Y sourced sample with fine Y_2O_3 in high number density has larger potential for future application once the Fe impurities and holes are reduced by modifying the grind mediums and oxidant addition. For grind mediums, coating the steel mediums with Cu or using tungsten mediums is expected to be an effective method to reduce the impurity. W with extremely high Mohs hardness is insoluble in Cu matrix, which is beneficial to the purity of Cu matrix. As for oxidant addition, modifying the oxidant form, content, and oxidation methods, such as oxidation by air, are also feasible and necessary to suppress the introduction of impurities.

In summary, the MA-HIP process of Y / Cu-Y sourced ODS-Cu by in-situ fabrication method were investigated to enhance the uniform distribution of Y, to form finer dispersive particles and to prevent the introduction of impurities. The results provided references for the future development of outstanding heat sink materials for fusion application.

Publication of the peer reviewed academic papers

(First author)

1. **B. Ma**, B. Huang, Y. Hishinuma, H. Noto and T. Muroga. “Influence of HIP Temperature on Yttria Dispersed Copper Alloys During In-Situ Fabrication Process”. Proceeding of the 10th international conferences devoted to advanced materials and processing (PRICM 10), (2019), p.626- 632.

2. **B. Ma**, Y. Hishinuma, Y. Shimada, H. Noto et al. “The size dependence of microstructure and hardness of MA powders for the MA-HIP processed Cu-Y_2O_3 dispersion-strengthened alloys”. Nuclear Materials and Energy, vol. 24, August, (2020), 1007732, p.5. https://doi.org/10.1016/j.nme.2020.100773.

3. **B. Ma**, Y. Hishinuma, H. Noto, Y. Shimada and T. Muroga. “Development of Y_2O_3 dispersion strengthened Cu alloy using Cu_6Y and Cu_2O addition through the MA-HIP process”. Fusion Engineering and Design, vol. 161, December, (2020), 112045, p.7. https://doi.org/10.1016/j.fusengdes.2020.112045.

4. **B. Ma**, Y, Hishinuma, H. Noto, T. Muroga. “Influence of Cu-Y compound content on the microstructure of Cu-Y_2O_3 dispersion strengthened alloys synthesized by MA and HIP process”. Plasma and Fusion Research., vol. 16, 2405053, (2021), p.4. https://doi.org/10.1585/pfr.16.2405053.

Publication of the peer reviewed academic papers

(Co-authors)

1. Y. Shimada, M. Kazukawa, Y. Hishinuma, K. Ikeda, H. Noto, **B. Ma**, M. Takeguchi, T. Muroga and T. J. Konno, “Multiscale structural characterization of yttria dispersed copper alloys fabricated by hot isostatic processing of mechanically alloyed powders”, Materialia, vol. 14, December, (2020), 100892, p.5. https://doi.org/10.1016/j.mtla.2020.100892

2. Y. Shimada, M. Mizumoto, Y. Hishinuma, K. Ikeda, K. Yoshida, H. Noto, **B. Ma**, T. Muroga, Y. Nagai and T. J. Konno, “Microstructural changes of oxide dispersion strengthened copper powders fabricated by mechanical alloying”, Fusion Engineering and Design, vol. 173, December, (2021), 112804, p.5. https://doi.org/10.1016/j.fusengdes.2021.112804

Acknowledgments

This doctoral thesis was completed under the guidance of my supervisors: Associate Prof. Yoshimitsu HISHINUMA, Assistant Prof. Hiroyuki NOTO, and Prof. Takeo MUROGA. It cannot be completed without the guidance of any one of my supervisors.

My deepest gratitude goes firstly to my supervisor, Associate Prof. Yoshimitsu HISHINUMA, who always support me concerned with doctoral research due to his professional knowledge and experience and my living in Japan. The great energy has been devoted to teaching me the experimental operation, analysis techniques, and guiding the preparation of this doctoral thesis.

Great Thanks go to my vice supervisor, Assistant Prof. Hiroyuki NOTO, who taught me the detail operation of every experiment which I did not know and encouraged me when I met trouble in my research works. Besides, he also taught me how to make presentation, how to show my research to the peers clearly.

Great gratitude also goes to my vice supervisor, Prof. Takeo MUROGA, who guided very key point of my research from the overall perspective based on his profound knowledge and rich research experience. Despite of the busy schedule, comments and suggestions on my research always fed back to me timely.

I would like to extend my acknowledgement to Prof. Suguru MASUZAKI, Prof. Takuya NAGASAKA, Prof. Izumi MURAKAMI, and Assistant Prof. Yukinori HAMAJI. They always give me professional suggestions and comments to improve my research works. Much thanks to Mr. Daisuke NAGATA for his contribution on the TEM analysis and sample preparation by FIB. I also extend thinks to the other members in the fusion systems division in NIFS for their contribution to this study. Besides, Prof. Nagato YANAGI, Prof. Katsuji ICHIGUCHI, Prof. Katsuyoshi TSUMORI, Prof. Masaki OSAKABE in NIFS, Prof. Kenji MATSUDA in University of Toyama, Associate Prof. Hideo WATANABE in Research Institute for Applied Mechanics, Kyushu University, Associate Prof. Naoko OONO in Yokohama National University, and Prof. Ryuta KASADA and Assistant Prof. Yusuke SHIMADA in Institute for Materials Research, Tohoku University also gave me many suggestions and comments about my research work. The NIFS staffs in research support division and library are also appreciated.

I would like to my warm appreciation to Associate Prof. Lei PENG at University of Science and Technology of China for his kindly guidance during master courses and constant help. I

am also thankful Prof. CunFeng YAO, Prof. TieLong SHEN, Associate Prof. HaiLong CHANG, Associate Prof. SiXiang ZHAO, Associate Prof. TianJi PENG, and Assistant Prof. Chao LIU at Institute of Modern Physics of the Chinese Academy of Sciences. Thanks for their helps in the previous research and living.

I also thankful to Associate Prof. Bo HUANG, Associate Prof. QiLai ZHOU, Dr. Xianghui YIN, Associate Prof. ShaoNing JIANG, Dr. Jie HUANG, Dr. WeiChao YAO, Mr. Le Quynh TRANG, Dr. Gaku, YAMAZAKI for friendship in Japan. The other colleagues and friends who shared happy time also included in this acknowledgement.

Finally, I would like to express my best appreciation to my parents for their love and encouragement.

MA Bing

August, 2021